UNIVERSITAT DE BARCELONA

Competition and Response: from Active Matter to Electrolytes under Confinement

Sara Dal Cengio

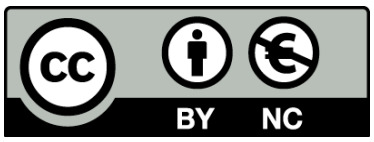

Tesi doctoral

Competition and Response: from Active Matter to Electrolytes under Confinement

Sara Dal Cengio

UNIVERSITAT DE BARCELONA

Competition and Response: from Active Matter to Electrolytes under Confinement

Programa de doctorat en Fisica

Autor: Sara Dal Cengio

Director: Ignacio Pagonabarraga

Tutor: Giancarlo Franzese

Barcelona 2020

UNIVERSITAT DE BARCELONA

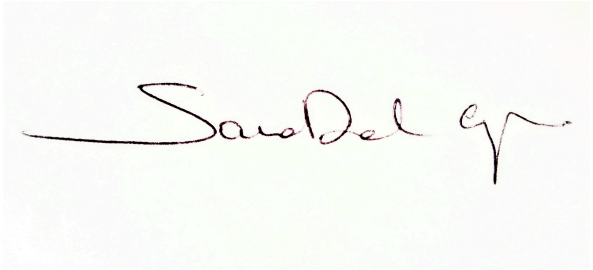

"Early morning corrected poem, then anatomy of frogs."

J. W. Goethe, a note on his personal diary (9 March 1797).

Acknowledgments

First of all, I would like to thank my supervisor Ignacio Pagonabarraga; under his guidance, I had the opportunity to freely develop my curiosity and truly *dig into science* in a way that was maybe disorienting at first but, after all, rewarding.
Each discussion with him was open and instructive, and I really hope that there will be more to come. I have also learned a great deal about physics, research and academia from Demian Levis. He inspired me in many ways and I hope we will keep in touch.

Admittedly, Lydéric Bocquet was like a second supervisor to me and I am very thankful to him for giving me the opportunity to spend over ten months in his group. I feel I have learned something from every member of the MicroMégas team and I hope to find such a dynamical working environment again in my future. In particular I would like to thank Anthony for being a brilliant collaborator and, most importantly, a really good friend. Come back soon to this side of the ocean!
The time I spent in Paris was incredibly intense and I eventually understood what Jérôme meant when saying that "you get inevitably absorbed by this city". I was extremely lucky to share this time with the family from "La Coloc" at the Maison Heinrich Heine in the Cité Universitaire. *Vielen Danke!*

I would like to acknowledge the European Union's Horizon 2020 research and innovation program for giving me the privilege to work as a Marie Skłodowska Curie fellow. My PhD experience wouldn't have been the same without the European network Nanotrans, that I was part of. Therein I met great people and I enjoyed spending time with them and seeing them finding their own way. Thank you Anthony, Ivan, Simon, Aitor, Lisa, Jannes, Meghna, Quentin, Bernhard, Lisbeth, Samuel, Mamisoa, Marco, Jérôme. I would also like to thank all the PI's for their commitment and in particular Benjamin, Jure and Marialore for the tireless work in organizing the annual meetings and the training activities.

Compared with my time in Paris, the years spent in Barcelona were, from a personal point of view, much more of a reflexive period specially thanks to Jérôme who became like a brother to me. I will never forget our endless conversations! Mi pequeña familia de Gran de Gracia eran Marc y Bea. Fueron los compañeros de cuarto perfectos para mí y mucho más. Gracias por todo, no veo la hora de planificar nuestro

próximo viaje. Gracias a Lucas por las charlas para el almuerzo y por hacerme soñar un poco al contarme tus aventuras. Gracias a Joan, Eloy y Luis por los consejos prácticos especialmente en lo que respecta a la burocracia catalana. Gracias a Jairo por su dulzura y las cenas que no me perdí. Gracias a toda la banda del la sexta planta por darme momentos de ligereza. Gracias a Muri, Alex y todos los visitantes de tránsito con los que compartí el buen rollo de la casa de carrer Providencia.

Una delle cose più belle che mi è successa in questi anni è stato assistere e partecipare alla nascita di una piccola comunità di amici/ricercatori/lettori/attivisti che si chiama ExTemporanea. Accade di rado che un gruppo di persone così eterogeneo ed affiatato si ritrovi nel momento giusto al posto giusto (che poi ha un nome ed è Festivaletteratura) per condividere idee, entusiasmo e, soprattutto, tempo. Ho assistito all'evoluzione di questo progetto e non vedo l'ora di scoprire quali strade inesplorate percorreremo insieme. Grazie a Matteo, Maria Elena, Emanuele, Giancarlo, Danilo, Lavinia, Elena Alma, Fulvio, Mattia, per offrirmi sempre una prospettiva diversa a cui pensare.

Infine, le persone a cui va il mio ringraziamento più grande sono i miei genitori, mia sorella Martina, la nonna Tina, gli zii Rossella e Silvio e, ovviamente, Andrea. Mi avete donato un sostegno e un affetto incondizionati di cui vi sarò per sempre grata. Siete la mia forza e a voi dedico questa tesi [1].

[1] Ora mi aspetto che la leggiate e mi facciate avere i vostri commenti.

Contents

Abstract

Most systems in Nature manifest complex transport phenomena arising from the interplay of multiple time and length scales, be them intrinsic in the system dynamics or externally enforced. It is the case, for instance, of a colony of migrating cells whose competing mechanisms of self-propulsion and interaction allow for the reorganization into different tissues. Or, by 'zooming in' and looking at the same system on a different scale, it is the case of the ionic channels located in the membranes of the aforesaid cells. These channels typically exhibit extraordinary ion selectivity and water permeability due to the interplay between geometric confinement, surface properties and external drivings.
Whether to investigate the collective structures of the former system or the nanofluidic properties of the latter one rests on the interests of the reader. In any case, she will find some food for thought in this Thesis.

Introduction

This Thesis is the result of three years I spent as a Ph.D. student at the Department of Condensed Matter Physics of the University of Barcelona under the supervision of prof. Ignacio Pagonabarraga. As the quotation at the head may suggest, you will not find here a discussion over a single research topic. More than anything else, this manuscript is the reflection of a time spent in finding my own way through the process of *researching*. As such, it involved some inspired and less-inspired moments, a lot of reading and, more importantly, people in the process of reasoning together. In particular, most of the ideas presented in Part I were shared and discussed with Demian Levis between Barcelona and Lausanne. He was the one who introduced me to the field of Active Matter. I also spent ten months from September 2018 to June 2019 as a visitor in the MicroMégas team at the Ecole Normale Supérieure in Paris. The material of Chapter 6 is work in progress that I have been elaborating during this time, together with Anthony Poggioli, from an idea of Lydéric Bocquet. In Paris, while working in the team of Lydéric Bocquet, I gained most of my understanding in the field of Nanofluidics which Part II is all about.

I have already named the two fields to which I would ascribe this Thesis, if needed. The first one is Active Matter, arguably the newest challenge in Non-Equilibrium Statistical Mechanics after Glassy Matter and Granular Matter. Unlike the latter systems which are slowly relaxing to, or externally driven out-of-equilibrium, Active Matter is composed of interacting units having their own source of motion. Each unit - be it a cell, a molecular motor, a auto-catalytic colloid - is capable of extracting energy from its environment to perform some task and, typically (as in the cases considered here), self-propel. Therefore active systems are driven out-of-equilibrium at the level of each constituent, in contrast with passive non-equilibrium systems, which are driven out-of-equilibrium by external global means (usually through their boundaries). This dichotomy of *global versus local* driving is the key feature of Active Matter which has been fascinating the community of statistical physicists in recent years. Activity - here intended as the ability to self-propel - is ubiquitous in living systems and gives rise to a rich many-body phenomenology which, from a theoretical point of view, is still largely elusive. To name but a few examples, ratchet-like behaviour [1, 2], spontaneous clustering [3, 4] and complex rheological responses [5, 6] were observed in recent experiments involving bacteria suspensions as well as artificial self-propelled colloids. None of these phenomena, being sustained

by the continuous dissipation of energy occurring at the level of each component, would be possible in passive systems.
In the attempt to characterize the departure from equilibrium of this novel class of systems, I took my first steps from posing the following question 1) How are the transport properties of a fluid affected by self-propulsion?
A starting point to address the question is the theory of linear response. In this context, the knowledge of a physical system is built upon slightly perturbing the system and measuring how it responds to external stimuli. Alternatively, if the system is originally in equilibrium, the same amount of information obtained by perturbing it is embedded in its spontaneous fluctuations. It is sufficient, in this case, to track the time correlations of the variables of interest to gain information on the non-equilibrium properties of the system, such as its transport coefficients. This is the content of the Fluctuation-Dissipation Theorem, arguably one of the key features and universal properties of equilibrium. As such, I take the validity/violation of the Fluctuation-Dissipation Theorem as a testbed to study the non-equilibrium nature of active systems. In Part I, I endeavour to address this issue by constructing a generic non-equilibrium framework and applying it to different models of Active Matter.

Part II is dedicated to a quite different subject which, just like Active Matter, has only recently emerged as a new scientific field: Nanofluidics - the study of water and ions transport at the nanometer scale. In the wake of the recent progress made in nanofluidic technology, new questions over the specificity of transport at the smallest scale have emerged. Exotic behaviours like non-linear responses [7,8], fast water flow [9,10] and high ionic selectivity [11,12] were recently observed in experiments involving nanometrically-confined electrolyte thus posing new challenges for the theorists. If one has to name the key feature of nanoscale systems, it would most likely be the *predominance of surface*. Nearly any object submerged in water acquires a net surface charge by releasing ions via dissociation events. In turn, ions distribute in the proximity of the object - be it a colloid or a channel wall - as a result of the balance of two opposing forces: thermal fluctuations and electrostatic attractions. This is an example of what I will later call an *entropy versus energy* competition (see Chapter 5). It gives rise to a collective phenomenon ubiquitous in confined electrolyte: the formation of a diffusive double-layer, i.e. the rearrangement of mobile charges to screen the charge of the surface. In this simple equilibrium picture, I have already introduced the two main ingredients that characterize an electrolyte system at the nanoscale: electrostatics and confinement. The following question thus arises: 2) what is the *role of surface* in ionic transport at the nanoscale? In order to answer this question, one has to introduce a third element, namely a force (or more than one) driving the system out-of-equilibrium coupling confinement and electrostatics to a dissipation mechanism. This is the subject matter of Part II.

So far, I haven't mentioned any applications neither in the field of Active Matter nor in the field of Nanofluidics. As a matter of fact, much could be said about it but this is not the subject matter of the Thesis. The closest thing to an application that you will find herein is the (exclusively theoretical) inquiry into the usage of

surface-driven ionic transport as a sensing tool (Chapter 6).

Overall, the Thesis aims at a fundamental understanding of the transport properties of the two classes of systems reported above. In both cases, the emergent response behaviour can be traced back to the intrinsic *multiscale nature* of the system which, ultimately, constitutes the underlying challenge of the present work. In the case of Active Matter, self-propulsion introduces a persistence (memory) in the particle dynamics which competes with the scale set by the inter-particle interactions, causing a departure from the standard response formulas. This is in turn a signature of the departure from equilibrium of active systems. As for electrolyte systems, the interplay of geometric confinement and electrostatic interactions strongly affects the transport properties in nanometric devices as opposed to the bulk.
The two broad questions stated in this introduction should then be taken as guidelines to navigate through the host of different theoretical techniques and reference models presented in the main body. Despite the variety of topics, the ultimate goal is onefold: capturing the essential features of scale competition and response.

Plan of the Thesis

The Thesis is divided into two parts which I tried to make symmetrical for the sake of aesthetics. Each part consists of a 'preamble' Chapter, setting the stage and introducing the formalism, and two Chapters where new results are presented and discussed, together with a brief state of the art and specific references therein. Each Chapter was given a self-contained structure, as much as possible.
In Chapter 1 the general framework and notation of stochastic modelling is established. In Chapter 2 I recall some general aspects of equilibrium stochastic dynamics that are important to clarify before moving to non-equilibrium dynamics. These are the principle of Detailed Balance and the Fluctuation-Dissipation Theorem. Then, an explicit connection between the breakdown of Detailed Balance and the concept of entropy production is drawn, allowing the derivation of general constraints a non-equilibrium stationary probability distribution must fulfil. An extended Fluctuation-Dissipation Relation valid for systems out-of-equilibrium is then derived and discussed. Chapter 3 is dedicated to the application of these results to simple models of self-propelled particles. I derive extended Fluctuation-Dissipation Relations and Green-Kubo expressions clarifying which features of these active model systems are genuinely non-equilibrium. Then, a small "Intermezzo" marks the division between Part I and Part II of the Thesis. Therein I discuss, with no claim for completeness, some aspects of Stochastic Thermodynamics which I explored mostly for personal interests. Chapter 4 is the preamble Chapter of Part II: it introduces the building blocks of electrolyte description. In Chapter 5 I study the phenomenon of Ionic Current Rectification in a nanofluidic diode. This is the nanofluidic analogue to a semiconductor diode and is a paradigmatic example of non-linear ionic transport. Using an effective description of the ionic dynamics, I explore the system response to an external electric field shedding light to the mechanism underlying rectification. Finally, in Chapter 6 I investigate the usage of

surface-driven ionic transport in the context of the Scanning Ionic Conductance Microscopy, a powerful microscopy technique to probe the topography and the surface charge of a given substrate.

Resum

Esta tesis recoge los resultados de tres años que pasé como estudiante de doctorato del Departamento de Física de la Materia Condensada de la Universidad de Barcelona bajo la supervisión del prof. Ignacio Pagonabarraga. Como puede sugerir la cita al principio, aquí no encontrará un discurso unitario sobre solamente un tema de investigación. Más que cualquier otra cosa, este manuscrito es el reflejo del tiempo dedicado en encontrar mi propio camino a través del proceso de *investigación*. Como tal, involucró momentos inspirados y menos inspirados, bastante lecturas y, lo que es más importante, personas en el proceso de razonamiento en conjunto. En particular, la mayoría de las ideas presentadas en la Parte I fueron compartidas y discutidas con Demian Levis entre Barcelona y Lausana. Él fue quien me introdujo en el campo de la materia activa. También pasé diez meses desde septiembre de 2018 hasta junio de 2019 como visitante en el equipo MicroMégas en la Ecole Normale Supérieure en París. El material del Capítulo 6 es un trabajo en progreso que he estado elaborando durante este tiempo, junto con Anthony Poggioli, a partir de una idea de Lydéric Bocquet. En París, mientras trabajaba en el equipo de Lydéric Bocquet, obtuve la mayor parte de mi comprensión en el campo de la nanofluídica, de lo que se trata la Parte II.

Ya he nombrado los dos campos a los que atribuiría esta tesis, si fuera necesario. El primero es la materia activa, posiblemente el desafío más nuevo en la mecánica estadística fuera de equilibrio después de la materia vítrea y la materia granular. A diferencia de los últimos sistemas los quales se relajan lentamente o se expulsan externamente fuera de equilibrio, la materia activa se compone de unidades interactivas que tienen su propia fuente de movimiento. Cada unidad - ya sea una célula, un motor molecular, un coloide autocatalítico - es capaz de extraer energía de su entorno para realizar alguna tarea y, típicamente (como en los casos que consideraremos aquí), autopropulsarse. Por lo tanto, los sistemas activos son propulsado fuera de equilibrio al nivel de cada componente, en contraste con los sistemas pasivos, que se impulsan fuera de equilibrio por medios globales externos (usualmente por medio de sus fronteras). Esta dicotomía de impulso *global versus local* es la característica clave de la materia activa que ha fascinado a la comunidad de físicos estadísticos en los últimos años. La actividad, que aquí entenderemos como la capacidad de autopropulsarse, es omnipresente en los sistemas vivos y presenta una rica fenomenología de muchos cuerpos que, desde un punto de vista teórico, todavía es bastante esquiva.

Por nombrar solo algunos ejemplos, se observó un comportamiento similar al de un trinquete [1,2], agrupamiento espontáneo [3,4] y respuestas reológicas complejas [5,6] en experimentos recientes con suspensiones de bacterias y coloides autopropulsados artificiales. Ninguno de estos fenómenos, sostenido por la disipación continua de energía que ocurre en el nivel de cada componente, sería posible en sistemas pasivos. En el intento de caracterizar la desviación del equilibrio de esta nueva clase de sistemas, tomé mis primeros pasos para plantear la siguiente pregunta 1) ¿Cómo se ven afectadas las propiedades de transporte de un fluido por la autopropulsión? Un punto de partida para abordar la cuestión es la teoría de la respuesta lineal. En este contexto, el conocimiento de un sistema físico se basa en perturbar ligeramente el sistema y medir cómo responde a estímulos externos. Alternativamente, si el sistema se ha equilibrado originalmente, la misma cantidad de información esta incrustada en sus fluctuaciones espontáneas. Es suficiente, en este caso, rastrear las correlaciones temporales de las variables de interés para obtener información sobre las propiedades de no equilibrio del sistema, como sus coeficientes de transporte. Este es el contenido del teorema de fluctuación-disipación, posiblemente una de las características clave y las propiedades universales del equilibrio. Como tal, tomo la validez / violación del teorema de fluctuación-disipación como un banco de pruebas para estudiar la naturaleza de no equilibrio de los sistemas activos. En la Parte I, me esfuerzo por abordar este problema construyendo un marco genérico de no equilibrio y aplicándolo a diferentes modelos de materias activas.

La Parte II está dedicada a un tema muy diferente que, al igual que la materia activa, ha surgido recientemente como un nuevo campo científico: la nanofluídica, el estudio del transporte de agua e iones a escala nanométrica. A raíz del reciente progreso realizado en la tecnología de nanofluídica, han surgido nuevas preguntas sobre la especificidad del transporte a la escala más pequeña. Comportamientos exóticos como respuestas no lineales [7, 8], flujo rápido de agua [9, 10] y alta selectividad iónica [11,12] fueron recientemente observados en experimentos con electrolitos confinados nanométricamente, lo que plantea nuevos desafíos para los teóricos. Si uno tiene que nombrar una característica clave de los sistemas a nanoescala, lo más probable es que sea el *predominio de la superficie*. Casi cualquier objeto sumergido en agua adquiere una carga superficial neta al liberar iones a través de eventos de disociación. A su vez, los iones se distribuyen en la proximidad del objeto, ya sea un coloide o una pared del canal, como resultado del equilibrio de dos fuerzas opuestas: fluctuaciones térmicas y atracciones electrostáticas. Este es un ejemplo de lo que más tarde llamaré una competencia *entropía versus energía* (ver Capítulo 5). Esto da lugar a un fenómeno colectivo ubicuo en electrolitos confinados: la formación de una doble capa difusa, es decir, la reorganización de las cargas móviles para proteger la carga de la superficie. En esta simple imagen de equilibrio, ya he introducido los dos ingredientes principales que caracterizan un sistema electrolítico a nanoescala: electrostática y confinamiento. Por lo tanto, surge la siguiente pregunta: 2) ¿Cuál es el *papel de la superficie* en el transporte iónico a nanoescala? Para responder a esta pregunta, uno tiene que introducir un tercer elemento, es dicir una fuerza (o más de una) que conduce al sistema fuera del equilibrio acoplando confinamiento y electrostática a un mecanismo de disipación. Este es el tema de la Parte II.

Hasta ahora, no he mencionado ninguna aplicación ni en el campo de la materia activa ni en el campo de la nanofluídica. De hecho, se podría decir mucho al respecto, pero este no es el tema de la tesis. Lo más parecido a una aplicación que encontrará aquí es la investigación (exclusivamente teórica) sobre el uso del transporte iónico de superficie como herramienta de detección (Capítulo 6).

En general, la tesis apunta a una comprensión fundamental de las propiedades de transporte de las dos clases de sistemas reportados anteriormente. En ambos casos, el comportamiento de respuesta emergente se remonta a la *naturaleza multiescala* intrínseca de los sistemas que, en última instancia, constituye el desafío fundamental del presente trabajo. En el caso de la materia activa, la autopropulsión introduce una persistencia (memoria) en la dinímica de las partículas que compite con la escala establecida por las interacciones entre partículas, lo que provoca una desviación de las fórmulas de respuesta estándar. Esto es a su vez una firma de la desviación del equilibrio de los sistemas activos. En cuanto a los sistemas electrolíticos, la interacción del confinamiento geométrico y las interacciones electrostáticas afecta fuertemente las propiedades de transporte en los dispositivos nanométricos en comparación con el volumen.
Las dos preguntas generales planteadas en esta introducción deben tomarse como pautas para navegar a través de la variedad de diferentes técnicas teóricas y modelos de referencia presentados en el cuerpo principal. A pesar de la variedad de temas, el objetivo final es sencillo: capturar las características esenciales de la competencia y la respuesta a escala.
La tesis se divide en dos partes, cada una de las cuales consiste en un capítulo de 'preámbulo', preparando el escenario e introduciendo el formalismo, y dos capítulos donde se presentan y discuten nuevos resultados (junto con un breve estado del arte y referencias específicas en el mismo). Cada capítulo tiene una estructura auto contenida, tanto como es posible.

En el Capítulo 1 se establece la notación y el marco general de modelado estocástico. En el Capítulo 2 recuerdo algunos aspectos generales de dinámica estocástica de equilibrio que son importantes para aclarar antes de pasar a la dinámica de no equilibrio. Estos son el principio del equilibrio detallado y el teorema de fluctuación-disipación. Luego, se establece una conexión explícita entre el desglose del equilibrio detallado y el concepto de producción de entropía, lo que permite la derivación de restricciones generales que una distribución de probabilidad estacionaria no de equilibrio debe cumplir. Luego se deriva y discute una relación extendida de fluctuación-disipación válida para sistemas fuera de equilibrio. El Capítulo 3 está dedicado a la aplicación de estos resultados a modelos simples de partículas autopropulsadas. Derivo relaciones extendidas de fluctuación-disipación y expresiones Green-Kubo que aclaran qué características de estos sistemas de modelos activos son genuinamente no equilibradas. Aqui un pequeño Intermezzo marca la distinción entre la Parte I y la Parte II de la tesis. Ahí discuto, sin reclamo de integridad, algunos aspectos de la termodinámica estocástica que exploré principalmente para intereses personales. El Capítulo 4 es el capítulo del preámbulo de la Parte II que contiene los componentes básicos de la descripción del campo medio de electrolitos. En el Capítulo 5

estudio el fenómeno de la rectificación de corriente iónica en un diodo nanofluídico. Este es el análogo nanofluídico de un diodo semiconductor y es un ejemplo paradigmático de transporte iónico no lineal. Usando un descripción efectiva de la dinámica iónica, exploro la respuesta del sistema a un campo eléctrico externo que arroja luz al mecanismo subyacente a la rectificación de corriente.
Finalmente, en el Capítulo 6 investigo el uso del transporte iónico impulsado por la superficie en el contexto de la microscopía de conductancia iónica de barrido, una poderosa técnica de microscopía para sondear la topografía y la carga superficial de un sustrato dado.

PART I

Chapter 1

Preamble: Stochastic Modelling

Ever since the earliest studies on Brownian Motion [13, 14], stochastic modelling plays a central role in the study of complex physical systems made up of many degrees of freedom. The fundamental abstraction underlying such modelling is the distinction of two classes of variables: a slow-varying set of state variables describing the *system* and a fast-varying set of 'random' variables describing the *environment*, or *bath*. Once the distinction is settled, the modelist typically writes a Langevin equation for each of the state variables Γ_i, comprising a noise term $\xi_i(t)$ due to the coupling with the (unobserved) degrees of freedom of the environment:

$$\dot{\Gamma}_i = \mathcal{A}_i + (2D_i)^{1/2}\,\xi_i(t)\,. \tag{1.1}$$

The physics of the system enters in Eq. (1.1) through the drift $\mathcal{A}_i$ and the nature of the noise $\xi_i(t)$, namely its amplitude D_i, here taken to be constant, and its statistics.

In some simple cases, the stochastic description of Eq. (1.1) may be rigorously derived from an underlying deterministic dynamics via a coarse-graining procedure [15]. Most of the time, however, as for the case of the stochastic models of active systems discussed in Chapter 3, Eq. (1.1) is the starting point to study a certain phenomenology of interest. As such, in the following treatment, Eq. (1.1) will have the status of a microscopic dynamics, the finest level of description available on the system. In this context, some issues arise on how to correctly draw the boundary between the system and the environment. How many slow variables are needed to adequately describe the system dynamics? In practice, the answer will depend on the domain of explanation and predictability of each specific model [16]. Since the noise $\xi_i(t)$ derives from the cumulative effect of many equilibrated degrees of freedom (the environment) one typically models it as Gaussian delta-correlated noise. Under this approximation, the stochastic variables Γ_i are 'memory-less' and all the theoretical machinery of Markovian processes becomes available. In particular, for a Markovian process the Langevin description of Eq. (1.1) is fully equivalent to the Fokker-Planck description, which will be largely employed in the next sections and Chapters. The advantage is to move from a stochastic equation (1.1) for the variables Γ_i to an ordinary differential equation for a probability density $\Psi(\{\Gamma_i\})$. Notably, the delta-correlated noise is itself an idealization as any fluctuation in the

real world has an intrinsic finite characteristic time τ. Whenever τ is comparable to the dynamics of the 'slow' variables Γ_i, the noise is said to be coloured and the system is non-Markovian. Many different Markovian approximations were developed in the '80s to deal with non-Markovian processes [17,18]. Therein, the tacit assumption is that it is possible to approximately describe the dynamics of the original process through a different Markovian model. This observation will show its relevance in Chapter 3 when dealing with Markovian approximations for active systems. As will be made clear, one of the key features of activity is indeed the introduction of a persistence time in the motion of self-propelled particles which breaks Markovianity together with Time-Reversal Symmetry.
In the rest of the Chapter, I introduce the general framework and notions used throughout Chapter 2 and 3. Any reader familiar with the formalism of stochastic processes may directly move to the next Chapter.

1.1 Fokker-Planck Equation

Our starting point is a generic system with N stochastic variables $\mathbf{\Gamma} \equiv \{\Gamma_i\}_{i=1}^N$ defined on a manifold $\mathcal{M} \subset \mathbb{R}^N$. Let introduce a probability distribution Ψ which assigns $\Psi(\mathbf{\Gamma}, t)$ to any point $\mathbf{\Gamma} \in \mathcal{M}$ at a time t. The implicit assumption is the requirement for Ψ to be smooth enough for its partial derivatives to exist.

Generically the time evolution of $\Psi(\mathbf{\Gamma}, t)$ is described by a generator $\Omega_0(\mathbf{\Gamma})$:

$$\partial_t \Psi(\mathbf{\Gamma}, t) = \Omega_0(\mathbf{\Gamma})\Psi(\mathbf{\Gamma}, t)\,, \tag{1.2}$$

together with an appropriate initial condition $\Psi(\mathbf{\Gamma}, 0)$. Formal integration of Eq. (1.2) leads to $\Psi(\mathbf{\Gamma}, t) = e^{\Omega_0 t}\Psi(\mathbf{\Gamma}, 0)$. Let denote Ψ_0 the steady-state solution of the dynamics above, meaning

$$\Omega_0 \Psi_0 = 0\,. \tag{1.3}$$

Under the hypothesis of Markovianity, the generator in Eq. (1.2) has the so-called Fokker-Planck form:

$$\boxed{\Omega_0(\mathbf{\Gamma}) = \sum_i \left(-\partial_i \mathcal{A}_i(\mathbf{\Gamma}) + \sum_j \partial_i \partial_j \mathcal{B}_{ij}(\mathbf{\Gamma}) \right)\,,} \tag{1.4}$$

where $\partial_i \equiv \partial/\partial\Gamma_i$, $\mathcal{A} \equiv \{\mathcal{A}_i\}_{i=1}^N$ is the drift vector and $\mathcal{B} \equiv \{\mathcal{B}_{ij}\}_{i,j=1}^N$ is the $N \times N$ diffusive matrix. In the following, unless explicitly stated otherwise, $\mathcal{B}$ is taken to be invertible and diagonal with constant entries, such that $\mathcal{B}_{ij} \equiv D_i \delta_{ij}$ and Eqs. (1.2) is the equivalent of Eq. (1.1).

The dynamics is fully specified by the knowledge of $\Psi(\mathbf{\Gamma}, t)$ or, equivalently, by the knowledge of the conditional probability density $P(\mathbf{\Gamma}, t|\mathbf{\Gamma}_0, t_0)$ defined as the probability to be in $\mathbf{\Gamma}$ at time t given the configuration $\mathbf{\Gamma}_0$ at time t_0. Eq. (1.2) can be recast in terms of $P(\mathbf{\Gamma}, t|\mathbf{\Gamma}_0, t_0)$ as

$$\partial_t P(\mathbf{\Gamma}, t|\mathbf{\Gamma}_0, t_0) = \Omega_0(\mathbf{\Gamma})P(\mathbf{\Gamma}, t|\mathbf{\Gamma}_0, t_0)\,, \tag{1.5}$$

which is often called *forward* equation to distinguish it from the *backward* equation:

$$\partial_{t_0} P(\mathbf{\Gamma}, t|\mathbf{\Gamma}_0, t_0) = -\Omega_0^\dagger(\mathbf{\Gamma}_0)P(\mathbf{\Gamma}, t|\mathbf{\Gamma}_0, t_0)\,, \tag{1.6}$$

where $\Omega_0^\dagger(\mathbf{\Gamma}) = \sum_i \mathcal{A}_i(\mathbf{\Gamma})\partial_i + D_i\partial_i^2$ is the adjoint of Ω_0. Both Eq. (1.2) and Eq. (1.6) are valid for positive times $t > t_0 > 0$, hence $P(\mathbf{\Gamma}, t|\mathbf{\Gamma}_0, t_0)$ must fulfil them simultaneously. The main difference between the two equations is the set of variables that are held fixed. In Eq. (1.2) one fixes the *initial* condition at time t_0 and looks at the evolution for $t > t_0$. In Eq. (1.6), instead, one fixes the *final* condition at time t and looks at the evolution for $t_0 < t$.

1.2 Symmetry Aspects under Time-Reversal

The variables Γ_i shall be distinguished according to their parity under the Time-Reversal operator $\mathcal{T}$

$$\boxed{\mathcal{T} : \mathbf{\Gamma} \in \mathcal{M} \mapsto \boldsymbol{\varepsilon}\mathbf{\Gamma} \equiv \{\varepsilon_i \Gamma_i\} \in \mathcal{M}, \varepsilon_i = \pm 1\,.} \tag{1.7}$$

Variables Γ_i for which $\varepsilon_i = 1$ are said even under Time-Reversal and variables for which $\varepsilon_i = -1$ are said to be odd. For instance, if one has in mind the dynamics of a particle in phase space, then $\mathbf{\Gamma} = (r, p)$ and

$$\mathcal{T} : (r,\, p) \mapsto (r,\, -p)\,. \tag{1.8}$$

The position variable r is even while momentum p is odd.

The Fokker-Planck equation stands for the conservation of the probability density and can thus be written in terms of a probability flux $\boldsymbol{J} \equiv \{J_i\}_{i=1}^N$:

$$\Omega_0 \Psi(\mathbf{\Gamma}, t) = -\boldsymbol{\nabla} \cdot \boldsymbol{J}(\mathbf{\Gamma}, t) \tag{1.9a}$$

$$J_i(\mathbf{\Gamma}, t) = \mathcal{A}_i(\mathbf{\Gamma})\Psi(\mathbf{\Gamma}, t) - D_i\partial_i\Psi(\mathbf{\Gamma}, t)\,, \tag{1.9b}$$

where $\boldsymbol{\nabla} \equiv \{\partial_i\}$. Since $\{\Gamma_i\}$ can be either even or odd under Time-Reversal, one can decompose the drift vector in a *reversible* and an *irreversible* part, $\mathcal{A} = \mathcal{A}^{\text{rev}} + \mathcal{A}^{\text{irr}}$, defined as

$$\boxed{\begin{aligned} \mathcal{A}_i^{\text{rev}}(\mathbf{\Gamma}) &\equiv \frac{1}{2}\left[\mathcal{A}_i(\mathbf{\Gamma}) - \varepsilon_i \mathcal{A}_i(\boldsymbol{\varepsilon}\mathbf{\Gamma})\right] && \text{(1.10a)} \\ \mathcal{A}_i^{\text{irr}}(\mathbf{\Gamma}) &\equiv \frac{1}{2}\left[\mathcal{A}_i(\mathbf{\Gamma}) + \varepsilon_i \mathcal{A}_i(\boldsymbol{\varepsilon}\mathbf{\Gamma})\right] && \text{(1.10b)} \end{aligned}}$$

which, under Time-Reversal transform as

$$\mathcal{A}_i^{\text{rev}}(\boldsymbol{\varepsilon}\mathbf{\Gamma}) = -\varepsilon_i \mathcal{A}_i^{\text{rev}}(\mathbf{\Gamma}), \qquad \mathcal{A}_i^{\text{irr}}(\boldsymbol{\varepsilon}\mathbf{\Gamma}) = \varepsilon_i \mathcal{A}_i^{\text{irr}}(\mathbf{\Gamma})\,. \tag{1.11}$$

This allows to identify two distinct contributions to the total probability flux $J_i(\mathbf{\Gamma}, t) = J_i^{\text{rev}}(\mathbf{\Gamma}, t) + J_i^{\text{irr}}(\mathbf{\Gamma}, t)$, where

$$\boxed{\begin{aligned} J_i^{\text{rev}}(\mathbf{\Gamma}, t) &= \mathcal{A}_i^{\text{rev}}(\mathbf{\Gamma})\Psi(\mathbf{\Gamma}, t) && \text{(1.12a)} \\ J_i^{\text{irr}}(\mathbf{\Gamma}, t) &= \mathcal{A}_i^{\text{irr}}(\mathbf{\Gamma})\Psi(\mathbf{\Gamma}, t) - D_i\partial_i\Psi(\mathbf{\Gamma}, t)\,. && \text{(1.12b)} \end{aligned}}$$

By denoting the steady-state flux as $\boldsymbol{J}_0$, the *steady-state velocity* is defined as

$$\boxed{\boldsymbol{\mathcal{V}}(\mathbf{\Gamma}) \equiv \boldsymbol{J}_0(\mathbf{\Gamma})/\Psi_0(\mathbf{\Gamma}) = \{\mathcal{V}_i^{\text{rev}} + \mathcal{V}_i^{\text{irr}}\}_{i=1}^N\,.} \tag{1.13}$$

[In the following, I report explicitly the time-dependence in the velocity $\boldsymbol{\mathcal{V}}(\boldsymbol{\Gamma}, t)$ to indicate $\boldsymbol{\mathcal{V}}(\boldsymbol{\Gamma}, t) \equiv \boldsymbol{J}(\boldsymbol{\Gamma}, t)/\Psi(\boldsymbol{\Gamma}, t)$]. The decomposition of the probability flux into two contributions with different symmetry under Time-Reversal will play a central role in the following treatment. All the dissipative terms are embedded in Eq. (1.12b) which is recognized to be the standard Helmholtz decomposition of $\mathcal{A}_i^{\text{irr}}$ into a conservative and a circulation part [19–21]. To illustrate the definitions above, let consider a simple example: a Brownian particle, moving in one dimension, at position $x(t)$ and momentum $p(t)$ at time t, i.e. $\boldsymbol{\Gamma} = (x, p)$, described by the following Langevin equation:

$$\dot{x}(t) = p(t) \qquad \dot{p}(t) = -U'(x) - \gamma p(t) + \sqrt{2\gamma k_B T}\xi(t) \tag{1.14}$$

where $-U'(x)$ is the total force exerted on the particle, which can either come from inter-particle interactions or an external field, γ is the drag coefficient and $\xi(t)$ is a Gaussian white noise of zero mean and unit variance. [Here and in the rest of the Thesis I set the mass $m \equiv 1$]. The last two terms of the right hand side account for the coupling of the particle with a thermal bath at temperature T, source of noise and dissipation. In equilibrium, the Fluctuation-Dissipation Theorem constraints the amplitude of the noise and dissipation to be related, as made apparent in the equation above. The latter Langevin equation, can be equivalently written as the Fokker-Planck equation, with the drift and diffusion vectors

$$\mathcal{A} = \begin{bmatrix} \mathcal{A}_x = p(t) \\ \mathcal{A}_p = -U'(x) - \gamma p(t) \end{bmatrix} \tag{1.15a}$$

$$\mathcal{B} = \begin{bmatrix} 0 & 0 \\ 0 & \gamma k_B T \end{bmatrix} . \tag{1.15b}$$

Under Time-Reversal, the dynamic variables transform as

$$\boldsymbol{\varepsilon}\boldsymbol{\Gamma} = \boldsymbol{\varepsilon} \begin{bmatrix} x \\ p \end{bmatrix} = \begin{bmatrix} x \\ -p \end{bmatrix} . \tag{1.16}$$

Let now apply the definition of the reversible and irreversible drift vectors Eqs. (1.10a-1.10b) and find

$$\mathcal{A}^{\text{rev}} = \begin{bmatrix} p(t) \\ -U'(x) \end{bmatrix} , \ \mathcal{A}^{\text{irr}} = \begin{bmatrix} 0 \\ -\gamma p(t) \end{bmatrix} . \tag{1.17}$$

In the overdamped limit, the Brownian particle can be described by

$$\dot{x}(t) = -\mu U'(x) + \sqrt{2\mu k_B T}\xi(t) \, , \tag{1.18}$$

where $\mu = 1/\gamma$. The drift and diffusion vectors thus read

$$\mathcal{A} = -\mu U'(x) = \mathcal{A}^{\text{irr}} \, , \qquad \mathcal{B} = \mu k_B T = D_x \, . \tag{1.19}$$

In this case, the only dynamic variable is x, which is even. The absence of odd variables implies the absence of reversible fluxes, and thus $\mathcal{A}^{\text{rev}}$ is identically zero. It is worth at this stage to make a few remarks. For the underdamped system, $\mathcal{B}$ is

non-invertible. This will have a consequence on the determination of the steady-state distribution fulfilling Detailed Balance as shown in the next Chapter; see therein for more details. Finally, in the absence of dissipation (and diffusion) the generator Ω_0 would be identified with the Liouville operator. In that case, the irreversible part of the flux would vanish and the motion would be purely reversible, as expected from Time-Reversal Symmetry of the 'microscopic' Hamilton equations of motion.

1.3 Observables

In this section let fix some notations and definitions that will be used in the following. Physical observables are represented by real functions acting on $\mathcal{M}$, such that $A : \mathbf{\Gamma} \in \mathcal{M} \mapsto A(\mathbf{\Gamma}) \in \mathbb{R}$. Their steady-state average is defined as

$$\boxed{\langle A \rangle_0 = \int_{\mathcal{M}} d\mathbf{\Gamma} A(\mathbf{\Gamma}) \Psi_0(\mathbf{\Gamma})} \tag{1.20}$$

and the ensemble average at time t is defined as

$$\boxed{\langle A \rangle_t = \int_{\mathcal{M}} d\mathbf{\Gamma} A(\mathbf{\Gamma}) \Psi(\mathbf{\Gamma}, t) = \int_{\mathcal{M}} d\mathbf{\Gamma} A(\mathbf{\Gamma}) e^{\Omega_0 t} \Psi(\mathbf{\Gamma}, 0)\,.} \tag{1.21}$$

The time evolution may be given to the observables (instead of the probability distribution) using the adjoint of the Fokker-Planck generator

$$\boxed{\langle A \rangle_t = \int_{\mathcal{M}} d\mathbf{\Gamma} e^{\Omega_0^\dagger t} A(\mathbf{\Gamma}) \Psi(\mathbf{\Gamma}, 0) \equiv \int_{\mathcal{M}} d\mathbf{\Gamma} A(t) \Psi(\mathbf{\Gamma}, 0).} \tag{1.22}$$

Both expressions of $\langle A \rangle_t$ are fully equivalent and are respectively referred to as the Schrödinger and Heisenberg representation, by analogy with Quantum Mechanics [22]. In the Schrödinger the time dependence is encoded in the probability density (analogous to the wave-function), while in the Heisenberg representation, the time dependence is encoded in the observables, which are now explicitly time-dependent and are evolved by the adjoint of the evolution generator (analogous to Hermitian operators acting on a Hilbert space).
Finally, let introduce the linear response function $R_A(t, s)$ which encodes the change of an observable A due to a perturbation h, applied on the system originally at steady state. It is defined as

$$\boxed{\langle A \rangle_t - \langle A \rangle_0 = \int_0^t ds R_A(t, s) h(s) + O(h^2)\,, \quad t > s.} \tag{1.23}$$

Chapter 2

Fluctuation-Dissipation Relations in the absence of Detailed Balance

2.1 Introduction

The Fluctuation-Dissipation Theorem (FDT) relates the correlations of spontaneous fluctuations, to the fluctuations induced by external stimuli [23]. In practice, it allows to probe the response to external fields by analysing the corresponding time-dependent equilibrium fluctuations, either in experiments or in simulations. For instance, it allows to infer transport or mechanical properties of soft materials from light scattering without ever perturbing them [24, 25]. The FDT plays a particular important role in Statistical Mechanics as it is among the very rare general results in non-equilibrium, although near to, conditions. It is valid for any equilibrium system (both in the classical and quantum realm) gently driven out-of-equilibrium by a small perturbation. Accordingly to the FDT, the response of an observable A at time t to a perturbation h, applied at time s, and causing the change in the energy of the system $E \to E - h(s)B$, is determined by an equilibrium correlation function as

$$\boxed{\left.\frac{\delta\langle A(t)\rangle}{\delta h(s)}\right|_{h\to 0} = R_A(t,s) = \beta\frac{\partial}{\partial s}\langle A(t)B(s)\rangle_{\text{eq}}, \quad t > s} \tag{2.1}$$

where $\langle A(t)B(s)\rangle_{\text{eq}}$ is the equilibrium correlation function between the observable A and the conjugated observable B at temperature $\beta^{-1} = k_B T$ [1].

In its general formulation above, the FDT was first derived in the context of Hamiltonian Mechanics [26, 27], where the dynamics is specified via a Liouville operator and the equations of motion are invariant under Time-Reversal. It has later been extended to stochastic descriptions [28] in which dissipative and noisy terms enter into the equations of motion standing for the coupling with the environment. As a result, the equations are no longer invariant under Time-Reversal. Nevertheless a footprint of reversibility holds at the stochastic description level under the name

[1] I consider, without loss of generality, observables with zero mean.

of Detailed Balance (DB) [29, 30]. As long as DB is guaranteed, the FDT holds, both in thermal and athermal states [31, 32].

For systems breaking DB, relentlessly evolving far-from-equilibrium, the FDT is no longer justified. The question of whether a similar relation as Eq. (2.1) can be derived in this case, has been the focus of a great deal of research efforts over the last decades. In particular, several extended Fluctuation-Dissipation Relations (FDR) have been derived, using different approaches, for systems in non-equilibrium steady-states (NESS). However, contrary to equilibrium states, no universal relation such as Eq. (2.1) exists for NESS. The establishment of a general extended FDR with the features of the equilibrium FDT, remains a central challenge towards the construction of a general framework to deal with non-equilibrium systems. In the context of stochastic dynamics, extended FDR for NESS have mostly focused on overdamped descriptions [33–39]. I refer to [40–42] for recent reviews on the topic.

Among the variety of non-equilibrium systems, Active Matter (embedding Living Matter) constitutes a particularly interesting class. As stated in the Introduction, the present goal is to answer the question of how the FDT is broken in interacting active particles systems and more generally to study how these systems respond to an external small perturbation. Although the non-equilibrium nature of active systems is intrinsically different from the one of passive driven systems, as for the construction of a linear response theory, the fundamental difficulty to be tackled in both cases is the breakdown of DB. For this reason the present Chapter is dedicated to a general discussion on DB and the consequences of its violation while the applications to archetypical models of active systems are reserved to the next Chapter. In the following sections, a general constraint on the NESS to be fulfilled by *any* Markovian dynamics, in presence of DB or not, is established. The framework and results obtained apply to both systems with only even variables and even and odd variables under Time-Reversal, such as overdamped and underdamped Langevin processes. Such constraint on the NESS stands for a relation between the nature of the non-equilibrium fluxes and the symmetry (under Time-Reversal) of the NESS distribution. Thus, an extended FDR for stochastic dynamics breaking DB is derived.

2.2 Equilibrium dynamics

2.2.1 Detailed Balance

Whether one interprets a stochastic dynamics as deriving from an underlying microscopic description fulfilling the laws of Classical or Quantum Mechanics or not, DB constitutes the key symmetry of equilibrium. A system is said to satisfy DB if, at stationarity, any microscopic process is balanced by the reversed one. It can thus be formally written as

$$\boxed{P(\mathbf{\Gamma}_f, t_f|\mathbf{\Gamma}_i, t_i)\Psi_0(\mathbf{\Gamma}_i) = P(\boldsymbol{\varepsilon}\,\mathbf{\Gamma}_i, t_f|\boldsymbol{\varepsilon}\mathbf{\Gamma}_f, t_i)\Psi_0(\boldsymbol{\varepsilon}\mathbf{\Gamma}_f)} \tag{2.2}$$

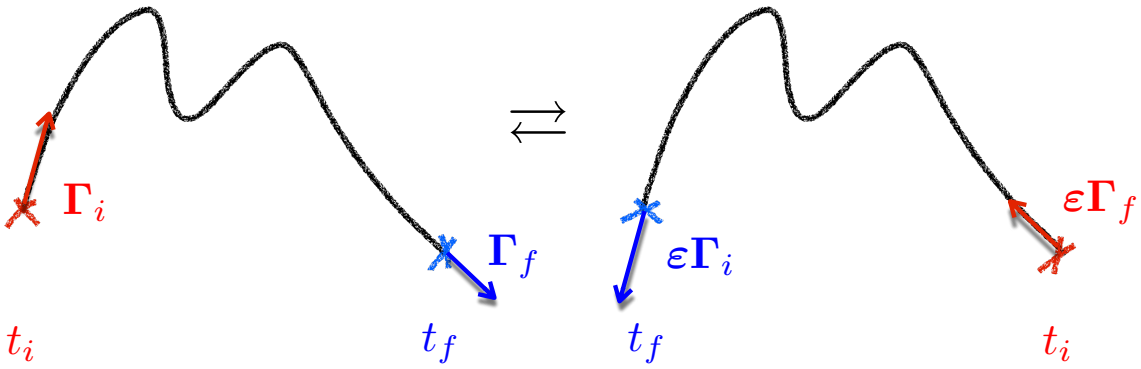

Figure 2.1: Illustration of a dynamics verifying Detailed Balance: the probability of both transitions, from state $\boldsymbol{\Gamma}_i$ to $\boldsymbol{\Gamma}_f$ and from $\boldsymbol{\epsilon\Gamma}_f$ to $\boldsymbol{\epsilon\Gamma}_i$, must be equal.

for any pair of states $(\boldsymbol{\Gamma}_i, \boldsymbol{\Gamma}_f)$ and at any times (t_i, t_f) (see cartoon Fig. 2.1). By setting $t_i = t_f$ in Eq. (2.2) one gets:

$$\Psi_0(\boldsymbol{\Gamma}) = \Psi_0(\boldsymbol{\varepsilon\Gamma}), \quad \forall\, \boldsymbol{\Gamma} \in \mathcal{M}\,. \tag{2.3}$$

It follows that the mean value of any odd *current-like* observable, i.e. $A(\boldsymbol{\varepsilon\Gamma}) = -A(\boldsymbol{\Gamma})$ must be zero if DB is fulfilled [2]. Rather than being a symmetry at the level of single trajectories (as for the microscopic description), DB is formulated in Eq. (2.3) as a symmetry property of the steady-state distribution $\Psi_0(\boldsymbol{\Gamma})$. Actually, a necessary and sufficient condition for DB to hold is the absence of irreversible fluxes in steady conditions [43]:

$$\boxed{\text{Detailed Balance} \Leftrightarrow \boldsymbol{J}_0^{\text{irr}} = 0} \tag{2.4}$$

where $\boldsymbol{J}_0^{\text{irr}} = \{\mathcal{A}_i^{\text{irr}}(\boldsymbol{\Gamma})\Psi_0(\boldsymbol{\Gamma}) - D_i\partial_i\Psi_0(\boldsymbol{\Gamma})\}_{i=1}^N$. This means that reversible steady-state fluxes are not constrained by DB. To illustrate this aspect let go back to the example of the Brownian particle. In the absence of even variables, i.e. in the overdamped regime, DB corresponds precisely to the absence of steady-state fluxes (since $J^{\text{rev}} = 0$). However, in the presence of odd (momentum-like) variables as in the underdamped description, reversible steady-state fluxes can be present in a system fulfilling DB (although physical currents must have all zero ensemble averages, see Eq. (2.3)) [44, 45].

The absence of irreversible fluxes can be rewritten as

$$\partial_i \log \Psi_0(\boldsymbol{\Gamma}) = D_i^{-1}\mathcal{A}_i^{\text{irr}}(\boldsymbol{\Gamma}), \tag{2.5}$$

which in turn imposes the so-called 'thermodynamic curvature' (the curl in N dimensions) [46] of the irreversible drift to vanish:

$$\boxed{D_i^{-1}\partial_j\mathcal{A}_i^{\text{irr}}(\boldsymbol{\Gamma}) - D_j^{-1}\partial_i\mathcal{A}_j^{\text{irr}}(\boldsymbol{\Gamma}) = 0\,.} \tag{2.6}$$

[2] Note that here I am referring to physical currents and not to the probability current J_i in Eq. (1.9). Indeed, Eq. (2.3) implies $\langle A\rangle_0 = \int d\boldsymbol{\Gamma} A(\boldsymbol{\varepsilon\Gamma})\Psi_0(\boldsymbol{\varepsilon\Gamma}) = -\int d\boldsymbol{\Gamma} A(\boldsymbol{\Gamma})\Psi_0(\boldsymbol{\Gamma}) = -\langle A\rangle_0$ if $A(\boldsymbol{\varepsilon\Gamma}) = -A(\boldsymbol{\Gamma})$.

The latter expression provides an alternative definition of DB in terms of geometrical properties of the drift and diffusion terms. The advantage of Eq. (2.6) over the definition in Eqs. (2.4-2.5) is that it allows to verify if a dynamics fulfils or not DB without the need of solving for $\Psi_0(\mathbf{\Gamma})$. The constraint imposed by DB on the steady-state currents provides a natural route to explicitly derive a steady solution. Whenever Eq. (2.6) is satisfied, one can derive a steady solution by direct integration. No such a procedure exists if DB is broken, and in this case solving the multivariate Fokker-Planck equation is typically prohibitive with no guarantee of a stationary solution at all. This is precisely the great advantage of equilibrium dynamics: the steady-state can be solved just by quadrature, giving the equilibrium distribution

$$\Psi_0(\mathbf{\Gamma}) = \Psi_{\rm eq}(\mathbf{\Gamma}) = \mathcal{N} \exp\left[\sum_i \int D_i^{-1} \mathcal{A}_i^{\rm irr} d\Gamma_i\right] , \tag{2.7}$$

with $\mathcal{N}$ the normalization constant such that $\int d\mathbf{\Gamma} \Psi_0(\mathbf{\Gamma}) = 1$.

It is straightforward to apply Eq. (2.7) to the case of an equilibrium Brownian particle in the overdamped limit, Eq. (1.18). In this case the integral in Eq. (2.7) gives the Boltzmann distribution $\Psi_{\rm eq}(\mathbf{\Gamma}) = \mathcal{N} \exp\left[-\beta U(x)\right]$. As mentioned in the previous Chapter, a little care must be taken when applying Eq. (2.7) to the underdamped particle of Eq. (1.14) - since in this case the diffusive matrix is non-invertible, see Eq. (1.15b). In this case, the integral over the phase space in Eq. (2.7) has to be carried on momenta only, to find

$$\Psi_{\rm eq}(\mathbf{\Gamma}) \sim \exp\left[-\beta(p^2/2 + \Lambda(x))\right] \tag{2.8}$$

with $\Lambda(x)$ a function of spatial coordinates to be determined by imposing stationarity (i.e. $\Omega_0 \Psi_0 = 0$). In the presence of odd variables (underdamped case), the steady-state distribution is not fully determined by DB, which only constraints irreversible fluxes, but one has also to explicitly apply the evolution equation to specify the dependence on positions, which, as expected, results in $\Lambda = U$.

2.2.2 The Fluctuation-Dissipation Theorem

Let focus now on the linear response of a system initially prepared in a steady-state. At $t = 0$ an infinitesimal perturbation is applied to the drift vector $\mathcal{A} \to \mathcal{A} + \delta\mathcal{A}$ which results in a change of the generator $\Omega_0 \to \Omega = \Omega_0 + \Omega_{\rm ext}$. The evolution equation (1.2) now reads:

$$\partial_t \Psi(\mathbf{\Gamma}, t) = \Omega \Psi(\mathbf{\Gamma}, t) = \left[\Omega_0(\mathbf{\Gamma}) + \Omega_{\rm ext}(\mathbf{\Gamma})\right] \Psi(\mathbf{\Gamma}, t) \,, \tag{2.9}$$

where

$$\Omega_{\rm ext}(\mathbf{\Gamma}) \Psi(\mathbf{\Gamma}, t) = -\boldsymbol{\nabla} \cdot \left[\delta\mathcal{A}(\mathbf{\Gamma}) \Psi(\mathbf{\Gamma}, t)\right] \tag{2.10}$$

accounts for the perturbation. Since the generator Ω does not explicitly depend on time, one can write [47]:

$$\int_0^t \frac{d}{ds} e^{\Omega s} ds = \int_0^t \Omega e^{\Omega s} ds = e^{\Omega t} - 1 \,. \tag{2.11}$$

By using the latter expression into $\Psi(\mathbf{\Gamma},t) = e^{\Omega t}\Psi(\mathbf{\Gamma},0)$ one obtains, to first order in $\delta\mathcal{A}$,

$$\Psi(\mathbf{\Gamma},t) = \Psi_0(\mathbf{\Gamma}) + \int_0^t ds\, e^{\Omega_0(\mathbf{\Gamma})s}\Omega_{\text{ext}}(\mathbf{\Gamma})\Psi_0(\mathbf{\Gamma})\,. \tag{2.12}$$

For an observable A, then the so-called Agarwal FDR [31] follows:

$$\boxed{\langle A\rangle_t - \langle A\rangle_0 = \int_0^t ds\,\langle A(s)B(0)\rangle_0\,, \qquad B(0) \equiv \frac{\Omega_{\text{ext}}(\mathbf{\Gamma})\Psi_0(\mathbf{\Gamma})}{\Psi_0(\mathbf{\Gamma})}} \tag{2.13}$$

where B is the observable conjugated to the perturbation $\delta\mathcal{A}$. Alternatively, using Eq. (2.10) into Eq. (2.13) the integrated response can be expressed as:

$$\boxed{\langle A\rangle_t - \langle A\rangle_0 = -\int_0^t ds\langle A(s)\left[\boldsymbol{\nabla}\cdot\delta\mathcal{A} + \delta\mathcal{A}\cdot\boldsymbol{\nabla}\log\Psi_0\right](0)\rangle_0} \tag{2.14}$$

which resembles the FDR as originally appeared in [48] in the context of dynamical systems. At this level, no equilibrium hypothesis has been made and, as such, Eqs. (2.13-2.14) remain valid also for NESS. For an equilibrium system fulfilling DB, i.e. $\Psi_0(\mathbf{\Gamma}) = \Psi_{\text{eq}}(\mathbf{\Gamma})$, the conjugated observable B can be computed explicitly.

As an illustration, let consider again a one-dimensional overdamped Brownian particle in contact with a thermal bath at temperature T that is perturbed by applying, at $t = 0$, a constant external force h. In this case $\Omega_0 = \mu\partial_x[k_BT\partial_x - F]$ with $F \equiv -U'(x)$ the conservative force acting on the particle and $\Omega_{\text{ext}} = -\mu h\partial_x$. From Eq. (2.7) one immediately obtains the Boltzmann distribution, and from Eq. (2.13)

$$\langle A\rangle_t - \langle A\rangle_0 = -\mu\beta h\int_0^t ds\langle A(s)F(0)\rangle_0\,. \tag{2.15}$$

If one now replaces $\mu F = \dot{x} - \sqrt{2\mu k_BT}\xi$ and use the fact that $R_A(t) = \sqrt{\beta\mu/2}\langle A(t)\xi(0)\rangle$ [49], the following familiar form of the FDT for Brownian suspensions is found:

$$\langle A\rangle_t - \langle A\rangle_0 = \beta h\int_0^t ds\langle A(s)\dot{x}(0)\rangle_0\,. \tag{2.16}$$

From this relation, it is straightforward to derive *Green-Kubo expressions* for transport coefficients, such as the mobility and diffusivity. For instance, by choosing $A \equiv \dot{x}$ one finds the well-known expressions

$$\mu = \lim_{t\to\infty}\frac{\langle\dot{x}\rangle_t}{h} = \beta\int_0^\infty ds\langle\dot{x}(s)\dot{x}(0)\rangle_0, \quad D = \int_0^\infty ds\langle\dot{x}(s)\dot{x}(0)\rangle_0\,. \tag{2.17}$$

2.3 Non-equilibrium dynamics

2.3.1 Quantifying the violations of Detailed Balance

In order to quantify the breakdown of DB let introduce the conditional probability to go from $\mathbf{\Gamma}$ to $\mathbf{\Gamma}_0$ forward in time (see Fig. 2.2):

$$\boxed{f(\mathbf{\Gamma}_0,t|\mathbf{\Gamma},t_0) \equiv \frac{\Psi_0(\boldsymbol{\varepsilon}\mathbf{\Gamma})}{\Psi_0(\mathbf{\Gamma}_0)}P(\boldsymbol{\varepsilon}\mathbf{\Gamma}_0,t|\boldsymbol{\varepsilon}\mathbf{\Gamma},t_0)\,.} \tag{2.18}$$

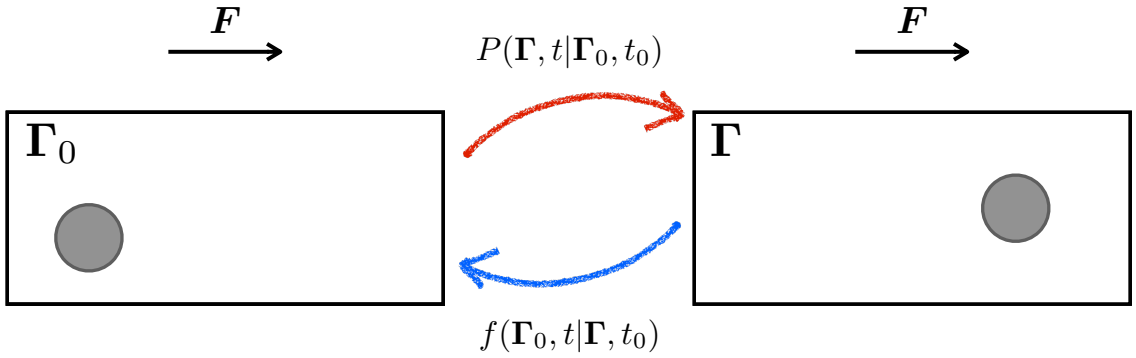

Figure 2.2: Illustration of the conditional probability f introduced to quantify violations of DB. A force $\boldsymbol{F}$ is applied to a colloidal particle, which favours motion towards the right, and thus $f(\boldsymbol{\Gamma}_0, t|\boldsymbol{\Gamma}, t_0) < P(\boldsymbol{\Gamma}, t|\boldsymbol{\Gamma}_0\, t_0)$. In the absence of external drive, DB is satisfied and there is no preference to move right or left, thus $f(\boldsymbol{\Gamma}_0, t|\boldsymbol{\Gamma}, t_0) = P(\boldsymbol{\Gamma}, t|\boldsymbol{\Gamma}_0\, t_0)$.

Whenever DB holds $f(\boldsymbol{\Gamma}_0, t|\boldsymbol{\Gamma}, t_0) = P(\boldsymbol{\Gamma}, t|\boldsymbol{\Gamma}_0\, t_0)$. When DB is violated, such identification is no longer valid. Nevertheless, it is still interesting to look at the evolution equation for $f(\boldsymbol{\Gamma}_0, t|\boldsymbol{\Gamma}, t_0)$ as it allows to quantify the breakdown of DB. Following the approach of [50] let write the backward evolution equation for $P(\boldsymbol{\varepsilon\Gamma}_0, t|\boldsymbol{\varepsilon\Gamma}, t_0)$:

$$\partial_t P(\boldsymbol{\varepsilon\Gamma}_0, t|\boldsymbol{\varepsilon\Gamma}, t_0) = \sum_i \varepsilon_i \mathcal{A}_i(\boldsymbol{\varepsilon\Gamma})\partial_i P(\boldsymbol{\varepsilon\Gamma}_0, t|\boldsymbol{\varepsilon\Gamma}, t_0) + D_i\partial_i^2 P(\boldsymbol{\varepsilon\Gamma}_0, t|\boldsymbol{\varepsilon\Gamma}, t_0)\,. \quad (2.19)$$

By multiplying both sides of the latter equation by $\Psi_0(\boldsymbol{\varepsilon\Gamma})/\Psi_0(\boldsymbol{\Gamma}_0)$ and using the definition of $f(\boldsymbol{\Gamma})_0, t|\boldsymbol{\Gamma}, t_0)$, one obtains

$$\begin{aligned}\partial_t f(\boldsymbol{\Gamma}_0, t|\boldsymbol{\Gamma}, t_0) = \sum_i \varepsilon_i \partial_i\Big(\mathcal{A}_i(\boldsymbol{\varepsilon\Gamma})f\Big) - \varepsilon_i f.\frac{\partial_i(\mathcal{A}_i(\boldsymbol{\varepsilon\Gamma})\Psi_0(\boldsymbol{\varepsilon\Gamma}))}{\Psi_0(\boldsymbol{\varepsilon}\Gamma)} \\ + D_i\left\{\partial_i^2 f - 2\partial_i\left(f.\frac{\partial_i\Psi_0(\boldsymbol{\varepsilon\Gamma})}{\Psi_0(\boldsymbol{\varepsilon\Gamma})}\right) + f.\frac{\partial_i^2\Psi_0(\boldsymbol{\varepsilon\Gamma})}{\Psi_0(\boldsymbol{\varepsilon\Gamma})}\right\} \quad (2.20)\end{aligned}$$

where, for simplicity, I write $f(\boldsymbol{\Gamma}_0, t|\boldsymbol{\Gamma}, t_0) \equiv f$. Let now split the drift vector into its reversible and irreversible parts to rewrite the first term on the *rhs* of Eq. (2.20) as

$$\begin{aligned}\sum_i \varepsilon_i\partial_i(\mathcal{A}_i(\boldsymbol{\varepsilon\Gamma})f) &= \sum_i \partial_i([-\mathcal{A}_i^{\mathrm{rev}}(\boldsymbol{\Gamma}) + \mathcal{A}_i^{\mathrm{irr}}(\boldsymbol{\Gamma})]f) \quad (2.21)\\ &= \sum_i\Big(-\partial_i[\mathcal{A}_i(\boldsymbol{\Gamma})f] + 2\partial_i\Big[\mathcal{A}_i^{\mathrm{irr}}(\boldsymbol{\Gamma})f\Big]\Big)\end{aligned}$$

By substituting back Eq. (2.21) into Eq. (2.20) and using the property $\Omega_0(\boldsymbol{\varepsilon\Gamma})\Psi_0(\boldsymbol{\varepsilon\Gamma}) = 0$ one finally gets

$$\boxed{\partial_t f = \Omega_0(\boldsymbol{\Gamma})f + \sum_i \partial_i\Big[f\Big(2\mathcal{A}_i^{\mathrm{irr}}(\boldsymbol{\Gamma}) - 2D_i\partial_i\log\Psi_0(\boldsymbol{\varepsilon\Gamma})\Big]\Big)\,.} \quad (2.22)$$

When DB holds, the Fokker-Planck equation is recovered: since the initial condition for $f(\boldsymbol{\Gamma}_0, t|\boldsymbol{\Gamma}, t_0)$ and $P(\boldsymbol{\Gamma}, t|\boldsymbol{\Gamma}_0, t_0)$ is the same by definition, it follows that $f =$

$P(\mathbf{\Gamma}, t|\mathbf{\Gamma}_0, t_0)$, as expected. By introducing the *Time-Reversal generator,* $\bar{\Omega}_0$, defined as

$$\partial_t f(\mathbf{\Gamma}_0, t|\mathbf{\Gamma}, t_0) \equiv \bar{\Omega}_0(\mathbf{\Gamma}) f(\mathbf{\Gamma}_0, t|\mathbf{\Gamma}, t_0) \tag{2.23}$$

and comparing Eq. (2.22) with Eq. (2.23) one founds an explicit expression for $\bar{\Omega}_0$ acting on f:

$$\bar{\Omega}_0(\mathbf{\Gamma}) f(\mathbf{\Gamma}_0, t|\mathbf{\Gamma}, t_0) = \Psi_0(\boldsymbol{\varepsilon}\mathbf{\Gamma})\Omega_0^\dagger(\boldsymbol{\varepsilon}\mathbf{\Gamma})\Big[f(\mathbf{\Gamma}_0, t|\mathbf{\Gamma}, t_0)\Psi_0(\boldsymbol{\varepsilon}\mathbf{\Gamma})^{-1}\Big]\,. \tag{2.24}$$

Notably, its adjoint

$$\boxed{\bar{\Omega}_0^\dagger(\mathbf{\Gamma}) = \Psi_0(\boldsymbol{\varepsilon}\mathbf{\Gamma})^{-1}\Omega_0(\boldsymbol{\varepsilon}\mathbf{\Gamma})\Psi_0(\boldsymbol{\varepsilon}\mathbf{\Gamma})} \tag{2.25}$$

has a precise dynamical meaning: it evolves the observable A along Time-Reversal paths, meaning

$$\langle A\rangle_{(-t)} \equiv \int d\mathbf{\Gamma}\Psi_0(\mathbf{\Gamma})e^{\bar{\Omega}_0^\dagger t}A(\mathbf{\Gamma}), \quad t>0 \tag{2.26}$$

generalizing the formulation of Baiesi and Maes [41] to systems with odd variables. The above definition of the Time-Reversal generator and the expression of its adjoint in terms of the original generator, do not rely on any assumption concerning the steady-state distribution. From Eq. (2.25), one easily finds the following expression quantifying the breakdown of DB in terms of irreversible probability fluxes:

$$\boxed{\frac{\Omega_0^\dagger(\mathbf{\Gamma}) - \bar{\Omega}_0^\dagger(\mathbf{\Gamma})}{2} = \frac{\boldsymbol{\varepsilon}\boldsymbol{J}_0^{\rm irr}(\boldsymbol{\varepsilon}\mathbf{\Gamma})}{\Psi_0(\boldsymbol{\varepsilon}\mathbf{\Gamma})}\cdot\boldsymbol{\nabla} \equiv \boldsymbol{\varepsilon}\boldsymbol{\mathcal{V}}^{\rm irr}(\boldsymbol{\varepsilon}\mathbf{\Gamma})\cdot\boldsymbol{\nabla}\,.} \tag{2.27}$$

It immediately follows that DB holds if and only if the Time-Reversal generator equals the original generator of the dynamics

$$\boxed{\text{Detailed Balance} \quad \Leftrightarrow \quad \Omega_0(\mathbf{\Gamma}) = \bar{\Omega}_0(\mathbf{\Gamma})\,.} \tag{2.28}$$

Since DB only constraints irreversible fluxes to vanish, it is thus expected that its breakdown only concerns their presence. The status of DB as a symmetry of the dynamics is now transparent. These expressions are general and can be exploited to quantify the breakdown of DB in systems with both odd and even variables, such as collections of interacting particles with inertia [51] or noisy RLC circuits [52].

2.3.2 General constraints on Non-Equilibrium Steady-States

It is useful to notice that the irreversible steady-state velocity quantifying the non-equilibrium character of the dynamics, or breakdown of DB, is directly related to the production of entropy in a NESS (see the 'Intermezzo' for more details). For a stochastic dynamics described by a Fokker-Planck equation, the total entropy is defined as the sum of the entropy of the system $S_{\rm sys}$ and the entropy of the bath $S_{\rm b}$:

$$\langle S_{\rm tot}\rangle_t = \langle S_{\rm sys}\rangle_t + \langle S_{\rm b}\rangle_t \tag{2.29}$$

where usually the entropy of the system is associated with the Gibbs entropy [53,54]

$$\langle S_{\rm sys}\rangle_t = -k_B \int d\mathbf{\Gamma}\Psi(\mathbf{\Gamma},t)\log\Psi(\mathbf{\Gamma},t)\,. \tag{2.30}$$

Upon identifying $\langle \dot{S}_{\rm b}\rangle_t$ as the total heat flow exchanged with the bath, the following expression for the rate of change of the total entropy is obtained [53, 54]:

$$\boxed{\langle \dot{S}_{\rm tot}\rangle_t = k_B \sum_i \int d\mathbf{\Gamma} D_i^{-1}\Psi(\mathbf{\Gamma},t)\left(\mathcal{V}_i^{\rm irr}(\mathbf{\Gamma},t)\right)^2 \geq 0\,.} \tag{2.31}$$

The total entropy can in turn be split into two contributions of very different nature, the house-keeping $\dot{S}_{\rm hk}$ and the excess $\dot{S}_{ex}$ entropy production [55–57]. The house-keeping term constitutes the entropy production necessary to sustain a NESS and it is positive as soon as DB is broken. In contrast, the excess term is the entropy production due to a non-equilibrium relaxation and should vanish whenever a steady-state is reached. For a stochastic dynamics as the one considered here, the house-keeping contribution was recently derived [58] and it reads:

$$\boxed{\langle \dot{S}_{\rm hk}\rangle_t = k_B \sum_i \int d\mathbf{\Gamma} D_i^{-1}\Psi(\mathbf{\Gamma},t)\left(\boldsymbol{\varepsilon}\mathcal{V}_i^{\rm irr}(\boldsymbol{\varepsilon}\mathbf{\Gamma})\right)^2 \geq 0\,,} \tag{2.32}$$

where one recognizes inside the integral the steady-state velocity quantifying the violations of DB. In stationary conditions, $\dot{S}_{\rm tot}$ must reduce to Eq. (2.32) , since no excess contribution is present. While this is obvious for even variables only, in presence of odd variables this observation provides a *general constraint on the steady-state velocity* such that:

$$\boxed{\left(\mathcal{V}_i^{\rm irr}(\boldsymbol{\varepsilon}\mathbf{\Gamma})\right)^2 = \left(\mathcal{V}_i^{\rm irr}(\mathbf{\Gamma})\right)^2\,.} \tag{2.33}$$

As will be shown below, this equality constraints any NESS and allows to relate the nature of the irreversible fluxes, responsible for the breakdown of DB, with the symmetry of the NESS distribution Ψ_0.

In order to illustrate this general result and its consequences, let first consider a paradigmatic non-equilibrium model: a one-dimensional particle in a periodic potential U, coupled to a thermal bath and driven out-of-equilibrium by a non-conservative force F[3]. The Langevin equation governing the dynamics of such system is (see Fig. (2.2))

$$\dot{x}(t) = p(t)\,,\quad \dot{p}(t) = -U'(x) + F - \gamma p(t) + \sqrt{2\gamma k_B T}\xi(t)\,. \tag{2.34}$$

In this simple case, the two components of the irreversible steady-state velocity read

$$\mathcal{V}_x^{\rm irr}(x,p) = 0 \tag{2.35a}$$

$$\mathcal{V}_p^{\rm irr}(x,p) = -\gamma p - \gamma k_B T \frac{\partial}{\partial p}\log\Psi_0(x,p). \tag{2.35b}$$

[3]Periodicity is needed in order to guarantee the existence of a steady-state.

As already mentioned, Ψ_0 does not necessarily have a given parity under Time-Reversal. Nevertheless (without lack of generality) one may rewrite it as:

$$\Psi_0(x,p) = \mathcal{N}\exp(-\Phi(x,p)) = \mathcal{N}\exp\left[-(\Phi_+ + \Phi_-)\right] \tag{2.36}$$

where the generalized potential Φ was decomposed into an even and odd contribution: $\Phi(x,-p)_\pm = \pm\Phi(x,p)$ [4]. Then, the general constraint Eq. (2.33) yields

$$\Phi_+(x,p) = \beta\frac{p^2}{2} + \Lambda(x) \tag{2.37a}$$

$$\mathcal{V}_p^{\text{irr}}(x,p) = \gamma k_B T\frac{\partial\Phi_-}{\partial p}\,, \tag{2.37b}$$

where $\Lambda(x)$ is any derivable function of x. Thus, the even part of the generalized potential must be of the latter form, meaning that even terms p^{2n} with $n > 1$ are strictly forbidden in the NESS distribution. As expected, the dependence of $\Psi(x,p)$ on the positions, which are associated to reversible fluxes, is not constrained at all. Instead, irreversible fluxes are given by (gradients of) the odd part of the generalized potential. Thus, Eq. (2.33) establishes a generic, and explicit, relationship between irreversible fluxes and the symmetry of the NESS distribution.

In the limit $U \to 0$, the NESS distribution of this simple model can be computed analytically and consists in a 'tilted' Gaussian distribution in p and a uniform distribution in x, such as :

$$\Psi_0(x,p) = \mathcal{N}\exp\left[-\frac{\left(p-\langle p\rangle\right)^2}{2k_BT}\right]\,, \tag{2.38}$$

where $\langle p\rangle = F/\gamma$ is the mean velocity of the particle. Combining Eq. (2.38) with Eq. (2.37b) one finds $\Phi_- = -pF/\gamma k_BT$ and consequently:

$$\mathcal{V}_p^{\text{irr}} = -F \tag{2.39a}$$

$$\langle\dot{S}_{\text{hk}}\rangle_0 = \frac{F^2}{\gamma T} > 0 \tag{2.39b}$$

which reveals the non-equilibrium character of this system and the nature of its steady-state velocity: it is proportional to the particle mean velocity, resulting in a positive house-keeping entropy production.

Now, turning back into a more general discussion, Eq. (2.33) can be rewritten in terms of the generalized potential in Eq. (2.36) as

$$\left[\mathcal{A}_i^{\text{irr}} + D_i\partial_i\Phi_+\right]D_i\partial_i\Phi_- = 0 \quad \forall i \tag{2.40}$$

which, in order to be verified, requires one of the two following set of conditions:

$$\partial_i\Phi_+(\mathbf{\Gamma}) = -D_i^{-1}\mathcal{A}_i^{\text{irr}}(\mathbf{\Gamma}) \quad \text{or} \quad \partial_i\Phi_- = 0\,. \tag{2.41}$$

[4] The generalized potential is assumed to be a differential function of the dynamic variables.

Note that if both constraints are fulfilled *simultaneously* then the system obeys DB [see Eq. (2.5)]. Eq. (2.33) 'relaxes' one of the two constraints, allowing to distinguish two different ways of breaking DB, namely

$$\Phi_-(\mathbf{\Gamma}) = 0 \quad \text{but} \quad \partial_i \Phi_+(\mathbf{\Gamma}) \neq -D_i^{-1}\mathcal{A}_i^{\rm irr}(\mathbf{\Gamma}) \tag{2.42a}$$

or

$$\partial_i \Phi_+(\mathbf{\Gamma}) = -D_i^{-1}\mathcal{A}_i^{\rm irr}(\mathbf{\Gamma}) \quad \text{but} \quad \Phi_-(\mathbf{\Gamma}) \neq 0\,. \tag{2.42b}$$

Any non-equilibrium system with only even variables falls into the first category. On the contrary, systems with odd variables, such as the driven underdamped Brownian particle considered above or the Active Ornstein-Uhlenbeck Particles treated in detail in the next Chapter, fall into the second category. For systems with odd variables, it follows that the irreversible flux is directly related to the odd part of the NESS distribution, such that:

$$\mathcal{V}_i^{\rm irr}(\mathbf{\Gamma}) = D_i \partial_i \Phi_-(\mathbf{\Gamma})\,. \tag{2.43}$$

2.3.3 Extended Fluctuation-Dissipation Relations

Let now consider a system initially prepared in a NESS with probability distribution Ψ_0. At time $t = 0$, a perturbation such that $\mathcal{A} \to \mathcal{A} + \delta\mathcal{A}$ is applied. Although the Agarwal FDR Eq. (2.13) remains valid, the lack of knowledge on Ψ_0 does not allow to derive an explicit expression of the response function in terms of NESS correlations. To move further, an option would be to provide a reliable scheme to approximate Ψ_0. I will follow this strategy in the next Chapter when dealing with active particles. However, some general expressions can be established through the NESS properties derived above. For instance, alternative FDRs can be written in a way that explicitly relate the non-equilibrium response of the system to the symmetry properties of Ψ_0.

The Agarwal FDR can be rewritten in terms of the even and odd part of the NESS distribution as

$$\begin{aligned}\langle A\rangle_t - \langle A\rangle_0 \;=\; \sum_i \Big\{ &- \int_0^t ds \langle A(s)(\partial_i \delta\mathcal{A}_i)(0)\rangle_0 + \int_0^t ds \langle A(s)(\delta\mathcal{A}_i \partial_i \Phi_+)(0)\rangle_0 \\ &+ \int_0^t ds \langle A(s)(\delta\mathcal{A}_i \partial_i \Phi_-)(0)\rangle_0 \Big\}\,.\end{aligned} \tag{2.44}$$

Then by making use of the relations, derived in the previous section, between the generalized potential and the irreversible steady-state velocity the following *extended FDR* is established

$$\begin{aligned}\langle A\rangle_t - \langle A\rangle_0 \;=\; \sum_i \Big\{ &- \int_0^t ds \langle A(s)(\partial_i \delta\mathcal{A}_i)(0)\rangle_0 - D_i^{-1} \int_0^t ds \langle A(s)(\delta\mathcal{A}_i \mathcal{A}_i^{\rm irr})(0)\rangle_0 \\ &+ D_i^{-1} \int_0^t ds \langle A(s)(\delta\mathcal{A}_i \mathcal{V}_i^{\rm irr})(0)\rangle_0 \Big\}\end{aligned} \tag{2.45}$$

which is valid both for overdamped and underdamped systems in the presence any type of external perturbation $\delta\mathcal{A}$. As such, it generalizes the FDR appearing in [34,

41,59], derived for an overdamped particle subjected to a conservative perturbation $\delta\mathcal{A} \equiv -\mu\partial_x U$, for which it reduces to:

$$\langle A\rangle_t - \langle A\rangle_0 = D_x^{-1}\mu \int_0^t ds \left(\left\langle A(s)\dot{U}(0)\right\rangle_0 - \left\langle A(s)\partial_x U(0)\mathcal{V}_x^{\mathrm{irr}}(0)\right\rangle_0 \right). \tag{2.46}$$

In particular, if the perturbation is taken to be a constant force of amplitude h, $U \equiv hx$, one ends up with the non-equilibrium extension of the FDT Eq. (2.16) as derived by Speck and Seifert [34]:

$$\langle A\rangle_t - \langle A\rangle_0 = D_x^{-1}\mu h \int_0^t ds \left(\langle A(s)\dot{x}(0)\rangle_0 - \left\langle A(s)\mathcal{V}_x^{\mathrm{irr}}(0)\right\rangle_0 \right). \tag{2.47}$$

The term comprising the irreversible steady-state velocity is responsible for the non-equilibrium character of the dynamics as it encodes the breakdown of DB. Note that, by comparing Eq. (2.44) and Eq. (2.45), in the presence of odd variables, full knowledge on Ψ_0 is not required to determine the response, but only on its odd part under Time-Reversal.

2.4 Conclusions

In this Chapter I have recalled, and discussed in detail, the pivotal role played by Detailed Balance as the defining feature of equilibrium dynamics, and how its breakdown out-of-equilibrium can be quantified by the presence of irreversible steady-state fluxes. I have analysed the symmetry properties of such fluxes under Time-Reversal for systems with odd and even variables, taking as illustrative examples Langevin processes describing Brownian particles both in the underdamped and overdamped regimes. A general formalism based on Fokker-Planck generators was developed allowing to express irreversible steady-fluxes in terms of the difference between the generator of the time-reversed dynamics and the original one. Further, by making the connection between the breakdown of Detailed Balance and the different contributions to the entropy production, a constraint of the irreversible steady-state fluxes was derived. This general result applies to non-equilibrium systems and provides non-trivial information for systems with dynamic variables which are odd under Time-Reversal. In particular, it constraints the functional dependence of the NESS distribution on its odd variables. Finally, the linear response of a system in a NESS was considered and an extended Fluctuation-Dissipation Relation derived, shedding light upon the nature of the different terms responsible for violations of the equilibrium Fluctuation-Dissipation Theorem.

Chapter 3

Fluctuation-Dissipation Relations in models of Active Matter

3.1 Introduction

In confronting the great variety of active systems and the rich phenomenology that they exhibit, the statistical physicist looks for some underlying principles via the construction of minimal models. Although idealistic, such an approach has proved useful to rationalize some aspects, and gain a general understanding, of the physics of Active Matter. In this context, the Active Brownian Particles (ABP) model [60] is arguably the benchmark model to study activity-induced collective behaviours and, in particular, to capture the interplay between self-propulsion and purely steric interactions. Both the dilute regime [61–65] and the high density regime of ABP [65–73] have been the subject of a great deal of research, and recently the full phase space diagram in two-dimensional space was established [74]. It was shown that while for some range of the density and activity parameters the 2D equilibrium melting scenario is maintained (with the activity overall destabilizing the ordered phase) the portion of phase space corresponding to high density and high activity is dominated by a purely out-of-equilibrium phase transition. The latter is referred to as motility-induced phase separation (MIPS) [75] and resembles an equilibrium liquid-gas transition but in the absence of attractive forces. While the microscopic picture of MIPS is fairly intuitive, being based on the slowing-down of particles in dense regions of space (due to steric interactions) and the simultaneous accumulation of particles in the slow region (due to persistence), a full understanding of the non-equilibrium nature of MIPS is still under construction. It was the original analogy between active particles and Lennard-Jones passive fluids that opens to the idea of using models that restore Detailed Balance (DB) [76, 77] to describe the non-equilibrium dynamics of active systems. The possibility to map ABP into an effective equilibrium description has a clear advantage. It allows to draw on the large body of knowledge of equilibrium Statistical Mechanics, and to define effective thermodynamic variables like free energy, pressure and temperature. In particular, it was shown that pressure is a state function for isotropic ABP [78, 79] and the analogous of an 'ideal gas law' for the swim pressure was derived [63], allowing for

a definition of an effective temperature in this latter case [62, 64, 80]. At the same time, orientation-dependent interactions destroy the equation of state for ABP [81], and the very same definition of effective temperature becomes controversial beyond the dilute regime [80, 82]. An effective equilibrium-like approach presents obvious limitations when it comes to quantifying the departure from equilibrium [83], while remaining a good place to start.
In this context, a recent body of literature has been dealing with the restoring of DB in ABP via Markovian approximations [84–88]. As will be discussed later in the Chapter, a standard way to microscopically account for self-propulsion in Brownian Motion is to include a coloured (persistent) Gaussian noise in the equations of motion. Originally proposed as an approximation of ABP to favour analytical treatments, this latter approach takes the name of Active Ornstein-Uhlenbeck particles (AOUP) model. Both ABP and AOUP have been recently studied by adapting methods from the theory of non-Markovian stochastic processes [18]. Interestingly, while originally developed to make sense of dye laser models, this host of techniques have found a renewed interest in the field of Active Matter. In particular, they have been employed to derive an effective steady state distribution for ABP and AOUP with a pairwise energy function capturing the emergence of attractive interactions from excluded-volume ones [84, 85] .
Compared to the great effort to characterize the phase space and the structure properties of active systems, which I tried to briefly summarize here, the transport properties of active fluids have received little attention. Here I aim to address the question of how systems of interacting active particles respond to an external small perturbation. A key step in this direction is to study the validity/violations of the Fluctuation-Dissipation Theorem (FDT) and characterize transport coefficients by establishing extended Green-Kubo expressions. So far, attempts to extend the FDT to characterize the linear response of active systems has been limited to specific cases or regimes, mostly considering activity as a small parameter. In [89, 90], activity is treated as the perturbation on an otherwise equilibrium state, while in [91] a Fluctuation-Dissipation Relation (FDR) is obtained in a small activity regime for which the dynamics of the system fulfils DB. In both cases, the reference state that is perturbed is not a genuine non-equilibrium steady state (NESS): in the first case, it is an equilibrium state with Boltzmann statistics, while in the latter an effective equilibrium state with a generalized potential. The fundamental difficulties arising from the violation of DB are therefore bypassed. The linear response beyond such a small activity limit has been analysed for a single active particle in [92]. In [93], response functions were obtained beyond such limit regimes, although they are not written in terms of NESS time correlation functions, as one wills for establishing FDR, but as weighted averages (in the spirit of Malliavin weight sampling [94]).
Another strategy consists in systematically quantifying the violation of the FDT through an effective temperature [62, 80, 82, 83, 95–100]. While this approach provides useful insights into the dynamics of NESS, it does not carry the same piece of information as a FDR, i.e. a generic way to assess the response function of an active system in terms of the steady-state fluctuations of measurable observables.
In the following, I study both ABP and AOUP and build from the general framework of out-of-equilibrium linear response developed in Chapter 2. For ABP the

non-interacting limit and an effective equilibrium regime resulting from a Markovian approximation are investigated. For AOUP a genuine, although approximated, non-equilibrium FDR is derived unveiling the interplay between activity and interactions. Furthermore, I discuss in detail the specificities of AOUP as compared with ABP as well as the different approximation schemes used in the literature to deal with many-body effects.

3.2 Active Brownian Particles

3.2.1 The model

Let consider N overdamped Active Brownian Particles moving in the 2D plane. They self-propel with a constant velocity v_0, along their orientation $\boldsymbol{n}_i = (\cos(\theta_i), \sin(\theta_i))$ and obey the following set of coupled Langevin equations

$$\boxed{\begin{aligned} \dot{\boldsymbol{r}}_i(t) &= \mu_0 \boldsymbol{F}_i + v_0 \boldsymbol{n}_i(t) + \boldsymbol{\xi}_i(t) && \text{(3.1a)} \\ \dot{\theta}_i(t) &= \nu_i(t)\,, && \text{(3.1b)} \end{aligned}}$$

where $\boldsymbol{F}_i = -\partial U/\partial \boldsymbol{r}_i$ accounts for all inter-particle potential forces (typically short-range repulsions) and μ_0 is the single particle mobility. The terms $\boldsymbol{\xi}$ and ν are zero-mean Gaussian noises verifying

$$\begin{aligned} \langle \boldsymbol{\xi}_i(t) \boldsymbol{\xi}_j(t') \rangle &= 2\mu_0 k_B T \delta_{ij} \delta(t-t') \mathbf{1} && \text{(3.2a)} \\ \langle \nu_i(t) \nu_j(t') \rangle &= 2 D_\theta \delta_{ij} \delta(t-t')\,, && \text{(3.2b)} \end{aligned}$$

with $\mathbf{1}$ the 2×2 unit matrix.
From the time integral of Eq. (3.1b), $\theta_i(t) = \theta_i(0) + \int_0^t dt' \nu_i(t')$ it is straightforward to compute the autocorrelation function of the orientation vector $\langle \boldsymbol{n}_i(t) \cdot \boldsymbol{n}_i(0) \rangle \equiv \langle \cos\theta_i(t) \cos\theta_i(0) \rangle + \langle \sin\theta_i(t) \sin\theta_i(0) \rangle = \langle \cos(\theta_i(t) - \theta_i(0)) \rangle$.
Recalling the Gaussian integral:

$$\langle \cos(x) \rangle = \Re \left[\langle e^{ix} \rangle \right] = \int_{-\infty}^{\infty} dx \frac{e^{-x^2/2\langle x^2 \rangle}}{\sqrt{2\pi \langle x^2 \rangle}} e^{ix} = e^{-\frac{\langle x^2 \rangle}{2}}\,, \tag{3.3}$$

together with the average:

$$\langle (\theta_i(t) - \theta_i(0))^2 \rangle = \int_0^t dt_1 \int_0^t dt_2 \langle \nu_i(t_1) \nu_i(t_2) \rangle = 2 D_\theta t \tag{3.4}$$

one finds:

$$\boxed{\langle \boldsymbol{n}_i(t) \cdot \boldsymbol{n}_i(0) \rangle = e^{-D_\theta t}\,.} \tag{3.5}$$

The Active Brownian Motion is therefore characterized by a persistence time $\tau = 1/D_\theta$ over which the particle loses memory of its original orientation. I define the Péclet number:

$$\boxed{\mathrm{Pe} = \frac{v_0}{\sigma D_\theta}} \tag{3.6}$$

where σ is a characteristic length-scale set, for instance, by the inter-particle potential. Equilibrium is recovered both in the limit of $v_0 \to 0$ or $\tau \to 0$. In both cases, the departure from equilibrium can be quantified by Pe. The generator, or Fokker-Planck operator, corresponding to the Langevin dynamics in Eqs. (3.1a-3.1b) is

$$\boxed{\Omega_0(\mathbf{\Gamma}) = \sum_i \frac{\partial}{\partial \boldsymbol{r}_i}(\mu_0 k_B T \frac{\partial}{\partial \boldsymbol{r}_i} - \mu_0 \boldsymbol{F}_i - v_0 \boldsymbol{n}_i) + D_\theta \sum_i \frac{\partial^2}{\partial \theta_i^2}} \tag{3.7}$$

where $\mathbf{\Gamma} \equiv \{\boldsymbol{r}_i, \theta_i\}$: All dynamical variables in ABP are considered even under Time-Reversal.

3.2.2 Non-equilibrium character and non-interacting regime

As mentioned in Chapter 2, for overdamped dynamics like ABP, there are no reversible probability fluxes such that $\boldsymbol{J}_0 \equiv \boldsymbol{J}_0^{\text{irr}}$ and the DB condition (2.4) corresponds to $\boldsymbol{J}_0 = 0$. Therefore in this case DB is fulfilled if and only if

$$\begin{cases} (\mu_0 \boldsymbol{F}_i + v_0 \boldsymbol{n}_i)\, \Psi_0(\mathbf{\Gamma}) = \mu_0 k_B T \frac{\partial}{\partial \boldsymbol{r}_i} \Psi_0(\mathbf{\Gamma}) \\ \frac{\partial}{\partial \theta_i} \Psi_0(\mathbf{\Gamma}) = 0 \end{cases}$$

with $\Psi_0(\mathbf{\Gamma})$ the steady state solution $\Omega_0 \Psi_0 = 0$. These two equations can not simultaneously hold due to the self-propulsion term, and therefore, ABP generically break DB. By integrating the first condition, one gets $\log \Psi_0 \sim -\beta[U - \sum_i v_0 \boldsymbol{n}_i \cdot \boldsymbol{r}_i/\mu_0]$. However, the second condition imposes Ψ_0 to be a function of positions only, which is inconsistent with the first condition because of the term in $\boldsymbol{n}_i \cdot \boldsymbol{r}_i$. In the passive case, $v_0 \to 0$, DB is recovered together with the standard Boltzmann distribution.

An illustrative example for which the steady-state velocity can be computed explicitly is a free ABP. The Fokker-Planck operator in this case reads

$$\Omega_0 = \left[\frac{\partial}{\boldsymbol{r}}(\mu_0 k_B T \frac{\partial}{\boldsymbol{r}} - v_0 \boldsymbol{n}) + D_\theta \frac{\partial^2}{\partial \theta^2}\right] . \tag{3.8}$$

It is straightforward to check that a stationary solution of the Fokker-Planck equation is $\Psi_0(\boldsymbol{r}, \theta) = \rho_0/2\pi$ [101]. The steady-state velocity corresponding to this homogeneous NESS is then

$$\boldsymbol{\mathcal{V}}^{\text{irr}}(t) = (\mathcal{V}_{\boldsymbol{r}}^{\text{irr}}, \mathcal{V}_\theta^{\text{irr}}) = (v_0 \boldsymbol{n}(t), 0)\,. \tag{3.9}$$

In order to apply the extended FDR in Eq. (2.47), let consider a constant force perturbation h applied along the x-axis. By choosing $A = \dot{x}$ in Eq. (2.47) one obtains

$$\frac{\langle \dot{x} \rangle_t}{h} = \beta \int_0^t ds \langle \dot{x}(s)\dot{x}(0)\rangle_0 - \beta v_0 \int_0^t ds \langle \dot{x}(s) \cos\theta(0)\rangle_0\,. \tag{3.10}$$

In the long time limit one recognizes on the *lhs* the particle mobility $\mu_0 \equiv \lim_{t\to\infty} \langle \dot{x} \rangle / h$ and, using Eq. (3.5) to compute the second integral in the *rhs*, obtains the following extended Stokes-Einstein relation for $t \to \infty$

$$\boxed{D/\mu_0 = k_B T + \frac{v_0^2}{2 D_\theta \mu_0} \equiv \frac{D_a}{\mu_0}} \tag{3.11}$$

where the active diffusion coefficient

$$D_a \equiv \mu_0 k_B T + v_0^2 \tau/2 \tag{3.12}$$

was introduced. Therefore, non-interacting ABP fulfil the Stokes-Einstein relation with an effective temperature

$$\boxed{T_{\text{eff}}/T = 1 + \frac{v_0^2}{2D_\theta \mu_0 k_B T}\,.} \tag{3.13}$$

Eq. (3.13) is in accordance with the ideal gas law previously derived [63, 64, 79]. It is worth noting here that, although in the non-interacting limit ABP admit a NESS which fulfils the Stokes-Einstein relation, Eq. (3.11), the model generically breaks DB in a fundamental way. This is a salient feature of ABP: they do not allow for a zero current steady-state solution.

3.2.3 Interacting regime: an effective Markovian description

As evidenced by the extended FDR Eq. (2.45), the response of a non-equilibrium system is not completely determined by NESS correlations of physical observables, but also depends on the specific form of its steady-state velocity. In order to go beyond the non-interacting limit considered above and establish explicit FDR for interacting ABP one can approximate the dynamics by an effective equilibrium one that fulfils DB. Such kind of approximation has been used for ABP (and also AOUP) and comes under different names, the most usual ones being Unified Coloured Noise and Fox approximation [18, 84, 88]. In both cases, DB is restored by approximating a non-Markovian dynamics with a Markovian one in the small-τ limit. The steady-state distribution of the new dynamics does not correspond to the equilibrium Boltzmann distribution in terms of the energy function of the original dynamics, but to a 'Boltzmann-like' distribution in terms of an effective energy function. Despite the non-Boltzmann character of the steady-state distribution resulting from these approaches, all the difficulties associated with the absence of DB are lifted and one can readily derive a FDR by direct application of the general results presented in the previous Chapter.

To be more specific, let now turn into the analysis of interacting ABP within the Fox approximation [102, 103]. The starting point is to integrate out the angular variables appearing in the ABP dynamics Eqs. (3.1a-3.1b). The equations of motion are then approximated by:

$$\boxed{\dot{\boldsymbol{r}}_i(t) = \mu_0 \boldsymbol{F}_i + \boldsymbol{\eta}_i(t)} \tag{3.14}$$

where the noise $\boldsymbol{\eta}_i$ is approximately Gaussian [104] with zero mean and variance

$$\langle \boldsymbol{\eta}_i(t) \boldsymbol{\eta}_j(s) \rangle = (2\mu_0 k_B T \delta(t-s) + v_0^2 e^{-|t-s|/\tau}/2)\delta_{ij} \mathbf{1}\,. \tag{3.15}$$

The first term on the *rhs* is the amplitude of the thermal noise coming from the coupling with the thermal bath while the second term is the athermal noise associated

with the self-propulsion. As usual [15], the integration of some stochastic variables introduces memory in the dynamics, here in the form of a coloured noise with correlation time τ. Therefore, the difficulty now resides on the non-Markovianity of Eq. (3.14), which cannot be formulated in terms of a Smoluchowski operator; a long standing problem in Statistical Mechanics [18, 102, 105, 106]. Note that even if it were possible to write down a Fokker-Planck equation for the probability distribution $\Psi(\mathbf{\Gamma}, t)$, this would *not* tantamount to a full specification of the dynamics in Eq. (3.14), making the problem highly unmanageable. One then typically attempts to derive an approximated Fokker-Planck-like equation from Eq. (3.14) and proceeds to *interpret it* as the Fokker-Planck equation of a Markovian process. The tacit assumption is that the new dynamics so obtained is an approximation of the actual dynamics and captures at least some of its features.

Fox originally developed a first order in τ expansion [102, 103] for a one-dimensional stochastic process with coloured noise (see Appendix 3.5 for details). Recently, the method was extended to multidimensional systems and applied to active dynamics [85, 86, 88]. Following this generalization, the ABP dynamics in the reduced configuration space $\tilde{\mathbf{\Gamma}} \equiv \{\boldsymbol{r}_i\}$ is approximated by an effective Fokker-Planck dynamics generated by the operator:

$$\boxed{\Omega_0^M(\tilde{\mathbf{\Gamma}}) = \sum_\alpha \partial_\alpha \left(\sum_\beta \partial_\beta \mathcal{D}_{\beta\alpha}(\tilde{\mathbf{\Gamma}}) - \mu_0 F_\alpha(\tilde{\mathbf{\Gamma}}) \right) ,} \tag{3.16}$$

where $\mathcal{D} \equiv \{\mathcal{D}_{\alpha\beta}\}_{\alpha,\beta=1}^{2N}$ is an effective $2N \times 2N$ diffusivity tensor and Greek indices run over both spatial coordinates and particle labels [88]. To first order in $\tau\mu_0\partial_\alpha F_\beta$, it reads

$$\mathcal{D}_{\alpha\beta}(\tilde{\mathbf{\Gamma}}) = \mu_0 k_B T \delta_{\alpha\beta} + \frac{v_0^2 \tau}{2} \left(\delta_{\alpha\beta} + \tau\mu_0 \partial_\alpha F_\beta(\tilde{\mathbf{\Gamma}}) \right) . \tag{3.17}$$

Note that the Fox approximation is meaningful only when $|\tau\mu_0\partial_\alpha F_\beta| < 1$.
I will now prove that this effective dynamics fulfils DB. The first step is to write the condition of DB, Eq. (2.4), for the stationary probability density $\Psi_0(\tilde{\mathbf{\Gamma}})$:

$$\sum_\beta \mathcal{D}_{\beta\alpha}(\tilde{\mathbf{\Gamma}}) \partial_\beta \Psi_0(\tilde{\mathbf{\Gamma}}) = \Psi_0(\tilde{\mathbf{\Gamma}}) \left(\mu_0 F_\alpha(\tilde{\mathbf{\Gamma}}) - \sum_\beta \partial_\beta \mathcal{D}_{\beta\alpha}(\tilde{\mathbf{\Gamma}}) \right) . \tag{3.18}$$

One then multiplies both sides by $(\mathcal{D}^{-1})_{\alpha\gamma}$ and sums over the index α to get:

$$\partial_\gamma \log \Psi_0(\tilde{\mathbf{\Gamma}}) = \sum_\alpha (\mathcal{D}^{-1})_{\alpha\gamma}(\tilde{\mathbf{\Gamma}}) \left[\mu_0 F_\alpha(\tilde{\mathbf{\Gamma}}) - \sum_\beta \partial_\beta \mathcal{D}_{\beta\alpha}(\tilde{\mathbf{\Gamma}}) \right] \equiv \beta F_\gamma^{\text{eff}}(\tilde{\mathbf{\Gamma}}) . \tag{3.19}$$

Using Eq. (3.17) and Eq. (3.19) the effective force may be re-expressed as (see Appendix 3.6):

$$\boxed{\beta F_\gamma^{\text{eff}}(\tilde{\mathbf{\Gamma}}) = \frac{\mu_0}{D_a} F_\gamma(\tilde{\mathbf{\Gamma}}) - \left(\frac{\mu_0 v_0 \tau}{2 D_a} \right)^2 \sum_\alpha \partial_\gamma (F_\alpha(\tilde{\mathbf{\Gamma}}))^2 - \partial_\gamma \log[\det D_a^{-1} \mathcal{D}(\tilde{\mathbf{\Gamma}})] .} \tag{3.20}$$

It is now straightforward to verify that the 'thermodynamic curvature' of the effective force in Eq. (3.20) vanishes:

$$\partial_\beta F_\gamma^{\text{eff}} - \partial_\gamma F_\beta^{\text{eff}} = 0\,. \tag{3.21}$$

This is precisely the condition of DB as stated in Eq. (2.6). This in turn implies that $\boldsymbol{F}^{\text{eff}}$ derives from an effective potential, and an analytical expression for Ψ_0 in terms of an effective energy function can be derived (see Appendix 3.6).

To derive the FDR a constant perturbation h is switched on along the $x-$direction for a tagged $n-$particle. Its equation of motion Eq. (3.14) in the $x-$component then reads $\dot{x}_n = \mu_0 F_n^x + \mu_0 h + \eta_i^x(t)$. By combining Eq. (3.19) with the extended FDR Eq. (2.14) it is found:

$$\langle A\rangle_t - \langle A\rangle_0 = -\mu_0\beta h \int_0^t ds \langle F_n^{\text{eff},x}(0)A(s)\rangle_0 \tag{3.22}$$

which is the analogous of the equilibrium FDT [Eq. (2.15)] with the effective force replacing the actual one. By choosing $A \equiv F_n^x$ into Eq. (3.22) one derives a Green-Kubo expression for the mobility that relies (only) on the Markovian approximation in Eq. (3.16):

$$\boxed{\mu = \mu_0 \left(1 - \mu_0\beta \int_0^\infty ds \langle F_n^{\text{eff},x}(0)F_n^x(s)\rangle_0\right)\,.} \tag{3.23}$$

As expected, Eq. (3.23) is identical to what one would get in the passive case by replacing $F_n^{\text{eff},x}$ by F_n^x. The non-equilibrium character of the original problem is now entirely encoded in the effective diffusivity (which depends on the relative positions of all the particles) and the effective forces (which do not derive from the Boltzmann potential) rather than on the (lack of) symmetries of the dynamics.
Before leaving this section, a diagonal approximation for $\mathcal{D}(\tilde{\boldsymbol{\Gamma}})$ can be introduced [85–88] by noticing that the effective diffusivity $\mathcal{D}(\tilde{\boldsymbol{\Gamma}})$ only enters in the expression for the effective force, Eq. (3.20), via its determinant. Thus, one may replace $\mathcal{D}(\tilde{\boldsymbol{\Gamma}})$ with a diagonal matrix with entry [84]:

$$\mathcal{D}_i(\tilde{\boldsymbol{\Gamma}}) = \mu_0 k_B T + \frac{v_0^2\tau}{2}\left(\frac{1}{1-\tau\mu_0\partial_i\cdot\boldsymbol{F}_i}\right) \tag{3.24}$$

for particle i, which preserves the determinant of the matrix in Eq. (3.17). Within this approximation, the effective force $\boldsymbol{F}_i^{\text{eff}}$ on particle i may be expressed as:

$$\boldsymbol{F}_i^{\text{eff}}(\tilde{\boldsymbol{\Gamma}}) = k_B T(\mu_0\boldsymbol{F}_i - \partial_i\mathcal{D}_i)/\mathcal{D}_i \tag{3.25}$$

and the Smoluchowski operator becomes:

$$\Omega_0^M(\tilde{\boldsymbol{\Gamma}}) = \sum_i \partial_i\cdot\mathcal{D}_i(\tilde{\boldsymbol{\Gamma}})\left[\partial_i - \beta\boldsymbol{F}_i^{eff}(\tilde{\boldsymbol{\Gamma}})\right]\,, \tag{3.26}$$

further simplifying the analysis of ABP within the Fox approximation. The possibility to neglect off-diagonal terms and use Eqs. (3.24-3.26) instead of the more convoluted Eq. (3.16) and Eq. (3.20) should be considered, in my opinion, more of an *ansatz* than an approximation.

3.2.4 Breakdown of the Stokes-Einstein Relation

By using the Eqs. (3.24-3.25) into Eq. (3.23) one finds an extended Green-Kubo expression in terms of the original inter-particle force:

$$\boxed{\begin{aligned}\frac{\mu}{\mu_0} =& 1 - \frac{\mu_0^2}{D_a}\int_0^\infty ds\langle F_n^x(0)F_n^x(s)\rangle_0 \\ &+ \frac{v_0^2\tau^2\mu_0^3}{2D_a^2}\int_0^\infty ds\langle F_n^x(0)\partial_n\cdot\boldsymbol{F}_n(0)F_n^x(s)\rangle_0 \\ &+ \frac{v_0^2\tau^2\mu_0^2}{2D_a}\int_0^\infty ds\langle \partial_n^x\partial_n\cdot\boldsymbol{F}_n(0)F_n^x(s)\rangle_0 \,.\end{aligned}} \tag{3.27}$$

For passive systems, only the terms in the first line survive, capturing how interactions affect the ideal gas mobility. Here, activity plays a role in the statistics of collisions, thus the force self-correlation function, and in the value of the prefactor via the single particle active diffusivity D_a. The remaining two terms $\propto (v_o\tau)^2$ correspond to subdominant higher order correlations involving many-body interactions. To characterize the departure from equilibrium linear response in terms of the Stokes-Einstein relation, one can use (see Appendix 3.7 for a proof):

$$\mu_0^2\langle F_n^x(0)\cdot F_n^x(t)\rangle_0 = \langle\mathcal{D}_n\rangle_0\,\delta(t) - \langle\dot{x}_n(0)\dot{x}_n(t)\rangle_0\,, \tag{3.28}$$

which relates the force and the velocity autocorrelation functions, and whose functional form depends only on the properties of the evolution operator (the special case for equilibrium dynamics was derived in [107]). Once identified the diffusivity with the velocity self-correlation function, the Green-Kubo expression is obtained

$$\boxed{D = D_a + \frac{\mu_0 v_0^2\tau^2}{2}\langle\partial_n\cdot\boldsymbol{F}_n\rangle_0 - \mu_0^2\int_0^\infty ds\langle F_n^x(0)F_n^x(s)\rangle_0} \tag{3.29}$$

which allows to express Eq. (3.27) as

$$\boxed{\frac{\mu}{\mu_0} = \frac{D}{D_a} - \frac{\mu_0 v_0^2\tau^2}{2D_a}\langle\partial_n\cdot\boldsymbol{F}_n\rangle_0 + \text{h.o.t.}} \tag{3.30}$$

where h.o.t refers to higher order terms. Eq. (3.30) reduces to the usual Stokes-Einstein relation in the passive limit. If $\partial_n\cdot\boldsymbol{F}_n = 0$ a modified Stokes-Einstein relation holds, $\mu = \beta^{\text{eff}}D$, with an effective temperature given by Eq. (3.13). Indeed, genuine non-equilibrium behaviour results from the combined effect of interactions and activity, as observed in active colloidal suspensions [64]. To illustrate these results and put them into test, I run particle-based simulations of ABP Eq. (3.1a-3.1b) with periodic boundary conditions.The pair potential $U(r) = (\sigma/r)^{12}$ and the following set of parameters: $\tau = 0.02, \mu_0 = 1$, and $\beta = 1$ are used. The Peclet number Pe and the mean density $\phi = (\pi\sigma^2 N/4L^2)$ are varied in a range for which the system remains homogeneous [Pe $\in (0:10)$ and $\phi \in (0.01:0.2)$].
I analyse the integrated response

$$\chi(t) = N^{-1}\lim_{h\to 0}\sum_i^N \frac{[\langle x_i(t) - x_i(0)\rangle]}{h} \tag{3.31}$$

of the particles' positions due to a constant force applied to all of them $\boldsymbol{h}_i = \varepsilon_i h \boldsymbol{u}_x$, where $\varepsilon_i = \pm 1$ with equal probability [80] and $\boldsymbol{u}_x$ is the versor in the $x-$direction. χ is computed using two different strategies: (i) by explicitly applying a small force and measuring the particle displacements it induces; (ii) by tracking the appropriate stochastic variables needed to compute the response function of interest using simulations of the unperturbed dynamics. The first 'direct method' involves computing displacements generated by a small perturbation that guarantees the linear regime. The second 'Malliavin weight (MW) method' overcomes the considerable numerical uncertainties (and cost) related to the control of a small perturbation parameter in Brownian dynamics simulations; it is thus extensively used in the following. This method, originally introduced in the context of Monte Carlo simulations of spin systems [108], and then generalized to Brownian dynamics [94, 109], was recently extended to active particles [82, 110].
I compute

$$D = N^{-1} \lim_{t\to\infty} \sum_i \langle [\boldsymbol{r}_i(t) - \boldsymbol{r}_i(0)]^2 \rangle / (4t) \tag{3.32}$$

from the long-time behaviour of the mean-square displacement (MSD). According to the MW method, the response function of interest can be expressed as [82, 94] (see Appendix 3.8 for details):

$$\chi(t) = N^{-1} \sum_i \langle x_i(t) q(t) \rangle \ , \tag{3.33}$$

where q is a Malliavin weight that evolves accordingly to

$$\dot{q}(t) = \sqrt{\frac{\beta}{2}} \sum_i \xi_i^x(t) \ , \tag{3.34}$$

and averages are taken over independent realizations of the unperturbed dynamics. I thus compute χ using Eq. (3.33) and extract $\mu = \lim_{t\to\infty} \chi(t)/t$ (after checking consistency with the direct method). D and μ are also computed using the Green-Kubo expressions previously obtained. To be concrete, the different terms involving correlations and gradients of the potential that appear in Eq. (3.27) and Eq. (3.29) are computed from simulations of ABP. The results obtained are shown in Fig. 3.1.

The diffusion coefficient follows the same growth $\sim \mathrm{Pe}^2$ as the ideal gas in the parameter range explored, but decreases with ϕ. Eq. (3.29) underestimates the value of D obtained from MSD but retains its functional dependence. The mobility is not affected by activity in the dilute regime but decreases as the density increases, as expected from Eq. (3.27) and Refs. [80, 82]. At finite density and Pe, μ decreases with density but remains roughly constant for $\mathrm{Pe} \gtrsim 2$. Such behaviour is reproduced by Eq. (3.27), although it overestimated the numerical value. Our Green-Kubo expressions predict the qualitative behaviour of D and μ, despite cannot reach a precise quantitative agreement at high Pe and ϕ. Although such mismatch, expected from the basic assumptions behind the approximations made (small value of τ and $\tau\mu_0\partial_i \cdot \boldsymbol{F}_i$; neither too active nor too dense), prevents quantitative agreement, the derived Green-Kubo expressions provide a general understanding on how the interplay between activity and interactions affects the transport properties of ABP.

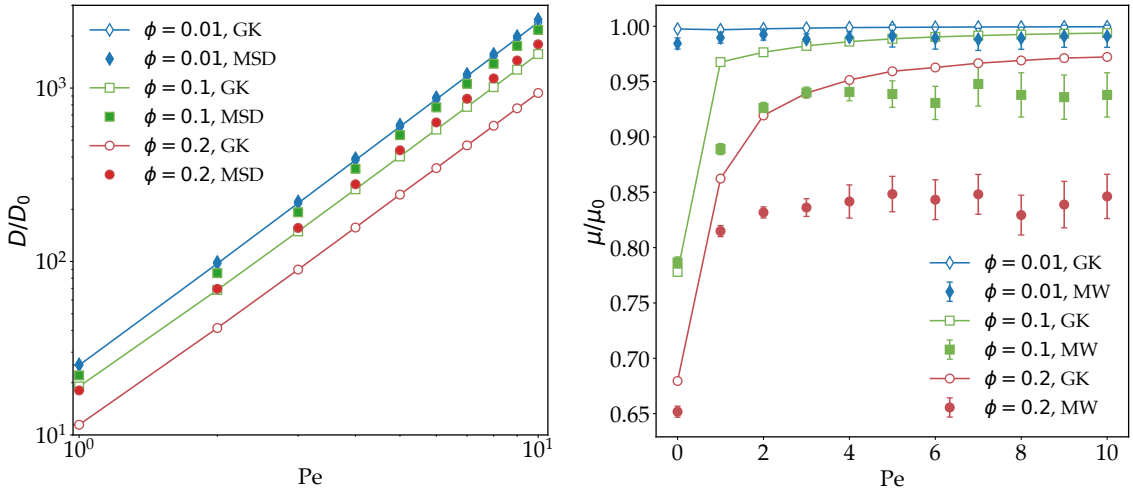

(a) (b)

Figure 3.1: Transport coefficients for ABP at $\phi = 0.01$, 0.1 and 0.2 as a function of Pe. (a) Diffusion coefficient obtained from the long time behaviour of the mean-squared displacement (MSD, with points) compared to the Green-Kubo expression Eq. (3.29) (GK, with line-points). (b) Mobility obtained from simulations of unperturbed ABP using Malliavin weights (MW, with error bars) compared to the Green-Kubo prediction Eq. (3.27) (GK, with point-lines).

3.3 Active Ornstein-Uhlenbeck Particles

3.3.1 The model

Let consider in this section a similar model of self-propelled particles, now governed by the following set of two-dimensional overdamped Langevin equations

$$\dot{\boldsymbol{r}}_i(t) = \mu_0 \boldsymbol{F}_i + \boldsymbol{v}_i \tag{3.35a}$$

$$\dot{\boldsymbol{v}}_i(t) = -\frac{\boldsymbol{v}_i}{\tau} + \sqrt{\frac{2D_0}{\tau^2}}\boldsymbol{\eta}_i(t)\,, \tag{3.35b}$$

where $\boldsymbol{v}_i$ is the fluctuating self-propulsion velocity which is described by an Ornstein-Uhlenbeck process with characteristic persistence time τ. For this reason, Eqs. (3.35a-3.35b) are referred to as Active Ornstein-Uhlenbeck Particles (AOUP). Self-propulsion introduces persistence in the spatio-temporal dynamics of the active particles via the autocorrelation function of the self-propulsion velocity

$$\langle \boldsymbol{v}_i(t)\boldsymbol{v}_j(t')\rangle = D_0/\tau e^{-|t-t'|/\tau}\delta_{ij}\mathbf{1}\,, \tag{3.36}$$

and reduces to passive (equilibrium) Brownian motion in the limit $\tau \to 0$, for which $\langle \boldsymbol{v}_i(t)\boldsymbol{v}_j(t')\rangle \to 2D_0\delta(t-t')\delta_{ij}\mathbf{1}$. Although a standard thermal noise could be added into the Langevin equation of AOUP, such contribution is assumed to be small with respect to the 'active noise' $\boldsymbol{v}$ and might be considered redundant, as it is not needed to recover equilibrium. As mentioned in the Introduction to this Chapter, AOUP

can be thought of as an approximate treatment of the ABP dynamics. Indeed, the reduced ABP dynamics obtained from the integration of the angular variables, Eq. (3.14), can be identified, in the absence of translational noise ($T = 0$), to the AOUP dynamics by setting $v_0^2/2$ (in ABP) to D_0/τ (in AOUP).

Although originally thought of as an overdamped process, Eq. (3.35a) involves velocity variables $\boldsymbol{v}$ that can be considered as being odd under Time-Reversal. Following this interpretation, Eq. (3.35a) can be rewritten as an underdamped Langevin process [91]

$$\dot{\boldsymbol{r}}_i(t) = \boldsymbol{p}_i \tag{3.37a}$$

$$\dot{\boldsymbol{p}}_i(t) = \mu_0(\sum_j \boldsymbol{p}_j \cdot \partial_j)\boldsymbol{F}_i - \frac{\boldsymbol{p}_i}{\tau} + \mu_0\frac{\boldsymbol{F}_i}{\tau} + \sqrt{\frac{2D_0}{\tau^2}}\boldsymbol{\eta}_i(t)\,, \tag{3.37b}$$

where $\partial_i \equiv \partial/\partial \boldsymbol{r}_i$. The corresponding generator reads

$$\Omega_0(\boldsymbol{\Gamma}) = \sum_i \left[-\boldsymbol{p}_i \cdot \partial_i - \partial_{\boldsymbol{p}_i} \cdot \left(\mu_0(\sum_j \boldsymbol{p}_j \cdot \partial_j)\boldsymbol{F}_i - \frac{\boldsymbol{p}_i}{\tau} + \mu_0\frac{\boldsymbol{F}_i}{\tau} - \frac{D_0}{\tau^2}\partial_{\boldsymbol{p}_i}\right)\right]\,, \tag{3.38}$$

where $\partial_{\boldsymbol{p}_i} \equiv \partial/\partial \boldsymbol{p}_i$ and $\boldsymbol{\Gamma} = \{\boldsymbol{r}_i, \boldsymbol{p}_i\}$.

3.3.2 Effective equilibrium regime

For the AOUP model, the DB condition Eq. (2.4) reduces to:

$$\frac{1}{\tau^2}\partial_{\boldsymbol{p}_i} \log \Psi_0(\boldsymbol{\Gamma}) = \beta(\sum_j \boldsymbol{p}_j \cdot \partial_j)\boldsymbol{F}_i - \frac{\boldsymbol{p}_i}{D_0\tau}\,. \tag{3.39}$$

where $\beta \equiv \mu_0/D_0$. Its formal solution can be expressed up to a function $\Lambda(\{\boldsymbol{r}_i\})$ that only depends on space variables such as

$$\Psi_0 = \exp\left[-\Lambda(\{\boldsymbol{r}_i\}) - \frac{\beta\tau^2}{2}(\sum_i \boldsymbol{p}_i \cdot \partial_i)^2 U - \sum_i \frac{\tau}{D_0}\frac{\boldsymbol{p}_i^2}{2}\right]\,, \tag{3.40}$$

In order for DB to hold, the system must fulfil the following equation

$$\sum_i \left[\partial_i\Lambda + \frac{\beta\tau^2}{2}(\sum_j \boldsymbol{p}_j \cdot \partial_j)^2\partial_i U - \frac{\beta^2 D_0\tau}{2}\partial_i \sum_j |\partial_j U|^2 - \beta\partial_i U\right]\Psi_0 = 0\,. \tag{3.41}$$

This equation does not have a solution because of the second term comprising a $p-$dependence. Interestingly, for a potential with vanishing third derivatives the latter term vanishes and an exact 'equilibrium' solution exists [91, 111]:

$$\Psi_{\text{eq}} = \mathcal{N}\exp\left[-\beta U - \frac{\tau}{2}\sum_i\left(\frac{\boldsymbol{p}_i^2}{D_0} + \beta^2 D_0|\partial_i U|^2\right) - \frac{\beta\tau^2}{2}(\sum_i \boldsymbol{p}_i \cdot \partial_i)^2 U\right]\,. \tag{3.42}$$

I wrote equilibrium in quotes because, contrary to the standard Boltzmann measure, the probability of a given configuration is not solely given by $e^{-\beta U}$, but by a more complicated function, also involving $\boldsymbol{p}$. This form is not *a priori* obvious from the mere inspection of the generator of the microscopic dynamics [The same remark holds for ABP within the Fox approximation discussed earlier, as the effective potential Eq. (3.20) can hardly be guessed from the original Fokker-Planck equation.] However, in this equilibrium-like regime, AOUP fulfil DB, there are no irreversible fluxes, and the FDT holds. An equilibrium solution also exists in the case of non-interacting particles $U = 0$ for which AOUP are formally equivalent to an ideal gas of underdamped particles. In all other cases, for a generic U, the model breaks DB and therefore falls out-of-equilibrium.

3.3.3 Non-equilibrium regime: Chapman-Enskog expansion

An approximated stationary distribution Ψ_0 for AOUP, beyond its equilibrium-like regime, has recently been derived via the Chapman-Enskog expansion by Bonilla [111]. The aim being to study the impact of activity on the response of an interacting system, I briefly present the Chapman-Enskog results as appeared in [111] and use them to establish extended FDR for AOUP.

The Chapman-Enskog expansion constitutes a standard perturbative approach to derive the Navier-Stokes equation from the Boltzmann equation [112, 113]. It is based on the notions of local equilibrium and time scale separation. The latter is accounted for by the introduction of a small parameter $\epsilon = \ell/L$ defined as the ratio between a microscopic and a macroscopic characteristic length. In kinetic theory, ℓ is typically the *mean free path* between collisional events and L the size of the system. Likewise, one may associate to the AOUP two different scales: a microscopic one associated to the persistence time τ and diffusive length $\sqrt{D_0\tau}$ (characterizing the local persistence due to activity), and a mesoscopic one associated to the interparticle interactions, with a 'slow' characteristic time τ_0 and a 'large' characteristic length L. Let introduce the ratio parameter $\epsilon \equiv \sqrt{D_0\tau}/L \equiv \tau/\tau_0$ and rescale the AOUP equations of motion Eqs. (3.37a-3.37b) according to $t \equiv t/\tau_0$, $\boldsymbol{r} \equiv \boldsymbol{r}/L$ and $\boldsymbol{F} \equiv \boldsymbol{F}L/\beta^{-1}$. The Fokker-Planck equation of AOUP can thus be written in the following non-dimensional form

$$\sum_i \partial_{\boldsymbol{p}_i} \cdot (\boldsymbol{p}_i + \partial_{\boldsymbol{p}_i})\,\Psi = \epsilon \partial_t \Psi + \epsilon \sum_i [\boldsymbol{p}_i \cdot \partial_i + \boldsymbol{F}_i \cdot \partial_{\boldsymbol{p}_i} + \epsilon \partial_{\boldsymbol{p}_i} \cdot (\sum_j \boldsymbol{p}_j \cdot \partial_j)\boldsymbol{F}_i]\Psi\,. \quad (3.43)$$

From here, the idea is to carry on a perturbative expansion in ϵ. For $\epsilon = 0$, a solution of Eq. (3.43) is:

$$\Psi^{(\epsilon=0)}(\boldsymbol{\Gamma}) = \frac{e^{-\sum_i \boldsymbol{p}_i^2/2}}{(2\pi)^N} R(\boldsymbol{r}, t) \quad (3.44)$$

where $R(\boldsymbol{r}, t)$ is the normalized marginal density such that $\int \Pi_i d\boldsymbol{r}_i R(\boldsymbol{r}, t) = 1$. For a system with strong time-scale separation, $\epsilon \ll 1$, one assumes that the functional dependence on $\{\boldsymbol{p}_i\}$ and R in Eq. (3.44) is preserved, and expand the probability distribution as a power series in ϵ:

$$\Psi(\boldsymbol{\Gamma}) = \frac{e^{-\sum_i \boldsymbol{p}_i^2/2}}{(2\pi)^N} R(\boldsymbol{r}, t; \epsilon) + \sum_j \epsilon^j \phi^{(j)}(\boldsymbol{\Gamma}, R)\,. \quad (3.45)$$

The crucial assumption of the Chapman-Enskog method is to still interpret R in Eq. (3.45) as the marginal distribution embedding the spatio-temporal dependence upon integration over the velocities. This corresponds to impose for $\phi^{(j)}$:

$$\int \Pi_i d\boldsymbol{p}_i \; \phi^{(j)}(\boldsymbol{\Gamma}, R) = 0 \quad \forall j \, . \tag{3.46}$$

The *ansatz* Eq. (3.45) is inserted into Eq. (3.43), resulting in a hierarchy of equations for the various terms in the expansion. The set of equations is solved up to $\sim o(\epsilon^3)$ and the following (now made dimensional) probability distribution [91,111] obtained:

$$\boxed{\begin{aligned}\Psi_0(\boldsymbol{\Gamma}) \simeq \mathcal{N} \exp\Bigg[&- \beta U - \sum_i \frac{\tau}{2}\left(\frac{\boldsymbol{p}_i^2}{D_0} + \beta^2 D_0 (\partial_i U)^2 - 3\beta D_0 \partial_i^2 U\right) \\ &- \frac{\tau^2}{2}\left(\beta (\sum_j \boldsymbol{p}_j \cdot \partial_j)^2 U + \beta D_0 \sum_{i,j} (\boldsymbol{p}_j \cdot \partial_j)\partial_i^2 U\right) + \frac{\tau^3}{6}\beta (\sum_j \boldsymbol{p}_j \cdot \partial_j)^3 U\Bigg] \, .\end{aligned}} \tag{3.47}$$

Some details on the derivation of Eq. (3.47) are given in the Appendix 3.10 for the one dimensional case. The generalization to higher dimensions is straightforward but lengthy (see also [111] for further details). It is now possible to compute the non-equilibrium response of AOUP up to third order in ϵ. First, let decompose Ψ_0 into its symmetric and antisymmetric parts (with respect to Time-Reversal):

$$\Phi_+ = \beta U + \sum_i \frac{\tau}{2}\left(\frac{\boldsymbol{p}_i^2}{D_0} + \beta^2 D_0 (\partial_i U)^2 - 3\beta D_0 \partial_i^2 U\right) + \frac{\tau^2}{2}\beta (\sum_j \boldsymbol{p}_j \cdot \partial_j)^2 U \tag{3.48a}$$

$$\Phi_- = \sum_{i,j} \frac{\tau^2}{2}\beta D_0 (\boldsymbol{p}_j \cdot \partial_j)\partial_i^2 U - \frac{\tau^3}{6}\beta (\sum_i \boldsymbol{p}_i \cdot \partial_i)^3 U \, . \tag{3.48b}$$

Note that, indeed Φ_+ does not contain powers of p larger than 2, as forbidden by the non-equilibrium constraint of Eq. (2.33). The signature of the departure from equilibrium is all embedded in Φ_- being different from zero (see Eq. (2.42b)). Particularly, the latter vanishes for a quadratic potential, as expected from the discussion in the previous section.

A constant force h is now applied along the x-axis on a tagged particle n. In this case, the extended FDR Eqs. (2.44-2.45) reads

$$\langle A \rangle_t - \langle A \rangle_0 = \delta \mathcal{A}_{p_n^x} \left[-(D_{p_n^x})^{-1} \int_0^t ds \langle A(s) \mathcal{A}^{\rm irr}_{p_n^x}(0) \rangle_0 + \int_0^t ds \langle A(s) \frac{\partial \Phi_-}{\partial p_n^x}(0) \rangle_0 \right] ,$$

where $\delta \mathcal{A}_{p_n^x} = \mu_0 h/\tau$ and $D_{p_n^x} = D_0/\tau^2$, leading to

$$\langle A \rangle_t - \langle A \rangle_0 = h \left[-\tau\beta \int_0^t ds \langle A(s) \mathcal{A}^{\rm irr}_{p_n^x}(0) \rangle_0 + \frac{\mu_0}{\tau} \int_0^t ds \langle A(s) \frac{\partial \Phi_-}{\partial p_n^x}(0) \rangle_0 \right] . \tag{3.49}$$

The first term is directly determined upon making the identification $\mathcal{A}^{\rm irr}_{p_n^x} = \mu_0 (\sum_j \boldsymbol{p}_j \cdot \partial_j) F_n^x - p_n^x/\tau$. The second integral requires the knowledge of the odd-symmetric part

of Ψ_0, which, to third order in ϵ is given by Eq. (3.48b). All in all, the following FDR for AOUP is derived

$$\langle A\rangle_t - \langle A\rangle_0 = \beta h\Bigg[\int_0^t ds\langle A(s)p_n^x(0)\rangle_0 - \tau\mu_0\int_0^t ds\langle A(s)(\sum_j \boldsymbol{p}_j\cdot\partial_j)F_n^x(0)\rangle_0$$
$$-\tfrac{1}{2}\mu_0\tau D_0\left(\int_0^t ds\langle A(s)\frac{\partial}{\partial x_n}(\sum_j \partial_j\cdot\boldsymbol{F}_j)(0)\rangle_0 - \frac{\tau}{D_0}\int_0^t ds\langle A(s)(\sum_j \boldsymbol{p}_j\cdot\partial_j)^2F_n^x(0)\rangle_0\right)\Bigg]. \tag{3.50}$$

By choosing $A\equiv p_n^x$ one eventually obtains an extended Stokes-Einstein relation:

$$\boxed{\begin{aligned}\mu = \beta\Bigg[D - \tau\mu_0\int_0^\infty ds\langle p_n^x(s)(\sum_j \boldsymbol{p}_j\cdot\partial_j)F_n^x(0)\rangle_0 \\ -\frac{1}{2}\mu_0\tau D_0\Big(\int_0^\infty ds\langle p_n^x(s)\frac{\partial}{\partial x_n}(\sum_j \partial_j\cdot\boldsymbol{F}_j)(0)\rangle_0 \\ -\frac{\tau}{D_0}\int_0^\infty ds\langle p_n^x(s)(\sum_j \boldsymbol{p}_j\cdot\partial_j)^2F_n^x(0)\rangle_0\Big)\Bigg],\end{aligned}} \tag{3.51}$$

where D is the many-body diffusivity $D=\int_0^\infty ds\langle p_n^x(s)p_n^x(0)\rangle$. The expression above embeds the violations to the usual Stokes-Einstein relation due to the interplay between activity and inter-particle interactions, up to order $o(\tau^2)$. In the absence of interactions the Stokes-Einstein relation is restored. This is also true for the case of a harmonic potential $U(r)=k|\boldsymbol{r}|^2/2$, for which one is left with

$$\mu = \beta^{\text{eff}}\int_0^t ds\langle p_n^x(0)p_n^x(s)\rangle_0\,, \tag{3.52}$$

being $\beta^{\text{eff}}=\beta(1+\mu_0\tau k)$ an effective temperature which depends on the stiffness of the external potential [62]. In contrast with ABP, the existence of a Stokes-Einstein relation for a harmonic potential in AOUP is due to the fact that the model fulfils DB.

3.4 Conclusion

The response of non-equilibrium systems is typically sensitive to details of the unperturbed initial state, hence the difficulty in establishing a general theory. Such lack of universality is encoded in the presence of the generalized potential in extended Fluctuation-Dissipation Relations, arising from the breakdown of Detailed Balance at the microscopic level.

While in Chapter 2 I have investigated the non-equilibrium linear response in a very general setting, in this Chapter I have focused on models of active systems, with the aim of setting the stage for a systematic response theory of active systems. In particular, I have focused on two very popular models of Active Matter, namely Active Brownian Particles (ABP) and Active Ornstein-Uhlenbeck Particles (AOUP).

While ABP generically break Detailed Balance, AOUP fulfil Detailed Balance in the dilute limit, or in the case of a harmonic potential. The non-equilibrium nature of these two model systems is therefore not equivalent. In the case of ABP, the Markov approximation method due to Fox was recalled and it was shown that the effective dynamics resulting from it fulfils Detailed Balance, and therefore also the standard Fluctuation-Dissipation Theorem. Within this approximation scheme, valid in the limit of small persistence time and moderate density, I put forward a closed Green-Kubo expression for the mobility and diffusivity. This allows to quantify the breakdown of the Stokes-Einstein relation due to the interplay between activity and inter-particle interactions. For AOUP I exploit the Chapman-Enskog expansion performed in [111] which allows to derive an extended Fluctuation-Dissipation Relation beyond its effective equilibrium regime. The violations of the Stokes-Einstein relation in these models of active particles as well as the possibility of quantifying them in terms of effective temperatures were discussed. Although some of the results presented here were known, as the existence of an effective equilibrium regime of AOUP and the NESS solution obtained from the Chapman-Enskog expansion, the discussion about the violations of DB and the FDT were scattered and scarce. The extended FDR, as well as the connection with the parity of the NESS distribution and the constraint on the steady-state velocity derived in Chapter 2, enrich previous discussions on non-equilibrium response, clarify the non-equilibrium nature of active model systems and provide a set of analytic results that should be of interest to study non-equilibrium systems in general, well beyond the context of active systems.

3.5 Appendix: 1D Fox approximation

I report here some details on the Markovian approximation as originally put forward by Fox [103]. Following the original paper, let consider the case of a one dimensional system, described by the Langevin equation:

$$\dot{x} = F(x) + \chi(t)\,, \tag{3.53}$$

where $\chi(t)$ is a Gaussian noise with correlation function $C(t-s) = \langle \chi(t)\chi(s)\rangle$. The Gaussian probability functional for $\chi(t)$ reads:

$$P[\chi] = \mathcal{N} \exp\left[-\frac{1}{2}\int ds \int ds' \chi(s)\chi(s')K(s-s')\right]\,, \tag{3.54}$$

in which K is the inverse of the correlation function, i.e. $\int dsK(t-s)C(s-s') = \delta(t-s')$ and $\mathcal{N}$ is a normalization constant. The probability functional enters in the formal solution of Eq. (3.53) expressed as the integral of the functional Dirac δ over all paths $\chi(t)$:

$$\Psi(y,t) = \int D[\chi]P[\chi]\delta(y - x(t))\,. \tag{3.55}$$

Its time derivative reads:

$$\frac{\partial \Psi(y,t)}{\partial t} = \int D[\chi]P[\chi]\left(-\frac{\partial}{\partial y}\delta(y-x(t))\dot{x}\right)\,. \tag{3.56}$$

By substituting into Eq. (3.56) the Langevin equation (3.53) one gets

$$\begin{aligned}\frac{\partial\Psi(y,t)}{\partial t} &= -\frac{\partial}{\partial y}\int D[\chi]P[\chi]\delta(y-x(t))\left[F(x)+\chi(t)\right] \\ &= -\frac{\partial}{\partial y}\left[F(y)\Psi(y,t)\right]-\frac{\partial}{\partial y}\int D[\chi]P[\chi]\chi(t)\delta(y-x(t))\,. \end{aligned} \tag{3.57}$$

Now using the functional derivative

$$\frac{\delta P[\chi]}{\delta\chi(t)} = -P[\chi]\int dsK(t-s)\chi(s) \tag{3.58}$$

the product $P[\chi]\chi(t)$ appearing into Eq. (3.57) can be rewritten as:

$$P[\chi]\chi(t) = P[\chi]\int ds\delta(t-s)\chi(s) = -\int ds'C(t-s')\frac{\delta P[\chi]}{\delta\chi(s')}\,. \tag{3.59}$$

Eq. (3.59) is thus substituted into Eq. (3.57) and integrated by part to get:

$$\begin{aligned}\frac{\partial\Psi(y,t)}{\partial t} &= -\frac{\partial}{\partial y}\left[F(y)\Psi(y,t)\right]+\frac{\partial}{\partial y}\int ds'C(t-s')\int D[\chi]\frac{\delta P[\chi]}{\delta\chi(s')}\delta(y-x(t)) \\ &= -\frac{\partial}{\partial y}\left[F(y)\Psi(y,t)\right]+\frac{\partial^2}{\partial y^2}\int ds'C(t-s')\int D[\chi]P[\chi]\delta(y-x(t))\frac{\delta x(t)}{\delta\chi(s')}\,. \end{aligned} \tag{3.60}$$

The following differential equation must be solved for $\delta x(t)/\delta\chi(s')$:

$$\frac{d}{dt}\frac{\delta x(t)}{\delta\chi(s')} = F'(x)\frac{\delta x(t)}{\delta\chi(s')}+\delta(t-s')\,. \tag{3.61}$$

By multiplying both sides of Eq. (3.61) by the factor $\exp\left[-\int_0^t d\tilde{s}F'\left[x(\tilde{s})\right]\right]$ and integrating, one gets:

$$\begin{aligned}\frac{\delta x(t)}{\partial\chi(s')} &= \int_0^t ds\;\delta(s-s')\exp\left[\int_s^t d\tilde{s}F'\left[x(\tilde{s})\right]\right] \\ &= \exp\left[\int_{s'}^t d\tilde{s}F'\left[x(\tilde{s})\right]\right]\Theta(t-s') \end{aligned} \tag{3.62}$$

Finally, Eq. (3.62) is substituted into Eq. (3.60) to derive:

$$\begin{aligned}&\frac{\partial\Psi(y,t)}{\partial t} = -\frac{\partial}{\partial y}\left[F(y)\Psi(y,t)\right] \\ &+\frac{\partial^2}{\partial y^2}\int_0^t ds'C(t-s')\int D[\chi]P[\chi]\delta(y-x(t))\exp\left[\int_{s'}^t dsF'\left[x(s)\right]\right]\,. \end{aligned} \tag{3.63}$$

Eq. (3.63) is not (yet) a Fokker-Planck-like equation. In particular, the non-Markovian character is embedded into the last integral which depends on $x(s)$ for $s<t$.
It is now time to specify the nature of the Gaussian noise via its correlation function $C(t-s')$. In the case of a white noise with $C(t-s') = 2D\delta(t-s')$ the second

term in Eq. (3.63) is readily integrated and the standard Fokker-Planck equation is obtained:

$$\frac{\partial \Psi(y,t)}{\partial t} = -\frac{\partial}{\partial y}\left[F(y)\Psi(y,t)\right] + D\frac{\partial^2}{\partial y^2}\Psi(y,t)\ . \tag{3.64}$$

Let now consider the case of an exponential decaying correlation function:

$$C(t-s') = \frac{D}{\tau}\exp\left[\frac{-(t-s')}{\tau}\right]\ . \tag{3.65}$$

By making the change of variable $t' = t - s'$ and approximating the argument of the exponent to first order in t' it follows:

$$\begin{aligned}\int_0^t ds' C(t-s')\exp\left[\int_{s'}^t dsF'\left[x(s)\right]\right] &= \int_0^t dt' C(t')\exp\left[\int_{t-t'}^t dsF'\left[x(s)\right]\right] \\ &\approx \int_0^t dt' C(t')\exp\left[F'\left[x(t)\right]t'\right]\ .\end{aligned} \tag{3.66}$$

Eq. (3.65) is then used explicitly into Eq. (3.66) and the integral is computed:

$$\frac{D}{\tau}\int_0^t dt'\exp\left[-t'\left(\frac{1}{\tau} - F'[x(t)]\right)\right] \approx \frac{D}{1-\tau F'\left[x(t)\right]} \tag{3.67}$$

where in the last step the limit for $t \to \infty$ was taken. Substituting Eq. (3.67) back into Eq. (3.63) one eventually obtains a Fokker-Planck-like equation:

$$\boxed{\frac{\partial \Psi(y,t)}{\partial t} = -\frac{\partial}{\partial y}\left[F(y)\Psi(y,t)\right] + \frac{\partial^2}{\partial y^2}\left[\frac{D}{1-\tau F'(y)}\right]\Psi(y,t)} \tag{3.68}$$

with an inhomogeneous effective diffusivity. Eq. (3.68) is the main result of Fox approach [103]. The approximation used in Eq. (3.66) is consistent with assuming a small persistence time τ, for which the correlation function $C(t')$ decays rapidly with increasing t'. In the limit $\tau \to 0$ one recovers the standard (and exact) Fokker-Planck equation (3.64).

3.6 Appendix: Effective equilibrium models for Active Matter in comparison

In this Appendix I attempt a comparison between the Fox approach and the Unified Coloured Noise Approximation (UCNA) [18]. Both the techniques were developed in the 80s [18, 102, 103, 114] for a one dimensional system and recently extended to multidimensional systems of active particles [84, 85]. This section should not be taken as an introduction to the topic of Markovian approximations nor as an extensive discussion over the two methods. Rather, it is aimed at a reader that is already familiar with the two approaches; the objective is to point out some similarities between them and give few mathematical details on the derivation of their approximated steady state distributions. Herein, I follow [88] to which I refer

for further details. Let start by writing the microscopic dynamics of a system of N interacting active particles in 2 dimensions as:

$$\dot{\boldsymbol{r}}_i(t) = \mu_0 \boldsymbol{F}_i + \boldsymbol{\xi}_i(t) + \boldsymbol{\chi}_i(t)\,. \tag{3.69}$$

$\boldsymbol{\xi}$ and $\boldsymbol{\chi}$ are two Gaussian noise terms with zero average and variance respectively given by $\langle \boldsymbol{\xi}_i(t)\boldsymbol{\xi}_j(t')\rangle = 2\mu_0 k_B T \delta_{ij}\mathbf{1}\delta(t-t')$ and $\langle \boldsymbol{\chi}_i(t)\boldsymbol{\chi}_j(t')\rangle = v_0^2/2\delta_{ij}e^{|t-t'|/\tau}\mathbf{1}$.

Note that the model given in Eq. (3.69) coincides with the reduced ABP dynamics in Eq. (3.14) with $\boldsymbol{\eta}_i(t) = \boldsymbol{\xi}_i(t) + \boldsymbol{\chi}_i(t)$. Alternatively, by identifying $\boldsymbol{\chi}_i(t)$ with the active fluctuating velocity $\boldsymbol{v}_i(t)$ (instead of a noise) which fulfils an Ornstein-Uhlenbeck equation, the model in Eq. (3.69) corresponds to the AOUP model (3.35a-3.35b) in presence of an extra thermal noise $\boldsymbol{\xi}_i(t)$.

All the next considerations rely on the assumption that the particles interact via a pairwise additive potential:

$$U(\{\boldsymbol{r}_i\}) = \sum_{k>i} u(|\boldsymbol{r}_i - \boldsymbol{r}_k|)\,, \tag{3.70}$$

so that $\boldsymbol{F}_i \equiv -\partial_i U$.

In [88] the probability flux $\boldsymbol{J} \equiv \{J_\alpha\} \in \mathbb{R}^{2N}$ for Fox and UCNA are respectively written as:

$$J_\alpha^{(\mathrm{UCNA})} = \sum_\beta (G^{-1})_{\alpha\beta}\left(\mu_0 F_\beta \Psi - D_a \sum_\gamma \partial_\gamma (G^{-1})_{\gamma\beta}\Psi\right) \tag{3.71a}$$

$$J_\alpha^{(\mathrm{Fox})} = \left(\mu_0 F_\alpha \Psi - \mu_0 k_B T \partial_\alpha \Psi - \frac{v_0^2\tau}{2}\sum_\beta \partial_\beta (G^{-1})_{\beta\alpha}\Psi\right)\,, \tag{3.71b}$$

where the Greek indexes run over both particles and spatial components. Note that the flux in Eq. (3.71b) follows from extending the method described in Appendix 3.5 to multidimensional systems (see [86]). The diagonal and off-diagonal components of the matrix $\boldsymbol{G}$ are respectively given by:

$$G_{\alpha\beta} = +\mu_0\tau\partial_\alpha\partial_\beta U \quad \forall \alpha \neq \beta \tag{3.72a}$$

$$G_{\alpha\alpha} = 1 + \mu_0\tau\partial_\alpha\partial_\alpha U\,. \tag{3.72b}$$

In Eq. (3.72a) one recognizes the off-diagonal elements of the $2N\times 2N$ Hessian matrix of the potential in Eq. (3.70). It follows that $\boldsymbol{G}$ is symmetric, so that $G_{\alpha\beta} = G_{\beta\alpha}$. As an example, I report the matrix $\boldsymbol{G}$ for a system of two particles. In this case, $\boldsymbol{G}$ is a 4×4 matrix and reads:

$$\boldsymbol{G} = \begin{bmatrix} 1+\mu_0\tau\partial_{x_1}\partial_{x_1}U & \mu_0\tau\partial_{x_1}\partial_{y_1}U & \mu_0\tau\partial_{x_1}\partial_{x_2}U & \mu_0\tau\partial_{x_1}\partial_{y_2}U \\ \mu_0\tau\partial_{y_1}\partial_{x_1}U & 1+\mu_0\tau\partial_{y_1}\partial_{y_1}U & \mu_0\tau\partial_{y_1}\partial_{x_2}U & \mu_0\tau\partial_{y_1}\partial_{y_2}U \\ \mu_0\tau\partial_{x_2}\partial_{x_1}U & \mu_0\tau\partial_{x_2}\partial_{y_1}U & 1+\mu_0\tau\partial_{x_2}\partial_{x_2}U & \mu_0\tau\partial_{x_2}\partial_{y_2}U \\ \mu_0\tau\partial_{y_2}\partial_{x_1}U & \mu_0\tau\partial_{y_2}\partial_{y_1}U & \mu_0\tau\partial_{y_2}\partial_{x_2}U & 1+\mu_0\tau\partial_{y_2}\partial_{y_2}U \end{bmatrix} \tag{3.73}$$

In this example, the determinant of $\boldsymbol{G}$ to first order in τ is:

$$\det \boldsymbol{G} \simeq 1 + \mu_0\tau\left(\partial_{x_1}^2 + \partial_{x_2}^2 + \partial_{y_1}^2 + \partial_{y_2}^2\right)U + \mathcal{O}(\tau^2). \tag{3.74}$$

Further, one may compute the cofactor C_{ij} to first order in τ for each element of the matrix $\boldsymbol{G}$ in order to find the elements of the inverse matrix $(G^{-1})_{ij} \equiv (-1)^{i+j} C_{ji}/\det \boldsymbol{G}$. Returning to the case of N particles, to first order in τ, it follows:

$$(G^{-1})_{\alpha\beta} \simeq \delta_{\alpha\beta} - \mu_0 \tau \partial_\alpha \partial_\beta U + \mathcal{O}(\tau^2) \tag{3.75a}$$

$$\det \boldsymbol{G} \simeq 1 + \mu_0 \tau \sum_\alpha \partial_\alpha^2 U + \mathcal{O}(\tau^2). \tag{3.75b}$$

For the model given by Eq. (3.69) the condition of Detailed Balance corresponds to require the vanishing of all fluxes $J_\alpha = 0$. In this case a convenient rewriting of Eqs. (3.71a-3.71b) is:

$$\mu_0 F_\alpha \Psi_0 - \sum_\beta \partial_\beta (\mathcal{D}_{\beta\alpha} \Psi_0) = 0\,, \tag{3.76}$$

where Ψ_0 is the stationary probability density and $\mathcal{D}$ is an effective diffusive matrix which reads as:

$$\mathcal{D}^{(\mathrm{UCNA})}_{\alpha\beta} \equiv D_a (G^{-1})_{\alpha\beta} \tag{3.77a}$$

$$\mathcal{D}^{(\mathrm{Fox})}_{\alpha\beta} \equiv \mu_0 k_B T \delta_{\alpha\beta} + \frac{v_0^2 \tau}{2} (G^{-1})_{\alpha\beta}\,. \tag{3.77b}$$

It follows that, at steady state, the difference between the UCNA and the Fox approximations only enters through the definition of the effective diffusivity matrix in Eqs. (3.77a-3.77b). By combining Eq. (3.77b) together with Eq. (3.75a) the expression (3.17) in the main text is obtained.
Interestingly, Eq. (3.77a) and Eq. (3.77b) coincides in the case of negligible thermal noise $v_0^2 \tau/2 \gg \mu_0 k_B T$. Also, note that taking $v_0 \to 0$ is not sufficient to recover the passive limit in Eq. (3.77a). In the UCNA approximation the parameter to be sent to zero in order to recover equilibrium is $\tau \to 0$. On the contrary, in the Fox approximation the passive limit is correctly recovered both in the limit $v_0 \to 0$ and $\tau \to 0$.
Requiring Detailed Balance for the UCNA model (as done for the Fox model in the main text) corresponds to set all fluxes in Eq. (3.71a) to zero:

$$\mu_0 F_\beta \Psi_0 - D_a \sum_\gamma (G^{-1})_{\gamma\beta} \partial_\gamma \Psi_0 - D_a \Psi_0 \sum_\gamma \partial_\gamma (G^{-1})_{\gamma\beta} = 0\,. \tag{3.78}$$

I multiply by $G_{\alpha\beta}$ and sum over β to get:

$$\mu_0 \Psi_0 \sum_\beta G_{\alpha\beta} F_\beta - D_a \Psi_0 \sum_{\gamma,\beta} G_{\alpha\beta} \partial_\gamma (G^{-1})_{\gamma\beta} = D_a \sum_{\gamma,\beta} G_{\alpha\beta} (G^{-1})_{\gamma\beta} \partial_\gamma \Psi_0\,. \tag{3.79}$$

Using the symmetry property of $\boldsymbol{G}$ the *rhs* of Eq. (3.79) reduces to $\partial_\alpha \Psi_0$. Further,by making use of the vectorial identity

$$\boldsymbol{\nabla} \cdot (\boldsymbol{G}^{-1} \boldsymbol{G}) = 0 = \sum_{\beta,\gamma} \left(G_{\beta\alpha} \partial_\gamma (G^{-1})_{\gamma\beta} + (G^{-1})_{\gamma\beta} \partial_\gamma G_{\beta\alpha} \right) = 0\,, \tag{3.80}$$

together with the symmetric property $G_{\beta\alpha} = G_{\alpha\beta}$, Eq. (3.79) becomes:

$$D_a \partial_\alpha \Psi_0 = \mu_0 \Psi_0 \sum_\beta G_{\alpha\beta} F_\beta + D_a \Psi_0 \sum_{\gamma,\beta} (G^{-1})_{\gamma\beta} \partial_\gamma G_{\beta\alpha}\,. \tag{3.81}$$

Given the equality $\partial_\gamma G_{\alpha\beta} = \partial_\alpha G_{\gamma\beta}$ one may write Eq. (3.81) as

$$\begin{aligned} D_a \partial_\alpha \Psi_0 &= \mu_0 \Psi_0 \sum_\beta G_{\alpha\beta} F_\beta + D_a \Psi_0 \sum_{\gamma,\beta} (G^{-1})_{\gamma\beta} \partial_\alpha G_{\gamma\beta} \\ &= \mu_0 \Psi_0 \sum_\beta G_{\alpha\beta} F_\beta + D_a \Psi_0 \partial_n \log\det \boldsymbol{G} \,. \end{aligned} \tag{3.82}$$

In the last step I made explicit use of the Jacobi formula $\sum_{\gamma,\beta}(G^{-1})_{\gamma\beta}\partial_\alpha G_{\beta\gamma} \equiv \mathrm{Tr}(\boldsymbol{G}^{-1}\partial_\alpha \boldsymbol{G}) = \partial_\alpha \log\det \boldsymbol{G}$. Let now insert the definitions of Eqs. (3.72a-3.72b) into Eq. (3.82) so that:

$$\partial_\alpha \log \Psi_0 = \frac{\mu_0}{D_a} F_\alpha - \frac{\mu_0^2 \tau}{2 D_a} \partial_\alpha \sum_\beta (\partial_\beta U)^2 + \partial_\alpha \log\det \boldsymbol{G} \,. \tag{3.83}$$

Both sides in Eq. (3.83) are expressed as gradients, such that Eq. (3.83) can be directly integrated to find the stationary distribution Ψ_0 which fulfils Detailed Balance [84]. In particular, if expressing the stationary distribution in terms of an effective potential function $\Psi_0 \propto \exp\left[-\mu_0 \Phi_{\text{eff}}^{(\text{UCNA})}/D_a\right]$ it is straightforward to find:

$$\boxed{\Phi_{\text{eff}}^{(\text{UCNA})} = U + \frac{\mu_0 \tau}{2} \sum_\beta (\partial_\beta U)^2 + \frac{D_a}{\mu_0} \log\det\left[D_a^{-1}\mathcal{D}\right] \,,} \tag{3.84}$$

where $\log(\boldsymbol{G}) = -\log(D_a^{-1}\mathcal{D})$ from the definition in Eq. (3.77a).
Along the same line, one can derive the effective potential within the Fox approximation starting from Eq. (3.20) in the main text. In this case the stationary distribution $\Psi_0 \propto \exp\left[-\mu_0 \Phi_{\text{eff}}^{(\text{Fox})}/D_a\right]$ is found:

$$\boxed{\Phi_{\text{eff}}^{(\text{Fox})} = U + \frac{\mu_0 v_0^2 \tau^2}{4 D_a} \sum_\beta (\partial_\beta U)^2 + \frac{D_a}{\mu_0} \log\det\left[D_a^{-1}\mathcal{D}\right] \,.} \tag{3.85}$$

By comparing Eq. (3.84) and Eq. (3.85) it follows that to first order in τ the Fox approximation returns a steady distribution very similar to that of UCNA. The two effective potentials become identical for $v_0^2\tau/2 \gg \mu_0 k_B T$ as expected.

3.7 Appendix: Details for the derivation of Eq. (3.28)

I report here some details on the derivation of the relation between the force-force autocorrelation function and the autocorrelation function of the velocity, Eq. (3.28) in the main text. For simplicity, I will sketch the derivation for a tagged particle n moving in a bath of overdamped equilibrium particles as presented in [107]. The extension to the effective dynamics given by the generator (3.26) is straightforward (but lengthy).
Let start by recalling that for a 2D isotropic system the velocity autocorrelation

function, $Z(t) = \frac{1}{2}\langle \boldsymbol{v}_n(t)\cdot\boldsymbol{v}_n(0)\rangle_0$, can be written in terms of the Fourier components $c_n(\boldsymbol{k},t) = \exp\left[-\boldsymbol{k}\cdot\boldsymbol{r}_n(t)\right]$ as [107]:

$$Z(t) = -\lim_{k\to 0}\frac{\partial^2}{\partial t^2}\frac{1}{k^2}\langle c_n(\boldsymbol{k},t)c_n(-\boldsymbol{k},0)\rangle_0\,. \tag{3.86}$$

Explicitly, the ensemble average $\langle\cdot\rangle_0$ in Eq. (3.86) reads:

$$\begin{aligned} Z(t) &= -\lim_{k\to 0}\frac{\partial^2}{\partial t^2}\frac{1}{k^2}\int d\tilde{\boldsymbol{\Gamma}}\Psi_0(\tilde{\boldsymbol{\Gamma}})e^{i\boldsymbol{k}\cdot\boldsymbol{r}_n}e^{\Omega_0^\dagger t}e^{-i\boldsymbol{k}\cdot\boldsymbol{r}_n} \\ &= -\lim_{k\to 0}\frac{\partial^2}{\partial t^2}\frac{1}{k^2}\int d\tilde{\boldsymbol{\Gamma}}e^{-i\boldsymbol{k}\cdot\boldsymbol{r}_n}e^{\Omega_0 t}\Psi_0(\tilde{\boldsymbol{\Gamma}})e^{i\boldsymbol{k}\cdot\boldsymbol{r}_n} \end{aligned} \tag{3.87}$$

where I have retained the same notation as in the main text with $\tilde{\boldsymbol{\Gamma}} \equiv \{\boldsymbol{r}_i\}_{i=1}^N$ and in the second step the definition of adjoint operator was used. By applying the Laplace transform $\mathcal{L}(f(t)) \equiv \int_0^\infty dt\, e^{-zt}f(t)$ to Eq. (3.87) one obtains:

$$\hat{Z}(z) = \lim_{k\to 0}\frac{z}{k^2}\Big\{1 - z\int d\tilde{\boldsymbol{\Gamma}}e^{-i\boldsymbol{k}\cdot\boldsymbol{r}_n}(z-\Omega_0)^{-1}\Psi_0(\tilde{\boldsymbol{\Gamma}})e^{i\boldsymbol{k}\cdot\boldsymbol{r}_n}\Big\} \tag{3.88}$$

where the property of the Laplace transform $\mathcal{L}(f''(t)) = z^2\mathcal{L}(f) - zf(0) - f'(0)$ was used. Introducing the operator identity:

$$(z-\Omega_0)^{-1} = \frac{1}{z}[1+\Omega_0(z-\Omega_0)^{-1}] = \frac{1}{z}\Big(1+\frac{1}{z}\Omega_0 + \frac{1}{z}\Omega_0(z-\Omega_0)^{-1}\Omega_0\Big)$$

one gets:

$$\begin{aligned} \tilde{Z}(z) &= \lim_{k\to 0}\frac{z}{k^2}\Big\{1 - z\int d\tilde{\boldsymbol{\Gamma}}e^{-i\boldsymbol{k}\cdot\boldsymbol{r}_n}\Big[\frac{1}{z}\Big(1+\frac{1}{z}\Omega_0+\frac{1}{z}\Omega_0(z-\Omega_0)^{-1}\Omega_0\Big)\Big]\Psi_0(\tilde{\boldsymbol{\Gamma}})e^{i\boldsymbol{k}\cdot\boldsymbol{r}_n}\Big\} \\ &= \lim_{k\to 0}\frac{(-1)}{k^2}\Big\{\int d\tilde{\boldsymbol{\Gamma}}\Psi_0(\tilde{\boldsymbol{\Gamma}})e^{i\boldsymbol{k}\cdot\boldsymbol{r}_n}\Omega_0^\dagger e^{-i\boldsymbol{k}\cdot\boldsymbol{r}_n} + \int d\tilde{\boldsymbol{\Gamma}}e^{-i\boldsymbol{k}\cdot\boldsymbol{r}_n}\Omega_0(z-\Omega_0)^{-1}\Omega_0\Psi_0(\tilde{\boldsymbol{\Gamma}})e^{i\boldsymbol{k}\cdot\boldsymbol{r}_n}\Big\} \\ &= \lim_{k\to 0}\frac{(-1)}{k^2}\Big\{\int d\tilde{\boldsymbol{\Gamma}}\Psi_0(\tilde{\boldsymbol{\Gamma}})e^{i\boldsymbol{k}\cdot\boldsymbol{r}_n}\Omega_0^\dagger e^{-i\boldsymbol{k}\cdot\boldsymbol{r}_n} + \int d\tilde{\boldsymbol{\Gamma}}\Omega_0^\dagger e^{-i\boldsymbol{k}\cdot\boldsymbol{r}_n}(z-\Omega_0)^{-1}\Omega_0\Psi_0(\tilde{\boldsymbol{\Gamma}})e^{i\boldsymbol{k}\cdot\boldsymbol{r}_n}\Big\}. \end{aligned} \tag{3.89}$$

At this point one needs to introduce the explicit expressions for the generator and its adjoint, which in the case of an equilibrium overdamped system read:

$$\Omega_0 = \mu_0\textstyle\sum_i \partial_i\cdot(k_BT\partial_i - \boldsymbol{F}_i)\;, \quad \Omega_0^\dagger = \mu_0\displaystyle\sum_i(k_BT\partial_i + \boldsymbol{F}_i)\cdot\partial_i\,. \tag{3.90}$$

By inserting Eqs. (3.90) into Eq. (3.89) and taking the long-wavelength limit $k\to 0$ neglecting the terms $o(k^2)$ one gets:

$$\tilde{Z}(z) = \Big\{\mu_0 k_BT - \frac{\mu_0^2}{2}\int d\tilde{\boldsymbol{\Gamma}}\boldsymbol{F}_n(z-\Omega_0)^{-1}\boldsymbol{F}_n\Psi_0(\tilde{\boldsymbol{\Gamma}})\Big\}\,. \tag{3.91}$$

The second term on the *rhs* is precisely the Laplace transform of the force-force correlation function so, by taking the inverse transformation one finds:

$$\frac{1}{2}\langle \boldsymbol{F}_n(t)\cdot\boldsymbol{F}_n(0)\rangle_0 = \frac{1}{\mu_0^2}\Big[\mu_0 k_BT\delta(t) - \frac{1}{2}\langle \boldsymbol{v}_n(t)\cdot\boldsymbol{v}_n(0)\rangle_0\Big]\;, \tag{3.92}$$

which is the equivalent of Eq. (3.28) for the overdamped dynamics given by the generators in Eq. (3.90). It can readily be shown that Eq. (3.28) follows from the same procedure by substituting into Eq. (3.89) the generators obtained from the Markovian approximation, namely:

$$\Omega_0^M = \sum_i \partial_i \cdot \mathcal{D}_i(\tilde{\mathbf{\Gamma}}) \left[\partial_i - \beta \boldsymbol{F}_i^{\text{eff}}(\tilde{\mathbf{\Gamma}})\right] \ , \quad \Omega_0^{M,\dagger} = \sum_i \left[\partial_i + \beta \boldsymbol{F}_i^{\text{eff}}(\tilde{\mathbf{\Gamma}})\right] \mathcal{D}_i(\tilde{\mathbf{\Gamma}}) \cdot \partial_i \quad (3.93)$$

with $\mathcal{D}_i(\tilde{\mathbf{\Gamma}})$ and $\boldsymbol{F}_i^{\text{eff}}(\tilde{\mathbf{\Gamma}})$ respectively given by Eq. (3.24) and Eq. (3.25).

3.8 Appendix: Response function computed from the dynamics of the unperturbed system

I recast here the derivation presented in the supplementary material of the paper from Warren and Allen [94] and apply it to the specific dynamics at hand. The goal is to find an expression for the variation of a given observable $\langle A \rangle$ with respect to some parameter λ quantifying an external drive, i.e. the response function of the observable A associated to a perturbation of magnitude λ:

$$\begin{aligned} \frac{\partial \langle A \rangle_t}{\partial \lambda} = \int d\mathbf{\Gamma} A(\mathbf{\Gamma}) \frac{\partial}{\partial \lambda} \Psi(\mathbf{\Gamma}, t) &= \int d\mathbf{\Gamma} A(\mathbf{\Gamma}) \Psi(\mathbf{\Gamma}, t) \frac{\partial}{\partial \lambda} \ln \Psi(\mathbf{\Gamma}, t) \\ &= \int d\mathbf{\Gamma} A(\mathbf{\Gamma}) \Psi(\mathbf{\Gamma}, t) Q_\lambda(\mathbf{\Gamma}, t) \end{aligned} \quad (3.94)$$

where I have defined

$$Q_\lambda(\mathbf{\Gamma}, t) \equiv \frac{\partial}{\partial \lambda} \ln \Psi(\mathbf{\Gamma}, t) \ . \quad (3.95)$$

The starting point is the introduction of an extra stochastic variable q_λ in the phase space $\mathbf{\Gamma}$ which in our case is the phase space of a 2D system of ABP such that $\mathbf{\Gamma} = \{\boldsymbol{r}_i, \theta_i\}_{i=1}^N$. One then introduces the joint probability density $\Psi(\mathbf{\Gamma}, q_\lambda, t)$ which is related to the probability density in the original phase space by

$$\Psi(\mathbf{\Gamma}, t) = \int dq_\lambda \Psi(\mathbf{\Gamma}, q_\lambda, t) \, , \quad (3.96)$$

and defines the conditional average $\langle q_\lambda \rangle_{\Gamma,t}$ as:

$$\langle q_\lambda \rangle_{\Gamma,t} \equiv \frac{\int dq_\lambda q_\lambda \Psi(\mathbf{\Gamma}, q_\lambda, t)}{\int dq_\lambda \Psi(\mathbf{\Gamma}, q_\lambda, t)} = \frac{\int dq_\lambda q_\lambda \Psi(\mathbf{\Gamma}, q_\lambda, t)}{\Psi(\mathbf{\Gamma}, t)} \ . \quad (3.97)$$

The idea now is to find the suitable evolution equation for the stochastic variable q_λ such that

$$\frac{\partial \langle A \rangle_t}{\partial \lambda} = \langle A q_\lambda \rangle_t \ . \quad (3.98)$$

This is useful because it reduces the calculation of the linear response function to a weighted average done over the unperturbed system (by 'just' tracking A and q_λ). First, note that if the following equality

$$\langle q_\lambda \rangle_{\Gamma,t} = Q_\lambda(\mathbf{\Gamma}, t) \quad (3.99)$$

holds, then

$$\frac{\partial \langle A \rangle_t}{\partial \lambda} = \langle A q_\lambda \rangle_t \, . \tag{3.100}$$

The proof goes as follows. By multiplying both sides of Eq. (3.97) by $\Psi(\mathbf{\Gamma}, t)$ and using the definition Eq. (3.95) it follows that:

$$\Psi(\mathbf{\Gamma}, t)\langle q_\lambda \rangle_{\mathbf{\Gamma},t} = \int dq_\lambda q_\lambda \Psi(\mathbf{\Gamma}, q_\lambda, t) = \Psi(\mathbf{\Gamma}, t) Q_\lambda(\mathbf{\Gamma}, t) = \frac{\partial}{\partial \lambda}\Psi(\mathbf{\Gamma}, t) \tag{3.101}$$

where in the second step the hypothesis (3.99) was used. It follows that:

$$\begin{aligned} \langle A q_\lambda \rangle_t &= \int d\mathbf{\Gamma} \int dq_\lambda \Psi(\mathbf{\Gamma}, q_\lambda, t) A(\mathbf{\Gamma}) q_\lambda = \int d\mathbf{\Gamma} A(\mathbf{\Gamma}) \Psi(\mathbf{\Gamma}, t) \langle q_\lambda \rangle_{\Gamma,t} \\ &= \int d\mathbf{\Gamma} A(\mathbf{\Gamma}) \Psi(\mathbf{\Gamma}, t) Q_\lambda(\mathbf{\Gamma}, t) = \frac{\partial \langle A \rangle}{\partial \lambda} \, . \end{aligned} \tag{3.102}$$

Now, the question is how to find in practice the appropriate equation of motion for q_λ, the so-called *Malliavin weight*, in order to ensure Eq. (3.99). To answer this question let first write the Chapman-Kolmogorov equation in terms of the conditional probability density $P(\mathbf{\Gamma}', t+\delta t|\mathbf{\Gamma}, t)$ to evolve from the state $\mathbf{\Gamma}$ to $\mathbf{\Gamma}'$ in a single time step δt :

$$\Psi(\mathbf{\Gamma}', t+\delta t) = \int d\mathbf{\Gamma} \Psi(\mathbf{\Gamma}, t) P(\mathbf{\Gamma}', t+\delta t|\mathbf{\Gamma}, t) \, , \tag{3.103}$$

and differentiate it with respect to λ so that:

$$Q_\lambda(\mathbf{\Gamma}', t+\delta t)\Psi(\mathbf{\Gamma}', t+\delta t) = \int d\mathbf{\Gamma} \left[Q_\lambda(\mathbf{\Gamma}, t) + \frac{\partial \log P}{\partial \lambda} \right] \Psi(\mathbf{\Gamma}, t) P \, , \tag{3.104}$$

where for simplicity I write $P = P(\mathbf{\Gamma}', t+\delta t|\mathbf{\Gamma}, t)$. At this stage one needs to specify the dynamics and write an explicit expression for $P(\mathbf{\Gamma}', t+\delta t|\mathbf{\Gamma}, t)$. The discretized version of the ABP dynamics Eqs. (3.1a-3.1b) in the simple Euler scheme reads:

$$\boldsymbol{r}_i' - \boldsymbol{r}_i = v_0 \boldsymbol{n}_i \delta t + \mu_0 \boldsymbol{F}_i \delta t + \sqrt{2\mu_0 k_B T \delta t}\boldsymbol{\xi}_i \equiv \Delta \boldsymbol{r}_i \tag{3.105a}$$

$$\theta_i' - \theta_i = \sqrt{2 D_\theta \delta t}\nu_i \equiv \Delta\theta_i \tag{3.105b}$$

and, equivalently, for the auxiliary variable q_λ:

$$\Delta q_\lambda \equiv q_\lambda' - q_\lambda \, . \tag{3.106}$$

In the path integral formalism, $P(\mathbf{\Gamma}', t+\delta t|\mathbf{\Gamma}, t)$ can be expressed as:

$$\begin{aligned} P(\mathbf{\Gamma}', t+\delta t|\mathbf{\Gamma}, t) &= \left\langle \delta(\boldsymbol{r}_i' - \boldsymbol{r}_i - \Delta\boldsymbol{r}_i)\delta(\theta_i' - \theta_i - \Delta\theta_i) \right\rangle_{noise} \\ &\equiv \int \left(\prod_i d\boldsymbol{\xi}_i d\nu_i \right) \Psi(\boldsymbol{\xi}_i)\Psi(\nu_i)\delta(\boldsymbol{r}_i' - \boldsymbol{r}_i - \Delta\boldsymbol{r}_i)\delta(\theta_i' - \theta_i - \Delta\theta_i) \, , \end{aligned} \tag{3.107}$$

where the Dirac delta functions enforce the equations of motion (3.105a-3.105b) and $\Psi(\boldsymbol{\xi}_i)$ and $\Psi(\nu_i)$ are the Gaussian probability distributions of the two noises. Thus, Eq. (3.103) can be rewritten as:

$$\begin{aligned} \Psi(\mathbf{\Gamma}', t+\delta t) &= \int \left(\prod_i d\boldsymbol{r}_i d\boldsymbol{\xi}_i d\theta_i d\nu_i \right) \Psi(\mathbf{\Gamma}, t)\Psi(\boldsymbol{\xi}_i)\Psi(\nu_i) \\ &\quad \delta(\boldsymbol{r}_i' - \boldsymbol{r}_i - \Delta\boldsymbol{r}_i)\delta(\theta_i' - \theta_i - \Delta\theta_i) \, , \end{aligned} \tag{3.108}$$

where $\prod_i d\boldsymbol{r}_i d\theta_i \equiv d\boldsymbol{\Gamma}$. An extended version of Eq. (3.108) for the joint probability density $\Psi(\boldsymbol{\Gamma}', q'_\lambda, t+\delta t)$ reads:

$$\begin{aligned}\Psi(\boldsymbol{\Gamma}', q'_\lambda, t+\delta t) &= \int \left(\prod_i d\boldsymbol{r}_i d\boldsymbol{\xi}_i d\theta_i d\nu_i\right) \int dq_\lambda \Psi(\boldsymbol{\Gamma}, q_\lambda, t)\Psi(\boldsymbol{\xi}_i)\Psi(\nu_i) \\ &\quad \delta(\boldsymbol{r}'_i - \boldsymbol{r}_i - \Delta\boldsymbol{r}_i)\delta(\theta'_i - \theta_i - \Delta\theta_i)\delta(q'_\lambda - q_\lambda - \Delta q_\lambda) \quad (3.109)\end{aligned}$$

It follows that:

$$\begin{aligned}&\langle q'_\lambda\rangle_{\Gamma', t+\delta t}\Psi(\boldsymbol{\Gamma}', t+\delta t) = \int dq'_\lambda q'_\lambda \Psi(\boldsymbol{\Gamma}', q'_\lambda, t+\delta t) \\ =\ & \int dq'_\lambda dq_\lambda q'_\lambda \int \left(\prod_i d\boldsymbol{r}_i d\boldsymbol{\xi}_i d\theta_i d\nu_i\right) \Psi(\boldsymbol{\Gamma}, q_\lambda, t)\Psi(\boldsymbol{\xi}_i)\Psi(\nu_i) \\ & \delta(\boldsymbol{r}'_i - \boldsymbol{r}_i - \Delta\boldsymbol{r}_i)\delta(\theta'_i - \theta_i - \Delta\theta_i)\delta(q'_\lambda - q_\lambda - \Delta q_\lambda) \\ =\ & \int dq_\lambda (q_\lambda + \Delta q) \int \left(\prod_i d\boldsymbol{r}_i d\boldsymbol{\xi}_i d\theta_i d\nu_i\right) \Psi(\boldsymbol{\Gamma}, q_\lambda, t)\Psi(\boldsymbol{\xi}_i)\Psi(\nu_i) \\ & \delta(\boldsymbol{r}'_i - \boldsymbol{r}_i - \Delta\boldsymbol{r}_i)\delta(\theta'_i - \theta_i - \Delta\theta_i) \\ =\ & \int dq_\lambda (q_\lambda + \Delta q) \int \left(\prod_i d\boldsymbol{r}_i d\theta_i\right) \Psi(\boldsymbol{\Gamma}, q_\lambda, t) P(\boldsymbol{\Gamma}', t+\delta t|\boldsymbol{\Gamma}, t) \\ =\ & \int \left(\prod_i d\boldsymbol{r}_i d\theta_i\right) (\langle q_\lambda\rangle_{\Gamma,t} + \Delta q)\Psi(\boldsymbol{\Gamma}, t) P(\boldsymbol{\Gamma}', t+\delta t|\boldsymbol{\Gamma}, t) \quad (3.110)\end{aligned}$$

where sequentially I have used Eq. (3.109), integrated in q'_λ, substituted Eq. (3.107), and finally integrated in q_λ. A direct comparison between Eq. (3.104) and Eq. (3.110) shows that in order to enforce the equality (3.99) one must choose:

$$\Delta q_\lambda = \frac{\partial \log P}{\partial \lambda} \,. \quad (3.111)$$

Since the noises $\boldsymbol{\xi}$ and ν are normalized and Gaussian, the conditional density in Eq. (3.107) explicitly reads:

$$P(\boldsymbol{\Gamma}', t+\delta t|\boldsymbol{\Gamma}, t) \propto$$
$$\Pi_i \exp\left[-\frac{(x'_i - x_i - v_0\cos\theta_i\delta t - \mu_0 F_i^x \delta t)^2}{4\mu_0 k_B T \delta t} - \frac{(y'_i - y_i - v_0\sin\theta_i\delta t - \mu_0 F_i^y\delta t)^2}{4\mu_0 k_B T\delta t} - \frac{(\theta'_i - \theta_i)^2}{4D_\theta \delta t}\right] . \quad (3.112)$$

In our specific case a constant perturbation is applied in the $x-$direction so that $F_i^x \to F_i^x + \epsilon_i \lambda \boldsymbol{u}_x$ thus, by differentiating Eq. (3.112) with respect to λ one gets:

$$\begin{aligned}\frac{\partial \ln P}{\partial \lambda} &= \frac{\beta}{2}\sum_i \left[(x'_i - x_i - v_0\cos\theta_i\delta t - \mu_0 F_i^x \delta t)\frac{\partial F_i^x}{\partial \lambda}\right] \\ &= \sqrt{\frac{\beta\mu_0\delta t}{2}}\sum_i \xi_i^x \frac{\partial F_i^x}{\partial \lambda} \,. \quad (3.113)\end{aligned}$$

It follows that the equation of motion for q_λ reads:

$$\boxed{\dot{q}_\lambda = \sqrt{\frac{\beta\mu_0}{2}}\sum_i \xi_i^x} \quad (3.114)$$

Finally, the response function of interest becomes

$$\boxed{\chi(t) = N^{-1} \sum_i \frac{\partial \langle x_i \rangle}{\partial \lambda}(t) = N^{-1} \sum_i \langle x_i q_\lambda \rangle = N^{-1} \sum_i \sqrt{\frac{\beta \mu_0}{2}} \int_0^t dt' \langle x_i(t) \xi_i^x(t') \rangle} \tag{3.115}$$

3.9 Appendix: Numerical measurement of the response function

In Fig. 3.2 the integrated response function obtained from unperturbed simulations of a Brownian suspension (Pe=0) (purple line) is compared with simulations where an external constant force is applied to all the particles $\boldsymbol{f}_i = \epsilon_i \lambda \boldsymbol{u}_x$, where $\epsilon_i = \pm 1$ with equal probability and $\lambda = 0.1$ (with purple points).

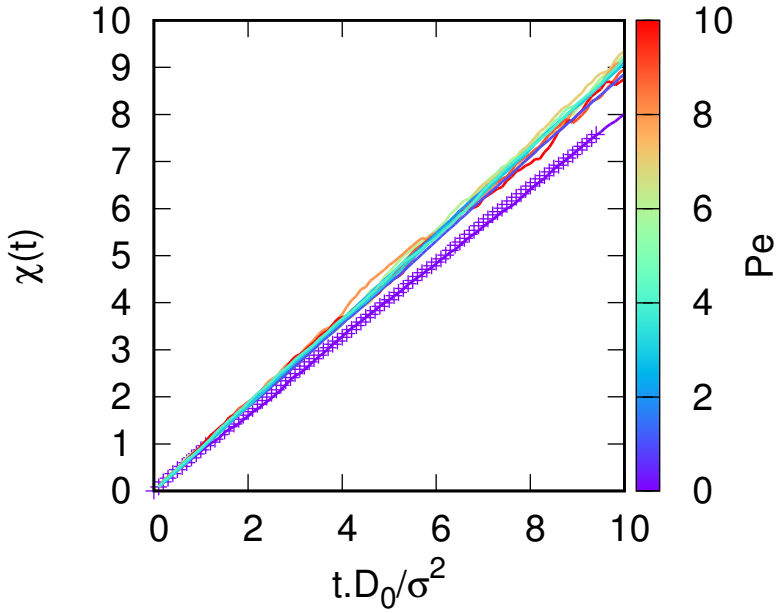

Figure 3.2: $\chi(t)$ vs. t for $N = 1000$ ABP at $\phi = 0.10$ and several Pe values (from Pe=0 to 10), obtained from simulations of the unperturbed system using Malliavin weights method (in lines, with a color code associated to each Pe value, from purple for Pe=0, to red for Pe=10). For Pe=0, the results obtained from simulations of the unperturbed system using Malliavin weights (purple line) are compared with the ones resulting from applying a small force (purple points).

In Fig. 3.2 it is also shown the integrated response function at different Pe, showing that the mobility (the slope of these curves) rapidly increases for small Pe but then saturates to a given value, as shown by the lines at different Pe numbers which fall on top of each other for Pe > 1. This behavior is captured by the Green-Kubo expression derived in the maintext.

3.10 Appendix: Chapman-Enskog method for 1D AOUP

Here I report some details of the Chapman-Enskog procedure for a one dimensional system of AOUP. The starting point is the evolution equation (3.43) together with the *ansatz* of Eqs. (3.45-3.46). By integrating (3.43) over p a conservation equation for R is obtained:

$$\partial_t R = -\partial_x \sum_j J^{(j)} = -\sum_j \epsilon^j \partial_x \int dp\, p\, \phi^{(j)} \equiv \sum_j \epsilon^j \mathcal{F}^{(j)} \tag{3.116}$$

where $J = \sum_j J^{(j)}$ is the probability flux.
By substituting (3.116) into (3.43) one obtains to first order in ϵ an equation for $\phi^{(1)}$:

$$\mathcal{O}(\epsilon) : \mathcal{L}[\phi^{(1)}] \equiv \partial_p(p\, \phi^{(1)} + \partial_p \phi^{(1)}) = p\frac{e^{-p^2/2}}{\sqrt{2\pi}}(\partial_x R + U' R) \tag{3.117}$$

In Eq. (3.117) $\phi^{(1)}$ has a Gaussian dependence in momenta so that:

$$\phi^{(1)} = -p\frac{e^{-p^2/2}}{\sqrt{2\pi}}\mathcal{D}R \tag{3.118}$$

with $\mathcal{D}R \equiv U'R + \partial_x R$. Note that $\mathcal{L}[e^{-p^2/2}] = 0$ such that the functions $\phi^{(j)}$ are defined up to a constant in p which is uniquely determined by conditions (3.46). The second order in ϵ reads:

$$\mathcal{O}(\epsilon^2) : \mathcal{L}[\phi^{(2)}] = \frac{e^{-p^2/2}}{\sqrt{2\pi}}[\mathcal{F}^{(1)}(R) + (p^2-1)U''R] + p\partial_x\phi^{(1)} - U'\partial_p\phi^{(1)} \tag{3.119}$$

From Eq. (3.118) and (3.119) it follows that $\phi^{(2)}$ is even in p, such that $\mathcal{F}^{(2)} = \int dp\, p\, \phi^{(2)} = 0$.
Using

$$\mathcal{L}\left[p^2\frac{e^{-p^2/2}}{\sqrt{2\pi}}\right] = -2(p^2-1)\frac{e^{-p^2/2}}{\sqrt{2\pi}} \tag{3.120}$$

one finds:

$$\phi^{(2)} = \alpha(x)(p^2-1)\frac{e^{-p^2/2}}{\sqrt{2\pi}} \tag{3.121}$$

with $\alpha = \frac{1}{2}(\partial_x \mathcal{D}R + U'\mathcal{D}R - U''R)$.
To third order in ϵ the evolution equation gives:

$$\mathcal{O}(\epsilon^3) : \mathcal{L}[\phi^{(3)}] = \frac{\delta\phi^{(1)}}{\delta R}\mathcal{F}^{(1)}(R) + p\partial_x\phi^{(2)} - U'\partial_p\phi^{(2)} - U''\partial_p(p\phi^{(1)}) \tag{3.122}$$

which, using (3.118) and (3.121), together with the identity:

$$\mathcal{L}\left[p^3\frac{e^{-p^2/2}}{\sqrt{2\pi}}\right] = \frac{e^{-p^2/2}}{\sqrt{2\pi}}3p(2-p^2) \tag{3.123}$$

gives:

$$\phi^{(3)} = p\frac{e^{-p^2/2}}{\sqrt{2\pi}}(\beta(x)p^2 + \gamma(x)) \tag{3.124}$$

with $\beta = -\frac{1}{3}(\mathcal{D}\alpha - U''\mathcal{D}R)$ and $\gamma = \mathcal{D}\partial_x\mathcal{D}R - \partial_x\alpha + U'\alpha$. The hierarchy of equations is truncated to $\sim o(\epsilon^3)$ and, going back to the conservative equation (3.116), an expression for the first three components of the flux as a function of R is found:

$$J^{(1)} = -\mathcal{D}R \tag{3.125a}$$
$$J^{(2)} = 0 \tag{3.125b}$$
$$J^{(3)} = \partial_x U'' R \tag{3.125c}$$

One has therefore a closed approximated equation for the evolution of R:

$$\frac{\partial R}{\partial t} = -\epsilon\partial_x[-\partial_x R - U'R + \epsilon^2\partial_x(U''R)] + o(\epsilon^3) \tag{3.126}$$

Eq. (3.126) is readily solved by looking at the zero-flux steady-state with solution:

$$R(x;\epsilon) = \exp\left[-U - \epsilon^2\left(\frac{1}{2}U'^2 - U''\right)\right] + o(\epsilon^3) \tag{3.127}$$

In turn Eq. (3.127) is used to find the explicit expressions of $\phi^{(1,2,3)}$ which are substituted in (3.45) to get:

$$\Psi_0(x,p;\epsilon) = \Psi^{(0)}\left[1 + \frac{\epsilon^2}{2}(1-p^2)U'' + \epsilon^3\left(\frac{p^3}{6}U''' - \frac{p}{2}U'''\right)\right] + o(\epsilon^3) \tag{3.128}$$

Finally, by using (3.127) into (3.128) and interpreting the term in square brackets as the linearisation of an exponential $\exp(x) \sim 1 + x$ one gets:

$$\Psi_0(x,p;\epsilon) \sim \exp\left[-\frac{p^2}{2} - U - \frac{\epsilon^2}{2}\left(p^2U'' + U'^2 - 3U''\right) + \frac{\epsilon^3}{2}\left(\frac{p^3}{3}U''' - pU'''\right)\right] + o(\epsilon^3) \tag{3.129}$$

Intermezzo

Stochastic Thermodynamics: some personal notes

In its original formulation Thermodynamics concerns the transformations between equilibrium states of macroscopic systems. Thermodynamically, a system is described by a set of measurable quantities, named thermodynamic state variables which may be classified into extensive properties (like volume or energy) or intensive properties (like temperature and pressure) depending on whether they vary or not with the size of the system.
A thermodynamic model consists of an equation of state expressing the relation among the state variables (the simplest example is the ideal gas law). It is a phenomenological model based on the observation of the system, i.e. the information collected from experimental measurements. As such, it strictly depends on the accuracy of the measurement tools which in turn set the scale of validity of the model. It can be argued that this reasoning in fact applies to all branches of physics.
Accordingly, Classical Thermodynamics applies on a macroscopic scale, describing a system as it must have looked to a scientist of the XIXth century [1].

The first law of Thermodynamics is the translation in the thermodynamic language of the principle of energy conservation for an isolated system (well-known in Classical Mechanics). Given the total internal energy of the system U, it relates its variation between two different equilibrium states ΔU with the work w performed on the system and the heat q absorbed by it:

$$\Delta U = q + w. \tag{3.130}$$

The internal energy U is an extensive state function and it only depends on the initial and final equilibrium states. This is not true for q and w which do not describe the equilibrium state of the system but rather its energy transformations among states. They are conventionally positive when resulting in an increase of the system energy.
The second law of Thermodynamics addresses the irreversibility of macroscopic processes. In order to account for the fact that macroscopic processes occur only in 'one

[1] Back then, the very existence of atoms was hypothetical. Nowadays it is well known that any heat transfer is connected with the thermal motions of molecules. Hence, Thermodynamics itself has a mechanical explanation, namely Statistical Mechanics.

direction' Thermodynamics introduces a second extensive function named entropy S. Contrary to the internal energy, S is not conserved during a transformation between two equilibrium states such that:

$$\Delta S \geq \frac{\Delta q}{T}\,, \tag{3.131}$$

where Δq is the heat exchange at a constant temperature T. The equality in Eq. (3.131) only holds for quasi-static (reversible) processes.

Q: *Can one generalize the thermodynamic framework to open systems subjected to some external forces?*

This is the goal of Non-Equilibrium Thermodynamics [115] which is based on a local formulation of the principles of Classical Thermodynamics. It assumes that it is possible to decompose the open system into small cells which can be thought to be locally in equilibrium, in the sense that their relaxation to equilibrium occurs in a much smaller time than the macroscopic time scale set by the observer. The hypothesis of a separation of scale, also known as Local Thermodynamic Equilibrium (LTE), allows to define local thermodynamic quantities and to treat them as continuous functions of space and time (x, t). The system is out-of-equilibrium if some irreversible processes are taking place which result in a production of entropy as stated by Eq. (3.131). Particularly for an isothermal system one might distinguish two contributions to the variation of entropy:

$$T\frac{dS(t)}{dt} = Te_p(t) + \dot{q}(t)\,, \tag{3.132}$$

where $\dot{q}(t)$ is the rate of heat absorbed by the system and $e_p(t)$ is entropy production rate. The former contribution is equal and opposite to the rate of heat dissipated into the bath (h_d), also named external entropy flow rate ($T\dot{S}_e$). The latter contribution is sometimes referred to as internal entropy production rate ($\dot{S}_i$). To unify the nomenclature (read jargon) then one may write:

$$\dot{q} = -h_d = -T\dot{S}_e \tag{3.133a}$$

$$\dot{S}_i = e_p\,. \tag{3.133b}$$

Another physical decomposition for the total heat $q(t)$ has been proposed to characterize non-equilibrium steady-states (NESS). Oono and Paniconi [116] proposed to divide the total heat into the sum of the excess heat $q_{ex}(t)$ due to the transformation between two different states and the house-keeping heat $q_{hk}(t)$ produced by sustaining a single NESS:

$$q(t) = q_{ex}(t) + q_{hk}(t)\,. \tag{3.134}$$

If the system is in a NESS the entropy is constant (and positive) and $q_{ex} = 0$. It follows that in this particular case $Te_p = -\dot{q}_{hk}$ and they do not depend on time.

A SIDE NOTE: Gibbs drew a useful connection between Equilibrium Thermodynamics and molecular systems with the introduction of the notion of ensemble in

Statistical Mechanics [117]. Ensembles do not exist in real life but are a very convenient mathematical trick to treat systems with many degrees of freedom. In this framework, all the thermodynamic quantities such as internal energy U, free energy G and entropy S can be recast as functionals of an ensemble probability density $\Psi(x,t)$ defined on a given phase space $\mathcal{M}$ such that $x \in \mathcal{M}$ [118]. In other words, they are expressed as ensemble averages:

$$\langle U \rangle_t = -k_B T \int dx \Psi(x,t) \log \Psi_{\text{eq}}(x) \tag{3.135a}$$

$$\langle S \rangle_t = -k_B \int dx \Psi(x,t) \log \Psi(x,t) \tag{3.135b}$$

$$\langle G \rangle_t = U - TS = k_B T \int dx \Psi(x,t) \log \left(\frac{\Psi(x,t)}{\Psi_{\text{eq}}(x)} \right) , \tag{3.135c}$$

where $\Psi_{\text{eq}}(x)$ is the long-time equilibrium probability density and k_B is the Boltzmann constant. Note that all quantities appearing in Eq. (3.132) and Eq. (3.134) are intended as macroscopic values, i.e. ensemble averages in the language of Statistical Mechanics.

Q: *Can one generalize the thermodynamic framework to systems that are not macroscopic?*

This question became more and more urgent at the end of the XXth century with the development of modern experimental techniques able to manipulate systems at the micro/nanoscale. The theory of Markov stochastic processes turned out to be the most suitable for the purpose.
Let consider an equilibrium system described by a Langevin equation:

$$\gamma \frac{dx}{dt} = F(x;\lambda) + \sqrt{2\gamma k_B T}\xi(t) , \tag{3.136}$$

where γ is the friction coefficient, $F = -\partial U(x,\lambda)/\partial x$ is the conservative force acting on x and $\xi(t)$ is a noise term. In particular $\xi(t)$ is assumed to be a Gaussian white noise (the formal derivate of the Wiener process) with zero average and unit delta-correlated variance. In Eq. (3.136) the possibility to perform some work on the system via an external parameter λ is included.
Sekimoto [119] was the first to draw a connection between the Langevin equation (3.136) and Thermodynamics. In his work Sekimoto starts by multiplying Eq. (3.136) by a infinitesimal change dx in order to obtain an energy balance:

$$0 = -\left(-\gamma \frac{dx}{dt} + \sqrt{2\gamma k_B T}\xi(t) \right) \circ dx - F(x;\lambda) \circ dx , \tag{3.137}$$

where $\circ$ indicates the Stratonovich multiplication [43]. The first term on the *rhs* is due to the coupling with the thermal bath, hence was interpreted as the infinitesimal heat dissipated into the bath ($-dq$). The exact differential of the internal energy is:

$$dU = \left(\frac{\partial U}{\partial x} \right) \circ dx + \left(\frac{\partial U}{\partial \lambda} \right) d\lambda . \tag{3.138}$$

By identifying the second term on the *rhs* as the infinitesimal work performed on the system by changing λ one obtains:

$$dU = dq + dw\,, \tag{3.139}$$

which is the first law of Thermodynamics for the Langevin system in Eq. (3.136) and it represents the foundation of Stochastic Energetics.
Following the same approach, Hatano and Sasa [120] derived an extended second law of Thermodynamics for the stochastic system described by Eq. (3.136). Using the decomposition of Oono and Paniconi, Eq. (3.134), the second law of Thermodynamics can be recast as:

$$T\langle \Delta S\rangle_0 \geq \langle q_{ex}\rangle_0\,, \tag{3.140}$$

where $\langle\cdot\rangle_0$ refers to the steady-state ensemble average. As mentioned above, q_{ex} is obtained by subtracting from the total heat the house-keeping heat q_{hk} which is steadily generated even when the state of the system does not change. Let consider the case of a Langevin dynamics in presence of a non-conservative force f, such that $F(x;\lambda)$ in Eq. (3.136) is now

$$F(x;\lambda) = -\frac{\partial U(x;\lambda)}{\partial x} + f. \tag{3.141}$$

Traditionally a stochastic system can be driven out-of-equilibrium either by the presence of non-conservative forces or by an external time-dependent protocol changing λ. The statistics of this system can be described by a steady-state probability density $\Psi_0(x;\lambda)$ which is assumed to have the following shape:

$$\Psi_0(x;\lambda) = e^{-\Phi(x;\lambda)}\,, \tag{3.142}$$

with $\Phi(x;\lambda)$ a generalized potential.
I won't report here the full derivation of Eq. (3.140) but I rather focus on some important identifications made by the authors. Particularly they rewrite Eq. (3.136) as:

$$\gamma\frac{dx}{dt} = \gamma\mathcal{V}(x;\lambda) - k_BT\frac{\partial\Phi(x;\lambda)}{\partial x} + \sqrt{2\gamma k_BT}\xi(t)\,, \tag{3.143}$$

where the steady state velocity

$$\mathcal{V}(x;\lambda) = \gamma^{-1}F(x;\lambda) + \gamma^{-1}k_BT\frac{\partial\Phi(x;\lambda)}{\partial x} \tag{3.144}$$

was introduced. By multiplying by $\dot{x}(t)dt$ and integrating over time one gets:

$$\begin{aligned}\int_0^\tau dt\left(\gamma\frac{dx}{dt} - \sqrt{2\gamma k_BT}\xi(t)\right)\circ\dot{x}(t) &= \gamma\int_0^\tau dt\;\mathcal{V}(x;\lambda)\circ\dot{x}(t) \\ -\;k_BT\int_0^\tau dt\frac{\partial\Phi(x;\lambda)}{\partial x}\circ\dot{x}(t) &- k_BT\int_0^\tau dt\frac{\partial\Phi(x;\lambda)}{\partial\lambda}\dot{\lambda} + k_BT\int_0^\tau dt\frac{\partial\Phi(x;\lambda)}{\partial\lambda}\dot{\lambda}\,,\end{aligned} \tag{3.145}$$

where the term containing the time derivative of the protocol λ was added and subtracted. From Eq. (3.137) one recognizes in the *lhs* the total heat transferred to

the bath ($-q(x,\tau)$) along the stochastic trajectory $x(0) \longrightarrow x(\tau)$. Then, by using the exact differential of the generalized potential:

$$d\Phi = \left(\frac{\partial \Phi(x;\lambda)}{\partial x} \circ dx + \frac{\partial \Phi(x;\lambda)}{\partial \lambda} d\lambda \right) , \tag{3.146}$$

Eq. (3.145) becomes:

$$q(x,\tau) = -\gamma \int_0^\tau dt\ \mathcal{V}(x;\lambda) \circ \dot{x}_i(t) + k_B T \Delta\phi - k_B T \int_0^\tau dt \frac{\partial \Phi(x;\lambda)}{\partial \lambda} \dot{\lambda} , \tag{3.147}$$

where $\Delta\Phi \equiv \Phi(x(\tau);\lambda(\tau)) - \Phi(x(0);\lambda(0))$. By identifying the house-keeping heat as:

$$q_{hk}(x,\tau;\lambda) = -\gamma \int_0^\tau dt\ \mathcal{V}(x;\lambda) \circ \dot{x}(t) , \tag{3.148}$$

it follows:

$$q_{ex}(x,\tau) = q(x,\tau) - q_{hk}(x,\tau) = -k_B T \int_0^\tau dt \frac{\partial \Phi(x;\lambda)}{\partial \lambda} \dot{\lambda} + k_B T \Delta\Phi . \tag{3.149}$$

Eqs. (3.147-3.149) are the expressions for respectively the total, house-keeping and excess heat absorbed by the system during a stochastic evolution of length τ. In order to be compared with thermodynamic quantities, one needs to take the ensemble averages, i.e. to average over noise realizations and over the stationary distribution Ψ_0. In particular, using Eq. (3.135b) with Eq. (3.142) it immediately follows that $\langle \Delta S \rangle_0 = k_B \langle \Delta\Phi \rangle_0$. The excess heat exchange, Eq. (3.149), then becomes

$$\boxed{\langle q_{ex}(x,\tau) \rangle_0 = -k_B T \left\langle \int_0^\tau dt \frac{\partial \Phi(x;\lambda)}{\partial \lambda} \dot{\lambda} \right\rangle_0 + T \langle \Delta S \rangle_0 .} \tag{3.150}$$

It is easy to show (check the paper for the derivation) that the first term on the *rhs* fulfils an integral fluctuation relation such that:

$$\left\langle \exp\left(- \int_0^\tau dt \frac{\partial \Phi(x;\lambda)}{\partial \lambda} \dot{\lambda} \right) \right\rangle_0 = 1 . \tag{3.151}$$

By Jensen's inequality it follows that $\left\langle - \int_0^\tau dt \frac{\partial \Phi(x;\lambda)}{\partial \lambda} \dot{\lambda} \right\rangle_0 \geq 0$ and Eq. (3.140) is obtained. The expression (3.148) for the house-keeping heat occurs frequently in the literature of Stochastic Thermodynamics.
In the same year of Hatano and Sasa, Qian [53] put forward a mesoscopic framework of Thermodynamics based on Eq. (3.136). It is convenient to introduce the Fokker-Planck equation for the time evolution of the probability density $\Psi(x,t;\lambda)$ associated to Eq. (3.136):

$$\partial_t \Psi(x,t;\lambda) = -\nabla J(x,t;\lambda) = -\nabla \left(\gamma^{-1} F(x;\lambda) - k_B T \gamma^{-1} \nabla \right) \Psi(x,t;\lambda) , \tag{3.152}$$

where J is the probability flux and $\nabla \equiv \partial/\partial x$. The time-dependent Gibbs entropy of the system is:

$$\langle S \rangle_t = -k_B \int dx \Psi(x,t;\lambda) \log \Psi(x,t;\lambda) . \tag{3.153}$$

Taking the time derivative of Eq. (3.153) one obtains for the rate of change of the entropy of the system:

$$\begin{aligned} T\langle \dot{S} \rangle_t &= -k_B T \left[\int dx \partial_t \Psi(x,t;\lambda) \log \Psi(x,t;\lambda) + \int dx \partial_t \Psi(x,t;\lambda) \right] \\ &= +k_B T \int dx \; \nabla J(x,t;\lambda) \left[\log \Psi(x,t;\lambda) + 1 \right] . \end{aligned} \tag{3.154}$$

By integrating by parts, adding and subtracting the force $F(x;\lambda)$ to the term inside the parenthesis one gets:

$$\begin{aligned} T\langle \dot{S} \rangle_t = &- \int dx [k_B T \nabla \log \Psi(x,t;\lambda) - F(x;\lambda)] J(x,t;\lambda) \\ &- \int dx F(x;\lambda) J(x,t;\lambda) . \end{aligned} \tag{3.155}$$

Applying Ito's formula [43] to Sekimoto's definition of dissipated heat one gets:

$$(-dq(t)) = F(x;\lambda) \circ dx = F(x;\lambda) dx + \frac{1}{2} dx \nabla F dx . \tag{3.156}$$

By substituting Eq. (3.136) into Eq. (3.156) and using the properties of the Wiener process $\xi(t)dt$ one finds:

$$\begin{aligned} (-dq(t)) = F(x;\lambda) &\left[\gamma^{-1} F(x;\lambda) dt + \sqrt{2\gamma^{-1} k_B T} \xi(t) dt \right] \\ &+ \gamma^{-1} k_B T \nabla F(x;\lambda) dt + \mathcal{O}(dt^2) . \end{aligned} \tag{3.157}$$

By taking the ensemble average of Eq. (3.157) one gets:

$$\begin{aligned} \langle \dot{q} \rangle_t &= -\gamma^{-1} \int dx F(x;\lambda) \left[F(x,t;\lambda) \Psi(x,t;\lambda) - k_B T \nabla \Psi(x,t;\lambda) \right] \\ &= - \int ds F(x;\lambda) J(x,t;\lambda) , \end{aligned} \tag{3.158}$$

which is precisely the last term in the *rhs* of Eq. (3.155). One may therefore rewrite Eq. (3.155) as:

$$\begin{aligned} T\langle \dot{S} \rangle_t &= - \int dx [k_B T \nabla \log \Psi(x,t;\lambda) - F(x;\lambda)] J(x,t;\lambda) + \langle \dot{q} \rangle_t \\ &\equiv T\langle e_p \rangle_t + \langle \dot{q} \rangle_t . \end{aligned} \tag{3.159}$$

Introducing the time-dependent velocity $\mathcal{V}(x,t;\lambda)$ as

$$\mathcal{V}(x,t;\lambda) = \gamma^{-1} F(x;\lambda) - \gamma^{-1} k_B T \nabla \log \Psi(x,t;\lambda) , \tag{3.160}$$

allows us to write the entropy production rate as:

$$\boxed{T\langle e_p \rangle_t = \int dx \, \gamma \mathcal{V}(x,t;\lambda) J(x,t;\lambda) .} \tag{3.161}$$

In alternative, the entropy production may be expressed as:

$$\boxed{T\langle e_p \rangle_t = \int dx \gamma \frac{(J(x,t;\lambda))^2}{\Psi(x,t;\lambda)} \geq 0 ,} \tag{3.162}$$

where the definition Eq. (3.160) was used. Note that Eq. (3.162) is always non-negative, in accordance with the second law of Thermodynamics. For this reason usually Eq. (3.162) is interpreted as the 'statistical version' of the second law of Thermodynamics[2].
Finally, a connection can be drawn between the result Eq. (3.161) by Qian and the definition of the house-keeping heat Eq. (3.148) put forward by Hatano and Sasa. As already mentioned, at steady state the entropy production rate must equate the heat flow released in the environment so that:

$$T\langle e_p\rangle_0 = \langle -\dot{q}_{hk}\rangle_0 \,. \tag{3.163}$$

This can be proved directly from Eq. (3.148) by taking the steady-state ensemble average . The starting point is the stochastic integral:

$$q_{hk}(x,\tau) = -\gamma \int_0^\tau dt\, \mathcal{V}(x;\lambda) \circ \dot{x}(t) \equiv -\gamma \int_{x(0)}^{x(\tau)} \mathcal{V}(x;\lambda) \circ dx(t) \,. \tag{3.164}$$

Let use Ito's formula to make the change of variable:

$$\mathcal{V}(x;\lambda) \circ dx(t) = \mathcal{V}(x;\lambda) \left[\gamma^{-1}F(x;\lambda)dt + \sqrt{2\gamma^{-1}k_BT}\xi(t)dt\right] + \gamma^{-1}k_BT\nabla\mathcal{V}(x;\lambda)dt \,. \tag{3.165}$$

The second term on the *rhs* vanishes after integrating over the noise statistics while the remaining terms can be directly averaged using $\Psi_0(x;\lambda)$ so that:

$$\begin{aligned}
\langle q_{hk}\rangle_0 &= -\int_0^\tau dt \int dx \mathcal{V}(x;\lambda)F(x;\lambda)\Psi_0(x;\lambda) - \int_0^\tau dt \int dx k_BT\nabla\mathcal{V}(x;\lambda)\Psi_0(x;\lambda) \\
&= -\int_0^\tau dt \int dx \mathcal{V}(x;\lambda)\left[F(x;\lambda)\Psi_0(x;\lambda) - k_BT\nabla\Psi_0(x;\lambda)\right] \\
&= -\gamma \int_0^\tau dt \int dx \mathcal{V}(x;\lambda)J(x;\lambda) \,.
\end{aligned} \tag{3.166}$$

By taking the time derivative of $\langle q_{hk}\rangle_0$ the equality (3.163) is eventually obtained.

[2]It is common to say that Eq. (3.162) reveals the very probabilistic nature of Thermodynamics. Historically speaking, this is not true.

PART II

Chapter 4

Preamble: Charged surfaces in liquids

In this Chapter, I review some of the basic concepts underlying the behaviour of electrolyte systems in contact with charged surfaces. Many of the results and notions discussed here will be widely used in the remainder of the Thesis. For the time being, I shall adopt the Poisson-Boltzmann (PB) formalism, which is a standard continuum theory of electrolytes [121, 122]. Therein, the ions are described as a continuous distribution of point-like charges interacting via an average electrostatic potential. Further, correlations among ions are neglected and the solvent is treated as a dielectric medium of uniform relative permittivity ϵ_r.
Let consider the following scenario (Fig. 4.1): a flat surface is immersed in a monovalent electrolyte solution of salt concentration c_s. The surface acquires a uniform surface charge density σ due to the binding/dissociation events occurring at the solid-liquid interface which are favoured by solvents with high dielectric constant like water ($\epsilon_r \approx 80$). As a consequence, a cloud of mobile counterions forms in the vicinity of the wall to balance the surface charge, which takes the name of diffuse double layer (DDL). The competition between electrostatic interactions and entropic (osmotic) forces maintains a *net charge* within the DDL, determining the profiles of the ionic concentrations $c_\pm$, the electrostatic potential Φ and the electric field E_y. Far from the surface, both the potential and the electric field vanish and the concentrations of the ionic species are set by the reservoir:

$$\Phi(y \to \infty) = 0 \tag{4.1a}$$
$$c_\pm(y \to \infty) = c_s. \tag{4.1b}$$

Let define now few important length scales associated with the electrolyte system. Later on in this Chapter, the physical meaning of these lengths will be made clear. The Bjerrum length is defined as the distance at which the interaction energy between two ions equates the thermal energy $k_B T$

$$\boxed{\ell_B = \frac{e^2}{4\pi\epsilon_0\epsilon_r k_B T}}, \tag{4.2}$$

where e is the elementary charge, ϵ_0 is the vacuum dielectric constant, k_B is the Boltzmann constant and T is the temperature. Intuitively, the Bjerrum length

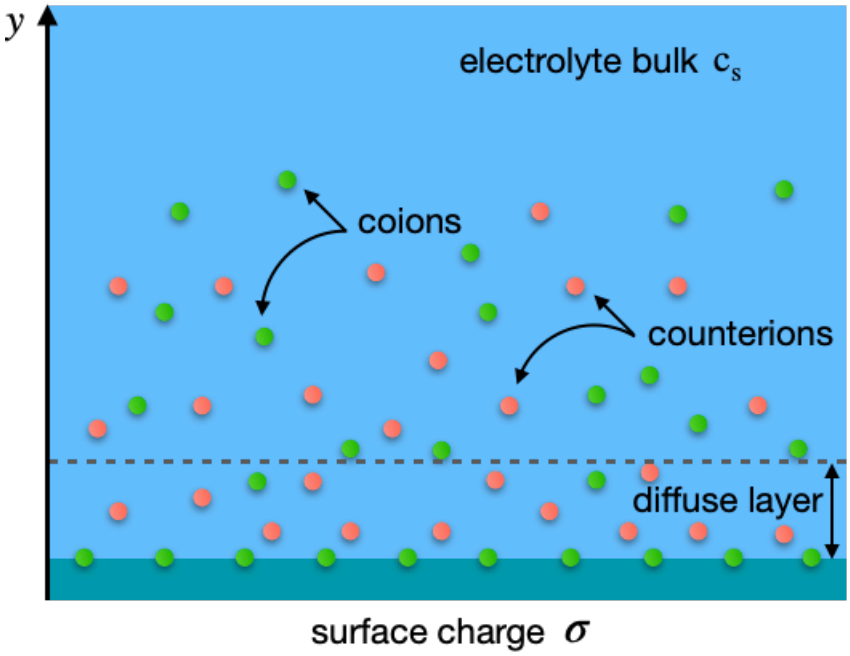

Figure 4.1: Schematic view of a charged surface immersed in an electrolyte solution with salt concentration c_s. The ions rearrange in the proximity of the surface to compensate for the surface charge giving rise to a net charge diffusive region, the diffuse double layer. The $y-$axis denotes the distance from the surface.

sets the 'molecular scale' of the system, giving the minimum distance between two identical ions in solution. It only depends on the temperature and the solvent properties hence, in the following, it will be treated as a constant. For water at room temperature $\ell_B \sim 7$Å.
The Gouy-Chapman length is the distance at which the interaction energy between an ion and the surface is of the order $\sim k_B T$

$$\boxed{\ell_{GC} = \frac{e}{2\pi\sigma\ell_B}\,.} \tag{4.3}$$

The Debye length is defined as

$$\boxed{\lambda_D = \sqrt{\frac{\epsilon_0\epsilon_r k_B T}{2e^2 c_s}}} \tag{4.4}$$

and characterizes the width of the DDL, i.e. the distance over which the imbalance of the surface charge is screened. Interestingly, it only depends on the salt concentration c_s spanning from tens of nanometers for very dilute systems ($c_s \sim 10^{-4}$M) down to few Ångtröm for high salt concentrations ($c_s \sim 1$M).
Finally, let introduce the Dukhin length as:

$$\boxed{\ell_{\mathrm{Du}} = \frac{|\sigma|}{2ec_s}\,,} \tag{4.5}$$

that is the ratio between the ions coming from the surface and that coming from the bulk.

4.1 The Poisson-Boltzmann theory

For a dilute electrolyte solution the chemical potential of the ions may be written as the sum of the ideal gas entropy and the electrostatic energy [123]:

$$\mu_\pm = k_B T \log(c_\pm \Lambda^3) \pm e\Phi \,, \tag{4.6}$$

where $1/\Lambda^3$ is a reference concentration. In equilibrium, the chemical potential of each ionic species is constant and equal to the reservoir potential $\mu_{res} = k_B T \log(c_s \Lambda^3)$. As a consequence, each ionic concentration obeys a Boltzmann distribution:

$$c_\pm = c_s e^{\mp e\Phi/k_B T} \,. \tag{4.7}$$

Eq. (4.7) must be complemented with the Poisson equation relating the electrostatic potential to the charge distribution $n_c = e(c_+ - c_-)$:

$$\frac{d^2\Phi}{dy^2} + \frac{n_c}{\epsilon_0 \epsilon_r} = 0 \,. \tag{4.8}$$

By combining Eq. (4.7) and Eq. (4.8) one obtains the Poisson-Boltzmann equation for the equilibrium electrostatic potential:

$$\boxed{\frac{d^2\Phi}{dy^2} = \frac{2ec_s}{\epsilon_0 \epsilon_r} \sinh\left(\frac{e\Phi}{k_B T}\right) \,.} \tag{4.9}$$

Eq. (4.9) is a non-linear second order differential equation and in order to solve for Φ, two boundary conditions are required. The bulk value is fixed by Eq. (4.1a) while the Gauss boundary condition applies at the wall:

$$\left.\frac{d\Phi}{dy}\right|_{y=0} = -\frac{\sigma}{\epsilon_0 \epsilon_r} \,, \tag{4.10}$$

where the electric field inside the surface ($y < 0$) is assumed to be zero[1].
For the planar configuration of Fig. 4.1 the Poisson-Boltzmann equation can be solved analytically. By multiplying Eq. (4.9) by $d\Phi/dy$ and using $d\cosh(e\Phi/k_B T)/dy = (k_B T)^{-1} e \sinh(e\Phi/k_B T) d\Phi/dy$ one obtains:

$$\frac{1}{2} d\left(\frac{d\Phi}{dy}\right)^2 = \frac{2c_s k_B T}{\epsilon_0 \epsilon_r} d\left(\cosh\left(\frac{e\Phi}{k_B T}\right)\right) \,. \tag{4.11}$$

Integrating between y and ∞ and using the boundary condition (4.1a) one obtains the first integral of the Poisson-Boltzmann equation:

$$\frac{1}{2}\left(\frac{d\Phi}{dy}\right)^2 = \frac{2c_s k_B T}{\epsilon_0 \epsilon_r}\left(\cosh\left(\frac{e\Phi}{k_B T}\right) - 1\right) \tag{4.12}$$

[1] This is a good approximation for a insulator with thickness much larger than the Debye length and with dielectric constant much smaller than the one of the solvent.

which, by using the identity $\text{sign}(x)\sqrt{(\cosh(x)-1)/2} = \sinh(x/2)$, becomes:

$$\boxed{\frac{d\Phi}{dy} = -\sqrt{\frac{8c_s k_B T}{\epsilon_0 \epsilon_r}} \sinh\left(\frac{e\Phi}{2k_B T}\right)} \,. \tag{4.13}$$

Some remarks follow from evaluating Eqs. (4.12-4.13) at the surface ($y = 0$). First, using the Gauss boundary condition (4.10) one derives the Grahame equation,

$$\sigma = \sqrt{8\epsilon_0 \epsilon_r k_B T c_s} \sinh\left(\frac{e\Phi_0}{2k_B T}\right) , \tag{4.14}$$

which relates the surface charge density σ to the potential at the surface Φ_0. In the Debye-Hückel regime, when $e\Phi_0 \ll k_B T$, Eq. (4.14) can be linearized and the potential Φ_0 becomes proportional to the surface charge density:

$$\sigma \simeq \frac{\epsilon_0 \epsilon_r}{\lambda_D} \Phi_0 \,. \tag{4.15}$$

Note that Eq. (4.15) is the equation of a planar capacitor with two plates holding a charge density $\pm\sigma$ at a distance λ_D and capacitance $C = \epsilon_0 \epsilon_r / \lambda_D$. This analogy is the reason for the name *diffuse double layer* [122]. Further, rewriting Eq. (4.12) in terms of Φ_0

$$2\cosh\left(\frac{e\Phi_0}{k_B T}\right) = 2 + \frac{\sigma^2}{2c_s k_B T \epsilon_0 \epsilon_r} = 2 + \left(\frac{\ell_{\text{Du}}}{\lambda_D}\right)^2 \tag{4.16}$$

and using Eq. (4.7):

$$\boxed{\frac{c_0}{c_s} = 2 + \left(\frac{\ell_{\text{Du}}}{\lambda_D}\right)^2} \,, \tag{4.17}$$

where $c_0 \equiv c_+(y=0) + c_-(y=0)$ is the total ionic concentration at the surface. This result shows that the ratio $\ell_{\text{Du}}/\lambda_D$ determines the total accumulation of ions within the diffuse layer with respect to the bulk concentration.
Going back to Eq. (4.12), it can be integrated as

$$\int_{\Phi_0}^{\Phi} d\Phi \left(\sinh\left(\frac{e\Phi}{2k_B T}\right)\right)^{-1} = -\int_0^y \sqrt{\frac{8c_s k_B T}{\epsilon_0 \epsilon_r}} dy \,, \tag{4.18}$$

which gives the following solution for the electrostatic potential:

$$\boxed{\Phi(y) = \frac{2k_B T}{\epsilon_0 \epsilon_r} \log\left(\frac{1 + \gamma e^{-y/\lambda_D}}{1 - \gamma e^{-y/\lambda_D}}\right)} \,, \tag{4.19}$$

where $\gamma = \tanh\left(e\Phi_0/4k_B T\right)$ and the identity $\tanh^{-1}(x) = \frac{1}{2}\log\left(\frac{1+x}{1-x}\right)$ was used. The Debye-Hückel regime ($\gamma \ll 1$) is recovered by linearizing Eq. (4.19) so that:

$$\Phi \simeq 4k_B T \gamma e^{-y/\lambda_D} . \tag{4.20}$$

It follows that, for $e|\Phi_0| \ll k_B T$, the electrostatic potential decays exponentially and the Debye length appears naturally as the decaying characteristic length. The (high) efficiency of the screening in Eq. (4.20) is due to the rearrangement of the counterions and the coions, respectively close to and far from the surface. As a consequence, for distances larger than $\sim \lambda_D$ the surface appears as almost neutral. The potential profile changes dramatically in salt-free systems ($c_s = 0$), where the only charges in solution are the counterions coming from the dissociation of surface groups [121]. In this case, the potential is found to scale logarithmically with the distance from the surface $\Phi(y) \sim \log(y + \ell_{GC})^2$. It follows that in the absence of added salt, charge screening is not as efficient as for electrolyte systems and the Gouy-Chapman length ℓ_{GC} (instead of the Debye length) characterizes the structure of the counterion diffusive layer close to the surface.

4.2 Electrolytes under confinement

Let now consider the case of an electrolyte solution that, instead of being in contact with a single surface, is confined between two equally charged surfaces held at a distance $2h$. The slab geometry depicted in Fig. 4.2 will be used in the following as a paradigmatic model of a nanoslit or nanochannel (I will use these two terms indistinctly for the time being). The prefix 'nano' refers to the fact that $h \sim \lambda_D$, typically tens of nanometers in experimental realizations [124]. In the slab geometry, the width L_z in the direction normal to the page is taken to be constant and much larger than h (ideally infinite) such that Φ and $c_\pm$ do not depend on z and the system is effectively 2D. The channel is open and in contact with two reservoirs (Fig 4.2). In the absence of any external force applied through the reservoirs, such as pressure, concentration or potential gradients, the equilibrium ionic distribution within the two surfaces, and far from the openings, is still determined by the Poisson-Boltzmann equation (4.9). In this configuration, the Gauss boundary condition applies at each surface

$$\left.\frac{d\Phi}{dy}\right|_{y=\pm h} = \pm\frac{\sigma}{\epsilon_0\epsilon_r} \tag{4.21}$$

and the symmetry condition $E_y = 0$ applies at the midplane ($y = 0$). However, the additional complexity due to the confinement does not allow for an analytical solution of Eq. (4.9) even in the simple geometry considered here.

Still, it is useful to partition the general problem into different limiting regimes which correspond to *qualitatively* different electrostatic scenarios. I report in Fig. 4.3 an attempt to give a unified representation of the various electrostatic regimes for the system at hands (see [121] for further details). The independent parameters in the two main axes are $\ell_{GC}/h \sim \sigma^{-1}$ and $\lambda_D/h \sim c_s^{-1/2}$, respectively associates with the surface charge and the bulk concentration. Note that the Dukhin length ℓ_{Du} can be re-expressed in terms of these parameters as

$$\ell_{\mathrm{Du}} = \frac{2\lambda_D^2}{\ell_{GC}} \tag{4.22}$$

and determines the (continuous) transition between two different regimes: the Debye-Hückel and the ideal gas. As anticipated, the Debye-Hückel regime corresponds to

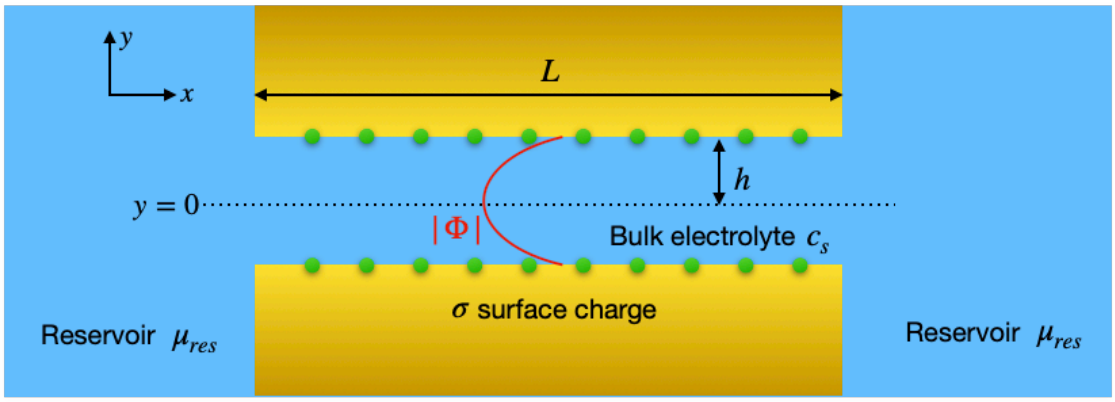

Figure 4.2: Schematic view of an electrolyte solution confined between two flat surfaces of length L and constant surface charge density σ held at a separation distance $2h$ from one another. I consider here a slab geometry in the $xy-$plane centred at the midplane $y = 0$. The channel width is assumed to be constant along the z direction pointing out of the page, and sufficiently large for the system to be effectively translationally invariant in z. Sufficiently far from the openings of the slit, the electrostatic potential only depends on y and fulfils the Poisson Equation (4.8). The profile of the potential within the two surfaces is sketched in red.

the case of small surface potential $e|\Phi_0| \ll k_B T \sim 25\text{mV}$ at room temperature. In this case the Poisson-Boltzmann equation is linearised and solved analytically giving

$$\Phi(y) = \Phi_m \cosh\left(\frac{y}{\lambda_D}\right) , \tag{4.23}$$

where Φ_m is the potential at $y = 0$. Note that the Debye-Hückel regime extends all the way from large separation and weak double layer overlap $\lambda_D \ll h$ to small separation and strong double layer overlap $\lambda_D \gg h$. The ideal gas regime corresponds to the case of strong double layer overlap $\lambda_D \gg h$ with electrostatic potential large and almost constant along y. In this regime both the surface charge density σ and the ionic concentration c_s are small such that the only contribution to the electrostatic pressure between the two surfaces comes from the entropy of mixing of the ions $P \sim (h)^{-1}$. Hence the name ideal 'gas' [121]. The bottom region of the diagram corresponds to the scenario of large surface charge density. Therein one distinguishes a region of efficient screening ($\lambda_D \ll h$) and a region of unscreened electrostatic interactions between the two surfaces ($\lambda_D \gg h$). In the former case the potential profile is obtained just by linear superposition of the profile of two isolated non-interacting surfaces.
Finally, it is important to stress that the transition lines between domains in Fig. 4.3 correspond to smooth transitions between different limiting expressions of the electrostatic potential $\Phi(y)$ and the electrostatic pressure $P(h)$.

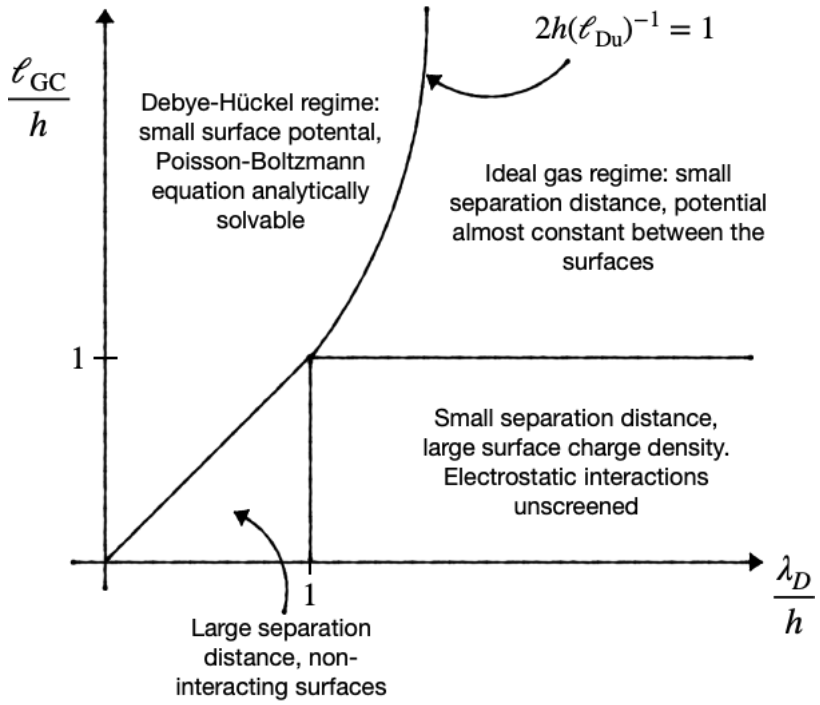

Figure 4.3: Unified view of the various limiting behaviours of the Poisson-Boltzmann equation (4.9) for an electrolyte solution confined between two surfaces (Fig. 4.2). In the main axes there are two dimensionless ratios, respectively the Gouy-Chapman length (4.3) and the Debye length (4.4) normalized by the geometric confinement h. Figure adapted from [121].

4.3 Local electroneutrality

By integrating the Poisson equation (4.8) from $y = -h$ to $y = +h$ and using the Gauss boundary condition (4.21) one finds:

$$\boxed{2\sigma + \int_{-h}^{-h} dy\, n_c = 0\,.} \tag{4.24}$$

Eq. (4.24) is the condition of local electroneutrality for the equilibrium system in Fig. 4.2. It indicates that the surface charge density is exactly compensated by the integrated net charge at every point in x. It follows that local electroneutrality is a direct consequence of the PB theory in equilibrium. It is instructive to introduce now dimensionless quantities by rescaling the electrostatic potential with k_BT/e, the $y-$variable with h and the charge density with $2ec_s$. The condition of local electroneutrality (4.24) thus becomes:

$$\boxed{\mathrm{Du} + \langle \mathrm{n_c} \rangle = 0} \tag{4.25}$$

where I have introduced the Dukhin number:

$$\boxed{\mathrm{Du} \equiv \frac{\ell_{\mathrm{Du}}}{\mathrm{h}}} \tag{4.26}$$

and the average along y: $\langle\rangle \equiv \frac{1}{2}\int_{-1}^{+1} dy$. Generally, when the system is driven out-of-equilibrium the condition of local electroneutrality does not hold any more. In presence of an external gradient along the longitudinal direction x the Poisson equation reads:

$$\frac{\partial^2\Phi}{\partial x^2} + \frac{\partial^2\Phi}{\partial y^2} + \frac{n_c}{\epsilon_0\epsilon_r} = 0\,. \tag{4.27}$$

Using the dimensionless quantities introduced above and rescaling the variable x with the length of the slit L one obtains:

$$\frac{h^2}{L^2}\frac{\partial^2\Phi}{\partial x^2} + \frac{\partial^2\Phi}{\partial y^2} + \frac{h^2}{\lambda_D^2}n_c = 0\,. \tag{4.28}$$

Eq. (4.28) is integrated in y to obtain:

$$\frac{\lambda_D^2}{L^2}\frac{d^2}{dx^2}\langle\Phi\rangle + \mathrm{Du} + \langle \mathrm{n_c}\rangle(\mathrm{x}) = 0\,. \tag{4.29}$$

It follows that Eq. (4.25) holds in non-equilibrium conditions if the first term in Eq. (4.29) can be neglected. By assuming L to be much larger than any other length scales in the system (in particular $\lambda_D/L \to 0$ and $h/L \to 0$) the condition of local electroneutrality is thus recovered. It follows that local electroneutrality is a direct consequence of assuming a scale separation between the transversal length scale and the longitudinal length scale. As will be discussed in the next Chapter, such scale separation is at the basis of another important assumption, namely the Fick-Jacobs approximation for the ionic concentrations. Before concluding this section, a final point should be noted. In the case of abrupt changes in the potential profile, such that $d^2\langle\Phi\rangle/dx^2 \gg 1$, the above reasoning is no longer applicable and electroneutrality breaks down. This occurs at either entrance of the nanoslit where both the concentration profile and the potential profile change rapidly as a consequence of the local change in geometry and surface charge. Typically the scale of this readjustment region is given by the Debye length. Thus, in the limit $\lambda_D/L \to 0$ the readjustment region can be treated as a point discontinuity in the ionic concentration and the electrostatic potential. Electroneutrality is then imposed at either side of the discontinuity.

4.4 Donnan equilibrium

Let now introduce an important concept associated with that of double layer overlap, namely the Donnan equilibrium potential. Let consider a slit of half width $h \ll \lambda_D \ll L$ in equilibrium with two reservoirs of chemical potential:

$$\mu_{res} = k_B T \log(c_s \Lambda^3)\,. \tag{4.30}$$

In this scenario the electrostatic potential, as well as the ionic concentrations $c_\pm$, is approximately uniform over the height of the channel (Fig. 4.4) and is indicated as $\Phi \equiv V_D$.

The chemical potential of the ionic species in the slit reads:

$$\mu_\pm = k_B T \log(c_\pm \Lambda^3) \pm e V_D\,, \tag{4.31}$$

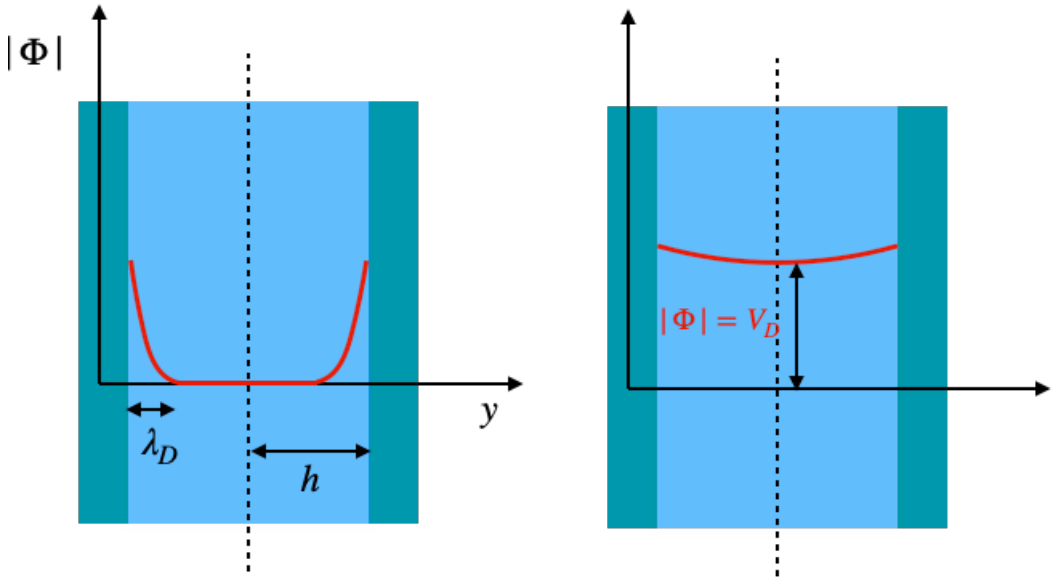

Figure 4.4: Sketch of the electrostatic potential profile (in red) in two channel configurations, respectively with $h \gg \lambda_D$ (left panel) and $h \ll \lambda_D$ (right panel). The latter case corresponds to having double layer overlap and an almost constant Donnan potential V_D inside the channel. The potential builds up in equilibrium as a consequence of the accumulation of counterions in the channel screening the surface charge.

which equates the chemical potential of the two reservoirs in equilibrium. Solving for the ionic concentrations one finds

$$c_\pm = c_s e^{\mp e V_D / k_B T} \tag{4.32}$$

and, consequently

$$c_+ \times c_- = c_s^2 \,. \tag{4.33}$$

By combining Eq. (4.33) with the condition of local electroneutrality:

$$c_+ = c_- - \frac{\sigma}{he} \,, \tag{4.34}$$

one finds

$$c_\pm = \mp \frac{\sigma}{2he} + \sqrt{\left(\frac{\sigma}{2he}\right)^2 + c_s^2} \,. \tag{4.35}$$

Taking the ratio c_-/c_+ from Eq. (4.32) one obtains for the Donnan potential the following expression:

$$\boxed{V_D = \frac{k_B T}{2e} S \log\left(\frac{\mathrm{Du} + \sqrt{\mathrm{Du}^2 + 1}}{-\mathrm{Du} + \sqrt{\mathrm{Du}^2 + 1}}\right)} \,, \tag{4.36}$$

where $S \equiv \mathrm{sign}(\sigma)$. Due to the supplementary charge brought by the two surfaces, a Donnan potential $V_D \neq 0$ builds up in the channel interior while being zero in the two reservoirs. At either ends of the slit, the Donnan potential drops off, in association with a discontinuity in the ionic concentrations.

4.5 The Poisson-Nernst-Planck equation

A common theoretical framework to describe ionic transport in nanofluidic systems is the so-called Poisson-Nernst-Planck (PNP) theory, which is the non-equilibrium variant of the PB theory introduced above. Let consider, once again, an electrolyte system in the slab geometry represented in Fig. 4.2. In presence of an external chemical potential difference $\Delta\mu$ applied through the reservoirs, the flux densities for the ionic species read:

$$\boldsymbol{j}_{\pm} = \mp e\frac{D_{\pm}}{k_B T}c_{\pm}\nabla\Phi - D_{\pm}\nabla c_{\pm}\,, \tag{4.37}$$

where $D_{\pm}$ are the diffusion coefficients of each ionic species. The first term in Eq. (4.37) is the electrophoretic contribution to the ionic flux, proportional to the external force here expressed as the gradient of the electrostatic energy. The second term is the diffusive contribution due to concentration gradients, according to Fick's law. In equilibrium when the flux vanishes Eq. (4.37) gives exactly the Boltzmann distribution (4.7). The Nernst-Planck equation is then obtained by combining Eq. (4.37) with the continuity equation for $c_{\pm}$, ensuring mass conservation:

$$\frac{\partial c_{\pm}}{\partial t} + \nabla\cdot\boldsymbol{j}_{\pm} = 0\,. \tag{4.38}$$

In the following Chapters I will investigate the response of confined electrolyte under steady state conditions in effective one dimensional model which corresponds to having constant ionic fluxes

$$j_{\pm} = \text{const}\,. \tag{4.39}$$

The problem description is finalized by coupling Eqs. (4.37-4.39) with the Poisson Equation (4.27) and with proper boundary conditions.
The PNP theory, likewise the PB theory, is a mean-field approximation treating the ions as point-like charges and neglecting ionic correlations. Therefore the limits of validity of the PNP equations are the same as for the PB theory [125]. Finally, note that in Eq. (4.37) the electroosmotic contribution to the ionic fluxes is neglected. This is the advective contribution due to the liquid flow induced by the external potential gradient within the DDL. In order to take it into account an extra term $+c_{\pm}v$ should be added to Eq. (4.37), with v the convective velocity described by the Navier-Stokes equation. Nonetheless, when $\Delta\mu$ is the only external force at play, previous works [126,127] have shown that neglecting the electroosmotic contribution in Eq. (4.37) is a good approximation for a wide range of surface charge and external potential magnitudes.

4.6 An alternative definition for ℓ_{Du}

In this section I introduce a 'dynamical' definition of the Dukhin length alternative to the one given in Eq. (4.5) and provide a mathematical proof of the equivalence of the two definitions in certain regimes. To this aim, I follow the approach presented in [128]. As described above, the DDL building up in the proximity of a charged

surface contains more ions than the bulk. This results in an extra conductance κ_s in the proximity of the surface and, in turn, an additional current in the presence of an applied electric field. Accordingly, the ratio between the surface conductance $\kappa_s \sim |\sigma|$ and the bulk conductance $\kappa_b \sim c_s$ defines a length scale, probing the relative amounts of free charge carriers in the DDL and in the bulk. This length can be identified with the Dukhin length, as:

$$\boxed{\ell_{\rm Du} = \frac{\kappa_s}{\kappa_b}\,.} \tag{4.40}$$

Let consider the system in Fig. 4.2 subject to an external electric field E_x directed along the $x-$ axis. For simplicity let take the diffusion coefficients of the two ionic species to be equal $D_+ = D_- = D$. Using Eq. (4.37) the electric current (per unit width) $I \equiv 2\int_{-h}^{0} dy\,(j_+ - j_-)$ can be written as:

$$\frac{I}{E_x} = \frac{2e^2 D}{k_B T}\int_{-h}^{0} dy\,(c_+ + c_-) = 2h\kappa_b + 2\kappa_s = 2h\kappa_b\left(1 + \frac{\ell_{\rm Du}}{h}\right)\,, \tag{4.41}$$

where in the second step I have decomposed the current into the bulk and the surface contributions using the definition of surface and bulk conductances. In the absence of surface charge one gets $\kappa_b = 2e^2 D c_s/k_B T$ which, substituted into Eq. (4.41), gives:

$$\frac{\ell_{\rm Du}}{h} = \frac{1}{2hc_s}\int_{-h}^{0} dy\,(c_+ + c_-) - 1 = \frac{1}{h}\left[\int_{-h}^{0} dy\cosh(e\Phi/k_B T) - 1\right]\,, \tag{4.42}$$

where in the second passage the Boltzmann distribution (4.7) was used. Let now assume $h \gg \lambda_D$ to extend the extremes of integration from $-\infty$ to 0, and write:

$$\ell_{\rm Du} = \int_{-\infty}^{0} dy\cosh(e\Phi/k_B T) - 1 = \int_{\Phi_0}^{0} d\Phi\left(\frac{d\Phi}{dy}\right)^{-1}\cosh(e\Phi/k_B T) - 1\,. \tag{4.43}$$

By using Eq. (4.13) together with the identity $\cosh(x) - 1 = 2\sinh^2(x/2)$ to integrate Eq. (4.43) one gets:

$$\ell_{\rm Du} = \sqrt{\frac{2\epsilon_0\epsilon_r k_B T}{e^2 c_s}}\left[\cosh\left(\frac{e\Phi_0}{2k_B T}\right) - 1\right]\,. \tag{4.44}$$

Finally using Eq. (4.16):

$$\boxed{\ell_{\rm Du} = \frac{|\sigma|}{2ec_s}\left(\sqrt{\left(\frac{\ell_{GC}}{\lambda_D}\right)^2 + 1} - \frac{\ell_{GC}}{\lambda_D}\right)\,.} \tag{4.45}$$

It follows that in the limit $\lambda_D \gg \ell_{GC}$ or equivalently $\ell_{\rm Du} \gg \lambda_D$ one finds $\ell_{Du} \simeq |\sigma|/2ec_s$ which is exactly the definition reported in Eq. (4.26).

Chapter 5

Confinement-controlled Rectification in a Nanofluidic Diode

5.1 Introduction

Dating back to the famous thought experiment of Maxwell's demon (1867), the dream of designing *force-free* transport devices has permeated different branches of physics, including nanofluidics. In this context, one can imagine the *ionic diode* [7], a nanofluidic device exhibiting ionic currents of unequal magnitude under voltages of equal magnitude and opposite polarity, as a realization of such a demon. The first realization of a nanometric ionic diode was reported by Siwy and Fuliński in a geometrically asymmetric nanochannel obtained by asymmetric chemical etching of a polymer foil [129]. Their conical channel demonstrated a strongly non-linear ionic current under ac voltage, resulting in a net average current under zero average forcing. Ionic Current Rectification (ICR) in conical nanochannels has since been extensively studied experimentally [8, 130–133], thanks to the considerable progress made over the last twenty years in nano-fabrication technologies [134]. ICR has also been observed in symmetric channels subject to a concentration gradient [135] and in the presence of a surface charge discontinuity [136].
Empirically, the two features necessary to observe current rectification have been identified as the presence of surface charge and broken symmetry in the direction of transport, irrespectively of the nature of the broken symmetry. Alongside practical applications in macromolecular sensing and manipulation [137, 138], energy harvesting [139–141] and water desalination [142, 143], the phenomenon raises fundamental questions on the nature of ionic transport at the nanoscale. At this length scale, surfaces and entropic confinement strongly influence mass transport leading to the emergence of non-linear and exotic responses [124], of which ICR is a prominent example. A rationalization of the latter would then be a testbed for understanding more complex behaviour occurring at the nanoscale [124] such as that of biological functionalized protein channels [11, 144, 145].

In nano-sized fluidic diodes, electrostatic interactions between charged species play a key role. In the presence of a surface charge density σ in contact with an

electrolyte solution, a diffuse double layer (DDL) builds up inside the channel with a characteristic decay given by the Debye length λ_D, defined in Eq. (4.4). In the so-called *entropic electrokinetic* regime [146] the Debye length is comparable to the tip of the nanopipette, i.e., the smallest aperture. This is typically the case in most synthetic realizations of nanochannels [133,147,148] as well as in biological ion channels. Notably, measures of ICR in micrometer-sized systems have been reported more recently in the literature [149, 150].
In contrast to λ_D, the Dukhin length ℓ_{Du} defined in Eq. (4.5) is a *phenomenological* length: it does not directly correspond to a physically observable length in the system. Therefore it can be much larger or smaller than the system's size [124].
The theoretical literature on ICR has been mostly confined to numerical simulations of the ion dynamics using the classical Poisson-Nernst-Planck (PNP) equations for dilute electrolyte solutions [127,151–153]. Such a framework has quantitatively captured the phenomenon, demonstrating that a mean field continuum description is still valid for ionic dynamics down to a few nanometers.
An early qualitative interpretation of ICR is traceable back to a paper of Dietrich Woermann [154] who rationalized the phenomenon in terms of ionic transference asymmetry between the ends of the channel.
At the same time, the study of particle transport over entropic barriers has attracted the attention in Non-Equilibrium Statistical Physics [146, 155–157]. The first attempt to characterize transport in confined systems dates back to the early work of Jacobs [158] and Zwanzig [159] who proposed the so-called *Fick-Jacobs approach* (FJ) to account for the transport of Brownian particles geometrically confined in a quasi-one-dimensional system. Under the assumption of a separation of scales between the longitudinal and the transversal coordinates, the latter is integrated and the description is reduced to an effective 1D equation now containing an entropic term. The approach has proved quantitative in channel geometry with smoothly varying cross-section, typically the case in nanofluidic experiments [133, 134, 160], both for free diffusion [161, 162] and under moderate external fields [163]. More recently, the approach has been extended to the regime of competition between energetic and entropic interactions in electrolyte dynamics [164].
The goal of the present Chapter is to gain insight on the fundamental mechanism controlling current rectification in a geometric diode, i.e., a conical channel with uniform charge density in contact with two reservoirs held at the same electrolyte concentration. Such a configuration corresponds to an extensively studied nanopipette experimental setup. Furthermore, it represents the conceptually intriguing case in which symmetry breaking originates only from the geometric confinement; such a system is thus able to harness *entropy* to rectify ionic current. To address the problem I adapt the FJ approach to a 2D conical slab geometry. Contrary to previous works considering channels much larger than the Debye length [8, 165], the present formalism allows us to investigate the regime of finite λ_D where partial Debye overlap occurs inside the channel, and to fully capture the interplay between energetic and entropic contributions.

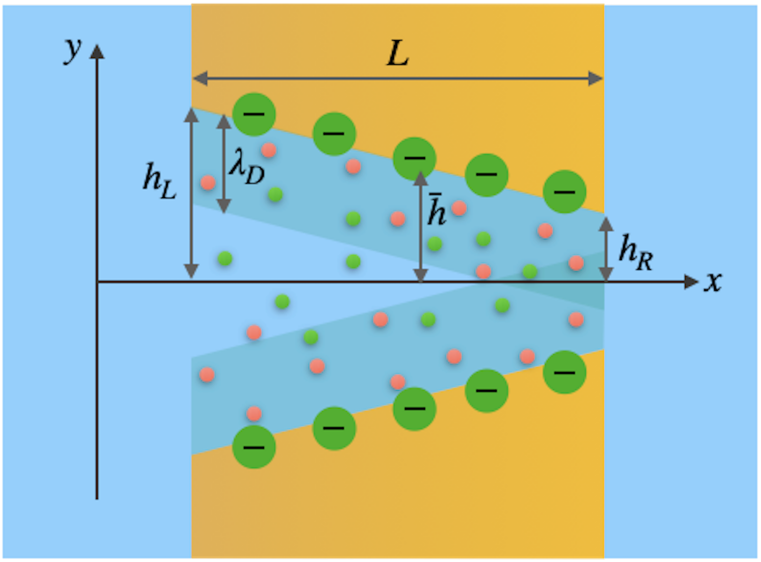

Figure 5.1: Schematic view of the channel in contact with two reservoirs at fixed salt concentration. The channel width is assumed to be constant along the z direction pointing out of the page. The channel walls carry a uniform negative charge density and a electrically charged double layer forms over a characteristic length λ_D.

5.2 Ionic dynamics

As shown schematically in Fig. 5.1, let consider an open channel with a slab conical geometry characterized by longitudinal size L, width L_z and an x-dependent height

$$h(x) = \bar{h} + \frac{kL}{2} - kx\,, \tag{5.1}$$

where $\bar{h}$ is the half-aperture of the channel and $k = |\partial_x h| = (h_L - h_R)/L$ is the difference between the left h_L and the right h_R channel half-heights in units of channel length. In the following sections the channel slope is varied by keeping fixed its half-height $\bar{h}$ and length L in order to compare systems with the same aspect ratio. The channel is filled with a symmetric monovalent electrolyte composed of species having equal diffusion coefficient D, in contact with two reservoirs at fixed temperature T and ionic concentration c_s. Each wall bears a uniform negative surface charge of density $\sigma < 0$. Let assume $L_z \gg \bar{h}$ so that the $z-$dependence of any variables of the model can be neglected and the resulting system is effectively 2D.
In order to characterize the ionic dynamics effective one-dimensional transport equations will be derived for the ionic concentration profiles $c_\pm$. The approach relies on the constraint of a small aspect ratio $\epsilon = \bar{h}/L \ll 1$, i.e. a slowly-varying channel geometry. In this case, the transversal relaxation dynamics with characteristic time $\tau_y \sim \bar{h}^2/D$ is decoupled from the longitudinal relaxation dynamics with $\tau_x \sim L^2/D$ and the ions are assumed to *instantaneously* adjust to the Boltzmann distribution (4.7) at each cross-section. Such separation of scale is known as the hypothesis of Local Thermodynamic Equilibrium (LTE) or, in this context, local Poisson-Boltzmann equilibrium.
Under this assumption the steady-state Nernst-Planck equation for the positive and

negative ionic species is given by:

$$\boxed{j_{\pm} = \mp \frac{De}{k_B T} c_{\pm}(x,y) \frac{\partial}{\partial x} \Phi(x,y) - D \frac{\partial}{\partial x} c_{\pm}(x,y)\,.} \tag{5.2}$$

where $j_{\pm}$ is the constant mass flux density along x, k_B is the Boltzmann constant, e is the elementary charge and $\Phi(x,y)$ is the total electrostatic potential inside the channel.
Eq. (5.2) must be supplemented by the Poisson equation relating the electrostatic potential to the spatial charge distribution $n_c = e(c_+ - c_-)$ inside the channel:

$$\boxed{\frac{\partial^2 \Phi}{\partial x^2} + \frac{\partial^2 \Phi}{\partial y^2} + \frac{n_c(x,y)}{\epsilon_0 \epsilon_r} = 0\,.} \tag{5.3}$$

In the next section Eq. (5.2) is reduced to an effective 1D equation by introducing the FJ *ansatz* for the ionic concentration profiles as explained in 5.2.1. For consistency, the same approximation is applied to the Poisson equation together with the assumption of small transversal variation of Φ (see section 5.2.2), which allows to formally integrate Eq. (5.3).

5.2.1 The Fick-Jacobs approach

Since the transversal and longitudinal dynamics are assumed to be decoupled, it is convenient to introduce the marginal concentration as the cross-sectional integral of the volumetric concentration:

$$c_{\pm}(x) = \frac{1}{2} \int_{-h(x)}^{+h(x)} dy\; c_{\pm}(x,y)\,. \tag{5.4}$$

Furthermore, following the approach of Zwanzig [159] let define $x-$dependent free energies $A_{\pm}(x)$ via:

$$e^{-\beta A_{\pm}(x)} \equiv \frac{1}{2\bar{h}} \int_{-h(x)}^{+h(x)} dy\; e^{\mp \beta e \Phi(x,y)}\,. \tag{5.5}$$

The FJ *ansatz* corresponds to factor the volumetric concentrations $c_{\pm}(x,y)$ into the product of the Boltzmann weight and the marginal concentration,

$$\boxed{c_{\pm}(x,y) \approx \frac{e^{\mp \beta e \Phi(x,y)}}{\frac{1}{2} \int_{-h(x)}^{+h(x)} dy\; e^{\mp \beta e \Phi(x,y)}} \cdot c_{\pm}(x)\,.} \tag{5.6}$$

Martens *et al* [155] proved that Eq. (5.6) can be recovered as the zero-order term of a perturbative expansion in series for the geometrical parameter k around the zero-transversal-flux solution. In his original derivation [159], Zwanzig showed that the range of validity of the FJ approach can be extended up to $k \leq 1$ upon including an extra $x-$dependence in the diffusivity $D \to D(x)$. Note that for a conical geometry like the one considered here the aforementioned modification reduces a simple rescaling of the diffusion coefficient thus making the theory here developed valid up

to $k \leq 1$ [162, 166].

By integrating Eq. (5.2) in the $y-$coordinate and using Eq. (5.6), an effective one-dimensional equation is obtained,

$$J_{\pm} = Dc_{\pm}(x) \left[\frac{\partial_x \frac{1}{2} \int_{-h(x)}^{+h(x)} e^{\mp \beta e \Phi(x,y)} dy}{\frac{1}{2} \int_{-h(x)}^{+h(x)} e^{\mp \beta e \Phi(x,y)} dy} \right] - D\partial_x c_{\pm}(x) \,, \tag{5.7}$$

where $J_{\pm} = 1/2 \int_{-h(x)}^{h(x)} dy \; j_{\pm}$ is the longitudinal mass flux per unit width for each species and $\partial_x = \partial/\partial x$. In Eq. (5.7) the concentrations $c_{\pm}(x)$ are the marginal ones; in the following, I refer to the marginal concentrations unless both the $x-$ and $y-$dependence are explicitly noted.
Now let introduce dimensionless variables. As reported in Table 5.1 the coordinate x is rescaled by the total length of the channel L and the coordinate y as well as the Debye length λ_D and the channel profile $h(x)$ by the half-height $\bar{h}$. In this way the channel profile reads

$$h(x) = 1 + \frac{\kappa}{2} - \kappa x \,, \tag{5.8}$$

where a rescaled channel slope $\kappa = k/\epsilon = kL/\bar{h}$ is introduced. Note that κ must fulfil $\kappa < 2$ for geometrical consistency.
The electrostatic potential is rescaled by the thermal one $k_B T/e$ and the volumetric concentrations $c_{\pm}(x, y)$ by the reservoir ionic strength $2c_s$. Consequently, the charge density n_c is rescaled by $2ec_s$, the mass flux J per unit width by $2Dc_s\bar{h}/L$ and the conductance per unit width, $G = \partial I/\partial \Delta V$ with I the total ionic current (per unit width) and ΔV the applied potential drop, by the bulk conductance $2Dc_s\bar{h}/L \times e^2/k_B T$.
In dimensionless form Eq. (5.7) reads:

$$\boxed{J_{\pm} = -c_{\pm}\Big[\partial_x \beta A_{\pm} + \partial_x \log c_{\pm}\Big] = -c_{\pm}\partial_x \mu_{\pm} \,,} \tag{5.9}$$

where the (dimensionless) chemical potential

$$\mu_{\pm}(x) = \log c_{\pm}(x) + \beta A_{\pm}(x) \tag{5.10}$$

was introduced. In Eq. (5.9) the electrophoretic contribution now appears in terms of the previously introduced effective free energies $A_{\pm}(x)$. Note that for a neutral species the effective free energy reduces to the standard Boltzmann entropy $\beta A(x) = -\log h(x)$. In this case $\frac{d}{dx}\beta A(x)$ is referred to as an *entropic force*, originating from the variation in 'phase-space volume' available for free diffusion along the channel. For a charged species A embeds both enthalpic and entropic contributions.
Eq. (5.9) must be integrated with the appropriate boundary conditions, i.e. by imposing continuity in the chemical potential at the ends of the channel [1].

[1] From Eq. (5.9) it follows that imposing a continuous chemical potential throughout the system corresponds to ensure finite fluxes everywhere.

Table 5.1: Adimensionalization of the independent and derived quantities of the model.

Variables	Rescaled variables
Longitudinal coordinate x	x/L
Transversal coordinate y	$y/\bar{h}$
Channel profile $h(x)$	$h(x)/\bar{h}$
Debye length λ_D	$\lambda_D/\bar{h}$
Channel slope κ	k/ϵ
Electrostatic potential Φ	$e\Phi/k_BT$
Volumetric concentrations $c_\pm$	$c_\pm/2c_s$
Charge density n_c	$n_c/2ec_s$
Mass fluxes $J_\pm$	$J_\pm/(2Dc_s\bar{h}/L)$
Differential conductance G	$G/(2Dc_s\bar{h}/L \times e^2/k_BT)$

Thus, a formal expression for the electric current $I = J_+ - J_-$ follows:

$$\boxed{I = -\frac{1}{2}\left[\frac{e^{-\Delta V/2} - e^{+\Delta V/2}}{\int_0^1 dx'\ e^{\beta A_+(x')}} - \frac{e^{+\Delta V/2} - e^{-\Delta V/2}}{\int_0^1 dx'\ e^{\beta A_-(x')}}\right],} \tag{5.11}$$

where the denominator is responsible for the non-linear (rectified) response of the channel, as it expresses the coupling between the external driving and the geometric asymmetry. For a flat channel, Eq. (5.11) reduces to the standard ohmic response [125] (per unit width) which in dimensional unit reads

$$I_{ohm} = \frac{De^2}{k_BT}\left[\frac{2c_-}{L} + \frac{2\sigma}{eL}\right]\ \Delta V. \tag{5.12}$$

5.2.2 Local Debye-Hückel approximation

In dimensionless units, the Poisson equation (5.3) reads

$$\epsilon^2\partial_x^2\Phi(x,y) + \partial_y^2\Phi(x,y) = -\frac{1}{\lambda_D^2}n_c(x,y)\,. \tag{5.13}$$

It is convenient to decompose the electrostatic potential as

$$\Phi(x,y) = \psi(x,y) + \langle\phi\rangle(x) + \phi_{ext}(x)\,, \tag{5.14}$$

where $\langle\phi\rangle = \frac{1}{2h(x)}\int_{-h(x)}^{+h(x)} dy\ \phi(x,y)$ is the average potential across y, $\psi = \phi - \langle\phi\rangle$ is the excess potential at each section and $\phi_{ext} = -\Delta V\left(x - \frac{1}{2}\right)$ is the potential drop applied externally, resulting in a constant electric field directed in the $x-$direction.

By using FJ approximation into Eq. (5.13) together with Eq. (5.14) and by linearizing in ψ under the assumption of small potential variation in the transversal direction, Eq. (5.13) reduces to

$$\epsilon^2 \partial_x^2 \Phi + \partial_y^2 \psi = -\frac{\lambda_D^{-2}}{h} \left[(c_+ - c_-) - (c_+ + c_-)\psi \right]. \tag{5.15}$$

I refer to the linearization used to derive Eq. (5.15) as a *local* Debye-Huckel (DH) approximation: the potential is linearized with respect to the local cross-sectional average preserving therefore global non-linearity. Note that the assumption of small ψ is more general than the standard DH hypothesis, which requires small surface potential Φ_0 as well as a moderate external potential ΔV. As such, the hypothesis of local DH allows to explore all the upper part of the diagram in Fig. 4.3, namely the Debye-Hückel regime and the ideal gas regime, for arbitrarily Dukhin number and arbitrarily external potential ΔV.
In the FJ regime, neglecting the $\mathcal{O}(\epsilon^2)$ terms, Eq. (5.15) reduces to a linear equation for ψ:

$$\partial_y^2 \psi = -\frac{\lambda_D^{-2}}{h} \left[(c_+ - c_-) - (c_+ + c_-)\psi \right]. \tag{5.16}$$

Consistently, the scaling argument applies as well to the electrostatic Gauss boundary condition, which after neglecting terms of $\mathcal{O}(\epsilon^2)$, and introducing rescaled variables, reduces to

$$\partial_y \phi \Big|_{y=\pm h} = \mp \frac{\mathrm{Du}}{\lambda_D^2} \tag{5.17}$$

where the Dukhin number Eq. (4.26) was introduced. It is straightforward to verify that the local PB hypothesis previously introduced implies local electroneutrality (4.24), in which the integrated charge density balances the surface charge density at each cross-section.
One may say that, to first order, the FJ *ansatz* and hypothesis of local electroneutrality are different naming for the same unique assumption, i.e. separation of transversal and longitudinal scales [167]. The reduced Poisson equation (5.16) can be formally integrated leading to

$$\boxed{\psi = -\frac{Du(x)}{\lambda_D(x)} \frac{\cosh(y/\lambda_D(x))}{\sinh(h(x)/\lambda_D(x))} + \frac{c_+(x) - c_-(x)}{c_+(x) + c_-(x)}}, \tag{5.18}$$

where the potential is naturally expressed in terms of a local Dukhin number and a local Debye length respectively defined as:

$$\lambda_D(x) \equiv \frac{\lambda_D}{\sqrt{\langle c \rangle(x)}} \tag{5.19a}$$

$$\mathrm{Du}(x) \equiv \frac{\mathrm{Du}}{\langle c \rangle(x)}, \tag{5.19b}$$

where

$$\langle c \rangle \equiv \frac{c_+(x) + c_-(x)}{h(x)} = \frac{1}{2h(x)} \int_{-h(x)}^{h(x)} dy\, c_+(x,y) + c_-(x,y) \tag{5.20}$$

is the volumetric cross-sectionally averaged concentration.
One recognizes the first term on the *rhs* of Eq. (5.18) to be the Debye-Huckel potential carrying an extra $x-$dependence due to the varying channel geometry. The second term on the *rhs* ensures local electroneutrality.
Operatively, Eqs. (5.9) and (5.16) need to be solved numerically. It is thus convenient to rewrite Eq. (5.9) in terms of ψ :

$$J_+ = -\partial_x c_+ + c_+[\partial_x \log h - (\partial_x\langle\phi\rangle - \Delta V) + \partial_x \log\langle e^{-\psi}\rangle] \tag{5.21a}$$

$$J_- = -\partial_x c_- + c_-[\partial_x \log h + (\partial_x\langle\phi\rangle - \Delta V) + \partial_x \log\langle e^{+\psi}\rangle] \tag{5.21b}$$

$$\partial_y^2\psi = -\frac{\lambda_D^{-2}}{h}[(c_+ - c_-) - (c_+ + c_-)\psi] \tag{5.21c}$$

so that the coupling between the concentration profiles and the electrostatic potential is made now explicit. Finite-element simulations (COMSOL) are used to solve the system of Eqs. (5.21a-5.21c) in order to look at the electric current I generated by the applied potential drop ΔV. (See Appendix 5.6 for details on the numerical simulations).
Previously proposed analytical approaches [154, 165, 168] assume λ_D to be the relevant parameter for ionic transport by treating separately the case of no overlap $\lambda_D \ll 1$ and strong overlap $\lambda_D \gg 1$. This is not necessary in the present framework, where λ_D can vary continuously spanning across different regimes in the electrostatic phase space. Nevertheless, it is useful at this stage to introduce the regime of strong Debye overlap as it represents a well-known scenario which will be used as a benchmark to compare with numerical results.

5.2.3 Strong Debye overlap, $\lambda_D \gg 1$

Let consider the regime in which the channel height is much smaller than the Debye length. The DDL extends all throughout the interior of the confined electrolyte, rendering the channel perfectly charge-selective. This scenario was discussed in Section 4.4 for an equilibrium flat configuration. Both the electrostatic potential $\Phi(x, y) \simeq \Phi(x)$ and the volumetric concentrations $c_\pm(x, y) \simeq \langle c_\pm\rangle(x)$ are approximately uniform in the transversal direction allowing for a substantial simplification of the mathematical problem at hand.
Together with local electroneutrality which in this case reads

$$h(x)\,[\langle c_+\rangle(x) - \langle c_-\rangle(x)] = \mathrm{Du}\,, \tag{5.22}$$

continuity in the chemical potential provides an expression for the Donnan potential at either end of the channel [125, 143, 151],

$$\Phi_L = \frac{1}{2}\log\left[\frac{-\mathrm{Du} + \sqrt{\mathrm{Du}^2 + h_L^2}}{+\mathrm{Du} + \sqrt{\mathrm{Du}^2 + h_L^2}}\right] + \frac{\Delta V}{2} \tag{5.23a}$$

$$\Phi_R = \frac{1}{2}\log\left[\frac{-\mathrm{Du} + \sqrt{\mathrm{Du}^2 + h_R^2}}{+\mathrm{Du} + \sqrt{\mathrm{Du}^2 + h_R^2}}\right] - \frac{\Delta V}{2}\,. \tag{5.23b}$$

Interestingly, already at equilibrium ($\Delta V = 0$) the varying geometry results in a non-uniform *tilted* Donnan potential across the channel.
Analogously, the concentrations at either end of the channel read

$$\langle c_L \rangle = \frac{\sqrt{\mathrm{Du}^2 + h_L^2}}{h_L} \tag{5.24a}$$

$$\langle c_R \rangle = \frac{\sqrt{\mathrm{Du}^2 + h_R^2}}{h_R} \,. \tag{5.24b}$$

Hence, a jump in concentration profiles builds up at each junction of the channel to compensate for the potential discontinuity Eqs. (5.23). Such a local balance is known in the literature as *local* Donnan equilibrium. These expressions will allow for asymptotic analytical predictions for the conductances when $\Delta V \to \pm\infty$.
The Nernst-Planck equation in this regime reduces to

$$2h(x)\left[\mp\langle c_\pm\rangle(x)\partial_x\Phi(x) - \partial_x\langle c_\pm\rangle(x)\right] = J_\pm \,, \tag{5.25}$$

which, rewritten in terms of the total mass flux $J = J_+ + J_-$ and electric current I, becomes

$$J = -2h(x)\partial_x\langle c\rangle(x) - 2\mathrm{Du}\ \partial_x\Phi \tag{5.26a}$$

$$I = -2h(x)\langle c\rangle(x)\partial_x\Phi + 2\mathrm{Du}\ \partial_x \log 2h(x) \,. \tag{5.26b}$$

In Eqs. (5.26a-5.26b) the hypothesis of local electroneutrality (5.22) was used to further simplify the expressions.

5.3 Results

5.3.1 Current response and limiting conductances

Let now look at the current response obtained by numerically solving the system of equations (5.21a-5.21c) under an applied potential difference ΔV. The two reservoirs are kept at the same ionic strength so that the only external force at play is a constant electric field along the $x-$coordinate. A positive (negative) ΔV corresponds to the anode being placed at the left (right) reservoir.
A standard measure of Ionic Current Rectification is given by the current-voltage (IV) curve reported in Fig. 5.2 for the case of $\lambda_D = 1/2$ and $\mathrm{Du} = 1/2$ and for different values of the channel slope. This regime corresponds to the case of partial Debye overlap inside the channel: by moving from left to right the ions experience the building up of a Donnan potential. The non-linear curves in Fig. 5.2 display the usual diode-like behaviour reported in the literature, with a preferential direction of ionic current. When the electric field is applied parallel to the $x-$direction with the counterions moving from base to tip, the current is suppressed with respect to the Ohmic response (grey curve) and the system is said to be in a *low conductance state*. On the contrary, when the electric field is applied antiparallel to the $x-$direction with the counterions moving from tip to base, the current is magnified and the system is said to be in a *high conductance state*.

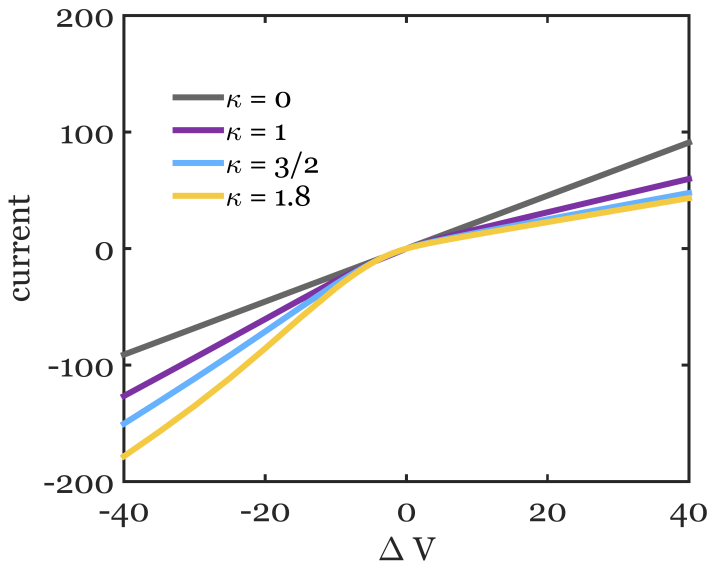

Figure 5.2: Dimensionless current I as a function of ΔV for a channel with $\lambda_D = 1/2$, $\mathrm{Du} = 1/2$ at different values of channel slope, respectively $\kappa = 0, 1, 3/2, 1.8$. For positive voltage drop (positive electric field) the system is in a low conductance state, the current being smaller than the Ohmic one (grey line). On the contrary for negative voltage drop (negative electric field) the current is magnified and the system is said to be in a high conductance state.

The rectification magnitude increases monotonously with the channel slope. This must come as no surprise since the channel slope is the only element introducing asymmetry in the system. For $\kappa \to 0$ the channel is flat and it behaves like a standard Ohmic resistor.
The numerical IV curves can be compared with analytical predictions of the limiting differential conductances

$$\boxed{G_{\pm\infty} = \lim_{\Delta V \to \pm\infty} \frac{\partial I}{\partial \Delta V}.} \tag{5.27}$$

For strong double layer overlap the equations of motion reduce to (5.26a-5.26b). By neglecting the diffusive contribution to the mass flow with respect to the electrophoretic contribution in (5.26a) and by integrating in x one obtains

$$J = 2\mathrm{Du}\Delta V. \tag{5.28}$$

Combining Eqs. (5.26a) and (5.26b) one solves for $\partial_x \langle c \rangle$ in terms of the ratio I/J:

$$2h\partial_x\langle c\rangle + \frac{(2\mathrm{Du})^2}{2h\langle c\rangle}\partial_x \log 2h = \left(\frac{2\mathrm{Du}}{2h\langle c\rangle}\frac{I}{J} - 1\right) J. \tag{5.29}$$

Eq. (5.29) is bound asymptotically if the prefactor on the *rhs* vanishes, i.e. $\mathrm{Du}I/h\langle c\rangle J \to 1$, when $\Delta V \to \pm\infty$. Accordingly the limiting conductance, $G_{\pm\infty}$, reduces to

$$\boxed{G_{\pm\infty} = \lim_{\Delta V \to \infty} 2h\langle c\rangle.} \tag{5.30}$$

Eq. (5.30) implies that the marginal concentration inside the channel approaches a uniform value in the limit $\Delta V \to \pm\infty$. When $\lambda_D \gg 1$ the analytical expressions for the concentration at the channel's ends are known, respectively Eq. (5.24a) for the left entrance and Eq. (5.24b) for the right entrance. It follows that (see Discussion section for further details)

$$G_{+\infty} = 2\sqrt{\mathrm{Du}^2 + h_R^2} \tag{5.31a}$$

$$G_{-\infty} = 2\sqrt{\mathrm{Du}^2 + h_L^2}\,. \tag{5.31b}$$

In Fig. (5.3) the IV curves is shown for $\lambda_D = 2$ and $\mathrm{Du} = 1$, i.e. in the regime of strong overlap. For $\kappa = 3/2$ the analytical predictions for the asymptotic curves $I_{\pm\infty} = \pm G_{\pm\infty}\Delta V$ obtained from (5.31) are reported with the dashed lines, showing that these analytical expressions accurately capture the numerical results. Further discussions on the saturation mechanism for the conductance are reported in the Discussion section.

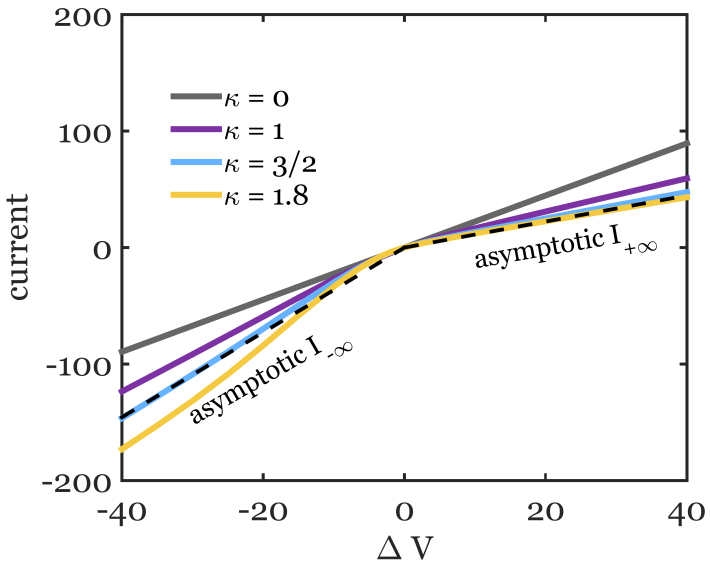

Figure 5.3: Dimensionless current I as a function of ΔV for a channel with $\lambda_D = 2$, $\mathrm{Du} = 1/2$ at different values of channel slope, respectively $\kappa = 0, 1, 1.5, 1.8$. The black dashed lines are the limiting currents for $\kappa = 3/2$ in the limit of $\Delta V \to \pm\infty$ using Eqs. (5.31).

From the comparison between Fig. 5.2 and Fig. 5.3 one observes that the quantitative structure of the IV curves does not change for partial double layer overlap ($\lambda_D = 1/2$) and strong double layer overlap with ($\lambda_D = 2$). The Debye length thus seems not to play a primary role in governing rectification. Notably, this is at odds with previous understanding of ICR which relies on λ_D as the main controlling parameter. In the next session this observation is further explored and clarified by looking closely at the dependence of ICR on the electrostatic length scales.

5.3.2 Current rectification ratio

In order to gain further insights on the rectified behaviour of the present system let introduce the rectification ratio η

$$\eta = \frac{|I(-\Delta V)|}{|I(+\Delta V)|}, \tag{5.32}$$

defined as the ratio between the absolute value of the current for opposite polarity of the external field. In the case of an ohmic resistor $\eta = 1$.
Fig. 5.4 displays η as a function of the external forcing, ΔV, for $\lambda_D = 1/2$ and $\lambda_D = 2$. Each plot shows the rectification ratio for different values of the channel slope. The asymptotic predictions for η obtained from Eqs. (5.31a) and (5.31b) are reported in Fig.5.4-b (dashed black lines).
Fig. 5.4 shows a saturation behaviour for large value of ΔV. The saturation value

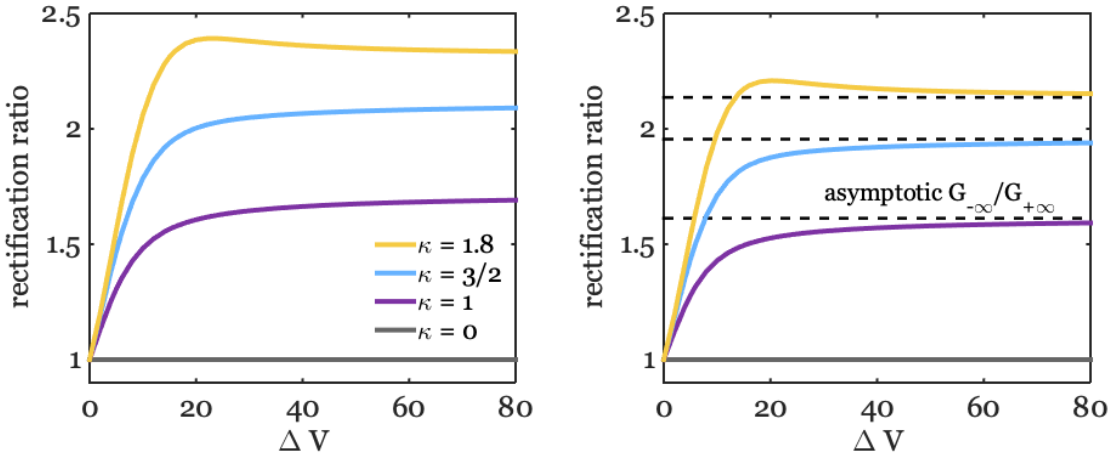

(a) (b)

Figure 5.4: (a) The rectification ratio η as a function of the amplitude $|\Delta V|$ in the case of $\lambda_D = 1/2$ and Du $= 1$ for $\kappa = 0$, $\kappa = 1$, $\kappa = 3/2$, and $\kappa = 1.8$. For a flat channel $\eta = 1$ and the response is linear (gray line). (b) The rectification ratio η as a function of the amplitude $|\Delta V|$ in the case of $\lambda_D = 2$ and Du $= 1$ for $\kappa = 0$, $\kappa = 1$, $\kappa = 3/2$, and $\kappa = 1.8$. The dashed black lines show the asymptotic value for η in the limit of $|\Delta V| \to \infty$.

increases with the channel slope as already observed for the IV curves. For strong overlap the analytical expressions (dashed lines) are in good agreement with the numerical results.
Let now turn our attention to the dependence of ICR on the Dukhin number. Fig 5.5 shows η as a function of the reference Dukhin number Du for $\lambda_D = 2$ and $\kappa = 3/2$ for different values of the external forcing. Interestingly, η shows a strongly non-monotonic dependence on Du with a maximum of rectification approximately at Du $\approx 1/2$. For Du $\ll 1$ or Du $\gg 1$ the rectification ratio $\eta \to 1$ and the standard ohmic behaviour is recovered. For values of Du close to unity the rectification ratio reaches a maximum which depends on the strength of the applied field upon reaching

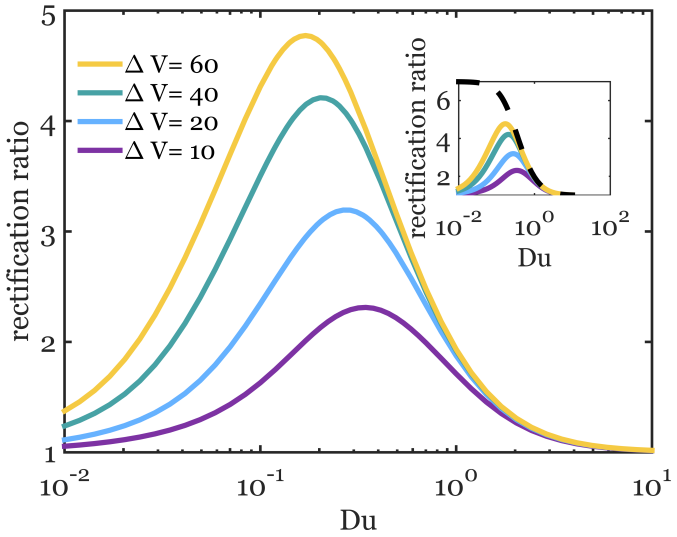

Figure 5.5: The rectification ratio η as a function of the reference Du for a channel with $\lambda_D = 2$ and $k = 3/2$ at different values of external forcing, respectively $\Delta V = 10, 20, 40, 60$. In the inset graph the analytical prediction for η in the regime of strong overlap and of $|\Delta V| \to \infty$ is reported. For sufficiently large Du it accurately estimates the behaviour of η while in the limit of Du $\to$ 0 it deviates from the numerical curves because of the breakdown of the hypothesis of strong overlap.

a saturation value as shown in Fig. 5.4.

The saturation value of ΔV is itself modulated by Du. Fig. 5.5 shows that Du is

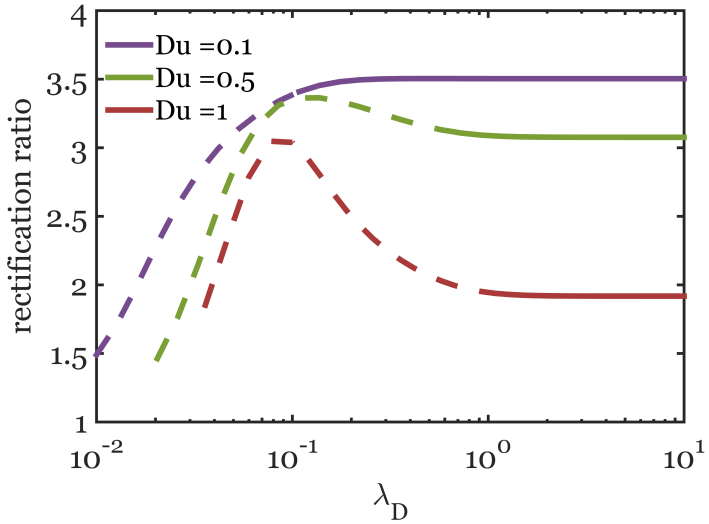

Figure 5.6: The rectification ratio η as a function of the Debye length for different values of the Dukhin, respectively Du $= 1/10$, Du $= 1/2$, Du $= 1$. The channel slope is $\kappa = 3/2$ and the potential drop $\Delta V = 40$. Dashed lines refer to the regime in which the approximation of local Debye-Hückel approximation is no longer justified.

a critical parameter controlling rectification, in contrast with λ_D that seems not to

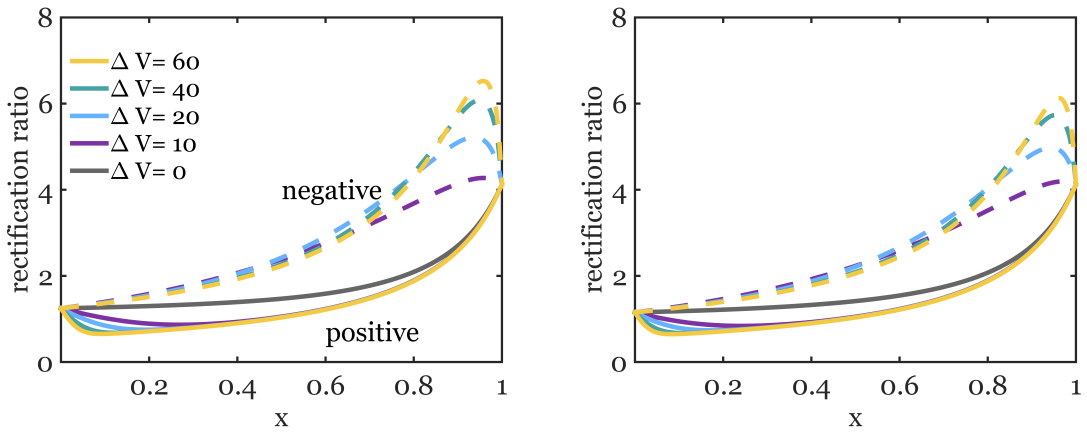

Figure 5.7: Volumetric cross-section average concentration $\langle c \rangle$ along the channel axis for different amplitude of the applied potential, respectively $\Delta V = 0$, $\Delta V = |10|$, $\Delta V = |20|$, $\Delta V = |40|$ and $\Delta V = |60|$. In the figures solid lines corresponds to a positive potential drop while dashed lines to a negative potential drop. Concentration profiles for the following choice of parameters: (a) $\lambda_D = 1/2$, Du $= 1$ and $\kappa = 3/2$ (b) $\lambda_D = 2$, Du $= 1$ and $\kappa = 3/2$.

be an adequate parameter to describe ICR. This is further illustrated by looking at Fig. 5.6, where η is plotted as a function of λ_D for three different values of Du. A dashed line is used when entering the regime in which linearization in ψ is no further justified. This happens in the limit of small λ_D when the potential at the centerline vanishes and $\psi \sim \Phi_0$. In the regime of partial and strong overlap no significant dependence on λ_D is shown. Albeit not quantitative, our results suggest that ICR decreases while approaching the limit of vanishing λ_D. In this limit it is known that ICR approaches a non-zero asymptotic value [169].

5.4 Discussion: The role of Dukhin number

The results of the previous section show that ICR is not primarily governed by the Debye length but rather by the Dukhin length. This suggests that the Dukhin number directly controls the high (low) conductance state, for negative (positive) potential drop. This can be understood in terms of ionic concentration enrichment and depletion for opposite polarity of the external field, as discussed in previous works [147, 154, 168]. The panel in Fig. 5.7 shows the volumetric cross-sectionally averaged concentration $\langle c \rangle$ along the channel axis for two different regimes of λ_D . In both figures an overall increase (decrease) of ionic concentration for negative (positive) ΔV is observed with respect to the equilibrium profile, represented by the grey line. Therefore the high conductance state for negative ΔV is due to an increase in ionic concentration inside the channel. The larger the external forcing, the stronger the accumulation of ions. On the contrary, when a positive voltage drop is applied the electrical conductance decreases due to the decrease of ionic concentration.
In order to understand the phenomenon of salt accumulation and depletion let now

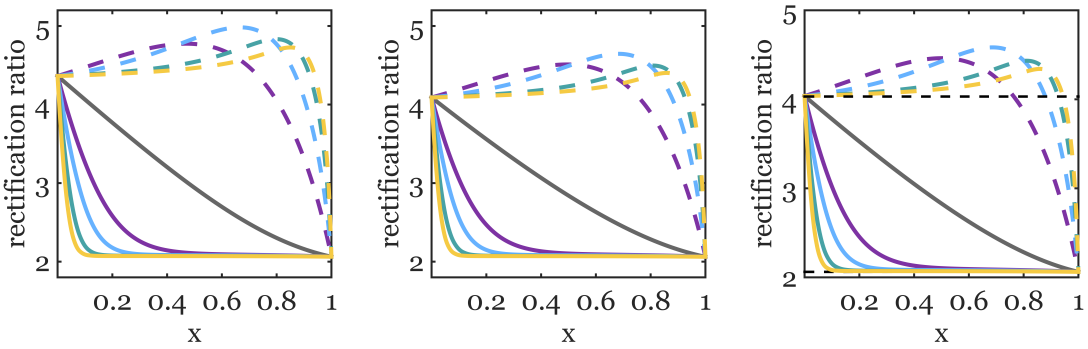

Figure 5.8: Marginal concentration c along the channel axis for different amplitude of the applied potential, respectively $\Delta V = 0$, $\Delta V = |10|$, $\Delta V = |20|$, $\Delta V = |40|$ and $\Delta V = |60|$. In the figures solid lines correspond to a positive potential drop while dashed lines to a negative potential drop. Concentration profiles for the following choice of parameters: (a) $\lambda_D = 1/2$, Du $= 1$ and $\kappa = 3/2$. (b) $\lambda_D = 1$, Du $= 1$ and $\kappa = 3/2$ (c) $\lambda_D = 2$, Du $= 1$ and $\kappa = 3/2$. The black dashed lines in (c) correspond to the boundary value for the marginal concentration due to the local Donnan equilibrium Eqs. (5.33).

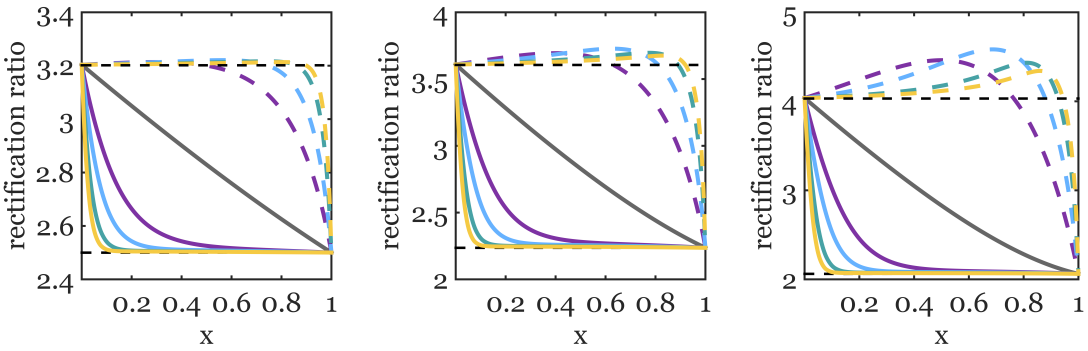

Figure 5.9: Marginal concentration c along the channel axis for different amplitude of the applied potential, respectively $\Delta V = 0$, $\Delta V = |10|$, $\Delta V = |20|$, $\Delta V = |40|$ and $\Delta V = |60|$. In the figures solid lines corresponds to a positive potential drop while dashed lines to a negative potential drop. Concentration profiles for the following choice of parameters: (a) $\lambda_D = 2$, Du $= 1$ and $\kappa = 1/2$. (b) $\lambda_D = 2$, Du $= 1$ and $\kappa = 1$ (c) $\lambda_D = 2$, Du $= 1$ and $\kappa = 3/2$. The black dashed lines corresponds to the boundary value for the marginal concentration due to the local Donnan equilibrium Eqs. (5.33).

turn our attention to the behaviour of the marginal concentrations for large fields. As anticipated, in the limit of very large potential drop the marginal concentrations are expected to saturate to a uniform value along the channel axis. Fig. 5.8 reports the marginal concentrations along the longitudinal axis for increasing value of λ_D (Fig. 5.8(a-c)). For increasing amplitude of the external forcing the marginal concentration indeed tends to a constant value which is determined by the boundary value at either end of the channel. In the case of a negative potential drop the marginal concentration saturates to the larger boundary value which is the value at the left end of the channel (base). On the other hand, for positive potential drop the marginal concentration saturates to the boundary value at the right site (tip). Fig. 5.8 also shows an overshoot in the marginal concentration for large (but finite) negative ΔV. The overshoot is not present in the case of positive ΔV which stands as an additional sign of the asymmetry in the system. The microscopic mechanism causing it is still not clear and requires further investigations. Fig. 5.9 reports the marginal concentration profiles for increasing slope of the channel showing a significant dependence of the overshot on κ.

Fig. 5.8-c displays the marginal concentrations for strong overlap, $\lambda_D \gg 1$. Local Donnan equilibrium builds up at the nanopore ends, controlling the corresponding marginal concentrations

$$c_L = 2h_L\sqrt{\left(\frac{\mathrm{Du}}{h_L}\right)^2 + 1} \tag{5.33a}$$

$$c_R = 2h_R\sqrt{\left(\frac{\mathrm{Du}}{h_R}\right)^2 + 1}\,. \tag{5.33b}$$

Asymptotically when $\mathrm{Du} \gg 1$, $c_L \to c_R$, i.e. $\eta \to 1$. In this regime transport is dominated by the surface and entropic interactions are negligible with respect to electrostatic interactions. As such, ions do not feel the symmetry breaking originated from the confinement and no current rectification is observed. That is to say, enthalpy wins.
The local marginal selectivity, $\gamma_\pm(x)$ (directly proportional to the ionic marginal concentrations), constitutes a second, relevant quantity. For the counterions, the local selectivity at either end of the channel respectively reads

$$\gamma_+^L = \frac{c_+^L}{(c_+^L + c_-^L)} = \frac{\frac{\mathrm{Du}}{h_L} + \sqrt{\left(\frac{\mathrm{Du}}{h_L}\right)^2 + 1}}{2\sqrt{\left(\frac{\mathrm{Du}}{h_L}\right)^2 + 1}} \tag{5.34a}$$

$$\gamma_+^R = \frac{c_+^R}{(c_+^R + c_-^R)} = \frac{\frac{\mathrm{Du}}{h_R} + \sqrt{\left(\frac{\mathrm{Du}}{h_R}\right)^2 + 1}}{2\sqrt{\left(\frac{\mathrm{Du}}{h_R}\right)^2 + 1}} \tag{5.34b}$$

making transparent the key role of the Dukhin number in controlling the local channel selectivity. Eq. (5.34) quantifies the relative importance of the counterion flux over the total transport. Due to the conical shape of the channel, γ_+^R is larger than

γ_-^L, meaning that counterion transfer in presence of an external driving is larger at the tip than at the base. Such imbalance in selectivities results in a transient ion readjustment when an external driving is switched on. In the case of counterions moving from tip to base (negative ΔV) this imbalance in selectivities results in a transient accumulation of ions inside the channel. On the contrary, when counterions move from base to tip (positive ΔV) there will be a relatively larger amount of ions leaving than entering the channel resulting in an overall decrease of salt concentration. In either case, the stationary state is reached when the non-equilibrium accumulation/depletion dynamics counterbalances the asymmetry of local selectivity induced by the geometry. Eq. (5.34) implies that the imbalance in selectivities is controlled by the asymmetry between Du/h_L and Du/h_R. Both $\mathrm{Du} \ll 1$ and $\mathrm{Du} \gg 1$ result in a uniform selectivity between the two ends of the channel, i.e. no rectification (see Fig. 5.10). High Dukhin number, $\mathrm{Du} \gg 1$, means that the selectivity of counterions at either end tends to one (that is the selectivity of coions tends to zero): the coions are completely excluded from the system and the geometrical asymmetry is nullified by the perfect selectivity of the channel. No bulk transport is present so that the entirety of transport takes place in the EDL. On the other side, for $\mathrm{Du} \ll 1$ the selectivity at either ends tends to its bulk value 1/2. In this regime, irrespective of the physical extension of the EDL the entirety of transport takes place in the unselective bulk and the ohmic bulk response is restored.

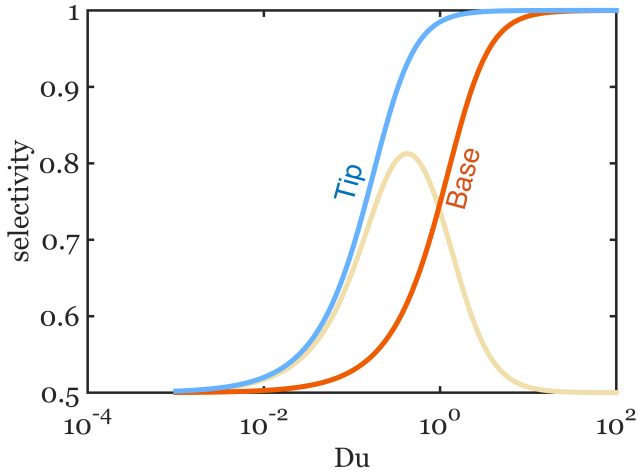

Figure 5.10: The counterion selectivity at the tip γ_+^R(blu) and at the base γ_+^L(red) of a channel with $k = 3/2$ as a function of the reference Dukhin number. For $\mathrm{Du} \sim 1/2$ the difference between the two selectivities (yellow curve) is maximized, leading to a maximum of rectification.

The asymmetry between Du^L/h_L and Du^R/h_R is maximized for $\mathrm{Du} \sim 1$ (in our case $\mathrm{Du} \sim 1/2$ because of the normalization used for the marginal concentrations).
The qualitative interpretation of ICR caused by an asymmetry in the local selectivity at either end of the nanochannel is consistent with the pioneer proposal of Woarmann [154]. However, the present analysis provides a fresh interpretation of an old puzzle. It shows that Du is the principal electrostatic parameter that locally controls the channel selectivity, with a secondary effect due to λ_D, while Woermann

pointed at λ_D as the main length to be compared with the channel confinement. Although it may fly against intuition, it is not the physical size of the EDL that determines the system capability to rectify ionic current.

5.5 Conclusion

In summary, in the present Chapter the phenomenon of Ionic Current Rectification was addressed from a theoretical point of view. I have specifically focused on the case of a geometric ionic diode where the symmetry breaking is caused only by the conical geometry of the system. The theoretical framework mainly relies on two assumptions: a slowly varying channel geometry and a small electrostatic potential variation in the transversal direction. These ingredients allow to derive formal expressions for the electrostatic potential, Eq. (5.18), and for the ionic current, Eq. (5.11), and to explore the response of the system for different values of λ_D and Du. The main outcome of the work is the identification of the Dukhin length as the primary electrostatic length scale controlling rectification. It follows that rectification is expected to be measured in systems with size comparable to the Dukhin length, which remarkably can reach the micrometer scale [124]. This fact may explain recent experimental works [149, 150] in which ICR is observed in mesoscopic pores.
To conclude by misquoting Wolfgang Pauli [2], it is a dynamical usage of surfaces that let the nanofluidic diode succeed where demons don't.

[2] as Pauli once said *God makes the bulk; the surface was invented by the devil.*

5.6 Appendix: numerical simulations

Here I report some details of the implementation in COMSOL for the numerical integration of the following equations:

$$J_+ = -\partial_x c_+ + c_+[\partial_x \log h - (\partial_x\langle\phi\rangle - \Delta V) + \partial_x \log\langle e^{-\psi}\rangle] \tag{5.35a}$$

$$J_- = -\partial_x c_- + c_-[\partial_x \log h + (\partial_x\langle\phi\rangle - \Delta V) + \partial_x \log\langle e^{+\psi}\rangle] \tag{5.35b}$$

$$\partial_y^2\psi = -\frac{\lambda_D^{-2}}{2h}[(c_+ - c_-) - (c_+ + c_-)\psi]\,. \tag{5.35c}$$

First of all let recall the appropriate boundary conditions for the system at hands. In both ends of the channel one has to impose continuity in the electrochemical potential for each species. Starting from the left side I write in adimensional variables:

$$\log\frac{1}{2} \pm \frac{\Delta V}{2} = \log c_\pm(0) + \beta A_\pm(0) \tag{5.36}$$

where, by definition:

$$e^{-\beta A_\pm(0)} = \frac{e^{\mp\frac{\Delta V}{2}}}{2}\int_{-h_L}^{+h_L} dy\; e^{\mp\phi(0,y)}\,. \tag{5.37}$$

By substituting Eq.(5.37) into (5.36) one obtains:

$$c_\pm(0) = \frac{1}{4}\int_{-h_L}^{+h_L} dy\; e^{\mp\phi_L(y)}\,, \tag{5.38}$$

where the boundary condition for $c_\pm(0)$ is expressed in terms of the function $\phi_L(y) \equiv \phi(0,y)$. The latter is obtained by solving the following transversal equation at $x = 0$:

$$\partial_y^2\phi_L = -\frac{\lambda_D^2}{1+\kappa/2}\left[\int_{-h_L}^{+h_L}\sinh(\phi_L) - (\phi_L - \langle\phi_L\rangle)\int_{-h_L}^{+h_L}\cosh(\phi_L)\right], \qquad x = 0 \tag{5.39}$$

where $\langle\phi_L\rangle = \frac{1}{2h_L}\int_{-h_L}^{h_L} dy\phi_L(y)$, $h_L = 1 + \frac{\kappa}{2}$ and it was used the fact that:

$$c_+(0) + c_-(0) = \frac{1}{2}\int_{-h_L}^{+h_L} dy\cosh(\phi_L(y)) \tag{5.40a}$$

$$c_+(0) - c_-(0) = \frac{1}{2}\int_{-h_L}^{+h_L} dy\sinh(\phi_L(y))\,. \tag{5.40b}$$

Eq. (5.39) can be then numerically integrated using the standard electrostatic boundary conditions:

$$\partial_y\phi_L(0) = 0 \tag{5.41a}$$

$$\partial_y\phi_L(\pm h_L) = \mp\frac{\mathrm{Du}}{\lambda_D^2}\,. \tag{5.41b}$$

Likewise, one finds the appropriate boundary value for $c_\pm(1)$ using :

$$c_\pm(1) = \frac{1}{4}\int_{-h_R}^{+h_R} dy\; e^{\mp\phi_R}\,. \tag{5.42}$$

Therefore the expressions (5.38) and (5.42) are now numbers which can be directly used as boundary conditions for the system in (5.35).
It is also convenient in COMSOL to rescale the y variable in the following way:

$$y \to h(x)y\prime \tag{5.43a}$$
$$f(x,y) \to f(x,h(x)y\prime) \equiv f\prime(x,y\prime)\,. \tag{5.43b}$$

In this way the original domain is mapped to a square domain substantially simplifying the COMSOL calculation. From the chain rule it follows:

$$\begin{aligned}\partial_x f(x,y) \to \partial_x f\prime(x,y\prime) &= \partial_x f\prime(x,y\prime) + \partial_{y\prime} f\prime(x,y\prime)\partial_x y\prime \\ &= \partial_x f\prime(x,y\prime) - \partial_{y\prime} f\prime(x,y\prime)\frac{y\prime}{h(x)}\partial_x h(x) \qquad (5.44a)\\ \partial_y f(x,y) \to \partial_y f\prime(x,y\prime) &= \partial_{y\prime} f\prime(x,y\prime)\partial_y y\prime \\ &= \partial_{y\prime} f\prime(x,y\prime)\frac{1}{h(x)}\,. \qquad (5.44b)\end{aligned}$$

The only variables in the model that depend on y are $\psi(x,y)$, $\phi_L(y)$ and $\phi_R(y)$. For each of them Eqs. (5.44) are applied so that the electrostatic boundary condition for ψ (likewise for ϕ_L and ϕ_R) becomes:

$$\partial_{y\prime}\psi\prime(x,y\prime=0) = 0 \tag{5.45a}$$
$$\partial_{y\prime}\psi\prime(x,y\prime=\pm 1) = \mp\frac{\mathrm{Du}}{\lambda_D^2}h(x) \tag{5.45b}$$

and the rescaled Poisson equation:

$$\partial_{y\prime}^2\psi\prime = -\lambda_D^2 h(x)\left[(c_+ - c_-) - \psi\prime(c_+ + c_-)\right]\,. \tag{5.46}$$

Chapter 6

Surface charge discontinuities as a sensing tool

6.1 Introduction

Surface charges are known to play a key role in interfacial science including nanofluidics [124], cell biology [170, 171] and materials science [172, 173]. They govern the properties of any surface which, immersed in an aqueous solution, acquires an electrically charged double layer (DDL) due to the dissociation of surface groups. Local detection and control of surface charges is accordingly crucial for nanoscale application such as advancing the study of live cells [174] as well as the design of bio-sensing [175, 176], drug delivery [177–179] and energy harvesting nanofluidic devices [140, 180, 181]. Standard techniques such as ζ potential measurements [182] or conductance measurements in nanoconduits [183, 184] provide an integral estimate of the surface charge and therefore are not suitable to resolve heterogeneous charge structures. On the contrary, pipette-based microscopies exploit ionic current for contact-free sensing and are posed to become a central tool for charge imaging with nanoscale resolution. In particular, scanning ion conductance microscopy (SICM) is a powerful technique that has proven extremely useful in topographical mapping of non-conductive samples [185]. It was first developed in 1989 [186] with the following operational principle (Fig. 6.1). A pipette is immersed in electrolyte solution and positioned above a sample also bathed in electrolyte. An ionic current is generated by a potential difference maintained between the base of the pipette, far from the substrate, and the bulk solution, far from the pipette. As the tip of the pipette is moved towards the sample an access resistance builds up due to the decrease of the space available for the ions to flow, with the ionic current strongly suppressed for separation distances of the order of the inner pipette radius [187]. This distance-dependent modulation of the ionic current is used to control the vertical position of the pipette as it scans the substrate to map the topography of the sample. Typically the pipette is maintained at a distance that results in $\sim 1\%$ reduction of the ionic current from its bulk value, corresponding to a separation distance of approximately one inner pipette radius [174, 188] and ensuring no direct contact between the probe and the sample. The resolution of the technique is determined by the

inner radius of the pipette (typically tens of nanometers) and compares well with the more invasive atomic force microscopy (AFM) [189] . Since its development SICM was largely employed to scan living cells in physiological buffer for (*i*) tracking the activity of individual ionic pores [174, 186, 190, 191], (*ii*) localizing single protein complexes and receptors in functioning cells [188, 192–194], (*iii*) real time imaging of dynamical processes at cell membranes [195–198]. SICM measurements are typically conducted at high ionic concentrations (e.g. $\sim 150\,\mathrm{mM}$) so that the DDL thickness and the Dukhin length are small relative to the separation distance and the ionic current is therefore insensible to surface charge [124,169,199] . Recent studies conducted at low ionic concentrations (e.g. $\sim 0.1 - 10$ mM of NaCl) for which the DDL thickness and the Dukhin length are comparable to the separation distance have demonstrated that the polarity of the substrate influences the ion selectivity of the pipette resulting in surface-induced rectification (SIR) of the ionic current [200,201]. In this case, the access conductance is modified by the permselectivity of the substrate DDL generally leading to a rectified ionic current response. Typically via comparison with continuum simulations, the sign and magnitude of the surface charge is extracted from SIR measurements with micrometric spatial resolution, allowing for simultaneous topography and charge mapping [202–207]. In the present chapter, a fundamentally different mechanism for charge detection via SICM is proposed, based on the long-range modification of applied electric fields in the presence of a discontinuity in surface charge [208]. Previous studies [128, 208] have demonstrated in different contexts that in presence of an applied electric field the discontinuity in surface ionic current associated with a discontinuity in surface charge requires a long-range reorientation of bulk current, and hence electric field lines, in order to satisfy charge continuity. The length scale of the perturbation to the bulk electric field was shown to be set by the Dukhin length, which can reach values on the order of tens or hundreds of nanometers for typical surface charge densities and ionic strengths [124, 169]. By means of finite element method (FEM) simulations, I demonstrate that this effect is detectable via SICM opening up to the possibility of employing SICM to detect surface charge features much smaller than what has previously been reported in the literature. I consider the case of an isolated charge patch on an otherwise neutral substrate and study how the pipette conductance is affected by the surface charge. A substantial modification of the ionic current is found and rationalized with an effective electrostatic model for the field structure. Similar to previous results for nanometric pores [128], it is proved that isolated charge features acquire an apparent electric size that is magnified in the case of high surface charge and/or low ionic strength. This mechanism could be promptly employed in SICM experiments to dramatically improve the resolution of the current technique.

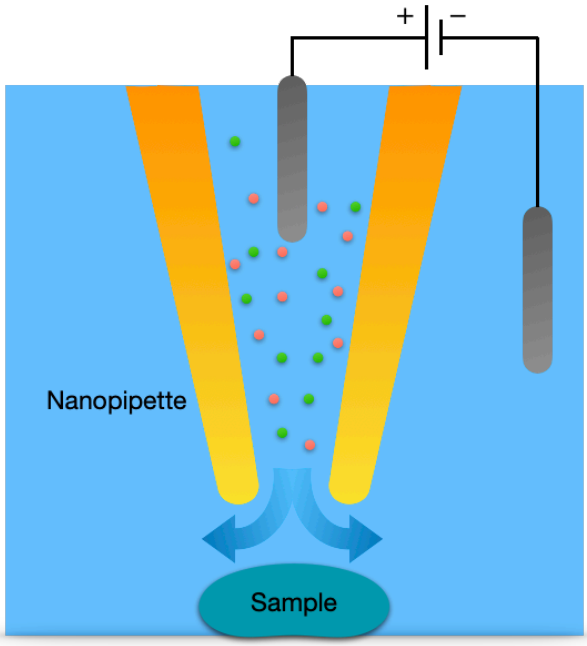

Figure 6.1: Illustration of the typical configuration of scanning ion conductance microscroscopy (SICM). A nanopipette is immersed in an electrolyte solution and brought in the proximity of the sample of interest. A potential difference is applied between the base of the pipette and the bulk inducing an ionic current through the pipette. Information over the sample topography and surface charge are inferred from the ionic current measurements, via a feedback control over the pipette position.

6.2 Long-range expression of surface charge discontinuities

In the standard picture of electrokinetics [121], electrostatic interactions between charged surfaces immersed in an electrolyte solution decay over the Debye length λ_D Eq. (4.4). Within a distance $\sim \lambda_D$ from the solid-liquid interface, an electrically charged cloud of counterions accumulates to screen the charge of the surface giving rise to an additional conductivity $\kappa_s \propto |\sigma|$, being σ the surface charge density. Accordingly, in the presence of an external electric field a surface current builds up which vanishes outside of the DDL where $\kappa_s = 0$. As first pointed out by Khair and Squires [208], such surface transport has important consequences for the electric field outside of the DDL in presence of finite size surfaces and, more generically, surface conduction discontinuities.

Let consider an isolated disk of charge on an otherwise neutral substrate immersed in an electrolyte solution and construct a cylindrical control volume of arbitrary radius r and height λ_D , such that the vertical extent of the DDL is contained within this volume (Fig. 6.2). In the presence of the total electric field $\boldsymbol{E} = (E_r, E_z)$ a bulk current per unit area $J_z \sim \kappa_b E_z$ exits vertically from the control volume sketch in Fig. 6.2, with κ_b the bulk conductivity. At steady state such current has to be equal and opposite in sign to the surface current per unit length $J_r \sim \kappa_s E_r$ leaving

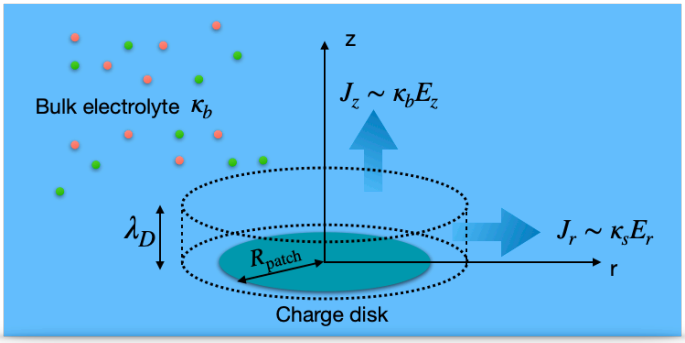

Figure 6.2: Illustration of a disk of charge immersed in an electrolyte solution characterized by a bulk conductivity κ_b. In the proximity of the charged patch an electrically charged diffuse layer builds up with an extent given by the Debye length λ_D. Within the diffuse layer there is an additional surface conductivity κ_s giving rise to an additional surface current in presence of an external electric field. The ionic current J_z leaving the element volume along z must then compensate the surface current J_r in order to ensure charge conservation across the double layer.

the DDL in the radial direction. The flux balance associated with an infinitesimal increase in the radial extent of the control volume δr therefore reads:

$$\sum_{volume} J_{out} - J_{in} = -\kappa_s(r)E_r \cdot 2\pi r + \left[\kappa_s(r)E_r + \partial_r[(\kappa_s(r)E_r]\delta r + \mathcal{O}(\delta r^2)\right] \cdot 2\pi(r+\delta r) + \kappa_b E_z \cdot 2\pi r \delta r = 0\,, \tag{6.1}$$

where $\partial_r \equiv \partial/\partial r$ and I have introduced an $r-$dependent surface conductivity defined as $\kappa_s(r) = \kappa_s \Theta(R_{\text{patch}} - r)$ with Θ the Heaviside function and R_{patch} the radius of the patch. This imposes the following condition on the normal and tangential electric field:

$$\kappa_b E_z + \frac{1}{r}\frac{d}{dr}[r\kappa_s(r)E_r] = 0 \tag{6.2}$$

at the boundary of the diffuse layer–*i.e.*, at a distance $\sim \lambda_D$ from the surface. Rewriting Eq. (6.2) in terms of the electrostatic potential, dividing by κ_b and rearranging terms one finds

$$\boxed{\frac{\partial \Phi}{\partial z} = -\frac{\ell_{\text{Du}}}{r}\frac{\partial}{\partial r}\left[r\Theta(R_{\text{patch}} - r)\frac{\partial \Phi}{\partial r}\right] \quad (z = \lambda_D)\,,} \tag{6.3}$$

where the definition Eq. (4.40) for the Dukhin length was used. Via Eq. (6.3), a straightforward consequence of charge conservation, one sees that a finite disk of charge induces a modification in the bulk electric field that is controlled by two length scale, respectively ℓ_{Du} and R_{patch}. Notably in the case of an infinite line of surface charge discontinuity in an otherwise uniform and planar distribution, the effective boundary condition given in Eq. (6.3) would contain only a single length scale: ℓ_{Du} [208].

The effect described by Eq. (6.3) is magnified when $\ell_{\mathrm{Du}}/\lambda_D \gg 1$, giving rise to long range gradients of the electric field far outside the DDL.

6.3 An effective electrostatic model

In the following I prove via numerical simulations that the surface-driven effect introduced above is detectable via SICM providing a new method for charge mapping alternative to SIR. In particular, two assumptions will be made to reduce the description of the ionic transport to an effective electrostatic model [208]: (*i*) the length scale over which the bulk electric field is modified by the surface charge discontinuity is much larger than the Debye length, such that the DDL, and hence the control volume, can be treated as infinitesimal in height, (*ii*) the ionic concentration outside of the DDL is uniform such that the bulk conductivity $\kappa_b$is taken as a constant. The former assumption is valid as long as the Dukhin length is large compared to the characteristic DDL thickness. In the latter assumption any voltage-dependent concentration accumulation/depletion effects associated with the surface charge [154] are neglected (see the Discussion section). Notably in the regime $\lambda_D \to 0$, Eq. (6.3) becomes an effective boundary condition *at* the interface ($z = 0$). Recalling the electrostatic boundary condition $\boldsymbol{E} \cdot \hat{\boldsymbol{n}} = \sigma/\epsilon_0\epsilon_r$ for the normal component of the electric field in the proximity of a conducting or thick insulating surface (with $\hat{\boldsymbol{n}}$ the outward versor to the surface) allows to rewrite Eq. (6.3) as:

$$-\left.\frac{\partial \Phi}{\partial z}\right|_{z=0} \equiv \sigma_{\mathrm{eff}}[\Phi] \quad (z = 0)\,, \tag{6.4}$$

where an effective surface charge density (with unit permittivity) is introduced

$$\sigma_{\mathrm{eff}}[\Phi(r)] \equiv \frac{\ell_{\mathrm{Du}}}{r}\frac{\partial}{\partial r}\left[r\Theta(R_{\mathrm{patch}} - r)\left.\frac{\partial}{\partial_r}\Phi\right|_{z=0}\right] \tag{6.5}$$

which is proportional to the true surface charge density via the Dukhin length and depends functionally on the electrostatic potential at the interface. In the bulk electrolyte outside the DDL, the steady-state continuity equation $\nabla\cdot\boldsymbol{i} = 0$ is imposed for the bulk current density $\boldsymbol{i} \equiv \kappa_b\boldsymbol{E} \equiv -\kappa_b\nabla\Phi$, such that

$$\boxed{\nabla^2\Phi = 0\,.} \tag{6.6}$$

Through Eqs. (6.4-6.6) I have entirely neglected the solute dynamics reducing the electrokinetic problem to an effective sourceless electrostatic problem with an exotic boundary condition. This notably reduces the computational cost of the problem allowing to perform three-dimensional simulations (see the section "Surface charge mapping" below), so far out of reach due to the computational complexity [203]. Before leaving this section, the description is further simplified by introducing dimensionless variables: the electrostatic potential Φ is rescaled by the thermal voltage k_BT/e, and all lengths are rescaled by the internal pipette radius R. Consequently, the conductance is rescaled by κ_bR, and the ionic current, by $\kappa_bR \times k_BT/e$. With

these rescalings, the boundary condition (6.3) becomes

$$\left.\frac{\partial\Phi}{\partial z}\right|_{z=0} = -\mathrm{Du}\frac{1}{r}\frac{\partial}{\partial r}\left[r\Theta(R_{\mathrm{patch}}-r)\left.\frac{\partial\Phi}{\partial r}\right|_{z=0}\right] \equiv \sigma_{\mathrm{eff}}[\Phi]\,, \tag{6.7}$$

with the Dukhin number given by $\mathrm{Du} \equiv \ell_{\mathrm{Du}}/\mathrm{R}$. The rescaled Laplace equation, Eq. (6.6), is unchanged. In what follows, unless explicitly stated otherwise, all equations, parameters and variables will be reported in these reduced units.

6.4 SICM approaching curves

6.4.1 Axisymmetric FEM model

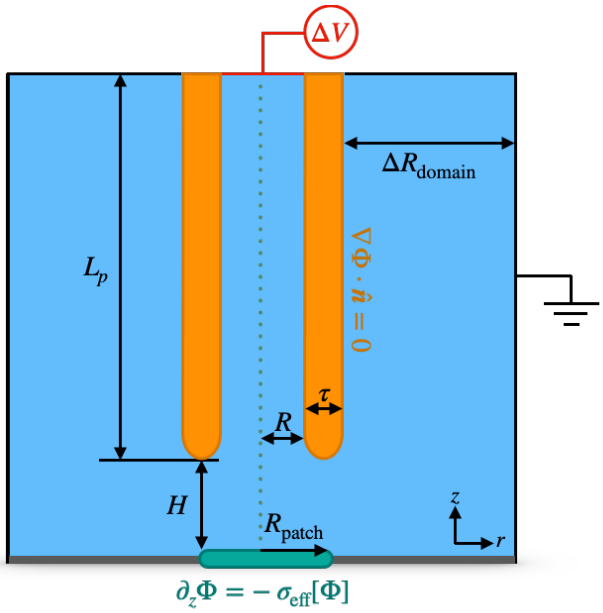

Figure 6.3: Illustration of the two dimensional axisymmetric model configuration. A nanotube of thickness τ, interior radius R and length L_p is held at a distance H from a patch with radius R_{patch} and an effective surface charge given by Eq. (6.4). The model boundary conditions are reported in the schematics: a potential ΔV is applied at the top of the pipette and the Neumann boundary condition Eq. (6.7) is applied at the bottom boundary. No flux boundary conditions are applied at the uncharged pipette walls and Dirichlet boundary conditions $\Phi = 0$ are applied in all remaining boundary domains. The dashed grey line is the axis of rotational symmetry.

Eq. (6.6) together with Eq. (6.7) must be solved numerically. Let first consider a 2D axisymmetric model containing a nanopipette of length L_p, thickness τ and inner radius $R \equiv 1$ held at a distance H from the center of the charged patch. For simplicity the pipette is assumed to be uncharged and the pipette thickness and inner radius to be constant (Fig. 6.3). The model domain has a total radial extent

$R+\tau+\Delta R_{\text{domain}}$ and a total vertical extent of $H+L_p$ where the parameters ΔR_{domain} and L_p have been adjusted to ensure that the numerical results are insensitive to the finite size domain (in all axisymmetric calculations, I take $L_p = \Delta R_{\text{domain}} = 10$). The Laplace equation (6.6) is solved using FEM simulations (COMSOL) with the boundary conditions indicated in Fig. 6.3. A fixed potential difference ΔV is applied at the base of the pipette while the remaining exterior domain boundaries (except the substrate) are held at $\Phi = 0$. Since the pipette's walls do not carry any charge, the no-flux boundary condition applies at these boundaries. Finally, the axisymmetric boundary condition Eq. (6.7) is applied on the lower boundary to account for the substrate. The ionic current across the pipette tip is computed as $I = -2\pi \int_0^1 dr\, r E_z$ for different Dukhin number, patch radius and separation distance, while keping the thickness fixed at $\tau = 1$. Values of the ratio of the wall thickness to the inner radius of order unity ($\tau \sim 1$) are typical of multiwalled carbon nanotubes [160].
I first validate the model by looking at the approach curve $I(H)$ in the absence of the patch (Du = 0). In this case the ionic current follows the geometrical prediction by Nitz *et al* [187]. By treating the pipette as a series of resistors the authors derived a semi-analytical scaling for the ionic current as a function of the distance H

$$I \propto I_{\text{bulk}} \left(1 + a/H\right)^{-1} , \tag{6.8}$$

where I_{bulk} is the saturation current when $H \to \infty$ and a is a length scale characterising the geometry of the pipette. As the pipette approaches the sample, the ionic current is geometrically hindered by the substrate and decreases to ultimately vanish at the contact-point. In Fig. 6.4 the numerical results are compared with the best-fit of the scaling in Eq. (6.8) finding a very good agreement. This indicates that the numerical model accurately reproduces the known physics of SICM in the absence of surface effects.

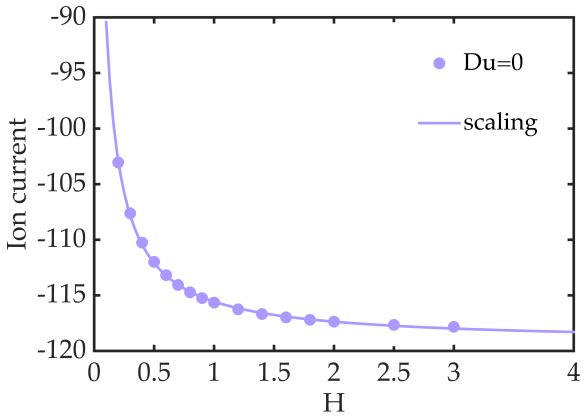

Figure 6.4: Dimensionless ionic current I as a function of the separation distance H in the absence of the patch (Du=0). The numerical results (dots) are compared with the analytical scaling Eq. (6.8) via a least-squares best fit. I_{sat} and a in Eq. (6.8) were used as fitting parameters. The results were obtained with the following choice of parameters: $\tau = 1$, $L_p = 10$, $\Delta R_{\text{domain}} = 10$, $\Delta V = 400$.

In Fig. 6.5 the absolute value of the ionic current (Fig. 6.5 a and c) and the current normalized by that obtained in the absence of the patch (Fig. 6.5 b and d)

are plotted as a function of the separation distance H and for several values of Du and $R_{\text{patch}} = 1$ (panels a and b) and $R_{\text{patch}} = 2$ (panels c and d). The approaching curves are significantly modified by the surface charge depending strongly both on Dukhin number and patch size. The supplementary contribution of the surface charge results in an increase of the measured ionic current owing to the additional transport in the DDL. The effect is more evident for the larger patch $R_{\text{patch}} = 2$, with the enhanced surface transport leading to an inversion of the approach curves for large Dukhin numbers (Fig. 6.5 c). In this case, the enhanced surface transport dominates over the natural drop associated with the steric hindrance down at least to the smallest distance examined here ($H = 0.2 \times R$ in dimensional unit). The signal grows with Dukhin number and reaches a magnitude $\gtrsim 10\%$ of the current obtained in the absence of the patch for separation distances $H \lesssim 1$. Notably, the signal reported here originates neither from double layer overlap nor from inhomogeneities in solute concentration generally, since the present model is not resolving the structure of the diffuse layer or the electrolyte dynamics.

6.4.2 Scaling of approach curves

The problem given by Eqs. (6.6-6.7) and the additional boundary conditions indicated in Fig. 6.3 is analytically intractable. Nevertheless, the scaling behaviour of the additional current induced by the surface charge (Fig. 6.5) can be extracted on the basis of a simplified model, which is introduced in the present section. Let first decompose the electrostatic potential as $\Phi = \Phi^{(0)} + \delta\Phi$ where $\Phi^{(0)}$ is the 'unperturbed' potential in the absence of the patch (Du = 0), and $\delta\Phi$ is the modification induced by the surface charge. The known [187] geometric influence on the electric field is then entirely contained in $\Phi^{(0)}$ and $\delta\Phi$ will be treated perturbatively [128] to determine the enhancement of the ionic current due to the surface charge. For the sake of analytical treatment, in what follows the complex no-flux boundary conditions induced by the pipette (Fig. 6.3) are neglected. Strictly speaking, I anticipate this approximation to be valid only when the Dukhin length and the patch size are small compared to either the separation distance H or internal radius R; however, the results indicate that the scaling so-obtained is more robust than these limits would suggest. Since the unperturbed field $\boldsymbol{E}^{(0)} \equiv -\nabla\Phi^{(0)}$ fulfils $E_z|_{z=0} = 0$ the boundary condition in Eq. (6.7) becomes

$$\frac{\partial}{\partial z}\delta\Phi\bigg|_{z=0} = -\mathrm{Du}\frac{1}{r}\frac{\partial}{\partial r}\left[r\Theta(R_{\text{patch}} - r)\,\frac{\partial}{\partial r}\Phi\bigg|_{z=0}\right]. \tag{6.9}$$

Eq. (6.9) must be complemented with the Laplace equation for $\delta\Phi$ in the bulk

$$\nabla^2\delta\Phi = 0 \tag{6.10}$$

and, since the influence of the pipette geometry on $\delta\Phi$ is neglected, homogeneous boundary conditions at a large distance $|\boldsymbol{r}| = \sqrt{r^2 + z^2}$ from the center of the patch:

$$\delta\Phi(\boldsymbol{r}) \xrightarrow[|\boldsymbol{r}|\to\infty]{} 0\,. \tag{6.11}$$

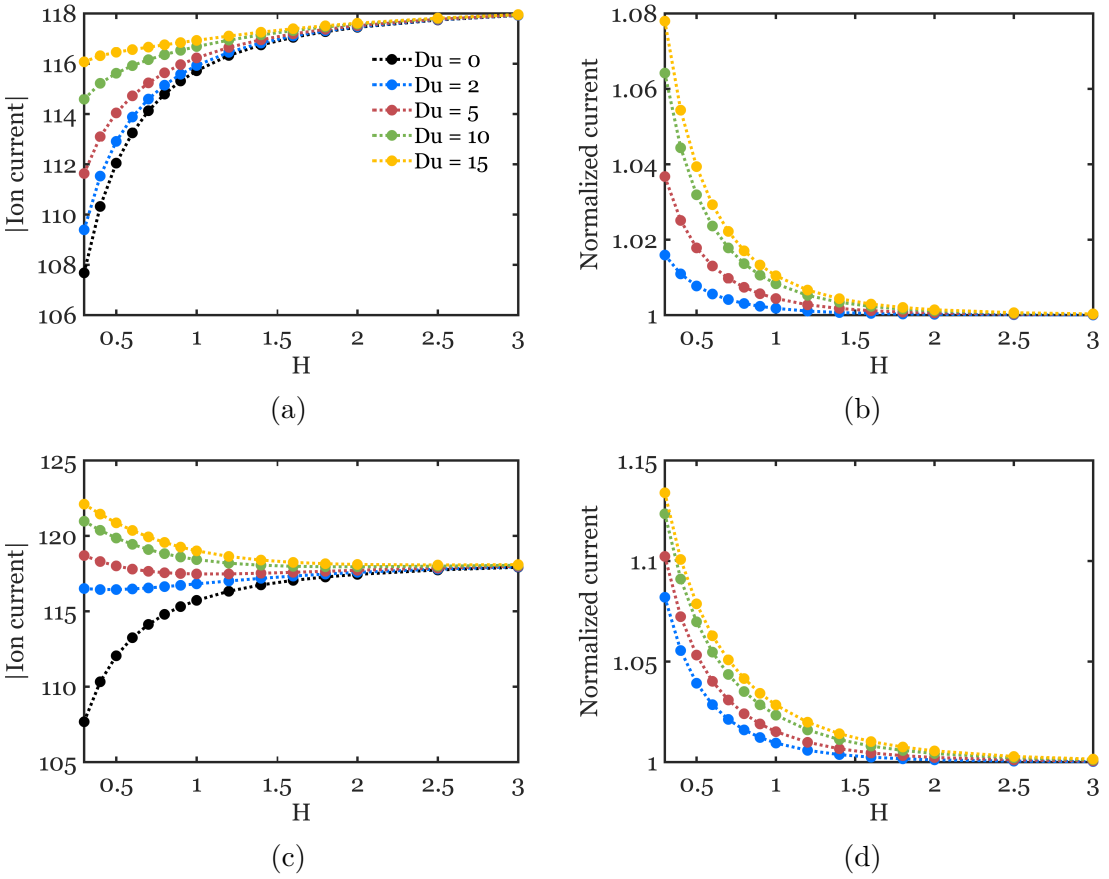

Figure 6.5: Ionic current as a function of separation distance H for $R_{\text{patch}} = 1$ (panels a and b) and $R_{\text{patch}} = 2$ (panels c and d) and several different values of Du, as indicated in the legend in panels a. Panels a and c show the absolute value of the ionic current, while panels b and d show the current normalized by that obtained in the absence of surface charge (Fig. 6.4). The filled circles are values obtained via finite element simulations and the dashed curves are guides for the eye. All curves are computed for $\tau = 1$, $L_p = \Delta R_{\text{domain}} = 10$ and $\Delta V = 400$.

The electrostatic problem of Eqs. (6.9-6.11) may be solved using the Green's function method (see Appendix 6.8) giving

$$\delta\Phi(\boldsymbol{r}) = -\int d\boldsymbol{\Sigma}_s \frac{1}{2\pi|\boldsymbol{r}-\boldsymbol{r}_s|}\left.\frac{\partial\delta\Phi}{\partial z_0}\right|_{z_0=0}, \tag{6.12}$$

where $\boldsymbol{r}_s \equiv \boldsymbol{r}_0|_{z_0=0}$ is the integration point confined at the solid-liquid interface and $d\boldsymbol{\Sigma}_s \equiv r_s dr_s d\theta_s$ is the surface element on the interface. The corresponding contribution to the electric field $\delta\boldsymbol{E} = \boldsymbol{E} - \boldsymbol{E}^{(0)} = -\nabla\delta\Phi$ is determined by differentiating Eq. (6.12) with respect to $\boldsymbol{r}$, such that

$$\delta\boldsymbol{E}(\boldsymbol{r}) = -\int d\boldsymbol{\Sigma}_s \frac{\boldsymbol{r}-\boldsymbol{r}_s}{2\pi|\boldsymbol{r}-\boldsymbol{r}_s|^3}\left.\frac{\partial\delta\Phi}{\partial z_0}\right|_{z_0=0}. \tag{6.13}$$

Since the pipette was entirely neglected in deriving Eq. (6.13), the latter will necessarily break down in the pipette interior; however let assume that it provides a

reasonable approximation up to the center point of the pipette tip ($\boldsymbol{r} = H\hat{\boldsymbol{z}}$). The additional current sensed by the pipette at a separation distance H may therefore be estimated as $\delta I = -2\pi \int_0^1 r dr \delta E_z|_{z=H} \propto -\pi \delta E_z(H\hat{\boldsymbol{z}})$. By evaluating Eq. (6.13) at $\boldsymbol{r} = H\hat{\boldsymbol{z}}$ one obtains

$$\delta \boldsymbol{E}(H\hat{\boldsymbol{z}}) = -\int d\boldsymbol{\Sigma}_s \frac{H\hat{\boldsymbol{z}} - \boldsymbol{r}_s}{2\pi(H^2 + r_s^2)^{3/2}} \left.\frac{\partial \delta\Phi}{\partial z_0}\right|_{z_0=0} . \tag{6.14}$$

The only angular dependence is contained in $\boldsymbol{r}_s$ and this term is killed by angular integration. One substitutes Eq. (6.9) into the remaining term in Eq. (6.14) to obtain:

$$\delta E_z(H\hat{\boldsymbol{z}}) = \mathrm{Du} \int dr_s \frac{H}{(H^2 + r_s^2)^{3/2}} \frac{\partial}{\partial r_s} \left(r_s \Theta(R_{\mathrm{patch}} - r_s) E_r(r_s)\right) . \tag{6.15}$$

Formal solution of Eq. (6.15) requires the knowledge of the full electric field E_r which is not accessible. Instead, the approach of Lee *et al* [128] can in treating (6.15) perturbatively and substituting in Eq. (6.15) the unperturbed field $E_r^{(0)}$ in order to determine the first order correction $\delta E_z^{(1)}$ to the electric field. The unperturbed field typically scales as $E_r^{(0)} \sim \Delta V/\ell_{\mathrm{drop}}$, where ℓ_{drop} stands for the characteristic length of the radial drop-off of the electrostatic field from the pipette tip. By substituting this scaling into Eq. (6.15) and integrating by parts one estimates the first order correction to the electric field. Consequently, the leading order modification to the ionic current is found to scale as:

$$\delta I \propto \mathrm{Du} \Delta V \frac{R_{\mathrm{patch}}^3}{H(H^2 + R_{\mathrm{patch}}^2)^{3/2}} , \tag{6.16}$$

and the corresponding conductance $\delta G \equiv \partial|\delta I|/\partial \Delta V$ at the pipette entrance as

$$\boxed{\delta G \propto \mathrm{Du} \frac{R_{\mathrm{patch}}^3}{H(H^2 + R_{\mathrm{patch}}^2)^{3/2}} .} \tag{6.17}$$

The scaling prediction in Eq. (6.17) is compared with the conductance anomaly computed from numerical simulations as the ionic conductance minus that obtained in the absence of the patch:

$$\delta G \equiv G(H; \mathrm{Du}) - \mathrm{G}(\mathrm{H}; \mathrm{Du} = 0) . \tag{6.18}$$

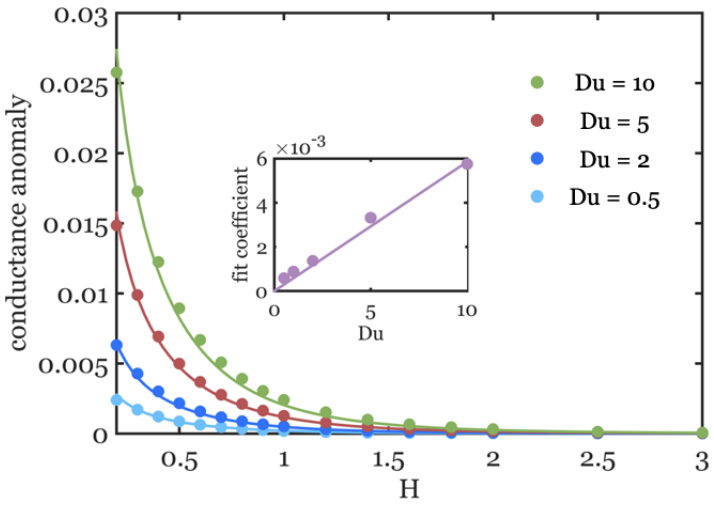

Figure 6.6: Conductance anomaly δG as a function of the separation distance H for several values of Dukhin number. The color dots indicate the numerical values of δG obtained via finite-element simulations and the solid lines are the fit to the numerical data using the function $\alpha(\mathrm{Du})\mathrm{R}^3_{\mathrm{patch}}/\mathrm{H}(\mathrm{H}^2+\mathrm{R}^2_{\mathrm{patch}})^{3/2}$. In the inset plot the color dots report the fit coefficient α for the curves showed in the main plot plus an additional curve for Du = 1. The solid line in the inset shows the best linear fit for α. All curves are computed for $R_{\mathrm{patch}} = 1$, $\tau = 1$, $L_p = 10$, $\Delta R_{\mathrm{domain}} = 10$.

In Fig. 6.6 and 6.7 δG is rescaled with the bulk conductance $G_{\mathrm{bulk}} \equiv I_{\mathrm{bulk}}/\Delta V$ for $H \to \infty$ extrapolated from the best fit in Fig. 6.4. The geometrical dependence of the normalized δG as a function of the separation distance H is reported in Fig. 6.6 for several values of Dukhin number and fixed $R_{\mathrm{patch}} = 1$. In order to test the veracity of the scaling relation in Eq. (6.17), the numerical results (filled circles) in Fig. 6.6 are fitted to a relationship of the form $\delta G = \alpha(\mathrm{Du})\mathrm{R}^3_{\mathrm{patch}}/\mathrm{H}(\mathrm{H}^2+\mathrm{R}_{\mathrm{patch}}2)^{3/2}$ (solid lines). One sees immediately that this functional dependence describes the numerical data extremely well over the range of Dukhin numbers examined. The dependence of the fitting coefficient $\alpha(\mathrm{Du})$ on the Dukhin number is further examined in the inner plot of Fig. 6.6. As anticipated by Eq. (6.17) the conductance anomaly scales linearly with the Dukhin number, in accordance with the prediction in Eq. (6.17), reaching up to $\mathcal{O}(10\%)$ of the bulk conductance. Surprisingly, although the calculated conductance anomaly in Eq. (6.17) is a leading order approximation in Du, this scaling relationship appears to be robust over a wide range of Dukhin numbers. Similarly Fig. 6.7 shows the numerically calculated conductance anomaly as a function of H for several patch sizes and fixed Du = 5. Again the scaling Eq. (6.17) is tested by fitting the numerical curves in Fig. 6.7 (filled circles) with the function $\delta G = \beta(R_{\mathrm{patch}})\mathrm{Du}/H(H^2+R_{\mathrm{patch}}2)^{3/2}$ (solid lines). Overall, the analytical prediction works reasonably well for all examined patch sizes although it appears to perform the best for $R_{\mathrm{patch}} \simeq 1$. The fit coefficient $\beta(R_{\mathrm{patch}})$ is reported in the inner plot of Fig. 6.7 as a function of the patch radius. The cubic dependence on the patch size (normalized with the pipette radius) found in Eq. (6.17) and confirmed in Fig. 6.7 is much stronger than the linear dependence on Dukhin number and prevails in the limit of $R_{\mathrm{patch}} \ll 1$. This suggests that the inner pipette radius puts a strong

limitation on the resolution when $R_{\text{patch}}/R \lesssim 1$. Although the surface-driven disturbance does scale with the Dukhin number as expected, ultimately is the pipette radius to set the resolution limit of the present mechanism for charge detection.

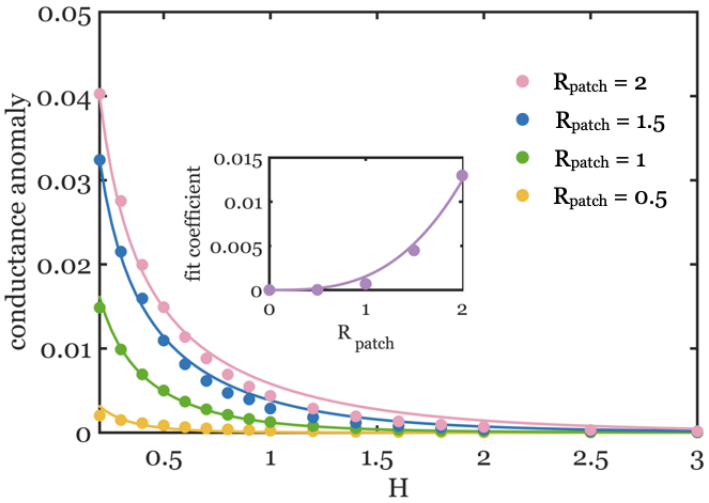

Figure 6.7: Conductance anomaly δG as a function of the separation distance H for several values of R_{patch}. The color dots indicate the numerical values of δG obtained via finite-element simulations and the solid lines are the fit to the numerical data using the function $\beta(R_{\text{patch}})\text{Du}/\text{H}(\text{H}^2 + \text{R}_{\text{patch}}^2)^{3/2}$. In the inset plot the color dots report the fit coefficient β for the curves showed in the main plot. The solid line in the inset shows the best cubic fit for β. All curves are computed for $\text{Du} = 5$, $\tau = 1$, $L_p = 10$, $\Delta R_{\text{domain}} = 10$.

6.5 Surface charge mapping

In order to access the off-center, lateral structure of the current response in the presence of a charged patch, one must abandon the axisymmetric model introduced above in favour of a model that allows the movement of the pipette off-set from the central reference axis. To this end, I consider both a 2D translationally invariant model and a 3D model implemented in COMSOL. This allows to simulate scanning measurements in which the pipette is held at a fixed distance H from the substrate and moved horizontally on top of it to map the surface charge distribution. The 3D calculations are computationally cumbersome, owing especially to the highly refined mesh needed to resolve the nontrivial boundary condition at the substrate, and they fail to converge for large values of Du. Hence the need to supplement these calculations with a 2D translationally invariant model.

6.5.1 Two-Dimensional Translationally Invariant Model

For the 2D translationally invariant model let consider a slab geometry in the $xy-$plane as shown in Fig. 6.8. The patch is now a semi infinite strip of charge centered in $x = 0$ with half-width R_{patch}. Likewise now the pipette has a slab/channel

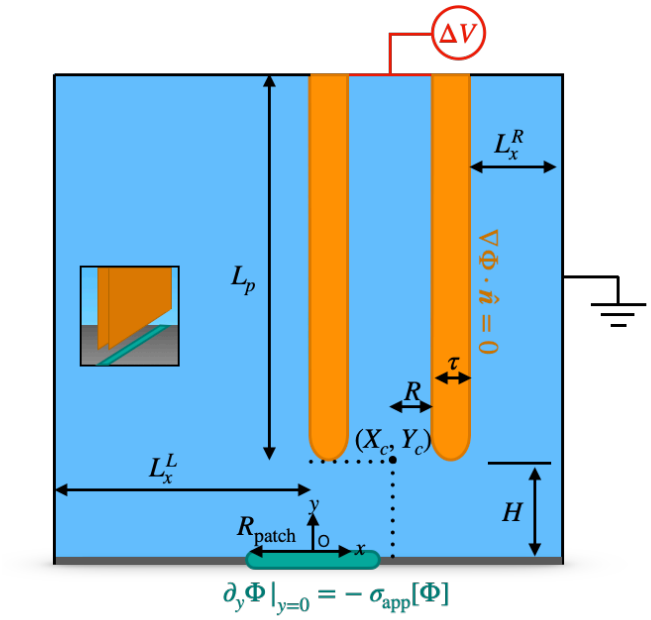

Figure 6.8: Illustration of the 2D translationally invariant model. A pipette of thickness τ, interior half-width R and length L_p is held at a distance H from an isolated strip of charge with half-width R_{patch} and an apparent surface charge given by Eq. (6.19). The origin O of the xy reference frame is taken to be the center of the patch. The pipette position is located in the point $(X_c, Y_c = H)$ indicated in the figure. The model boundary conditions are reported in the schematics: a potential ΔV is applied at the top of the pipette and Neumann boundary condition Eq. (6.19) is applied at the bottom boundary. No flux boundary condition is applied at the uncharged pipette walls and Dirichlet boundary condition $\Phi = 0$ is applied in all remaining boundary domains. The total horizontal extent of the domain is $L_x^L + X_c + R + \tau + L_x^R$ and the total vertical extent is $L_p + H$.

configuration with half width $R \equiv 1$, thickness τ, and length L_p. As in the axisymmetric model, the electrostatic potential Φ fulfils the Laplace equation (6.6) in the bulk and an effective boundary condition at the solid-liquid interface ($y = 0$) which in this configuration reads:

$$\left.\frac{\partial\Phi}{\partial y}\right|_{y=0} = -\mathrm{Du}\frac{\partial}{\partial x}\left[\Theta(R_{\text{patch}} - |x|)\left.\frac{\partial\Phi}{\partial x}\right|_{y=0}\right] . \tag{6.19}$$

All other boundary conditions are identical to those imposed previously as indicated in Fig. 6.8. While this configuration is less physically meaningful than the axisymmetric model considered above (or the 3D model considered below), the goal here is to get a qualitative sense of the lateral structure of the current response across a charged patch. It will be shown below that the qualitative features of the current response observed in the 2D translationally invariant model are indeed reproduced in the full 3D model (in the accessible range of Dukhin numbers). The translationally invariant configuration allows to fix the vertical position of the pipette at $Y_c = H$ and compute the ionic current as a function of the pipette centerline X_c

while moving it along the $x-$axis. In Fig. 6.9 the conductance anomaly is reported, expressed as percentage increment of the conductivity in the absence of the patch and obtained via lateral scanning measurements over a patch of half-width $R_{\text{patch}} = 1$ for different values of separation distance H and Dukhin number Du. As anticipated, the signal increases monotonically with Dukhin number, reaching up to $15 - 20\%$ of the background conductance measured in the absence of the surface charge (Fig. 6.9). This suggests that the present mechanism for charge detection could be readily tested in experiments with the SICM techniques currently available. This is true even when the Dukhin length is smaller than both the inner amplitude of the pipette (Du < 1) and the half-patch size (Du $< \text{R}_{\text{patch}}$), as shown in Fig. 6.9-a. For most configurations a local maximum of the signal is observed in the proximity of the charge discontinuities at $X_c = \pm R_{\text{patch}}$ and a local minumum at $X_c = 0$. This structure is especially prevalent for small to intermediate Dukhin numbers (Fig. 6.9 a and b) and disappears for Du $= 5$ for separation distances $H \gtrsim 0.5$. This suggests an enhanced sensitivity of the method to charge discontinuities, corroborating the initial hypothesis, as well as a competition between the signals from the charge discontinuity and from the uniform surface charge in the central region of the patch, with the latter apparently dominating for large Dukhin numbers. The signal in Fig. 6.9 decreases significantly at a distance $X_c = R_{\text{patch}} + R + \tau$ from the center, *i.e.* when the pipette has passed fully over the patch. This observation suggests that the technique can be used for estimating the extent of charge features from the structure of SICM measurements. Notably, the higher sensitivity towards the charge discontinuity makes the present mechanism particularly suitable for an estimation of the edges of spatially distributed charge features.

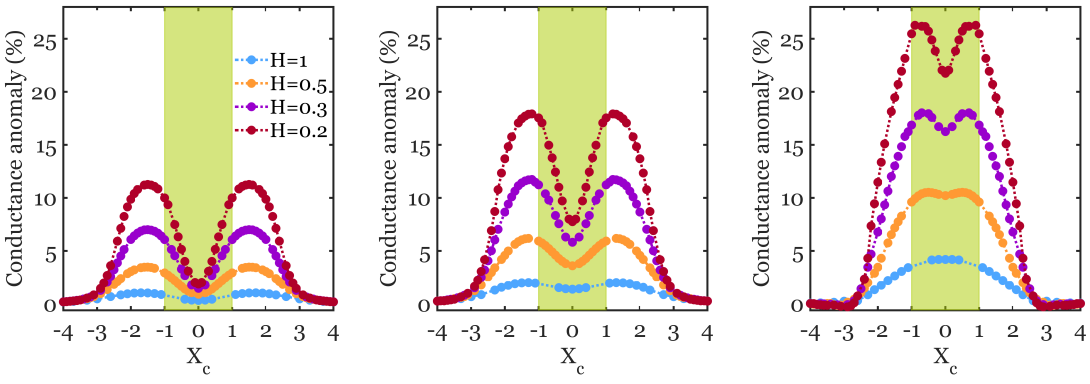

Figure 6.9: Conductance anomaly as a percentage of the unperturbed conductance versus pipette position along the $x-$axis for several separation distances H, as indicated in the legend in panel a, and for a) Du $= 0.5$, b) Du $= 2$ and c) Du $= 5$. The filled circles are values obtained via finite element simulations and the dashed curves are guides for the eye. The green shading indicates the location of the charged strip. All curves are computed for $R_{\text{patch}} = 1$, $\tau = 1$, $L_p = 10$ and $L_x^L = L_x^R = 10$.

6.5.2 Three-Dimensional Model

In order to confirm the newfound features observed in Fig. 6.9, let now introduce a full 3D FEM model. As noted above, the 3D calculations are computationally intensive and converge only for small to intermediate values of Du. The configuration of the 3D model is sketched in Fig. 6.10. A pipette of square cross-section with uniform half-side of length $R \equiv 1$ and thickness τ is moved horizontally in the $xy-$plane parallel to the substrate at a distance $z = H$ from it. The substrate contains a square patch of half-side of length R_{patch} characterized by our typical boundary condition (6.7) adapted to the present geometry:

$$\left.\frac{\partial \Phi}{\partial z}\right|_{z=0} = \mathrm{Du} \nabla_H \cdot \left[\Theta(R_{\text{patch}} - |x|)\Theta(R_{\text{patch}} - |y|)\boldsymbol{E}|_{z=0}\right] , \tag{6.20}$$

where $\nabla_H \equiv (\partial/\partial x, \partial/\partial y)$ is the horizontal gradient operator. As usual, the electrostatic potential verifies the Laplace equation (6.6) and the additional boundary conditions induced by the SICM configuration (Fig. 6.10). I adopt a square configuration for the patch and pipette to avoid errors associated with the resolution of circular features in a rectangular meshing pattern (see the Appendix 6.9 for more details).

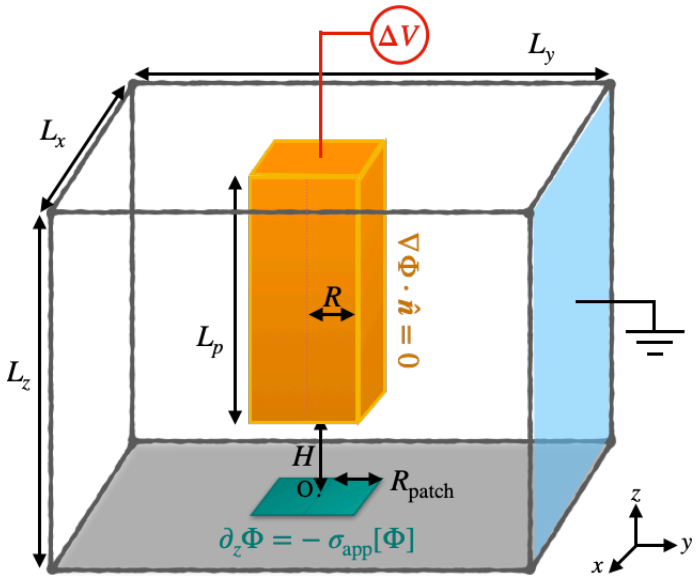

Figure 6.10: Schematics of the three-dimensional geometry used in COMSOL to simulate the scanning measurements of an SICM configuration. A rectangular pipette of constant half-width R, length L_p and thickness τ (not shown in the illustration) is placed on top of a square patch with half size R_{patch} at a distance H. The origin O of the xyz reference frame is taken to be the center of the patch. The model boundary conditions are reported in the schematics: a potential ΔV is applied at the top of the pipette and Neumann boundary condition Eq. (6.20) is applied at the bottom plane. No flux boundary conditions are applied at the uncharged pipette walls and Dirichlet boundary condition $\Phi = 0$ are applied in the remaining boundaries.

In Fig. 6.11 and 6.12 the conductance anomaly maps obtained from horizontal

scan of a squared patch of size $R_{\text{patch}} = 1$ and $R_{\text{patch}} = 0.5$ are shown for several different Dukhin numbers. All scans are conducted at a separation distance $H = 0.2$ from the substrate and the conductance anomaly is plotted as a function of the position $(X_c, Y_c, Z_c = H)$ of the center of the pipette. For clarity, the position of the charged patch is indicated by a dashed red square in each panel. Furthermore, for each bidimensional surface map the corresponding lateral line scan obtained by fixing the $y-$position of the pipette at $Y_c = 0$ is reported. This allows a direct comparison between the results of the three dimensional model and the results of the $2D$ translationally invariant model (Fig. 6.9). One notes immediately that the presence of the charged patch produces a positive conductance anomaly, and the region of enhanced conductivity forms a ring-like shape centered on the charge discontinuity, with the largest anomalies occurring at the corners of the patch. This is qualitatively identical to the results of the 2D transversally invariant model, and it confirms the predominant role of the discontinuities in the observed signal, at least for the small to intermediate values of Du examined in the 3D model. This is particularly evident for the case of a smaller patch and intermediate Du reported in Fig. 6.12, for which the charge patch is almost exclusively detectable via the charge discontinuities. As before, the conductance anomaly grows with Dukhin number while the signal difference between the center of the patch and the boundary decreases. Overall, the 3D model produces a weaker signal than the translationally invariant model (Fig. 6.9), presumably owing to the fact that the patch is finite in all spatial directions in this configuration. Nevertheless, for all values of Du shown in Fig. 6.11 the conductance anomaly at the patch's boundaries is $\gtrsim 1\%$ of the conductance obtained in the absence of the patch, well within the threshold of experimental detectability using current SICM techniques. Such results demonstrate the capability of the surface-driven mechanism investigated here to produce high-resolution visualizations of isolated charged features, and surface charge discontinuities.

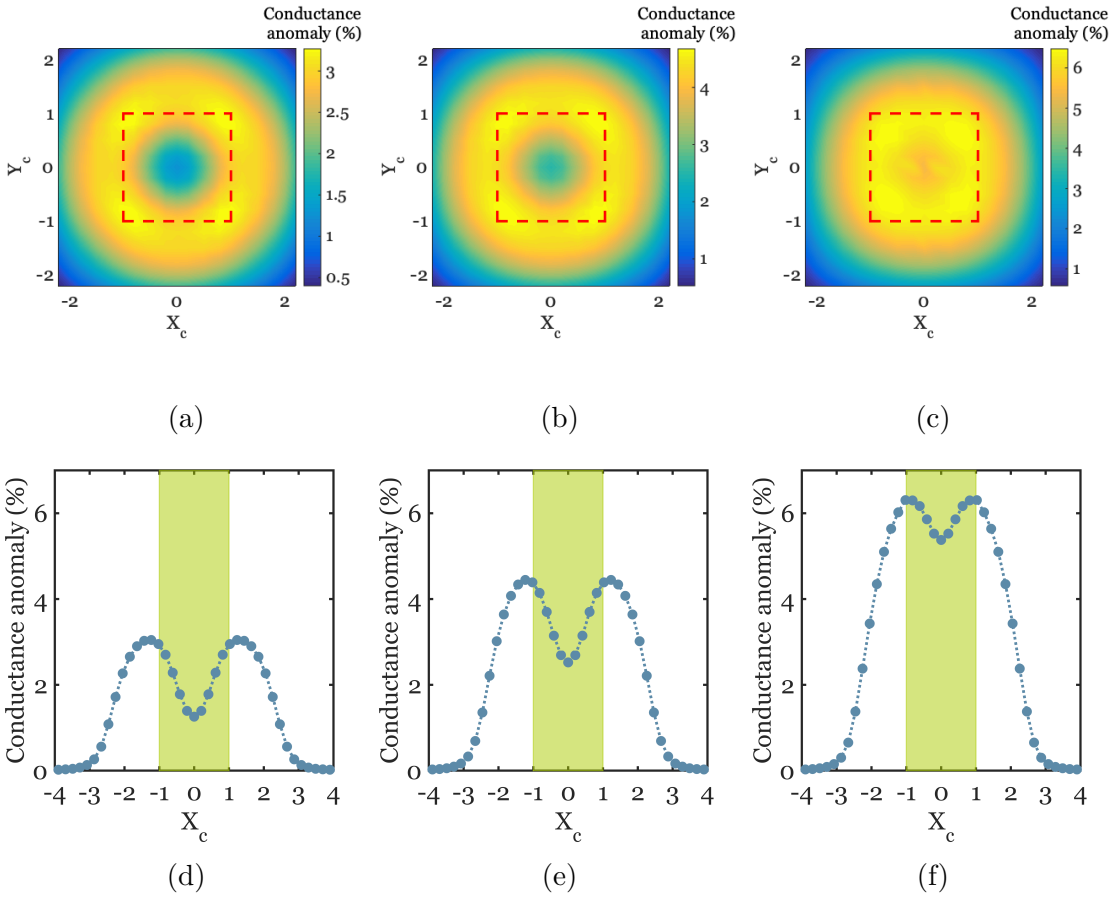

Figure 6.11: Upper panel: Conductance anomaly maps of a square patch of side half-length $R_{\text{patch}} = 1$ obtained from a pipette held at a separation distance $H = 0.2$ and with a) Du $= 0.5$, b) Du $= 1$ and c) Du $= 2$. The dashed red square in each panel indicates the location of the patch. Bilinear interpolation of the raw datas from numerical simulations is used to generate the surface map. Bottom panel: Corresponding line scan for $Y_c = 0$ obtained from the bidimensional map reported on top. The green shading indicates the location of the charge patch. All curves are computed for $R_{\text{patch}} = 1$, $\tau = 1$, $L_p = 10$, $L_x = 17$ and $L_y = 17$.

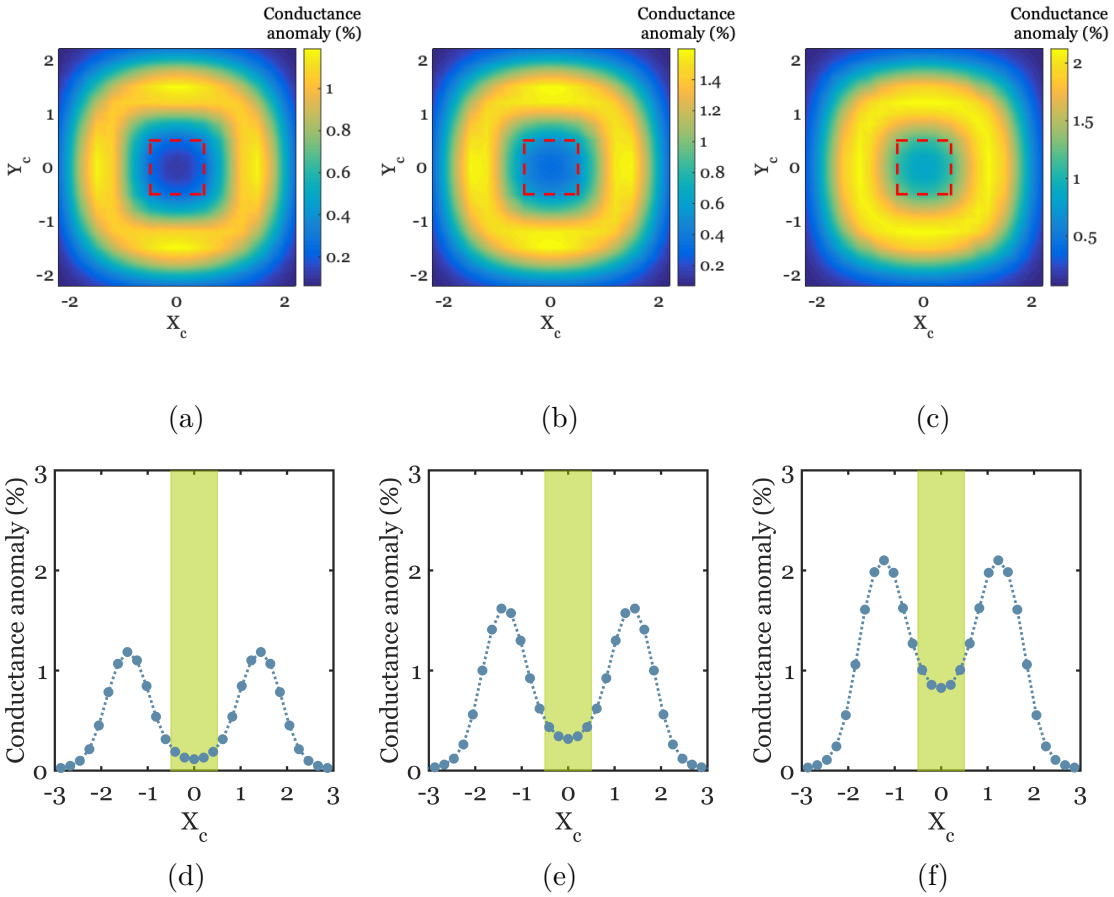

Figure 6.12: Upper panel: Conductance anomaly maps of a square patch of side half-length $R_{\text{patch}} = 0.5$ obtained from a pipette held at a separation distance $H = 0.2$ and with a) Du $= 0.5$, b) Du $= 1$ and c) Du $= 2$. The dashed red square in each panel indicates the location of the patch. Bilinear interpolation of the raw datas from numerical simulations is used to generate the surface map. Bottom panel: Corresponding line scan for $Y_c = 0$ obtained from the bidimensional map reported on top. The green shading indicates the location of the charge patch. All curves are computed for $R_{\text{patch}} = 0.5$, $\tau = 1$, $L_p = 10$, $L_x = 17$ and $L_y = 17$.

6.6 Discussion

Approach curves like the ones showed in Fig. 6.5 and surface bidimensional maps as reported in Fig. 6.11-6.12 are standard measures of the effect of surface charges in the context of scanning probe microscopies. Although apparently similar to the approach curves and surface maps previously reported [202,206,207,209] in the context of SIR-based SICM, the signal presented here is fundamentally different in nature. Surface charge visualization based on SIR exploits ionic current rectification due to local concentration polarization effects taking place at the interface between regions of different permselectivity; here the tip of the pipette and the DDL of the substrate (Fig. 6.13-b). As such, the signal measured using SIR strongly depends on the polarity of the applied potential bias according to whether the counterion-enriched DDL

results in a local accumulation or depletion of ions. In standard ICR, as sketch in Fig. 6.13-a (and discussed extensively in the previous Chapter), a local imbalance in ion selectivity between two (or more) coupled regions induces rectification that is mainly controlled by the ratio between the local Dukhin length and the inner pipette radius [8, 169, 199]. This is likely to apply also to SIR, and would explain previous results in which SIR was measured at tip-to-substrate distances much larger than the Debye length [200, 203, 204]. The present Chapter focused on a less investigated

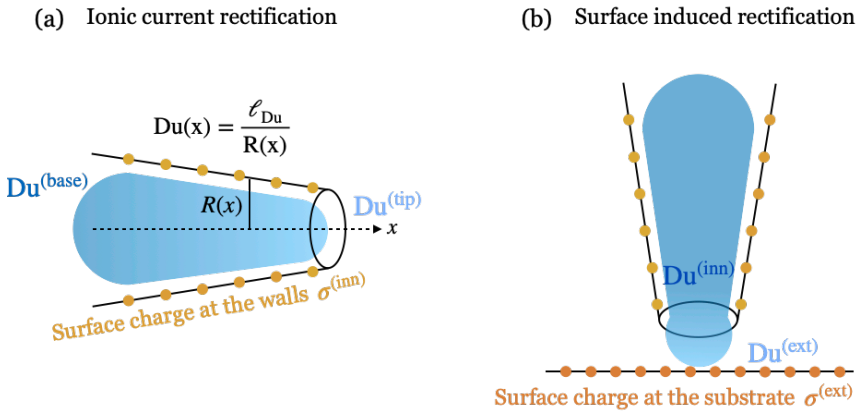

Figure 6.13: (a) Sketch of the working principle of ICR in a conical nanopipette with uniform surface charge. In this case the asymmetry is introduced by the $x-$dependent radius which results in a longitudinally varying Dukhin number. The unbalance causing rectification in this context is between the Dukhin number at the tip and the Dukhin number at the base when $\mathrm{Du}^{\mathrm{tip}} \neq \mathrm{Du}^{\mathrm{base}} \sim 1$. (b) Sketch of the working principle of SIR. In this case the nanopipette is brought in the proximity of a charged substrate and the unbalance between the Dukhin number at the tip of the pipette ($\mathrm{Du}^{\mathrm{inn}}$) and the Dukhin number at the DDL of the substrate ($\mathrm{Du}^{\mathrm{ext}}$) such that $\mathrm{Du}^{\mathrm{inn}} \neq \mathrm{Du}^{\mathrm{ext}}$ causes rectification.

but equally important effect due to surface charge inhomogeneities: the deformation of applied bulk electric fields due to ion charge conservation. As previously discussed [208], this effect is predominant in the regime of large surface potential Φ_0 beyond the standard Debye-Hückel regime, where $\ell_{\mathrm{Du}}/\lambda_D \sim e^{e|\Phi_0|/k_BT} \gg 1$. This is typically the case for moderate-to-high surface charges ($10 - 100\,\mathrm{mC/m^2}$) at moderate electrolyte concentrations ($0.1 - 1\,\mathrm{mM}$). The signal reported in the previous section is entirely due to the supplementary surface-driven current building up in the proximity of the surface charge. As such, it is independent of both the polarity of the applied electric field and the polarity of the substrate. Notably, in contrast with rectifying behaviours which saturate at large Dukhin number [8, 169, 199], the present mechanism increases linearly with Du thus suggesting the possibility of amplifying the resolution of current SICM techniques in certain regimes. In particular I anticipate that two criteria are prerequisite for the isolation and the maximization of the effect discussed here: (i) Dukhin length associated with the surface charge at the tip of the pipette $\ell_{\mathrm{Du}}^{(\mathrm{inn})} \propto \sigma^{(\mathrm{inn})}$ and (ii) Dukhin length associated with the surface charge of the substrate $\ell_{\mathrm{Du}}^{(\mathrm{ext})} \propto \sigma^{(\mathrm{ext})}$ both much larger than the pipette radius,

such that $\mathrm{Du}^{(\mathrm{inn})} \equiv \ell_{\mathrm{Du}}^{(\mathrm{inn})}/\mathrm{R} \sim \mathrm{Du}^{(\mathrm{ext})} \equiv \ell_{\mathrm{Du}}^{(\mathrm{ext})}/\mathrm{R} \gg 1$. Such a regime can be easily achieved by employing single multiwalls nanotubes of nanometric radii $\mathcal{O}(1-10)$ nm as previously done in different contexts [9, 160]. In this regime, both ICR and SIR are suppressed while the effect of surface charge discontinuities is maximized, potentially allowing for molecular scale resolution of single charge features.

6.7 Conclusions

Up to now, surface charge detection via scanning ion conductance microscopy has been based on (and limited to) the direct probing of the diffuse double layer at the surface. Typically, electrostatic interactions between the nanopipette and the double layer induce local current rectification which in turn is used to map the surface charge distribution. In the present Chapter, an alternative mechanism for charge detection via SICM is proposed based on the long-range, surface-mediated perturbation of electric fields in electrolyte solutions [208]. It was demonstrated via continuum (FEM) simulations and an analytical scaling argument that (*i*) this mechanism is detectable using a current-based probe microscopy and (*ii*) it can be exploited to substantially improve the resolution of surface charge mapping via SICM. In particular, signals are found to be on the order of $1-10\%$ well within the range of experimental detectability, and it was shown that the proposed technique offers nanometric resolution, an improvement over current methodologies. The technique has proven to be highly sensitive to discontinuities in surface charge, suggesting that it would be highly applicable to the mapping of small scale, rapidly varying charge features. I anticipate this mechanism to be useful in nanotube-based SICM experiments paving the way for charge detection of isolated charged features down to $\sim$ 1nm.

6.8 Appendix: Green's function on a semi-infinite domain

For completeness, I provide some mathematical details of the derivation of main text Eq. (6.12). From main text Eqs. (6.10-6.11), the problem to be solved is

$$\nabla^2 \delta\Phi = 0 \tag{6.21}$$

in the semi-infinite domain $\Omega \equiv \{(x, y, z) \in \mathbb{R} \times \mathbb{R} \times (0, \infty)\}$ above the $xy-$plane ($z > 0$), subject to

$$\left.\frac{\partial \delta\Phi}{\partial z}\right|_{z=0} = -\mathrm{Du}\frac{1}{r}\frac{\partial}{\partial r}\left[r\Theta(R_{\mathrm{patch}} - r)\left.\frac{\partial \Phi}{\partial r}\right|_{z=0}\right] \tag{6.22}$$

on the $xy-$plane, and

$$\delta\Phi(\boldsymbol{r}) \xrightarrow[|\boldsymbol{r}|\to\infty]{} 0 \tag{6.23}$$

at infinity (*i.e.*, as $|\boldsymbol{r}| \equiv \sqrt{r^2 + z^2} \to \infty$). The problem statement and geometry are sketched in Fig. 6.14.

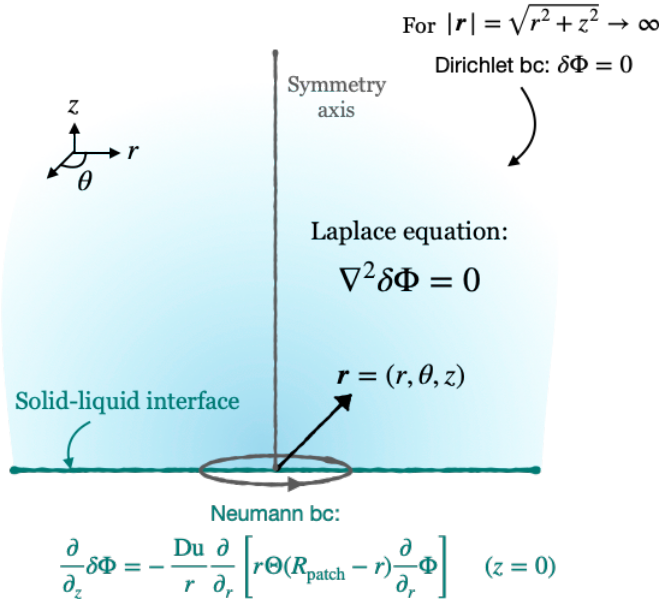

Figure 6.14: Schematic of the electrostatic problem given by Eqs. (6.21-6.23) (main text Eqs. (6.10-6.11). The Laplace equation for $\delta\Phi$ is solved in a semi-infinite domain bounded at $z = 0$ by the electrically charged substrate. The latter is accounted for by the effective Neumann boundary condition given in Eq. (6.22).

Let start by recalling Green's theorem for the Laplacian operator ∇^2, stated in terms of two arbitrary scalar fields ϕ, $\psi : \Omega \to \mathbb{R}$ defined on a 3D spatial domain Ω bounded by the surface $\partial\Omega$:

$$\int_\Omega d^3\boldsymbol{r}\left(\phi\nabla^2\psi - \psi\nabla^2\phi\right) = \oint_{\partial\Omega} d\boldsymbol{\Sigma}\cdot\left(\phi\nabla\psi - \psi\nabla\phi\right). \tag{6.24}$$

In the above, $d\boldsymbol{\Sigma}$ is a surface element on $\partial\Omega$ with direction given by the outward normal. Let introduce a Green's function satisfying

$$\nabla^2_{\boldsymbol{r}} G(\boldsymbol{r},\boldsymbol{r}_0) = \nabla^2_{\boldsymbol{r}_0} G(\boldsymbol{r},\boldsymbol{r}_0) = -\delta^{(3)}(\boldsymbol{r}-\boldsymbol{r}_0), \tag{6.25}$$

and set $\phi = \delta\Phi$ and $\psi = G$ in Eq. (6.24) to obtain

$$\delta\Phi(\boldsymbol{r}) = \int_{\partial\Omega} d\boldsymbol{\Sigma}_0 \cdot \left[G(\boldsymbol{r},\boldsymbol{r}_0)\nabla_{\boldsymbol{r}_0}\delta\Phi(\boldsymbol{r}_0) - \delta\Phi(\boldsymbol{r}_0)\nabla_{\boldsymbol{r}_0} G(\boldsymbol{r},\boldsymbol{r}_0)\right], \tag{6.26}$$

where I have made use of Eq. (6.21) and set the variable of integration to $\boldsymbol{r}_0$. Eq. (6.26) must be complemented with a proper choice of boundary conditions for the Green's function. From the boundary condition given in Eq. (6.23), the second term on the *rhs* vanishes everywhere but at the solid-liquid interface. One can similarly eliminate the first term on the *rhs* by requiring $G(\boldsymbol{r},\boldsymbol{r}_0) \to 0$ for $|\boldsymbol{r}_0| \to \infty$ (or equivalently $|\boldsymbol{r}| \to \infty$). It follows

$$\delta\Phi(\boldsymbol{r}) = -\int d\Sigma_s \left[G(\boldsymbol{r},\boldsymbol{r}_s)\left.\frac{\partial}{\partial z_0}\delta\Phi(\boldsymbol{r}_0)\right|_{z_0=0} - \delta\Phi(\boldsymbol{r}_s)\left.\frac{\partial}{\partial z_0} G(\boldsymbol{r},\boldsymbol{r}_0)\right|_{z_0=0}\right], \tag{6.27}$$

where $\boldsymbol{r}_s \equiv \boldsymbol{r}_0|_{z_0=0}$ is the source point confined to the solid-liquid interface ($z_0 = 0$), and $\Sigma_s \equiv r_s dr_s d\theta_s$ is the scalar surface element on the interface. The minus sign in Eq. (6.27) is due to the fact that $d\boldsymbol{\Sigma}_s\cdot\nabla \equiv -d\Sigma_s\partial/\partial z_0$. To further simplify Eq. (6.27) one can impose homogeneous Neumann boundary condition on the Green's function at the interface:

$$\begin{aligned}
\delta\Phi(\boldsymbol{r}) &= -\int r_s dr_s d\theta_s G(\boldsymbol{r},\boldsymbol{r}_s)\left.\frac{\partial}{\partial z_0}\delta\Phi(\boldsymbol{r}_0)\right|_{z_0=0} \\
&= \mathrm{Du}\int dr_s d\theta_s G(\boldsymbol{r},\boldsymbol{r}_s)\frac{\partial}{\partial r_s}\left[r_s\Theta(r_{patch}-r_s)\left.\frac{\partial}{\partial r_s}\Phi\right|_{z_0=0}\right],
\end{aligned} \tag{6.28}$$

where in the second line Eq. (6.22) was inserted.

Let now solve for the Green's function appearing in Eq. (6.28) and verifying Eq. (6.25), along with a homogeneous Dirichlet boundary condition at infinity and a homogeneous Neumann condition at the interface; that is, to solve

$$\nabla^2_{\boldsymbol{r}} G(\boldsymbol{r},\boldsymbol{r}_0) = \nabla^2_{\boldsymbol{r}_0} G(\boldsymbol{r},\boldsymbol{r}_0) = -\delta^{(3)}(\boldsymbol{r}-\boldsymbol{r}_0), \tag{6.29}$$

subject to

$$G(\boldsymbol{r},\boldsymbol{r}_0) \xrightarrow[|\boldsymbol{r}|,|\boldsymbol{r}_0|\to\infty]{} 0, \quad \text{and} \tag{6.30}$$

$$\left.\frac{\partial}{\partial z} G(\boldsymbol{r},\boldsymbol{r}_0)\right|_{z=0} = \left.\frac{\partial}{\partial z_0} G(\boldsymbol{r},\boldsymbol{r}_0)\right|_{z_0=0} = 0\,. \tag{6.31}$$

Homogeneous Dirichlet conditions are satisfied by the free-space Green's function:

$$G_\infty(\boldsymbol{r},\boldsymbol{r}_0) = -\frac{1}{4\pi|\boldsymbol{r}-\boldsymbol{r}_0|}. \tag{6.32}$$

In order to satisfy Eq. (6.31), the method of images is applied, adding to the free-space solution its reflection with respect to the interface:

$$V(\boldsymbol{r}, \boldsymbol{r}_{0\prime}) = -\frac{1}{4\pi|\boldsymbol{r} - \boldsymbol{r}_{0\prime}|}, \tag{6.33}$$

where $\boldsymbol{r}_{0\prime} = (r_0, -z_0)$ is the reflection of the source coordinate with respect to the interface. The full Green's function verifying Eqs. (6.29-6.31) is thus given by $G(\boldsymbol{r}, \boldsymbol{r}_0) = G_\infty(\boldsymbol{r}, \boldsymbol{r}_0) + V(\boldsymbol{r}, \boldsymbol{r}_{0\prime})$, which is evaluated at $z_0 = 0$ to obtain

$$G(\boldsymbol{r}, \boldsymbol{r}_s) = -\frac{1}{2\pi|\boldsymbol{r} - \boldsymbol{r}_s|}\,. \tag{6.34}$$

Eqs. (6.28) and (6.34) together give main text Eq. (6.12).

6.9 Appendix: 3D FEM simulations

All FEM calculations reported in the main text were performed using COMSOL Multiphysics (5.3a). Three-dimensional configurations turned out to be computationally intense and difficult to properly mesh and were only feasible for simple geometries and low surface charges (small Dukhin numbers). In particular COMSOL proved to be more robust with rectangular geometries than with circular geometries due to the rectangular meshing patterns generated by default in COMSOL for 3D geometries. For this reason, I opted for a rectangular pipette and a square patch as illustrated schematically in Fig. 6.15 (a reproduction of main text Fig. 6.10). The Laplace equation (6.6) was solved with the boundary condition given in Eq. (6.20) imposed on the bottom plane and all other boundary conditions as reported in Fig 6.15. The pipette was moved horizontally in the $xy-$plane parallel to the bottom plane at a fixed height H, and the current was computed at the pipette tip, cross-checked against the current at the base and the average current in the pipette, as a function of the lateral position. In Table 6.1 I report the values of the dimensionless parameters used for generating the scans in Fig. 6.11. The parameter β refers to the half-width of the second-order continuous Heaviside function 'flc2hs' used in COMSOL to implement the boundary condition Eq. (6.20).

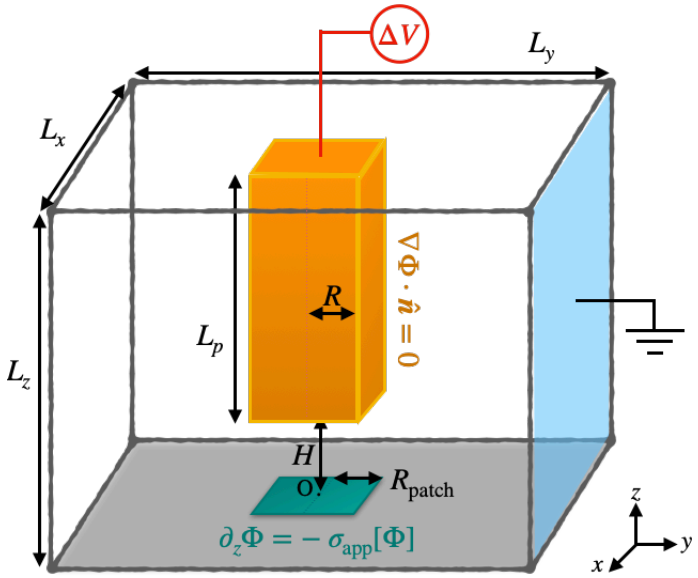

Figure 6.15: Schematics of the three-dimensional geometry used in COMSOL to simulate the scanning measurements of an SICM experiment. A rectangular pipette of constant half-width R, length L_p and thickness τ (not shown in the illustration) is placed on top of a square patch of half-width R_{patch} at a separation distance H. The origin O of the xyz reference frame is taken to be the center of the patch. The model boundary conditions are reported in the schematic: a potential ΔV is applied at the top of the pipette and an implicit Neumann boundary condition Eq. (6.20) is applied at the bottom boundary. No-flux boundary conditions are applied at the uncharged pipette walls, and the homogeneous Dirichlet boundary condition $\Phi = 0$ is applied on all remaining boundaries.

Table 6.1: Parameters used in 3D simulations for Fig. 6.11 .

Parameters of the model
$L_p = 10$
$R_{\text{patch}} = 1$
$H = 0.2$
$R = 1$
$\tau = 1$
$L_x = L_y = R + L_p + \tau + 5$
$L_z = L_p + H$
$\beta = 0.1$
$\Delta V = 400$

In order to properly resolve the spatial inhomogeneity of the Heaviside function in Eq. (6.20), an inhomogeneous mesh was implemented at the bottom boundary and refined in the proximity of the discontinuities. The mesh-independence of the results was checked by examining the current as a function of the maximum mesh element size in the vicinity of the the discontinuities. In Fig. 6.16 the current is

normalized by the value obtained for the smallest mesh size achievable with the computer resources at hands. The simulations in Figs. 6.11-6.12 were performed with a maximum mesh element size (normalized by the pipette half-width) of 0.003. For the latter value the simulations appear to be converged at least for values up to Du $\lesssim 1$ (Fig. 6.16).

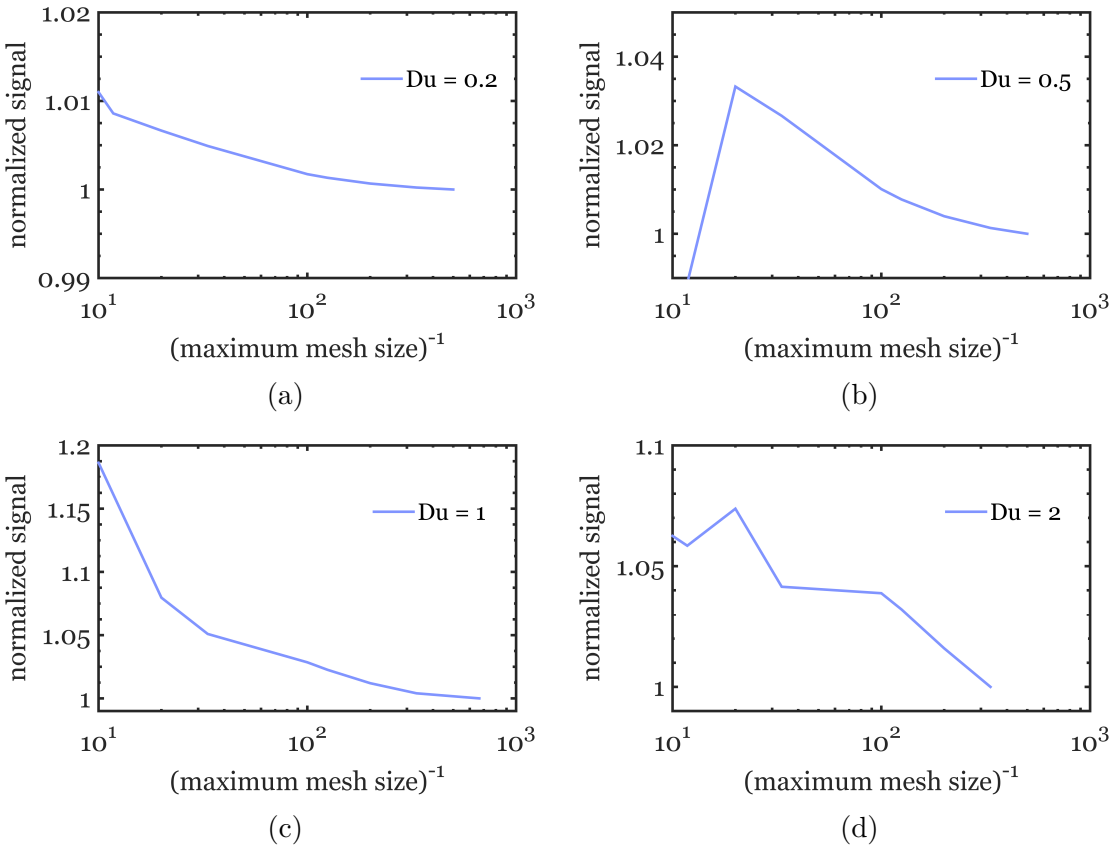

Figure 6.16: Ionic current as a function of the reciprocal of the maximum mesh element size in the vicinity of the discontinuities for different values of Dukhin number: a) Du = 0.2, b) Du = 0.5, c) Du = 1 and d) Du = 2. The current is normalized in each panel by the value of ionic current obtained for the smallest element size. For the simulations in Figs. 6.11-6.12 I took (maximum mesh size)$^{-1}$ = 3000.

Conclusions

Two are the classes of systems that this thesis aims at studying: active systems and electrolytes under confinement. For each of them, I started off in the introduction by posing a question on the relationship between the non-trivial transport properties that the system exhibits and its multiscale nature. The objective of the thesis was precisely to unveil such connection, using the tools of Statistical Physics.
The quest is both practical and fundamental in nature, as it involves the investigation of the transport coefficients of the two systems starting from minimal phenomenological models.
In the case of Active Matter the essential feature to deal with is the capability of each constituent to *self-propel*, i.e. to convert local energy into directed motion. By doing so, the system intrinsically breaks Detailed Balance (DB) and naturally evolves out-of-equilibrium. This is precisely the major challenge to be tackled when it comes to study the transport properties of an active system as the Fluctuation-Dissipation Theorem (FDT) is here inevitably violated.
As for electrolytes under confinement, the main feature to address is the *large surface-to-volume ratio* typical of the nanoscale and the resulting strong interaction between the electrolyte solution and the solid interface. As a consequence, the standard features of electrolyte transport in bulk, well described by the phenomenological laws of Electrokinetics, here break down.
In both scenarios, the call is to step outside the standard formalism and build a theory (or more than one) able to capture the specificity of the response in the two classes of systems.
The present thesis takes steps in this direction and the main results herein collected can be summarized as follows:

- Development of a general formalism for the linear response of non-equilibrium systems exclusively based on the hypothesis of Markovianity. The formalism includes both even and odd variables with respect to Time-Reversal and, as such, applies generally to overdamped and underdamped dynamics. An explicit expression for the Time-Reversal operator, Eq. (2.25), was derived directly from the Fokker-Planck equation and further linked with the breakdown of Detailed Balance in presence of irreversible fluxes in Eq. (2.27). Making use of the notion of house-keeping entropy production which quantifies the irreversibility in a non-equilibrium steady state, general constraints to be fulfilled by any non-equilibrium probability distribution were derived in

Eq. (2.41) and promptly used into a generalized Fluctuation-Dissipation Relation in Eq. (2.45).

- Derivation of Fluctuation-Dissipation Relations for two reference models of active systems, respectively Active Brownian Particle (ABP) and Active Ornstein Uhlenbeck Particle (AOUP). Particular emphasis was directed to the role of interparticle interactions and self-propulsion. The validity of the FDT in the dilute regime as well as its breakdown in presence of interparticle interactions were discussed in both models, highlighting the fundamental differences and similarities between the two. Closed Green-Kubo expressions, respectively Eq. (3.29) and Eq. (3.51) for ABP and AOUP, were derived making use of two different theoretical techniques: a Markovian approximation that restores Detailed Balance and a Chapman-Enskog expansion which explicitly breaks it.

- Identification of the Dukhin length as the primarily electrokinetic length governing the phenomena of channel selectivity and ionic current rectification (ICR) in a geometric nanofluidic diode. The non-linear response in a nanofluidic diode was characterized via numerical and analytical methods starting from an effective theoretical model embedding both electrostatic and entropic interactions. Analytical expressions for the potential profile Eq. (5.18), the ionic current Eq. (5.11) and the limiting conductances Eqs. (5.31a-5.31b) in the case of strong Debye overlap were obtained.

- Extensive investigation via FEM simulations and a semi-analytical scaling theory of the role of the Dukhin length in a model of scanning ionic conductance microscopy (SICM). It was shown than the sensitivity of the microscopy technique considerably improves with high Dukhin lengths opening to the detection of isolated charge features of order of $\sim$ nm. In this context, the Dukhin length turned out to behave as a physical length setting the effective size of the charge feature. The analytical scaling for the ionic conductance in Eq. (6.17) was derived from an effective electrostatic model and shows very good agreement with the results obtained from numerical simulations.

Finally, it is now time to delineate possible future directions of research; some of practical implications potential, some other of more speculative character. A natural continuation of Chapter 3 is the study of more complex transport coefficients such as the shear viscosity of an active suspensions subjected to a velocity gradient. This would help shedding light on the rheological properties of active fluids, as recently investigated in bacterial baths [5, 6]. In this context an important role is played by non-isotropic interactions, such as velocity-alignment interactions or torque-like terms known to lead to a flocking transition [210]. Another interesting direction to explore is the adaptation of the Chapman-Enskog approach to the ABP model in order to derive a genuine, although approximated, out-of-equilibrium steady state distribution for the latter model. Such a probability distribution would explicitly break Detailed Balance potentially capturing more of the phenomenology of ABP as compared to DB-restoring approaches discussed in the thesis. At the same time, the Chapman-Enskog method relies on a formal expansion in the persistence time τ and,

as such, is bound to small τ values failing to reproduce high-activity (persistence) behaviour. Recent studies [83,211] precisely points at the crucial role played by the parameter τ in quantifying the departure from equilibrium. All in all, a framework to characterise transport properties beyond small-τ expansions is desirable and yet to be developed.

Finally, the theoretical treatments presented in Part II of the thesis calls for an experimental validation. In particular, the identification of the Dukhin length as the primary parameter controlling ICR suggests a potential upscaling in the technology of energy conversion and reverse osmosis by exploitation of micrometer-sized channels [212]. At the same time, the fundamentally new mechanism proposed to exploit high Dukhin numbers for charge detection in SICM will have to be verified in nanotube-based experimental setups. This is an immediate goal from the present work as the preliminary results here reported suggest a potential improvement of the spatial resolution of the current technique.

Publications

- S.D.C, Demian Levis, Ignacio Pagonabarraga, "Linear Response Theory and Green-Kubo Relations for Active Matter", *Physical Review Letters*, vol. 123, no. 23, p. 238003, 2019.
- S.D.C., Ignacio Pagonabarraga, "Confinement-controlled rectification in a geometric nanofluidic diode", *The Journal of Chemical Physics*, vol. 151, no. 4, p. 0044707, 2019.
- S.D.C., Demian Levis, Ignacio Pagonabarraga, " Fluctuaiton-Dissipation Relations in the absence of Detailed Balance: formalism and applications to Active Matter", *submitted*.
- S.D.C, Anthony R. Poggioli, Lyderic Bocquet, *In preparation*.

Bibliography

[1] R. Di Leonardo, L. Angelani, D. Dell'Arciprete, G. Ruocco, V. Iebba, S. Schippa, M. Conte, F. Mecarini, F. De Angelis, and E. Di Fabrizio, "Bacterial ratchet motors," *Proceedings of the National Academy of Sciences*, vol. 107, no. 21, pp. 9541–9545, 2010. (Cited on pages 3 and 8.)

[2] A. Sokolov, M. M. Apodaca, B. A. Grzybowski, and I. S. Aranson, "Swimming bacteria power microscopic gears," *Proceedings of the National Academy of Sciences*, vol. 107, no. 3, pp. 969–974, 2010. (Cited on pages 3 and 8.)

[3] J. Palacci, S. Sacanna, A. P. Steinberg, D. J. Pine, and P. M. Chaikin, "Living crystals of light-activated colloidal surfers," *Science*, vol. 339, no. 6122, pp. 936–940, 2013. (Cited on pages 3 and 8.)

[4] I. Theurkauff, C. Cottin-Bizonne, J. Palacci, C. Ybert, and L. Bocquet, "Dynamic clustering in active colloidal suspensions with chemical signaling," *Physical Review Letters*, vol. 108, p. 268303, 2012. (Cited on pages 3 and 8.)

[5] H. M. López, J. Gachelin, C. Douarche, H. Auradou, and E. Clément, "Turning bacteria suspensions into superfluids," *Physical Review Letters*, vol. 115, no. 2, p. 028301, 2015. (Cited on pages 3, 8, and 128.)

[6] S. Rafaï, L. Jibuti, and P. Peyla, "Effective viscosity of microswimmer suspensions," *Physical Review Letters*, vol. 104, no. 9, p. 098102, 2010. (Cited on pages 3, 8, and 128.)

[7] L.-J. Cheng and L. J. Guo, "Nanofluidic diodes," *Chemical Society Reviews*, vol. 39, pp. 923–938, 2010. (Cited on pages 4, 8, and 81.)

[8] L. Jubin, A. R. Poggioli, A. Siria, and L. Bocquet, "Dramatic pressure-sensitive ion conduction in conical nanopores," *Proceedings of the National Academy of Sciences*, vol. 115, no. 16, pp. 4063–4068, 2018. (Cited on pages 4, 8, 81, 82, and 119.)

[9] E. Secchi, S. Marbach, A. Niguès, D. Stein, A. Siria, and L. Bocquet, "Massive radius-dependent flow slippage in carbon nanotubes," *Nature*, vol. 537, no. 7619, pp. 210–213, 2016. (Cited on pages 4, 8, and 120.)

[10] R. H. Tunuguntla, R. Y. Henley, Y.-C. Yao, T. Anh Pham, M. Wanunu, and A. Noy, "Enhanced water permeability and tunable ion selectivity in sub nanometer carbon nanotube porins," *Science*, vol. 357, no. 6353, pp. 792–796, 2017. (Cited on pages 4 and 8.)

[11] H. Sui, B.-G. Han, J. K. Lee, P. Walian, and B. K. Jap, "Structural basis of water-specific transport through the aqp1 water channel," *Nature*, vol. 414, no. 6866, pp. 872–878, 2001. (Cited on pages 4, 8, and 81.)

[12] L. Cantley, J. L. Swett, D. Lloyd, D. A. Cullen, K. Zhou, P. V. Bedworth, S. Heise, A. J. Rondinone, Z. Xu, S. Sinton, and J. S. Bunch, "Voltage gated inter-cation selective ion channels from graphene nanopores," *Nanoscale*, vol. 11, pp. 9856–9861, 2019. (Cited on pages 4 and 8.)

[13] A. Einstein, *Investigations on the Theory of the Brownian Movement*. Dover Books on Physics Series, Dover Publications, 1956. (Cited on page 13.)

[14] D. S. Lemons and A. Gythiel, "Paul langevin's 1908 paper "on the theory of brownian motion" ["sur la théorie du mouvement brownien," c. r. acad. sci. (paris) 146, 530–533 (1908)]," *American Journal of Physics*, vol. 65, no. 11, pp. 1079–1081, 1997. (Cited on page 13.)

[15] R. Zwanzig, *Nonequilibrium Statistical Mechanics*. Oxford University Press, 2001. (Cited on pages 13 and 36.)

[16] R. Levins and R. Lewontin, *The Dialectical Biologist*. Harvard University Press, 1985. (Cited on page 13.)

[17] N. G. van Kampen, "Langevin-like equation with colored noise," *Journal of Statistical Physics*, vol. 54, no. 5, pp. 1289–1308, 1989. (Cited on page 14.)

[18] P. Hänggi and P. Jung, "Colored noise in dynamical systems," *Advances in Chemical Physics*, vol. 89, pp. 239–326, 1994. (Cited on pages 14, 32, 35, 36, and 47.)

[19] H. Qian, "Vector field formalism and analysis for a class of thermal ratchets," *Physical Review Letters*, vol. 81, pp. 3063–3066, 1998. (Cited on page 16.)

[20] H. Qian, M. Qian, and X. Tang, "Thermodynamics of the general diffusion process: Time-reversibility and entropy production," *Journal of Statistical Physics*, vol. 107, no. 5, pp. 1129–1141, 2002. (Cited on page 16.)

[21] J. Wang, L. Xu, and E. Wang, "Potential landscape and flux framework of nonequilibrium networks: Robustness, dissipation, and coherence of biochemical oscillations," *Proceedings of the National Academy of Sciences*, vol. 105, no. 34, pp. 12271–12276, 2008. (Cited on page 16.)

[22] D. J. Evans and G. P. Morriss, *Statistical Mechanics of Nonequilibrium Liquids*. Cambridge University Press, 2008. (Cited on page 17.)

[23] R. Kubo, M. Toda, and N. Hashitsume, *Statistical physics II: nonequilibrium statistical mechanics*, vol. 31. Springer Science & Business Media, 1991. (Cited on page 19.)

[24] W. Brown, *Dynamic light scattering: the method and some applications*, vol. 313. Clarendon Press Oxford, 1993. (Cited on page 19.)

[25] L. Cipelletti and L. Ramos, "Slow dynamics in glassy soft matter," *Journal of Physics: Condensed Matter*, vol. 17, no. 6, pp. 253–285, 2005. (Cited on page 19.)

[26] R. Kubo, "Statistical-mechanical theory of irreversible processes. i. general theory and simple applications to magnetic and conduction problems," *Journal of the Physical Society of Japan*, vol. 12, no. 6, pp. 570–586, 1957. (Cited on page 19.)

[27] R. Kubo, "The fluctuation-dissipation theorem," *Reports on progress in physics*, vol. 29, no. 1, p. 255, 1966. (Cited on page 19.)

[28] P. Hänggi and H. Thomas, "Stochastic processes: Time evolution, symmetries and linear response," *Physics Reports*, vol. 88, no. 4, pp. 207–319, 1982. (Cited on page 19.)

[29] H. Risken, "Fokker-planck equation," in *The Fokker-Planck Equation*, pp. 63–95, Springer, 1996. (Cited on page 20.)

[30] R. Graham and H. Haken, "Generalized thermodynamic potential for markoff systems in detailed balance and far from thermal equilibrium," *Zeitschrift für Physik A Hadrons and nuclei*, vol. 243, no. 3, pp. 289–302, 1971. (Cited on page 20.)

[31] G. Agarwal, "Fluctuation-dissipation theorems for systems in non-thermal equilibrium and applications," *Zeitschrift für Physik A Hadrons and nuclei*, vol. 252, no. 1, pp. 25–38, 1972. (Cited on pages 20 and 23.)

[32] H. Haken, "Exact stationary solution of a fokker-planck equation for multimode laser action including phase locking," *Zeitschrift für Physik A Hadrons and nuclei*, vol. 219, no. 3, pp. 246–268, 1969. (Cited on page 20.)

[33] T. Harada and S.-i. Sasa, "Equality connecting energy dissipation with a violation of the fluctuation-response relation," *Physical Review Letters*, vol. 95, p. 130602, 2005. (Cited on page 20.)

[34] T. Speck and U. Seifert, "Restoring a fluctuation-dissipation theorem in a nonequilibrium steady state," *EPL (Europhysics Letters)*, vol. 74, no. 3, p. 391, 2006. (Cited on pages 20, 28, and 29.)

[35] J. Prost, J.-F. Joanny, and J. Parrondo, "Generalized fluctuation-dissipation theorem for steady-state systems," *Physical Review Letters*, vol. 103, no. 9, p. 090601, 2009. (Cited on page 20.)

[36] M. Baiesi, C. Maes, and B. Wynants, "Fluctuations and response of nonequilibrium states," *Physical Review Letters*, vol. 103, no. 1, p. 010602, 2009. (Cited on page 20.)

[37] R. Chetrite and K. Gawędzki, "Eulerian and lagrangian pictures of nonequilibrium diffusions," *Journal of Statistical Physics*, vol. 137, no. 5, p. 890, 2009. (Cited on page 20.)

[38] U. Seifert and T. Speck, "Fluctuation-dissipation theorem in nonequilibrium steady states," *EPL (Europhysics Letters)*, vol. 89, no. 1, p. 10007, 2010. (Cited on page 20.)

[39] J. Kurchan, "Fluctuation theorem for stochastic dynamics," *Journal of Physics A: Mathematical and General*, vol. 31, no. 16, pp. 3719–3729, 1998. (Cited on page 20.)

[40] U. M. B. Marconi, A. Puglisi, L. Rondoni, and A. Vulpiani, "Fluctuation–dissipation: response theory in statistical physics," *Physics reports*, vol. 461, no. 4-6, pp. 111–195, 2008. (Cited on page 20.)

[41] M. Baiesi and C. Maes, "An update on the nonequilibrium linear response," *New Journal of Physics*, vol. 15, no. 1, p. 013004, 2013. (Cited on pages 20, 25, and 28.)

[42] A. Sarracino and A. Vulpiani, "On the fluctuation-dissipation relation in non-equilibrium and non-hamiltonian systems," *Chaos: An Interdisciplinary Journal of Nonlinear Science*, vol. 29, no. 8, p. 083132, 2019. (Cited on page 20.)

[43] C. Gardiner, *Stochastic methods*. Springer Berlin, 2009. (Cited on pages 21, 61, and 64.)

[44] J. Tailleur, S. Tănase-Nicola, and J. Kurchan, "Kramers equation and supersymmetry," *Journal of Statistical Physics*, vol. 122, no. 4, pp. 557–595, 2006. (Cited on page 21.)

[45] J. Kurchan, "Six out of equilibrium lectures," *arXiv preprint arXiv:0901.1271*, 2009. (Cited on page 21.)

[46] M. Polettini, "Of dice and men. subjective priors, gauge invariance, and nonequilibrium thermodynamics," *arXiv preprint arXiv:1307.2057*, 2013. (Cited on page 21.)

[47] M. Fuchs and M. E. Cates, "Integration through transients for brownian particles under steady shear," *Journal of Physics: Condensed Matter*, vol. 17, no. 20, p. 1681, 2005. (Cited on page 22.)

[48] M. Falcioni, S. Isola, and A. Vulpiani, "Correlation functions and relaxation properties in chaotic dynamics and statistical mechanics," *Physics Letters A*, vol. 144, no. 6, pp. 341–346, 1990. (Cited on page 23.)

[49] L. F. Cugliandolo, J. Kurchan, and G. Parisi, "Off equilibrium dynamics and aging in unfrustrated systems," *Journal de Physique I*, vol. 4, no. 11, pp. 1641–1656, 1994. (Cited on page 23.)

[50] H. Ge, "Time reversibility and nonequilibrium thermodynamics of second-order stochastic processes," *Physical Review E*, vol. 89, p. 022127, 2014. (Cited on page 24.)

[51] M. Baiesi, E. Boksenbojm, C. Maes, and B. Wynants, "Nonequilibrium linear response for markov dynamics, ii: Inertial dynamics," *Journal of Statistical Physics*, vol. 139, pp. 492–505, 2010. (Cited on page 25.)

[52] N. Freitas, J.-C. Delvenne, and M. Esposito, "Stochastic and quantum thermodynamics of driven rlc networks," *Physical Review X*, vol. 10, p. 031005, 2020. (Cited on page 25.)

[53] H. Qian, "Mesoscopic nonequilibrium thermodynamics of single macromolecules and dynamic entropy-energy compensation," *Physical Review E*, vol. 65, p. 016102, 2001. (Cited on pages 26 and 63.)

[54] U. Seifert, "Entropy production along a stochastic trajectory and an integral fluctuation theorem," *Physical Review Letters*, vol. 95, p. 040602, 2005. (Cited on page 26.)

[55] H. Ge, "Extended forms of the second law for general time-dependent stochastic processes," *Physical Review E*, vol. 80, p. 021137, 2009. (Cited on page 26.)

[56] M. Esposito and C. Van den Broeck, "Three detailed fluctuation theorems," *Physical Review Letters*, vol. 104, p. 090601, 2010. (Cited on page 26.)

[57] C. Van den Broeck and M. Esposito, "Three faces of the second law. ii. fokker-planck formulation," *Physical Review E*, vol. 82, p. 011144, 2010. (Cited on page 26.)

[58] R. E. Spinney and I. J. Ford, "Entropy production in full phase space for continuous stochastic dynamics," *Physical Review E*, vol. 85, p. 051113, 2012. (Cited on page 26.)

[59] H. Feng and J. Wang, "Potential and flux decomposition for dynamical systems and non-equilibrium thermodynamics: Curvature, gauge field, and generalized fluctuation-dissipation theorem," *The Journal of Chemical Physics*, vol. 135, no. 23, p. 234511, 2011. (Cited on page 28.)

[60] P. Romanczuk, M. Bär, W. Ebeling, B. Lindner, and L. Schimansky-Geier, "Active brownian particles," *The European Physical Journal Special Topics*, vol. 202, no. 1, pp. 1–162, 2012. (Cited on page 31.)

[61] J. Elgeti and G. Gompper, "Wall accumulation of self-propelled spheres," *EPL (Europhysics Letters)*, vol. 101, no. 4, p. 48003, 2013. (Cited on page 31.)

[62] G. Szamel, "Self-propelled particle in an external potential: Existence of an effective temperature," *Physical Review E*, vol. 90, no. 1, p. 012111, 2014. (Cited on pages 31, 32, and 44.)

[63] S. C. Takatori, W. Yan, and J. F. Brady, "Swim pressure: stress generation in active matter," *Physical Review Letters*, vol. 113, no. 2, p. 028103, 2014. (Cited on pages 31 and 35.)

[64] F. Ginot, I. Theurkauff, D. Levis, C. Ybert, L. Bocquet, L. Berthier, and C. Cottin-Bizonne, "Nonequilibrium equation of state in suspensions of active colloids," *Physical Review X*, vol. 5, no. 1, p. 011004, 2015. (Cited on pages 31, 32, 35, and 38.)

[65] É. Fodor and M. C. Marchetti, "The statistical physics of active matter: From self-catalytic colloids to living cells," *Physica A: Statistical Mechanics and its Applications*, vol. 504, pp. 106–120, 2018. (Cited on page 31.)

[66] Y. Fily and M. C. Marchetti, "Athermal phase separation of self-propelled particles with no alignment," *Physical Review Letters*, vol. 108, no. 23, p. 235702, 2012. (Cited on page 31.)

[67] G. S. Redner, M. F. Hagan, and A. Baskaran, "Structure and dynamics of a phase-separating active colloidal fluid," *Physical Review Letters*, vol. 110, no. 5, p. 055701, 2013. (Cited on page 31.)

[68] J. Bialké, H. Löwen, and T. Speck, "Microscopic theory for the phase separation of self-propelled repulsive disks," *EPL (Europhysics Letters)*, vol. 103, no. 3, p. 30008, 2013. (Cited on page 31.)

[69] A. Wysocki, R. G. Winkler, and G. Gompper, "Cooperative motion of active brownian spheres in three-dimensional dense suspensions," *EPL (Europhysics Letters)*, vol. 105, no. 4, p. 48004, 2014. (Cited on page 31.)

[70] J. Stenhammar, D. Marenduzzo, R. J. Allen, and M. E. Cates, "Phase behaviour of active brownian particles: the role of dimensionality," *Soft Matter*, vol. 10, pp. 1489–1499, 2014. (Cited on page 31.)

[71] G. Briand and O. Dauchot, "Crystallization of self-propelled hard discs," *Physical Review Letters*, vol. 117, p. 098004, 2016. (Cited on page 31.)

[72] A. Wysocki and H. Rieger, "Capillary action in scalar active matter," *Physical Review Letters*, vol. 124, p. 048001, 2020. (Cited on page 31.)

[73] L. Berthier, E. Flenner, and G. Szamel, "Glassy dynamics in dense systems of active particles," *The Journal of Chemical Physics*, vol. 150, no. 20, p. 200901, 2019. (Cited on page 31.)

[74] P. Digregorio, D. Levis, A. Suma, L. F. Cugliandolo, G. Gonnella, and I. Pagonabarraga, "Full phase diagram of active brownian disks: from melting to motility-induced phase separation," *Physical Review Letters*, vol. 121, no. 9, p. 098003, 2018. (Cited on page 31.)

[75] M. E. Cates and J. Tailleur, "Motility-induced phase separation," *Annual Review of Condensed Matter Physics*, vol. 6, no. 1, pp. 219–244, 2015. (Cited on page 31.)

[76] M. E. Cates and J. Tailleur, "When are active brownian particles and run-and-tumble particles equivalent? consequences for motility-induced phase separation," *EPL (Europhysics Letters)*, vol. 101, no. 2, p. 20010, 2013. (Cited on page 31.)

[77] T. Speck, J. Bialké, A. M. Menzel, and H. Löwen, "Effective cahn-hilliard equation for the phase separation of active brownian particles," *Physical Review Letters*, vol. 112, p. 218304, 2014. (Cited on page 31.)

[78] A. P. Solon, J. Stenhammar, R. Wittkowski, M. Kardar, Y. Kafri, M. E. Cates, and J. Tailleur, "Pressure and phase equilibria in interacting active brownian spheres," *Physical Review Letters*, vol. 114, no. 19, p. 198301, 2015. (Cited on page 31.)

[79] D. Levis, J. Codina, and I. Pagonabarraga, "Active brownian equation of state: metastability and phase coexistence," *Soft Matter*, vol. 13, pp. 8113–8119, 2017. (Cited on pages 31 and 35.)

[80] D. Levis and L. Berthier, "From single-particle to collective effective temperatures in an active fluid of self-propelled particles," *EPL (Europhysics Letters)*, vol. 111, no. 6, p. 60006, 2015. (Cited on pages 32 and 39.)

[81] A. P. Solon, Y. Fily, A. Baskaran, M. E. Cates, K. M. Kafri, Y., and J. Tailleur, "Pressure is not a state function for generic active fluids," *Nature Physics*, vol. 11, no. 8, pp. 673–678, 2015. (Cited on page 32.)

[82] L. F. Cugliandolo, G. Gonnella, and I. Petrelli, "Effective temperature in active brownian particles," *Fluctuation and Noise Letters*, vol. 18, no. 02, p. 1940008, 2019. (Cited on pages 32 and 39.)

[83] E. Flenner and G. Szamel, "Active matter: quantifying the departure from equilibrium," *arXiv preprint arXiv:2004.11925*, 2020. (Cited on pages 32 and 129.)

[84] U. M. B. Marconi and C. Maggi, "Towards a statistical mechanical theory of active fluids," *Soft matter*, vol. 11, no. 45, pp. 8768–8781, 2015. (Cited on pages 32, 35, 37, 47, and 50.)

[85] T. F. Farage, P. Krinninger, and J. M. Brader, "Effective interactions in active brownian suspensions," *Physical Review E*, vol. 91, no. 4, p. 042310, 2015. (Cited on pages 32, 36, 37, and 47.)

[86] M. Rein and T. Speck, "Applicability of effective pair potentials for active brownian particles," *The European Physical Journal E*, vol. 39, no. 9, p. 84, 2016. (Cited on pages 32, 36, 37, and 48.)

[87] R. Wittmann and J. M. Brader, "Active brownian particles at interfaces: An effective equilibrium approach," *EPL (Europhysics Letters)*, vol. 114, no. 6, p. 68004, 2016. (Cited on pages 32 and 37.)

[88] R. Wittmann, C. Maggi, A. Sharma, A. Scacchi, J. M. Brader, and U. M. B. Marconi, "Effective equilibrium states in the colored-noise model for active matter i. pairwise forces in the fox and unified colored noise approximations," *Journal of Statistical Mechanics: Theory and Experiment*, p. 113207, 2017. (Cited on pages 32, 35, 36, 37, 47, and 48.)

[89] A. Sharma and J. M. Brader, "Communication: Green-kubo approach to the average swim speed in active brownian systems," *The Journal of Chemical Physics*, vol. 145, no. 16, p. 161101, 2016. (Cited on page 32.)

[90] A. Liluashvili, J. Ónody, and T. Voigtmann, "Mode-coupling theory for active brownian particles," *Physical Review E*, vol. 96, no. 6, p. 062608, 2017. (Cited on page 32.)

[91] É. Fodor, C. Nardini, M. E. Cates, J. Tailleur, P. Visco, and F. van Wijland, "How far from equilibrium is active matter?," *Physical Review Letters*, vol. 117, no. 3, p. 038103, 2016. (Cited on pages 32, 41, and 43.)

[92] L. Caprini, U. M. B. Marconi, and A. Vulpiani, "Linear response and correlation of a self-propelled particle in the presence of external fields," *Journal of Statistical Mechanics: Theory and Experiment*, vol. 2018, no. 3, p. 033203, 2018. (Cited on page 32.)

[93] K. Asheichyk, A. P. Solon, C. M. Rohwer, and M. Krüger, "Response of active brownian particles to shear flow," *The Journal of Chemical Physics*, vol. 150, no. 14, p. 144111, 2019. (Cited on page 32.)

[94] P. B. Warren and R. J. Allen, "Malliavin weight sampling for computing sensitivity coefficients in brownian dynamics simulations," *Physical Review Letters*, vol. 109, no. 25, p. 250601, 2012. (Cited on pages 32, 39, and 52.)

[95] L. F. Cugliandolo, "The effective temperature," *Journal of Physics A: Mathematical and Theoretical*, vol. 44, no. 48, p. 483001, 2011. (Cited on page 32.)

[96] D. Loi, S. Mossa, and L. F. Cugliandolo, "Effective temperature of active matter," *Physical Review E*, vol. 77, no. 5, p. 051111, 2008. (Cited on page 32.)

[97] E. Ben-Isaac, Y. Park, G. Popescu, F. L. Brown, N. S. Gov, and Y. Shokef, "Effective temperature of red-blood-cell membrane fluctuations," *Physical Review Letters*, vol. 106, no. 23, p. 238103, 2011. (Cited on page 32.)

[98] S. Eldeen, R. Muoio, P. Blaisdell-Pijuan, N. La, M. Gomez, A. Vidal, and W. Ahmed, "Quantifying the non-equilibrium activity of an active colloid," *Soft Matter*, pp. –, 2020. (Cited on page 32.)

[99] S. Mandal, B. Liebchen, and H. Löwen, "Motility-induced temperature difference in coexisting phases," *Physical Review Letters*, vol. 123, no. 22, p. 228001, 2019. (Cited on page 32.)

[100] I. Petrelli, L. F. Cugliandolo, G. Gonnella, and A. Suma, "Effective temperatures in inhomogeneous passive and active bidimensional brownian particle systems," *Physical Review E*, vol. 102, p. 012609, 2020. (Cited on page 32.)

[101] A. P. Solon, M. Cates, and J. Tailleur, "Active brownian particles and run-and-tumble particles: A comparative study," *The European Physical Journal Special Topics*, vol. 224, no. 7, pp. 1231–1262, 2015. (Cited on page 34.)

[102] R. F. Fox, "Uniform convergence to an effective fokker-planck equation for weakly colored noise," *Physical Review A*, vol. 34, no. 5, p. 4525, 1986. (Cited on pages 35, 36, and 47.)

[103] R. F. Fox, "Functional-calculus approach to stochastic differential equations," *Physical Review A*, vol. 33, no. 1, p. 467, 1986. (Cited on pages 35, 36, 45, and 47.)

[104] A. Ghosh, J. Samuel, and S. Sinha, "A "gaussian" for diffusion on the sphere," *EPL (Europhysics Letters)*, vol. 98, no. 3, p. 30003, 2012. (Cited on page 35.)

[105] S. Adelman, "Fokker–planck equations for simple non-markovian systems," *The Journal of Chemical Physics*, vol. 64, no. 1, pp. 124–130, 1976. (Cited on page 36.)

[106] M. San Miguel and J. Sancho, "A colored-noise approach to brownian motion in position space. corrections to the smoluchowski equation," *Journal of Statistical Physics*, vol. 22, no. 5, pp. 605–624, 1980. (Cited on page 36.)

[107] S. Hanna, W. Hess, and R. Klein, "The velocity autocorrelation function of an overdamped brownian system with hard-core interactions," *Journal of Physics A: Mathematical and General*, vol. 14, no. 12, p. L493, 1981. (Cited on pages 38, 50, and 51.)

[108] C. Chatelain, "A far-from-equilibrium fluctuation–dissipation relation for an ising–glauber-like model," *Journal of Physics A: Mathematical and General*, vol. 36, no. 43, p. 10739, 2003. (Cited on page 39.)

[109] P. Warren and R. Allen, "Malliavin weight sampling: a practical guide," *Entropy*, vol. 16, no. 1, pp. 221–232, 2014. (Cited on page 39.)

[110] G. Szamel, "Evaluating linear response in active systems with no perturbing field," *EPL (Europhysics Letters)*, vol. 117, no. 5, p. 50010, 2017. (Cited on page 39.)

[111] L. Bonilla, "Active ornstein-uhlenbeck particles," *Physical Review E*, vol. 100, no. 2, p. 022601, 2019. (Cited on pages 41, 42, 43, and 45.)

[112] H. Grad, *Principles of the Kinetic Theory of Gases*, pp. 205–294. Berlin, Heidelberg: Springer Berlin Heidelberg, 1958. (Cited on page 42.)

[113] R. Soto, *Kinetic Theory and Transport Phenomena*. Oxford Master Series in Physics, Oxford University Press, 2016. (Cited on page 42.)

[114] P. Jung and P. Hänggi, "Dynamical systems: A unified colored-noise approximation," *Physical Review A*, vol. 35, pp. 4464–4466, 1987. (Cited on page 47.)

[115] S. de Groot and P. Mazur, *Non-equilibrium Thermodynamics*. Dover Books on Physics, Dover Publications, 1984. (Cited on page 60.)

[116] Y. Oono and M. Paniconi, "Steady State Thermodynamics," *Progress of Theoretical Physics Supplement*, vol. 130, pp. 29–44, 1998. (Cited on page 60.)

[117] J. W. Gibbs, *Elementary Principles in Statistical Mechanics: Developed with Especial Reference to the Rational Foundation of Thermodynamics*. Cambridge Library Collection - Mathematics, Cambridge University Press, 2010. (Cited on page 61.)

[118] H. Ge and H. Qian, "Physical origins of entropy production, free energy dissipation, and their mathematical representations," *Physical Review E*, vol. 81, p. 051133, 2010. (Cited on page 61.)

[119] K. Sekimoto, "Langevin Equation and Thermodynamics," *Progress of Theoretical Physics Supplement*, vol. 130, pp. 17–27, 1998. (Cited on page 61.)

[120] T. Hatano and S.-i. Sasa, "Steady-state thermodynamics of langevin systems," *Physical Review Letters*, vol. 86, pp. 3463–3466, 2001. (Cited on page 62.)

[121] D. Andelman, "Chapter 12 - electrostatic properties of membranes: The poisson-boltzmann theory," in *Structure and Dynamics of Membranes* (R. Lipowsky and E. Sackmann, eds.), vol. 1 of *Handbook of Biological Physics*, pp. 603 – 642, North-Holland, 1995. (Cited on pages 69, 73, 74, 75, and 103.)

[122] J. Israelachvili, *Intermolecular and Surface Forces*. Intermolecular and Surface Forces, Elsevier Science, 2015. (Cited on pages 69 and 72.)

[123] J.-L. Barrat and J.-P. Hansen, *Basic Concepts for Simple and Complex Liquids*. Cambridge University Press, 2003. (Cited on page 71.)

[124] L. Bocquet and E. Charlaix, "Nanofluidics, from bulk to interfaces," *Chemical Society Reviews*, vol. 39, pp. 1073–1095, 2010. (Cited on pages 73, 81, 82, 98, 101, and 102.)

[125] R. B. Schoch, J. Han, and P. Renaud, "Transport phenomena in nanofluidics," *Reviews of Modern Physics*, vol. 80, pp. 839–883, 2008. (Cited on pages 78, 86, and 88.)

[126] I. Vlassiouk, S. Smirnov, and Z. Siwy, "Nanofluidic ionic diodes. comparison of analytical and numerical solutions," *ACS Nano*, vol. 2, no. 8, pp. 1589–1602, 2008. (Cited on page 78.)

[127] Y. Ai, M. Zhang, S. W. Joo, M. A. Cheney, and S. Qian, "Effects of electroosmotic flow on ionic current rectification in conical nanopores," *The Journal of Physical Chemistry C*, vol. 114, no. 9, pp. 3883–3890, 2010. (Cited on pages 78 and 82.)

[128] C. Lee, L. Joly, A. Siria, A.-L. Biance, R. Fulcrand, and L. Bocquet, "Large apparent electric size of solid-state nanopores due to spatially extended surface conduction," *Nano Letters*, vol. 12, no. 8, pp. 4037–4044, 2012. PMID: 22746297. (Cited on pages 78, 102, 108, and 110.)

[129] Z. Siwy and A. Fuliński, "Fabrication of a synthetic nanopore ion pump," *Physical Review Letters*, vol. 89, p. 198103, 2002. (Cited on page 81.)

[130] Z. Siwy, I. D. Kosińska, A. Fuliński, and C. R. Martin, "Asymmetric diffusion through synthetic nanopores," *Physical Review Letters*, vol. 94, p. 048102, 2005. (Cited on page 81.)

[131] S. Umehara, N. Pourmand, C. D. Webb, R. W. Davis, K. Yasuda, and M. Karhanek, "Current rectification with poly-l-lysine-coated quartz nanopipettes," *Nano Letters*, vol. 6, no. 11, pp. 2486–2492, 2006. PMID: 17090078. (Cited on page 81.)

[132] G. Nguyen, I. Vlassiouk, and Z. S. Siwy, "Comparison of bipolar and unipolar ionic diodes," *Nanotechnology*, vol. 21, no. 26, p. 265301, 2010. (Cited on page 81.)

[133] N. Laohakunakorn, V. V. Thacker, M. Muthukumar, and U. F. Keyser, "Electroosmotic flow reversal outside glass nanopores," *Nano Letters*, vol. 15, no. 1, pp. 695–702, 2015. PMID: 25490120. (Cited on pages 81 and 82.)

[134] J. M. Perry, K. Zhou, Z. D. Harms, and S. C. Jacobson, "Ion transport in nanofluidic funnels," *ACS Nano*, vol. 4, no. 7, pp. 3897–3902, 2010. PMID: 20590127. (Cited on pages 81 and 82.)

[135] L.-J. Cheng and L. J. Guo, "Rectified ion transport through concentration gradient in homogeneous silica nanochannels," *Nano Letters*, vol. 7, no. 10, pp. 3165–3171, 2007. PMID: 17894519. (Cited on page 81.)

[136] R. Karnik, C. Duan, K. Castelino, H. Daiguji, and A. Majumdar, "Rectification of ionic current in a nanofluidic diode," *Nano Letters*, vol. 7, no. 3, pp. 547–551, 2007. PMID: 17311461. (Cited on page 81.)

[137] C. C. Harrell, Y. Choi, L. P. Horne, L. A. Baker, Z. S. Siwy, and C. R. Martin, "Resistive-pulse dna detection with a conical nanopore sensor," *Langmuir*, vol. 22, no. 25, pp. 10837–10843, 2006. PMID: 17129068. (Cited on page 81.)

[138] R. Wei, V. Gatterdam, R. Wieneke, R. Tampé, and U. Rant, "Stochastic sensing of proteins with receptor-modified solid-state nanopores," *Nature Nanotechnology*, vol. 7, no. 4, pp. 257–263, 2012. (Cited on page 81.)

[139] Y. Xie, X. Wang, J. Xue, K. Jin, L. Chen, and Y. Wang, "Electric energy generation in single track-etched nanopores," *Applied Physics Letters*, vol. 93, no. 16, p. 163116, 2008. (Cited on page 81.)

[140] A. Siria, P. Poncharal, A.-L. Biance, R. Fulcrand, X. Blase, S. T. Purcell, and L. Bocquet, "Giant osmotic energy conversion measured in a single transmembrane boron nitride nanotube," *Nature*, vol. 494, no. 7438, pp. 455–458, 2013. (Cited on pages 81 and 101.)

[141] X. Wu, P. Ramiah Rajasekaran, and C. R. Martin, "An alternating current electroosmotic pump based on conical nanopore membranes," *ACS Nano*, vol. 10, no. 4, pp. 4637–4643, 2016. PMID: 27046145. (Cited on page 81.)

[142] Y. Zhang and G. C. Schatz, "Conical nanopores for efficient ion pumping and desalination," *The Journal of Physical Chemistry Letters*, vol. 8, no. 13, pp. 2842–2848, 2017. PMID: 28590134. (Cited on page 81.)

[143] C. B. Picallo, S. Gravelle, L. Joly, E. Charlaix, and L. Bocquet, "Nanofluidic osmotic diodes: Theory and molecular dynamics simulations," *Physical Review Letters*, vol. 111, p. 244501, 2013. (Cited on pages 81 and 88.)

[144] T. Tsong and T. Xie, "Ion pump as molecular ratchet and effects of noise: electric activation of cation pumping by na,k-atpase," *Applied Physics A*, vol. 75, no. 2, pp. 345–352, 2002. (Cited on page 81.)

[145] S. Bhattacharya, J. Muzard, L. Payet, J. Mathé, U. Bockelmann, A. Aksimentiev, and V. Viasnoff, "Rectification of the current in α-hemolysin pore depends on the cation type: The alkali series probed by molecular dynamics simulations and experiments," *The Journal of Physical Chemistry C*, vol. 115, no. 10, pp. 4255–4264, 2011. PMID: 21860669. (Cited on page 81.)

[146] P. Malgaretti, I. Pagonabarraga, and M. Rubi, "Entropic transport in confined media: a challenge for computational studies in biological and soft-matter systems," *Frontiers in Physics*, vol. 1, p. 21, 2013. (Cited on page 82.)

[147] Z. Siwy, "Ion-current rectification in nanopores and nanotubes with broken symmetry," *Advanced Functional Materials*, vol. 16, no. 6, pp. 735–746, 2006. (Cited on pages 82 and 94.)

[148] L.-J. Cheng and L. J. Guo, "Ionic current rectification, breakdown, and switching in heterogeneous oxide nanofluidic devices," *ACS Nano*, vol. 3, no. 3, pp. 575–584, 2009. (Cited on page 82.)

[149] X. He, K. Zhang, T. Li, Y. Jiang, P. Yu, and L. Mao, "Micrometer-scale ion current rectification at polyelectrolyte brush-modified micropipets," *Journal of the American Chemical Society*, vol. 139, no. 4, pp. 1396–1399, 2017. PMID: 28095691. (Cited on pages 82 and 98.)

[150] C.-Y. Lin, L.-H. Yeh, and Z. S. Siwy, "Voltage-induced modulation of ionic concentrations and ion current rectification in mesopores with highly charged

pore walls," *The Journal of Physical Chemistry Letters*, vol. 9, no. 2, pp. 393–398, 2018. PMID: 29303587. (Cited on pages 82 and 98.)

[151] D. m. c. Constantin and Z. S. Siwy, "Poisson-nernst-planck model of ion current rectification through a nanofluidic diode," *Physical Review E*, vol. 76, p. 041202, 2007. (Cited on pages 82 and 88.)

[152] C. Kubeil and A. Bund, "The role of nanopore geometry for the rectification of ionic currents," *The Journal of Physical Chemistry C*, vol. 115, no. 16, pp. 7866–7873, 2011. (Cited on page 82.)

[153] J. Wang, M. Zhang, J. Zhai, and L. Jiang, "Theoretical simulation of the ion current rectification (icr) in nano-pores based on the poisson–nernst–planck (pnp) model," *Physical Chemistry Chemical Physics*, vol. 16, pp. 23–32, 2014. (Cited on page 82.)

[154] D. Woermann, "Electrochemical transport properties of a cone-shaped nanopore: high and low electrical conductivity states depending on the sign of an applied electrical potential difference," *Physical Chemistry Chemical Physics*, vol. 5, pp. 1853–1858, 2003. (Cited on pages 82, 88, 94, 97, and 105.)

[155] S. Martens, G. Schmid, L. Schimansky-Geier, and P. Hänggi, "Entropic particle transport: Higher-order corrections to the fick-jacobs diffusion equation," *Physical Review E*, vol. 83, p. 051135, 2011. (Cited on pages 82 and 84.)

[156] X. Yang, C. Liu, Y. Li, F. Marchesoni, P. Hänggi, and H. P. Zhang, "Hydrodynamic and entropic effects on colloidal diffusion in corrugated channels," *Proceedings of the National Academy of Sciences*, vol. 114, no. 36, pp. 9564–9569, 2017. (Cited on page 82.)

[157] S. Marbach, D. S. Dean, and L. Bocquet, "Transport and dispersion across wiggling nanopores," *Nature Physics*, vol. 14, no. 11, pp. 1108–1113, 2018. (Cited on page 82.)

[158] M. Jacobs, *Diffusion Processes*. Springer Berlin Heidelberg, 1967. (Cited on page 82.)

[159] R. Zwanzig, "Diffusion past an entropy barrier," *The Journal of Physical Chemistry*, vol. 96, no. 10, pp. 3926–3930, 1992. (Cited on pages 82 and 84.)

[160] E. Secchi, A. Niguès, L. Jubin, A. Siria, and L. Bocquet, "Scaling behavior for ionic transport and its fluctuations in individual carbon nanotubes," *Physical Review Letters*, vol. 116, p. 154501, 2016. (Cited on pages 82, 107, and 120.)

[161] P. S. Burada, G. Schmid, D. Reguera, J. M. Rubí, and P. Hänggi, "Biased diffusion in confined media: Test of the fick-jacobs approximation and validity criteria," *Physical Review E*, vol. 75, p. 051111, 2007. (Cited on page 82.)

[162] A. M. Berezhkovskii, L. Dagdug, and S. M. Bezrukov, "Range of applicability of modified fick-jacobs equation in two dimensions," *The Journal of Chemical Physics*, vol. 143, no. 16, p. 164102, 2015. (Cited on pages 82 and 85.)

[163] D. Reguera, G. Schmid, P. S. Burada, J. M. Rubí, P. Reimann, and P. Hänggi, "Entropic transport: Kinetics, scaling, and control mechanisms," *Physical Review Letters*, vol. 96, p. 130603, 2006. (Cited on page 82.)

[164] P. Malgaretti, I. Pagonabarraga, and J. M. Rubi, "Entropic electrokinetics: Recirculation, particle separation, and negative mobility," *Physical Review Letters*, vol. 113, p. 128301, 2014. (Cited on page 82.)

[165] I. D. Kosińska, I. Goychuk, M. Kostur, G. Schmid, and P. Hänggi, "Rectification in synthetic conical nanopores: A one-dimensional poisson-nernst-planck model," *Physical Review E*, vol. 77, p. 031131, 2008. (Cited on pages 82 and 88.)

[166] A. M. Berezhkovskii, L. Dagdug, and S. M. Bezrukov, "First passage, looping, and direct transition in expanding and narrowing tubes: Effects of the entropy potential," *The Journal of Chemical Physics*, vol. 147, no. 13, p. 134104, 2017. (Cited on page 85.)

[167] A. D. MacGillivray, "Nernst-planck equations and the electroneutrality and donnan equilibrium assumptions," *The Journal of Chemical Physics*, vol. 48, no. 7, pp. 2903–2907, 1968. (Cited on page 87.)

[168] J. Cervera, B. Schiedt, R. Neumann, S. Mafé, and P. Ramírez, "Ionic conduction, rectification, and selectivity in single conical nanopores," *The Journal of Chemical Physics*, vol. 124, no. 10, p. 104706, 2006. (Cited on pages 88 and 94.)

[169] A. R. Poggioli, A. Siria, and L. Bocquet, "Beyond the tradeoff: Dynamic selectivity in ionic transport and current rectification," *The Journal of Physical Chemistry B*, vol. 123, no. 5, pp. 1171–1185, 2019. (Cited on pages 94, 102, and 119.)

[170] N. M. Goldenberg and B. E. Steinberg, "Surface charge: A key determinant of protein localization and function," *Cancer Research*, vol. 70, no. 4, pp. 1277–1280, 2010. (Cited on page 101.)

[171] S. McLaughlin and D. Murray, "Plasma membrane phosphoinositide organization by protein electrostatics," *Nature*, vol. 438, no. 7068, pp. 605–611, 2005. (Cited on page 101.)

[172] C. Hu and L. Dai, "Doping of carbon materials for metal-free electrocatalysis," *Advanced Materials*, vol. 31, no. 7, p. 1804672, 2019. (Cited on page 101.)

[173] Q. Sun, D. Wang, Y. Li, J. Zhang, S. Ye, J. Cui, L. Chen, Z. Wang, H.-J. Butt, D. Vollmer, and X. Deng, "Surface charge printing for programmed droplet transport," *Nature Materials*, vol. 18, no. 9, pp. 936–941, 2019. (Cited on page 101.)

[174] D. Klenerman, Y. E. Korchev, and S. J. Davis, "Imaging and characterisation of the surface of live cells," *Current Opinion in Chemical Biology*, vol. 15,

no. 5, pp. 696 – 703, 2011. Molecular Machines/Analytical Techniques. (Cited on pages 101 and 102.)

[175] S. J. Kim, Y.-A. Song, and J. Han, "Nanofluidic concentration devices for biomolecules utilizing ion concentration polarization: theory, fabrication, and applications," *Chemical Society Reviews*, vol. 39, pp. 912–922, 2010. (Cited on page 101.)

[176] R. M. Penner, "Chemical sensing with nanowires," *Annual Review of Analytical Chemistry*, vol. 5, no. 1, pp. 461–485, 2012. PMID: 22524224. (Cited on page 101.)

[177] Y. Takahashi, A. I. Shevchuk, P. Novak, Y. Zhang, N. Ebejer, J. V. Macpherson, P. R. Unwin, A. J. Pollard, D. Roy, C. A. Clifford, H. Shiku, T. Matsue, D. Klenerman, and Y. E. Korchev, "Multifunctional nanoprobes for nanoscale chemical imaging and localized chemical delivery at surfaces and interfaces," *Angewandte Chemie International Edition*, vol. 50, no. 41, pp. 9638–9642, 2011. (Cited on page 101.)

[178] E. Fröhlich, "The role of surface charge in cellular uptake and cytotoxicity of medical nanoparticles," *International Journal of Nanomedicine*, vol. 7, pp. 5577–5591, 2012. (Cited on page 101.)

[179] Y.-Y. Yuan, C.-Q. Mao, X.-J. Du, J.-Z. Du, F. Wang, and J. Wang, "Surface charge switchable nanoparticles based on zwitterionic polymer for enhanced drug delivery to tumor," *Advanced Materials*, vol. 24, no. 40, pp. 5476–5480, 2012. (Cited on page 101.)

[180] B. E. Logan and M. Elimelech, "Membrane-based processes for sustainable power generation using water," *Nature*, vol. 488, no. 7411, pp. 313–319, 2012. (Cited on page 101.)

[181] D. J. Rankin and D. M. Huang, "The effect of hydrodynamic slip on membrane-based salinity-gradient-driven energy harvesting," *Langmuir*, vol. 32, no. 14, pp. 3420–3432, 2016. PMID: 26991373. (Cited on page 101.)

[182] R. Sprycha, "Electrical double layer at alumina/electrolyte interface: I. surface charge and zeta potential," *Journal of Colloid and Interface Science*, vol. 127, no. 1, pp. 1 – 11, 1989. (Cited on page 101.)

[183] J. Liu, D. Wang, M. Kvetny, W. Brown, Y. Li, and G. Wang, "Noninvasive surface coverage determination of chemically modified conical nanopores that rectify ion transport," *Analytical chemistry*, vol. 84, no. 16, p. 6926—6929, 2012. (Cited on page 101.)

[184] J. Liu, M. Kvetny, J. Feng, D. Wang, B. Wu, W. Brown, and G. Wang, "Surface charge density determination of single conical nanopores based on normalized ion current rectification," *Langmuir*, vol. 28, no. 2, pp. 1588–1595, 2012. PMID: 22182684. (Cited on page 101.)

[185] C.-C. Chen, Y. Zhou, and L. A. Baker, "Scanning ion conductance microscopy," *Annual Review of Analytical Chemistry*, vol. 5, no. 1, pp. 207–228, 2012. PMID: 22524219. (Cited on page 101.)

[186] P. Hansma, B. Drake, O. Marti, S. Gould, and C. Prater, "The scanning ion-conductance microscope," *Science*, vol. 243, no. 4891, pp. 641–643, 1989. (Cited on pages 101 and 102.)

[187] H. Nitz, J. Kamp, and H. Fuchs, "A combined scanning ion-conductance and shear-force microscope," *Probe Microscopy*, vol. 1, pp. 187–200, 1998. (Cited on pages 101, 107, and 108.)

[188] Y. Korchev, C. Bashford, M. Milovanovic, I. Vodyanoy, and M. Lab, "Scanning ion conductance microscopy of living cells," *Biophysical Journal*, vol. 73, no. 2, pp. 653 – 658, 1997. (Cited on pages 101 and 102.)

[189] J. Seifert, J. Rheinlaender, P. Novak, Y. E. Korchev, and T. E. Schäffer, "Comparison of atomic force microscopy and scanning ion conductance microscopy for live cell imaging," *Langmuir*, vol. 31, no. 24, pp. 6807–6813, 2015. (Cited on page 102.)

[190] P. Novak, J. Gorelik, U. Vivekananda, A. I. Shevchuk, Y. S. Ermolyuk, R. J. Bailey, A. J. Bushby, G. W. J. Moss, D. A. Rusakov, D. Klenerman, D. M. Kullmann, K. E. Volynski, and Y. E. Korchev, "Nanoscale-targeted patch-clamp recordings of functional presynaptic ion channels," *Neuron*, vol. 79, no. 6, pp. 1067–1077, 2013. (Cited on page 102.)

[191] D. Momotenko, K. McKelvey, M. Kang, G. N. Meloni, and P. R. Unwin, "Simultaneous interfacial reactivity and topography mapping with scanning ion conductance microscopy," *Analytical Chemistry*, vol. 88, no. 5, pp. 2838–2846, 2016. (Cited on page 102.)

[192] A. I. Shevchuk, G. I. Frolenkov, D. Sánchez, P. S. James, N. Freedman, M. J. Lab, R. Jones, D. Klenerman, and Y. E. Korchev, "Imaging proteins in membranes of living cells by high-resolution scanning ion conductance microscopy," *Angewandte Chemie International Edition*, vol. 45, no. 14, pp. 2212–2216, 2006. (Cited on page 102.)

[193] P. Novak, C. Li, A. I. Shevchuk, R. Stepanyan, M. Caldwell, S. Hughes, T. G. Smart, J. Gorelik, V. P. Ostanin, M. J. Lab, G. W. J. Moss, G. I. Frolenkov, D. Klenerman, and Y. E. Korchev, "Nanoscale live-cell imaging using hopping probe ion conductance microscopy," *Nature Methods*, vol. 6, no. 4, pp. 279–281, 2009. (Cited on page 102.)

[194] S. Zhang, S.-J. Cho, K. Busuttil, C. Wang, F. Besenbacher, and M. Dong, "Scanning ion conductance microscopy studies of amyloid fibrils at nanoscale," *Nanoscale*, vol. 4, pp. 3105–3110, 2012. (Cited on page 102.)

[195] J. Gorelik, A. I. Shevchuk, G. I. Frolenkov, I. A. Diakonov, M. J. Lab, C. J. Kros, G. P. Richardson, I. Vodyanoy, C. R. W. Edwards, D. Klenerman, and Y. E. Korchev, "Dynamic assembly of surface structures in living cells," *Proceedings of the National Academy of Sciences*, vol. 100, no. 10, pp. 5819–5822, 2003. (Cited on page 102.)

[196] M. Böcker, S. Muschter, E. K. Schmitt, C. Steinem, and T. E. Schäffer, "Imaging and patterning of pore-suspending membranes with scanning ion conductance microscopy," *Langmuir*, vol. 25, no. 5, pp. 3022–3028, 2009. (Cited on page 102.)

[197] P. Novak, A. Shevchuk, P. Ruenraroengsak, M. Miragoli, A. J. Thorley, D. Klenerman, M. J. Lab, T. D. Tetley, J. Gorelik, and Y. E. Korchev, "Imaging single nanoparticle interactions with human lung cells using fast ion conductance microscopy," *Nano Letters*, vol. 14, no. 3, pp. 1202–1207, 2014. PMID: 24555574. (Cited on page 102.)

[198] Y. Takahashi, Y. Zhou, T. Miyamoto, H. Higashi, N. Nakamichi, Y. Takeda, Y. Kato, Y. Korchev, and T. Fukuma, "High-speed sicm for the visualization of nanoscale dynamic structural changes in hippocampal neurons," *Analytical Chemistry*, vol. 92, no. 2, pp. 2159–2167, 2020. PMID: 31840491. (Cited on page 102.)

[199] S. Dal Cengio and I. Pagonabarraga, "Confinement-controlled rectification in a geometric nanofluidic diode," *The Journal of Chemical Physics*, vol. 151, no. 4, p. 044707, 2019. (Cited on pages 102 and 119.)

[200] N. Sa and L. A. Baker, "Rectification of nanopores at surfaces," *Journal of the American Chemical Society*, vol. 133, no. 27, pp. 10398–10401, 2011. PMID: 21675734. (Cited on pages 102 and 119.)

[201] N. Sa, W.-J. Lan, W. Shi, and L. A. Baker, "Rectification of ion current in nanopipettes by external substrates," *ACS Nano*, vol. 7, no. 12, pp. 11272–11282, 2013. PMID: 24200344. (Cited on page 102.)

[202] K. McKelvey, S. L. Kinnear, D. Perry, D. Momotenko, and P. R. Unwin, "Surface charge mapping with a nanopipette," *Journal of the American Chemical Society*, vol. 136, no. 39, pp. 13735–13744, 2014. PMID: 25181551. (Cited on pages 102 and 118.)

[203] L. H. Klausen, T. Fuhs, and M. Dong, "Mapping surface charge density of lipid bilayers by quantitative surface conductivity microscopy," *Nature Communications*, vol. 7, no. 1, p. 12447, 2014. (Cited on pages 102, 105, and 119.)

[204] D. Perry, B. Paulose Nadappuram, D. Momotenko, P. D. Voyias, A. Page, G. Tripathi, B. G. Frenguelli, and P. R. Unwin, "Surface charge visualization at viable living cells," *Journal of the American Chemical Society*, vol. 138, no. 9, pp. 3152–3160, 2016. PMID: 26871001. (Cited on pages 102 and 119.)

[205] C. Zhu, L. Zhou, M. Choi, and L. A. Baker, "Mapping surface charge of individual microdomains with scanning ion conductance microscopy," *ChemElectroChem*, vol. 5, no. 20, pp. 2986–2990, 2018. (Cited on page 102.)

[206] L. Dorwling-Carter, M. Aramesh, H. Han, T. Zambelli, and D. Momotenko, "Combined ion conductance and atomic force microscope for fast simultaneous topographical and surface charge imaging," *Analytical Chemistry*, vol. 90, no. 19, pp. 11453–11460, 2018. PMID: 30148616. (Cited on pages 102 and 118.)

[207] F. M. Maddar, D. Perry, R. Brooks, A. Page, and P. R. Unwin, "Nanoscale surface charge visualization of human hair," *Analytical Chemistry*, vol. 91, no. 7, pp. 4632–4639, 2019. (Cited on pages 102 and 118.)

[208] A. S. Khair and T. M. Squires, "Surprising consequences of ion conservation in electro-osmosis over a surface charge discontinuity," *Journal of Fluid Mechanics*, vol. 615, p. 323–334, 2008. (Cited on pages 102, 103, 104, 105, 119, and 120.)

[209] R. W. Clarke, A. Zhukov, O. Richards, N. Johnson, V. Ostanin, and D. Klenerman, "Pipette–surface interaction: Current enhancement and intrinsic force," *Journal of the American Chemical Society*, vol. 135, no. 1, pp. 322–329, 2013. PMID: 23210472. (Cited on page 118.)

[210] T. Vicsek and A. Zafeiris, "Collective motion," *Physics Reports*, vol. 517, no. 3, pp. 71 – 140, 2012. Collective motion. (Cited on page 128.)

[211] E. Woillez, Y. Zhao, Y. Kafri, V. Lecomte, and J. Tailleur, "Activated escape of a self-propelled particle from a metastable state," *Physical Review Letters*, vol. 122, p. 258001, Jun 2019. (Cited on page 129.)

[212] A. Siria, M.-L. Bocquet, and L. Bocquet, "New avenues for the large-scale harvesting of blue energy," *Nature Reviews Chemistry*, vol. 1, p. 0091, 2017. (Cited on page 129.)